REPORT DOCUMENTATION PAGE

Form Approved OMB NO. 0704-0188

1. REPORT DATE (DD-MM-YYYY)	2. REPORT TYPE	3. DATES COVERED (From - To)
24-01-2020	Final Report	1-May-2016 - 30-Oct-2019

4. TITLE AND SUBTITLE

Final Report: Plasmon-phonon and plasmon-magnon interaction in metamaterials: multi-physics paradigm for acousto-optical and magneto-optical technologies

5a. CONTRACT NUMBER
W911NF-16-1-0261

5b. GRANT NUMBER

5c. PROGRAM ELEMENT NUMBER
611102

6. AUTHORS

5d. PROJECT NUMBER

5e. TASK NUMBER

5f. WORK UNIT NUMBER

7. PERFORMING ORGANIZATION NAMES AND ADDRESSES

University of Massachusetts - Lowell
600 Suffolk Street, Suite 226

Lowell, MA 01854 -3643

8. PERFORMING ORGANIZATION REPORT NUMBER

9. SPONSORING/MONITORING AGENCY NAME(S) AND ADDRESS (ES)

U.S. Army Research Office
P.O. Box 12211
Research Triangle Park, NC 27709-2211

10. SPONSOR/MONITOR'S ACRONYM(S)
ARO

11. SPONSOR/MONITOR'S REPORT NUMBER(S)
68104-PH.20

12. DISTRIBUTION AVAILIBILITY STATEMENT

Approved for public release; distribution is unlimited.

13. SUPPLEMENTARY NOTES

The views, opinions and/or findings contained in this report are those of the author(s) and should not contrued as an official Department of the Army position, policy or decision, unless so designated by other documentation.

14. ABSTRACT

15. SUBJECT TERMS

16. SECURITY CLASSIFICATION OF:			17. LIMITATION OF ABSTRACT	15. NUMBER OF PAGES	19a. NAME OF RESPONSIBLE PERSON
a. REPORT	b. ABSTRACT	c. THIS PAGE			Viktor Podolskiy
UU	UU	UU	UU		19b. TELEPHONE NUMBER
					978-934-3398

RPPR Final Report
as of 05-May-2020

Agency Code:

Proposal Number: 68104PH **Agreement Number: W911NF-16-1-0261**
INVESTIGATOR(S):

Name: Phd Viktor Podolskiy
Email: Viktor_Podolskiy@uml.edu
Phone Number: 9789343398
Principal: Y

Organization: **University of Massachusetts - Lowell**
Address: 600 Suffolk Street, Suite 226, Lowell, MA 018543643
Country: USA
DUNS Number: 956072490 EIN: 043167352
Report Date: 30-Jan-2020 Date Received: 24-Jan-2020
Final Report for Period Beginning 01-May-2016 and Ending 30-Oct-2019
Title: Plasmon-phonon and plasmon-magnon interaction in metamaterials: multi-physics paradigm for acousto-optical and magneto-optical technologies
Begin Performance Period: 01-May-2016 **End Performance Period:** 30-Oct-2019
Report Term: 0-Other
Submitted By: Phd Viktor Podolskiy Email: Viktor_Podolskiy@uml.edu
Phone: (978) 934-3398
Distribution Statement: 1-Approved for public release; distribution is unlimited.

STEM Degrees: 3 **STEM Participants:** 4

Major Goals: This program aimed to comprehensively address the plasmon-phonon and plasmon-magnon interaction in complex composite optical structures, often referred to as metamaterials. In particular, we focused on a material platform that comprises arrays of aligned plasmonic nanowires that are embedded into dielectric host. The program was a collaboration between University of Massachusetts at Lowell where the group of V. Podolskiy, PI of the project, worked on the theoretical aspects of the proposed work and King's College London where the group of A. Zayats, co-PI of the project, worked on experimental efforts. The program, as originally proposed, has two main thrusts: (i) understanding the acousto-optical phenomena in nanowire metamaterials, and (ii) understanding the magneto-optical phenomena in composites. The original time-table called for thrust (i) extending over first two years of the program and thrust (ii) taking the two latter years. The program was extended through a no-cost extension for a period of 6 months

See attachment for details

Accomplishments: We have developed and validated analytical description of the response of coupled magneto-optical plasmonic systems and utilized our theoretical and numerical techniques to analyze the behavior of Au nanowires that are surrounded by Ni shells

On the acoustic side of the program, we have optimized the structural parameters of the nanowire arrays to match the acoustic spectrum of nanowire arrays to capabilities of the pump-probe spectroscopy in our labs. The samples have been fabricated and analyzed. We are finalising the manuscripts on this subject. Acousto-optical studies of naturally occurring hyperbolic materials (CuS) have also been carried out, deminstrating effective generation of coherent phonons in plasmonic materials

A number of related projects aimed at understanding of multi-physics interactions in composites have been completed, as detailed in the attached file. Overall, the program resulted in 11 peer reviewed publications, several theses, and multiple conference presentations.

Training Opportunities: Two graduate students at U Mass Lowell and one graduate student at King's College London have been being directly supported by the program. In addition, the program has contributed to one M.S. and one completed Ph.D. theses one at UML and one Ph.D. thesis at KCL.

RPPR Final Report
as of 05-May-2020

Results Dissemination: The results have been disseminated through 11 peer-reviewed publications, theses, as well as through multiple (invited and contributed) conference presentations.

Honors and Awards: Prof. Podolskiy, PI of the program, has been elected Fellow of the American Physical Society (APS)

Protocol Activity Status:

Technology Transfer: Nothing to Report

PARTICIPANTS:

Participant Type: PD/PI
Participant: Viktor Podolskiy
Person Months Worked: 1.00 **Funding Support:**
Project Contribution:
International Collaboration:
International Travel:
National Academy Member: N
Other Collaborators:

Participant Type: Postdoctoral (scholar, fellow or other postdoctoral position)
Participant: Anton Bykov
Person Months Worked: 2.00 **Funding Support:**
Project Contribution:
International Collaboration:
International Travel:
National Academy Member: N
Other Collaborators:

Participant Type: Graduate Student (research assistant)
Participant: Abantika Ghosh
Person Months Worked: 3.00 **Funding Support:**
Project Contribution:
International Collaboration:
International Travel:
National Academy Member: N
Other Collaborators:

ARTICLES:

RPPR Final Report
as of 05-May-2020

Publication Type: Journal Article Peer Reviewed: Y **Publication Status:** 1-Published
Journal: Light: Science & Applications
Publication Identifier Type: DOI Publication Identifier: 10.1038/lsa.2016.273
Volume: 6 Issue: 6 First Page #: e16273
Date Submitted: 8/26/17 12:00AM Date Published: 6/1/17 4:00AM
Publication Location:
Article Title: Spontaneous emission in non-local materials
Authors: Pavel Ginzburg, Diane J Roth, Mazhar E Nasir, Paulina Segovia, Alexey V Krasavin, James Levitt, Liisa
Keywords: metamaterials, nonlocality, purcell effect
Abstract: Light–matter interactions can be strongly modified by the surrounding environment. Here, we report on the first experimental observation of molecular spontaneous emission inside a highly non-local metamaterial based on a plasmonic nanorod assembly. We show that the emission process is dominated not only by the topology of its local effective medium dispersion, but also by the non-local response of the composite, so that metamaterials with different geometric parameters but the same local effective medium properties exhibit different Purcell factors. A record-high enhancement of a decay rate is observed, in agreement with the developed quantitative description of the Purcell effect in a non-local medium. An engineered material non-locality introduces an additional degree of freedom into quantum electrodynamics, enabling new applications in quantum information processing, photochemistry, imaging and sensing with macroscopic composites.
Distribution Statement: 3-Distribution authorized to U.S. Government Agencies and their contractors
Acknowledged Federal Support: **Y**

Publication Type: Journal Article Peer Reviewed: Y **Publication Status:** 1-Published
Journal: Advanced Optical Materials
Publication Identifier Type: DOI Publication Identifier: 10.1002/adom.201700299
Volume: 5 Issue: 15 First Page #: 1700299
Date Submitted: 8/26/17 12:00AM Date Published: 8/1/17 8:00AM
Publication Location:
Article Title: Geometry Defines Ultrafast Hot-Carrier Dynamics and Kerr Nonlinearity in Plasmonic Metamaterial Waveguides and Cavities
Authors: Silvia Peruch, Andres Neira, Gregory A. Wurtz, Brian Wells, Viktor A. Podolskiy, Anatoly V. Zayats
Keywords: metamaterials, optical nonlocality, nonlinear optics
Abstract: Hot carrier dynamics in plasmonic nanorod metamaterials and its influence on the metamaterial's optical Kerr nonlinearity is studied. The electron temperature distribution induced by an optical pump in the metallic component of the plasmonic metamaterial leads to geometry-dependent variations of the optical response and its dynamics as observed in both the transmission and reflection properties of the metamaterial slab. Thus, the ultrafast dynamics of a metamaterial's optical response can be controlled via modal engineering. Both the transient response relaxation time and magnitude of the nonlinearity are shown to depend on the modal-induced spatial profile of the electron temperature distribution and the hot-electron diffusion in nanorods. The nonlocal effects, depending on the excitation-induced losses in the metal, are shown to dictate the modal structure of the metamaterial slab and the associated dynamics of its nonlinear response. The opportunity of controlling the electron tempe
Distribution Statement: 3-Distribution authorized to U.S. Government Agencies and their contractors
Acknowledged Federal Support: **Y**

RPPR Final Report
as of 05-May-2020

Publication Type: Journal Article Peer Reviewed: Y **Publication Status:** 1-Published
Journal: Advanced Optical Materials
Publication Identifier Type: DOI Publication Identifier: 10.1002/adom.201600941
Volume: 5 Issue: 9 First Page #: 1600941
Date Submitted: 8/26/17 12:00AM Date Published: 5/1/17 4:00AM
Publication Location:
Article Title: Control of the Stokes Shift with Strong Coupling
Authors: Ekembu K. Tanyi, Hannah Thuman, Nicolas Brown, Samantha Koutsares, Viktor A. Podolskiy, Mikhail A
Keywords: Strong coupling, plasmonics
Abstract: Strong coupling of excitons in macroscopic ensembles of quantum emitters and cavities (or surface plasmons) can lead to dramatic change of the optical properties and modification of the dispersion curves, characterized by the normal mode splitting of the order of 1 eV. Such gigantic alteration of the hybrid energy states enables scores of unparalleled physical phenomena and functionalities, ranging from enhancement of electrical conductivity to control of chemical reactions. While coupling of single emitters to a cavity is a pure quantum mechanical phenomenon, the origin of the strong coupling involving large ensembles of molecules is the subject of controversy. In this work, the strong coupling of rhodamine 6G dye molecules with silver Fabry–Perot cavities is studied and the significant increase of the Stokes shift between the excitation and the emission bands of hybridized molecules is demonstrated. The proposed empirical model of the underlying physics calls for the quantum mechanic
Distribution Statement: 3-Distribution authorized to U.S. Government Agencies and their contractors
Acknowledged Federal Support: **Y**

Publication Type: Journal Article Peer Reviewed: Y **Publication Status:** 1-Published
Journal: Optics Express
Publication Identifier Type: DOI Publication Identifier: 10.1364/OE.26.017541
Volume: 26 Issue: 13 First Page #: 17541
Date Submitted: 8/29/18 12:00AM Date Published: 6/1/18 12:00AM
Publication Location:
Article Title: Low-frequency nonlocal and hyperbolic modes in corrugated wire metamaterials
Authors: Bo Fan, Dmitry Filonov, Pavel Ginzburg, Viktor A. Podolskiy
Keywords: Plasmonics, metamaterial
Abstract: Metamaterials based on arrays of aligned plasmonic nanowires have recently attracted significant attention due to their unique optical properties that combine tunable strong anisotropy and nonlocality. These optical responses provide a platform for implementation of novel sensing, imaging, and quantum optics applications. Basic building blocks, used for construction of those peculiar composites, are plasmonic metals, such as gold and silver, which have moderate negative values of permittivities at the optical spectral range. Scaling the plasmonic behavior to lower frequencies remains a longstanding challenge also owing to the emergence of strong spatial dispersion in homogenized artificial composites. At lower THz and GHz frequencies, the electromagnetic response of noble metals approaches that of perfect electric conductors, preventing straightforward scaling of visible-frequency plasmonics to the frequency domains that are important for a vast range of applications, including...
Distribution Statement: 3-Distribution authorized to U.S. Government Agencies and their contractors
Acknowledged Federal Support: **Y**

RPPR Final Report
as of 05-May-2020

Publication Type: Journal Article Peer Reviewed: Y **Publication Status:** 1-Published
Journal: Optics Letters
Publication Identifier Type: DOI Publication Identifier: 10.1364/OL.43.002668
Volume: 43 Issue: 11 First Page #: 2668
Date Submitted: 8/29/18 12:00AM Date Published: 5/1/18 12:00AM
Publication Location:
Article Title: Directional emission of rhodamine 6G on top of a silver grating
Authors: E. K. Tanyi, S. Mashhadi, S. D. Bhattacharyya, T. Galfsky, V. Menon, E. Simmons, V. A. Podolskiy, N. M
Keywords: Metamaterials; Thin films, optical properties.
Abstract: We have observed directional spontaneous emission of rhodamine 6G dye deposited on top of a silver grating and found that its angular distribution patterns were very different in TE and TM polarizations. The latter was related to the dispersion curves determined based on the polarized reflection spectra measured at multiple incidence angles. The most intriguing finding of this Letter was a resonance, which was coupled with TE-polarized light and determined the characteristic double-crescent patterns in the TE polarized spontaneous emission. This observation, as well as nearly similar resonance observed in TM polarization, was tentatively explained in terms of leaky waveguide modes supported by a film of dye-doped polymer.
Distribution Statement: 3-Distribution authorized to U.S. Government Agencies and their contractors
Acknowledged Federal Support: **Y**

Publication Type: Journal Article Peer Reviewed: Y **Publication Status:** 1-Published
Journal: ACS Photonics
Publication Identifier Type: DOI Publication Identifier: 10.1021/acsphotonics.7b00690
Volume: 4 Issue: 10 First Page #: 2470
Date Submitted: 8/29/18 12:00AM Date Published: 10/1/17 4:00AM
Publication Location:
Article Title: Nonlocal Effects in Transition Hyperbolic Metamaterials
Authors: B. Wells, Zh. A. Kudyshev, N. Litchinitser, V. A. Podolskiy
Keywords: spatial dispersion, nonlocality, nanowire metamaterials, transition metamaterials, epsilon-near-zero, field enhancement
Abstract: Light?matter interactions at a particular point in a material may be dominated by properties of the medium at this point, or they could be affected by the electromagnetic properties of the medium in the surrounding regions. In the former case, the medium is said to be local, while in the latter, it is nonlocal. Recent studies of light?matter interactions in composite optical metamaterials showed that nonlocal effects enable new optical phenomena that are not acounted for by the conventional, local effective medium description. Up until now the majority of studies focused on metamaterials with spatially uniform material parameters. However, optical metamaterials with electromagnetic material parameters gradually changing from positive to negative values, so-called transition materials, have been predicted to induce a strong enhancement of the local electric or magnetic field in the vicinity of the zero refractive index point. This opens new opportunities for sensing and low-intensity...
Distribution Statement: 3-Distribution authorized to U.S. Government Agencies and their contractors
Acknowledged Federal Support: **Y**

RPPR Final Report
as of 05-May-2020

Publication Type: Journal Article Peer Reviewed: Y **Publication Status:** 1-Published
Journal: Optics Express
Publication Identifier Type: DOI Publication Identifier: 10.1364/OE.26.030588
Volume: 26 Issue: 23 First Page #: 30588
Date Submitted: 8/27/19 12:00AM Date Published: 11/1/18 4:00AM
Publication Location:
Article Title: Single-transverse-mode broadband InAs quantum dot superluminescent light emitting diodes by parity-time symmetry
Authors: Ruizhe Yao, Chi-Sen Lee, Viktor Podolskiy, Wei Guo
Keywords: light emitting diode, parity time symmetry, quantum dot
Abstract: Parity-time (PT) symmetry breaking in counterintuitive gain/loss coupled waveguide designs is numerically and theoretically investigated. The PT symmetry mode selection conditions are determined theoretically. Single-transverse-mode broadband InAs quantum dot (QD) superluminescent light emitting diodes (SLEDs) are fabricated and characterized; the PT symmetric broad-area SLEDs contain laterally coupled gain and loss PT- symmetric waveguides. Single-transverse-mode operation is achieved by parity-time symmetry breaking. The broadband SLEDs exhibit a uniform Gaussian-like emission spectrum with the 3-dB bandwidth of 110 nm. Far-field characteristics of the coupled waveguide SLEDs exhibit a single-lobe far-field pattern when the gain and loss waveguides are biased at the injection current of 600 mA and 60 mA, respectively
Distribution Statement: 1-Approved for public release; distribution is unlimited.
Acknowledged Federal Support: **Y**

Publication Type: Journal Article Peer Reviewed: Y **Publication Status:** 1-Published
Journal: Optica
Publication Identifier Type: DOI Publication Identifier: 10.1364/OPTICA.5.001502
Volume: 5 Issue: 12 First Page #: 1502
Date Submitted: 8/27/19 12:00AM Date Published: 11/1/18 4:00AM
Publication Location:
Article Title: Structural second-order nonlinearity in plasmonic metamaterials
Authors: Brian Wells, Anton Yu. Bykov, Giuseppe Marino, Mazhar E. Nasir, Anatoly V. Zayats, Viktor A. Podolskiy
Keywords: metamaterials, nonlinear optics, plasmonics
Abstract: Nonlinear processes are at the core of many optical technologies whose further development require optimized materials suitable for nanoscale integration. Here we demonstrate the emergence of a strong bulk second-order nonlinear response in a plasmonic nanorod composite comprised of centrosymmetric materials. We develop an effective-medium description of the underlying physics, compare its predictions to the experimental results, and analyze the limits of its applicability. We demonstrate strong tunable generation of the ??-polarized second-harmonic light in response to either ??- or ??-polarized excitation. High second-harmonic enhancement is observed for fundamental frequencies in the epsilon-near-zero spectral range. The work demonstrates emergence of structurally tunable nonlinear optical response in plasmonic composites and presents a new nonlinear optical platform suitable for integrated nonlinear photonics.
Distribution Statement: 1-Approved for public release; distribution is unlimited.
Acknowledged Federal Support: **Y**

RPPR Final Report
as of 05-May-2020

Publication Type: Journal Article Peer Reviewed: Y **Publication Status:** 1-Published
Journal: Laser & Photonics Reviews
Publication Identifier Type: DOI Publication Identifier: 10.1002/lpor.201900101
Volume: Issue: First Page #: 1900101
Date Submitted: 8/27/19 12:00AM Date Published: 8/1/19 4:00AM
Publication Location:
Article Title: Singlet–Triplet Transition Rate Enhancement inside Hyperbolic Metamaterials
Authors: Diane J. Roth, Pavel Ginzburg, Liisa M. Hirvonen, James A. Levitt, Mazhar E. Nasir, Klaus Suhling, Dav
Keywords: metamaterials, radiation decay engineering
Abstract: The spontaneous emission process is known to be largely affected by the surrounding electromagnetic environment of emitters, which manifests itself via the Purcell enhancement of decay rates. This phenomenon has been extensively investigated in the case of dipolar transitions in quantum systems, commonly delivering fast decay rates in comparison to forbidden transitions such as high-order multipolar transitions or spin-forbidden, singlet–triplet phosphorescence processes. Here, a decay rate enhancement of almost 2750-fold is demonstrated for a ruthenium-based phosphorescent emitter located inside a plasmonic hyperbolic metamaterial. The standard electromagnetic local density of states description, typically employed for the Purcell factor analysis of dipolar transitions, is unable to account for a photoluminescence enhancement of this magnitude, which is attributed to the interplay between the local density of states and strongly inhomogeneous electromagnetic fields inside the metamate
Distribution Statement: 1-Approved for public release; distribution is unlimited.
Acknowledged Federal Support: **Y**

Publication Type: Journal Article Peer Reviewed: Y **Publication Status:** 1-Published
Journal: Laser & Photonics Reviews
Publication Identifier Type: DOI Publication Identifier: 10.1002/lpor.201800154
Volume: 13 Issue: 1 First Page #: 1800154
Date Submitted: 8/27/19 12:00AM Date Published: 1/1/19 5:00AM
Publication Location:
Article Title: Electrically Injected Parity Time-Symmetric Single Transverse-Mode Lasers
Authors: Ruizhe Yao, Chi-Sen Lee, Viktor Podolskiy, Wei Guo
Keywords: parity time symmetry, quantum dot laser
Abstract: Single transverse–mode operation of broad area–coupled waveguide lasers enabled by parity-time (PT) symmetry is demonstrated. The PT-symmetric laser operates on coupled waveguide cavities with electrically tuned gain and loss. Such a counterintuitive waveguide design enables PT-symmetric breaking, causing unique mode selection and ultimately enables single-mode operation. By electrically tuning the loss in the loss region of the coupled waveguide cavity, several different PT-symmetric phases are analyzed theoretically, and the corresponding PT-symmetric phase transition is demonstrated experimentally in the coupled waveguide laser.
Distribution Statement: 1-Approved for public release; distribution is unlimited.
Acknowledged Federal Support: **Y**

RPPR Final Report
as of 05-May-2020

Publication Type: Journal Article Peer Reviewed: Y **Publication Status:** 1-Published
Journal: Advanced Optical Materials
Publication Identifier Type: DOI Publication Identifier: 10.1002/adom.201801420
Volume: Issue: First Page #: 1801420
Date Submitted: 8/27/19 12:00AM Date Published: 3/1/19 5:00AM
Publication Location:
Article Title: Magneto-Optical Metamaterials: Nonreciprocal Transmission and Faraday Effect Enhancement
Authors: Bo Fan, Mazhar E. Nasir, Luke H. Nicholls, Anatoly V. Zayats, Viktor A. Podolskiy
Keywords: Metamaterials, faraday effect, non-reciprocity, magneto-optics
Abstract: Magneto-optical effects are at the heart of modern technologies providing opportunities for polarization control in laser physics and optical communications, metrology, and in high-density data storage. Here a new type of a hyperbolic magneto-optical metamaterial based on Au–Ni nanorod arrays is developed. The metamaterial exhibits an enhanced magneto-optical response with large rotation of the polarization plane and nonreciprocal light transmission. The effective medium model that incorporates both plasmonic and magnetooptical phenomena in complex multicomponent nanorod media is proposed and validated. The experimental and theoretical results indicate that the magnetooptical response of the nanostructured metamaterial is drastically enhanced and spectrally modified with respect to bulk ferromagnetic media due to interplay between strong anisotropy and magnetic field induced polarization rotation.
Distribution Statement: 1-Approved for public release; distribution is unlimited.
Acknowledged Federal Support: **Y**

CONFERENCE PAPERS:

Publication Type: Conference Paper or Presentation **Publication Status:** 1-Published
Conference Name: CLEO/QELS 2017
Date Received: 27-Aug-2017 Conference Date: 18-May-2017 Date Published: 18-May-2017
Conference Location: San Jose, CA
Paper Title: Magneto-optical nanowire metamaterials
Authors: Bo Fan, Mazhar Nasir, Anatoly Zayats, Viktor Podolskiy
Acknowledged Federal Support: **Y**

Publication Type: Conference Paper or Presentation **Publication Status:** 1-Published
Conference Name: CLEO/QELS
Date Received: 29-Aug-2018 Conference Date: 17-May-2018 Date Published: 13-May-2018
Conference Location: San Jose, CA, USA
Paper Title: Structural Second Order Nonlinearity in Metamaterials
Authors: B. Wells, A. Bykov, G. Marino, M.Nasir, A.V. Zayats, V.A. Podolskiy
Acknowledged Federal Support: **Y**

Publication Type: Conference Paper or Presentation **Publication Status:** 1-Published
Conference Name: CLEO: QELS_Fundamental Science
Date Received: 27-Aug-2019 Conference Date: 05-May-2019 Date Published:
Conference Location: San Jose, California
Paper Title: Field Enhancement and Ultrafast Plasmonics In Nonlocal Transitional Metamaterials
Authors: B. Wells, R. M. Córdova-Castro, A. V. Zayats, and V. A. Podolskiy
Acknowledged Federal Support: **Y**

RPPR Final Report
as of 05-May-2020

Publication Type: Conference Paper or Presentation **Publication Status:** 1-Published
Conference Name: Nonlinear Optics
Date Received: 27-Aug-2019 Conference Date: 15-Jul-2019 Date Published: 15-Jul-2019
Conference Location: Waikoloa Beach, Hawaii
Paper Title: Strong Structural Nonlinearity from Plasmonic Metamaterials in the Infrared
Authors: B.M. Wells, A. Yu. Bykov, G. Marino, M. E. Nasir, A. V. Zayats, and V. A. Podolskiy
Acknowledged Federal Support: **Y**

DISSERTATIONS:

Publication Type: Thesis or Dissertation
Institution: U Mass Lowell
Date Received: 29-Aug-2018 Completion Date: 11/17/17 7:12AM
Title: VALIDITY OF EFFECTIVE MEDIUM TECHNIQUES FOR DESCRIBING OPTICS OF NONLOCAL NANOWIRE ARRAYS
Authors: P. Catalano
Acknowledged Federal Support: **Y**

Publication Type: Thesis or Dissertation
Institution: University of M
Date Received: 27-Aug-2019 Completion Date: 8/8/18 8:32PM
Title: Engineered materials and structures for magneto-optics, long-wave plasmonics, and subwavelength imaging
Authors: Bo Fan
Acknowledged Federal Support: **Y**

Publication Type: Thesis or Dissertation
Institution: Kings College London
Date Received: 27-Aug-2019 Completion Date: 4/30/19 4:00AM
Title: Hyperbolic Plasmonic Materials
Authors: Margoth Cordova Castro
Acknowledged Federal Support: **Y**

WEBSITES:

URL: http://faculty.uml.edu/vpodolskiy/codes/
Date Received: 24-Jan-2020
Title: V. Podolskiy research codes
Description: V. Podolskiy research codes released for non-profit use

1 *PLASMON-PHONON AND PLASMON-MAGNON INTERACTION IN METAMATERIALS: MULTI-PHYSICS PARADIGM FOR ACOUSTO-OPTICAL AND MAGNETO-OPTICAL TECHNOLOGIES*

V.A. Podolskiy and A.V. Zayats

Final report: May, 01 2016 to Oct, 30 2019

2 SCIENTIFIC PROGRESS AND ACCOMPLISHMENTS:

2.1 OVERVIEW OF PROJECTS GOALS AND OBJECTIVES

The program aim was to comprehensively address the plasmon-phonon and plasmon-magnon interaction in complex composite optical structures, often referred to as metamaterials. In particular, we focus on a material platform that comprises arrays of aligned plasmonic nanowires that are embedded into dielectric host. The program is a collaboration between University of Massachusetts at Lowell where the group of V. Podolskiy, PI of the project, works on the theoretical aspects of the proposed work and King's College London where the group of A. Zayats, co-PI of the project, works on experimental efforts.

The program, as originally proposed, **has two main thrusts**: (i) understanding the acousto-optical phenomena in nanowire metamaterials, and (ii) understanding the magneto-optical phenomena in composites. The original time-table called for thrust (i) extending over first two years of the program and thrust (ii) taking the two latter years.

Plasmonic nanowire metamaterial platform emerges as one of the most practical metamaterial configurations. Over the years, plasmonic nanowire arrays have been demonstrated to enable record figures of merit in biosensing, acousto-optical sensing, as well as open new direction in nonlinear optics and in lifetime engineering [1-4]. The origin of these unusual phenomena often can be traced to unique, hyperbolic, dispersion relationship of the plane waves propagating inside the uniaxial material that is formed by aligned nanowire arrays,

$$\frac{k_x^2+k_y^2}{\epsilon_{zz}}+\frac{k_z^2}{\epsilon_\perp}=\frac{\omega^2}{c^2} \quad \text{.....(1)}$$

Where effective medium parameters relating to the permittivity of metals (ϵ_m) and dielectric (ϵ_d), and to the volumetric concentration of nanowires in the composite p, respectively, are given by

$$\epsilon_{zz}=p\,\epsilon_m+(1-p)\epsilon_d \quad \text{.....(2)}$$

$$\epsilon_\perp=\frac{p\,\epsilon_m E_m+(1-p)\epsilon_d E_d}{p\,E_m+(1-p)E_d} \quad \text{.....(3)}$$

with $E_m=2E_d\epsilon_d/(\epsilon_m+\epsilon_d)$ [1]. It has been shown that the effective parameters ϵ_{zz} and $\epsilon_\perp$ can be of different sign for a substantial part of optical spectrum stretching from visible through IR bands.

It has been shown that while reflection and transmission of light through nanowire metamaterials are reasonably well described by the (local) effective medium response, given by Eqs. (1…3), light generation

inside the composite (that includes fluorescence, harmonic generation, etc.) is significantly affected by plasmon polaritons propagating along the wires [5]. The effective medium description of the composite can be generalized to take into account the effects of these modes. However, the extended effective medium permittivity becomes nonlocal (explicitly dependent on the wavevector). Adequate description of photon-plasmon interactions in nanowires has been developed with help of previous ARO funding.

The main motivation of this project was to move beyond pure optical response of metamaterials and analyze the interplay between plasmonic interaction in the composites, as well as magnetic and acoustic modes that can be supported by the system. Table 1 summarizes the goals and initial projected timeline of the project, along with current progress.

	Yr 1	Yr 2 (Option 1)	Yr 3 (Option 2)
Aim 1 (plasmon-phonon interactions)	(N) Acouto-optical coupling in composites		
	(A) nonlocal hyper-crystals	(A) Homogenization of acoustic and multi-physics response of metamaterials	
	(E) photo-acoustic properties of metamaterials	(E) Pump-probe studies of plasmon-phonon coupling	
Aim 2 (plasmon-magnon interaction)	(N) Magneto-optical coupling and spin waves in metamaterials		
		(A) Spin-waves in composites	(A) Non-reciprocal dynamics in nonlocal metamaterials
	(E) Spin-waves in composites	(E) Spin-waves in composites	(E) Non-reciprocal dynamics in nonlocal metamaterials
Key	Completed	In progress	Not started

Table 1. Projected timeline of the project; (A), (N), and (E) correspond to analytical, numerical, and experimental sub-tasks respectively.

We have developed and validated analytical description of the response of coupled magneto-optical plasmonic systems and utilized our theoretical and numerical techniques to analyze the behavior of Au nanowires that are surrounded by Ni shells [6].

On the acoustic side of the program, we have optimized the structural parameters of the nanowire arrays to match the acoustic spectrum of nanowire arrays to capabilities of the pump-probe spectroscopy in our labs. The samples have been fabricated and analyzed. We are finalising the manuscripts on this subject. Acousto-optical studies of naturally occurring hyperbolic materials (CuS) have also been carried out, deminstrating effective generation of coherent phonons in plasmonic materials.

In addition to the main aims of the proposal, we have undertaken several efforts that are highly synergistic with the proposed formalism. In particular, we have demonstrated strong structural second harmonic generation in nanowire composites, and have developed novel material platform for linear and nonlinear optics. We have also explored implications of PT-symmetry breaking for lasing and LED structures [7,8].

2.2 RESEARCH OVER THE PERIOD

Overall, ARO funding has contributed to publication of 11 peer-reviewed manuscripts, 2 Ph.D. theses, and 1 MS thesis [6-19], as well as multiple conference presentations. The team is currently working on three additional publications to be submitted to peer-reviewed journals in the coming months.

2.2.1 Magneto-Optical response of composites

Over the term of the project we have developed novel material platform for plasmon-enhanced magneto optical response. The platform represents a further development of plasmonic nanorod platform that the team has been working on for the past several years. Plasmonic magneto-optical nanorods represent a multi-shelled wire structures comprising regular arrays of plasmonic wires surrounded by ~5-nm-thick magneto-optical shells deposited in the dielectric host materials. (Fig.1)

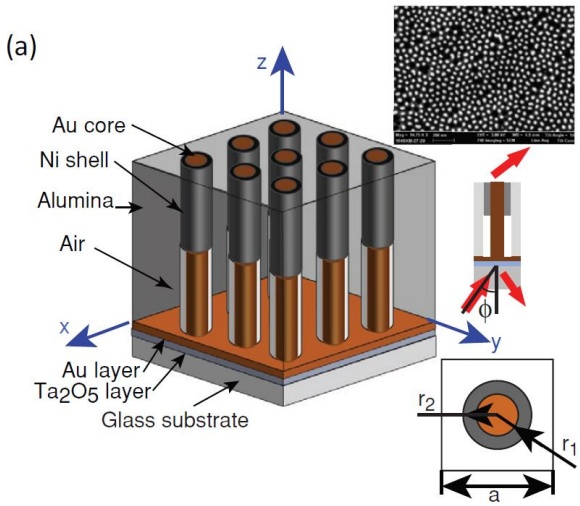

Fig.1. Geometry of the plasmonic nanowires with magneto-optical shells

Over the course of the program we have perfected protocols for fabricating these complex composites and developed effective medium description of their optical response. Importantly, the comparison of our experimental data and theoretical predictions indicates that magneto-optical response of nanostructured Ni is significantly stronger than that of its bulk counterpart, providing an opportunity to demonstrate both polarization plane rotation and asymmetric transmission (Fig.2), phenomenon that is unique to anisotropic magnetooptical materials. The manuscript summarizing these studies has been published in Adv.Opt.Mat[6] and the relevant results been disseminated to the scientific community at multiple conferences. We are finalising a manuscript detailing the dynamics of the guided modes in magneto-optical arrays.

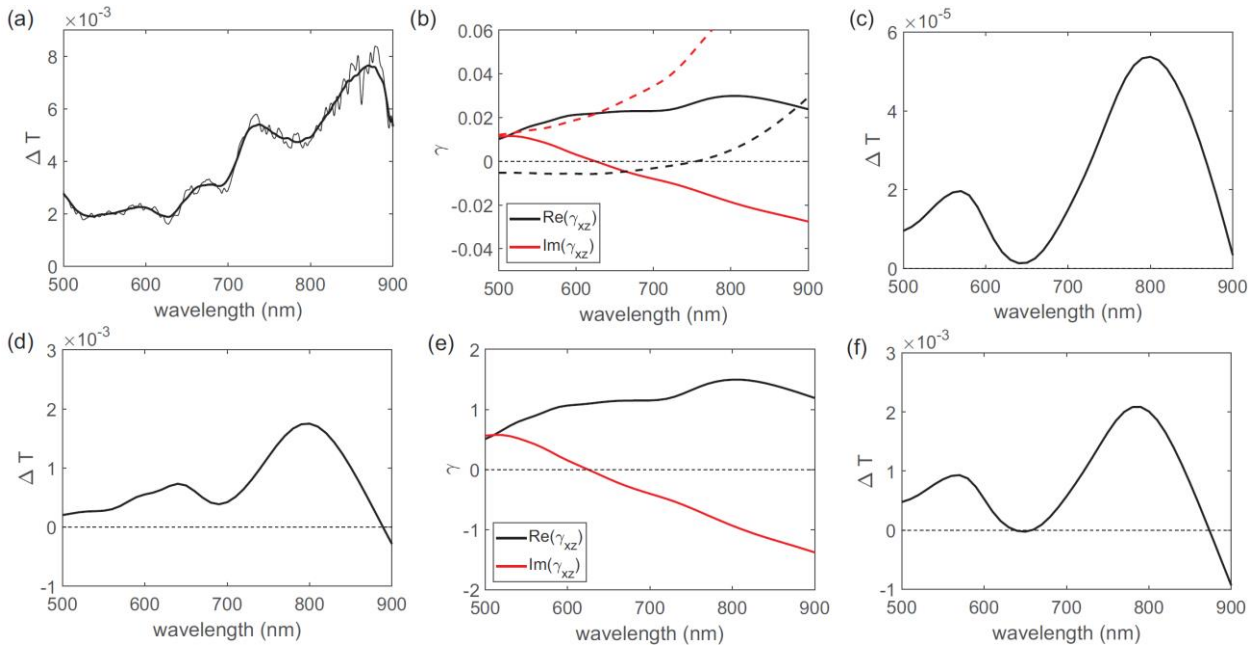

Fig.2 Asymmetric transmission, a hallmark of the anisotropic magnetooptical materials; (a) experimental data; (b) magneto-optical response of bulk Ni (dashed line) and predicted response of the composite (solid lines). (c) predicted transmission asymmetry for the sample shown in Fig.1, assuming the response in (b); note that this response is several orders of magnitude weaker than the one observed in experiment. Panel (e) shows the response of the composite assuming that the magneto-optical behavior of Ni is enhanced 50 times with respect to tabulated data; panels (d) and (f) show the transmission asymmetry obtained using full-wave solutions of Maxwell equations and effective medium theory, respectively.

Finally, the numerical implementation of the effective medium response is freely available on the PI www[20]

2.2.2 Acoustic response of nanorod composites

We have analyzed numerically the acoustic modes of nanowire composites, and have utilized the resulting numerical calculations to optimize the structure of the metamaterial to support the acoustic mode in the ~10 GHz frequency range that is accessible in our pump-probe experiments. As outlined in the Report 3, the metamaterial targeting 150-nm-thick, 55-nm diameter wires separated by 100 nm, in alumina matrix, has been fabricated and characterized. As detailed in the Report 3, pump-probe spectroscopy revealed the presence of the fundamental mode with ~9 GHz frequency, in line with the theoretical predictions.

Acousto-optical effects in a naturally occurring hyperbolic material were studied demonstrating the excitation of coherent phonons, which is not typical for plasmonic materials [21].

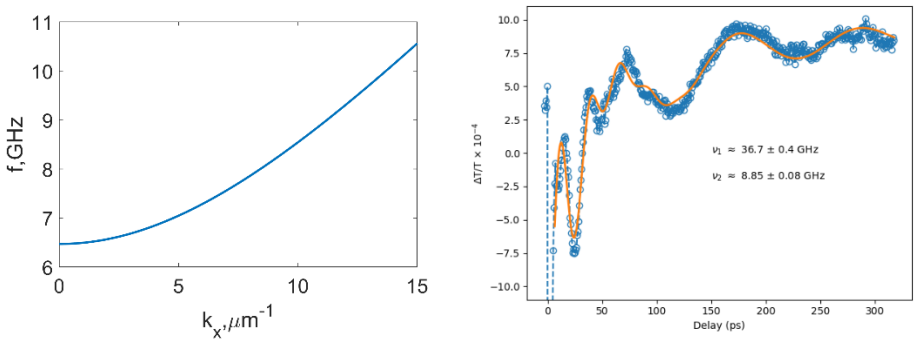

Fig.3 Dispersion of the main acoustic mode in nanowire metamaterials, calculated theoretically (left) and the pump-probe experiments demonstrating excitation of the acoustic mode (right)

2.2.3 Successes in nano-photonics beyond magneto-optics and acousto-optics

In addition to analysis of acousto- and magneto-optical response of metamaterials the team has completed a number of related projects, aimed at better understanding material properties of nanowire and wire-inspired composites. In particular, the team has

- ✓ Discovered theoretically and demonstrated experimentally existence of strong structural nonlinear response in plasmonic nanorod composites [13]. This discovery provides an alternative (to optimization of homogeneous media) approach to nonlinear optics and has potential to open a new research subfield
- ✓ Demonstrated the inter-relationship between geometry and ultrafast (hot-carrier) dynamics in composites [19]
- ✓ Demonstrated strong influence of structural nonlocality of metamaterials on light emission properties. Importantly, we have shown that structural nonlocality affects emission from both dipolar [17] and dipole-prohibited[12] transitions (Fig.4)

In particular, we have analyzed emission kinetics of Ruthenium-dpp-based complex in water, deposited on glass (used as a reference) and deposited inside the nonlocal wire metamaterial. We have discovered that metamaterial accelerates the spin-flip transition of Ru-dpp by a factor of $\sim 3 \times 10^3$. Importantly, we have also demonstrated that conventional theory of Purcell enhancement (developed with dipolar transitions in mind) is not applicable to spin-flip and other dipole-prohibited transitions.

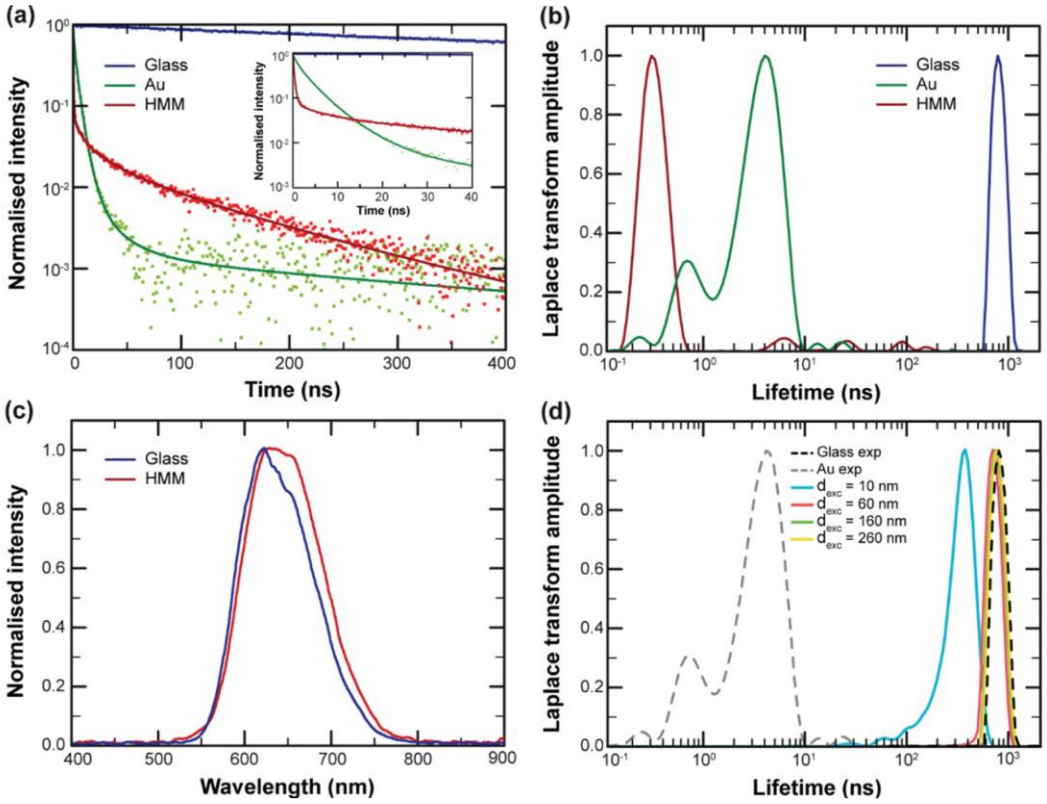

Fig.4 (a) emission kinetics of Ru-dpp in water on glass substrate (blue), on gold substrate (green), and in nonlocal metamaterial (red); note the strong non-single-exponential decay (dots represent experimental data; lines correspond to Laplace transform. (b) Lifetime distributions representing the fits from (a); (c) emission spectra of Ru in water deposited on glass and in the metamaterial; (d) theoretical calculations of lifetime distributions above the solid gold film recalculated from the glass spectrum[12].

2.2.4 Structural nonlocality for intensity enhancement in plasmonic nanocone arrays

We have previously introduced the plasmonic nanocone platform and demonstrated the utility of this platform to tune optical spectra beyond what is available with nanorod composites [22]. In the course of this program we have further analyzed the dynamics of optical response in this new material platform. We have demonstrated that structural nonlocality, that modifies optical response in nanowire composites, dominates optics of even lossy nanocone composites. In particular, the cone-shaped geometry of metamaterial illuminated by an incident electromagnetic wave promotes excitation of the additional wave. This additional wave propagates towards the apex of the cone, simultaneously concentrating the local optical intensity in its vicinity. As result, plasmonic nanocone metamaterials enable broadband enhancement of electromagnetic radiation at the well-defined ~10-nm-sized spatial areas. Out analysis further suggests that when the hot-spots are excited by the ultrafast pulses, the formation of the hot-spot is delayed with respect to excitation pulse by approximately 10 fs (Fig.5) [23]

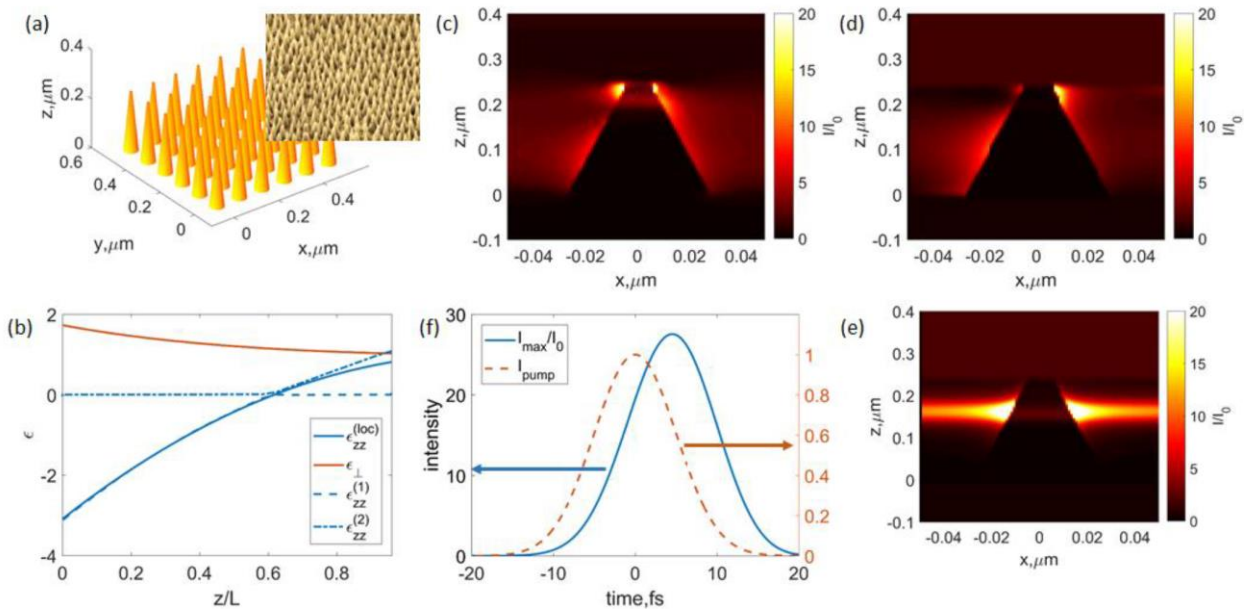

Fig. 5 (a) Schematic geometry (main figure) and SEM image (inset) of the nanocone metamaterial; (b) z-dependence of the diagonal components of the effective permittivity tensor at a wavelength of $\lambda_0 = 700\ nm$; (c,d,e) the intensity distributions in the nanocone metamaterial calculated with (c) full-wave solutions of the Maxwell equations, (d) nonlocal, and (e) local effective medium theories; (f) time-dependence of the maximum local intensity in the nanocone metamaterial excited by a 10-fs-long Gaussian pulse; solid and dashed lines represent metamaterial response and the incident field, respectively (note difference in vertical scales); in panels (c-f) the metamaterial is excited by a p-polarized light incident at $\sim 30^o$ from vacuum from the tip-side of the metamaterial.

2.2.5 Nonlocal hyperbolic metamaterials at radio frequencies.

Plasmonic nanowire platform found numerous applications at the visible and near-infrared frequency ranges. However, there is significant interest in realizing similar applications at lower, radio frequency range. Unfortunately, PEC-like response of gold and other noble metals at lower frequencies prohibits straightforward mapping of nanowire or nanocone platforms to these lower frequencies. To address this fundamental challenge, we have developed an approach to realize nonlocal hyperbolic response in low-frequency (RF) photonics[14]. The technique, summarized in Fig. 6 relies on spoof plasmons supported by the corrugated PEC surfaces to take on the role of visible-frequency plasmonic modes. As seen in Fig.6, the metamaterial comprising arrays of corrugated PEC wires supports three different modes; two of which have transverse character and one of which has field profile that strongly resembles that of the additional wave in plasmonic wire metamaterials. Importantly, our research indicates that the dispersion of the three waves in corrugated wire RF composites can be mapped to the analytical results derived for smooth visible-frequency plasmonic wires[5]

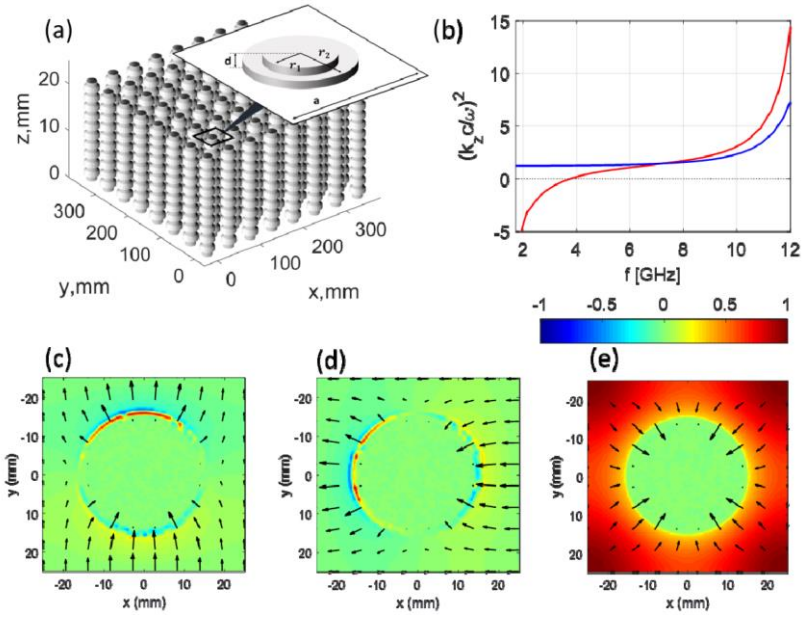

Fig.6 (a) geometry of corrugated wire spoof-plasmonic metamaterial; panel (b) illustrates dispersion of the modes supported by the system, while panel (c) illustrates the distribution of the electric field in these modes across the unit cell (arrows represent E_x, E_y components while color background represents E_z field)

2.2.6 Machine learning-based subwavelength imaging

We are developing a novel technique capable to characterize deep subwavelength (~100-nm) geometries with visible and near-IR light. The new approach, outlined in Fig.7, that combines the recently-developed analytical interscale mixing microscopy [24] with machine learning paradigms provides a novel avenue for characterization and spectroscopy of small objects. In particular, the experimental setup previously utilized in interscale mixing microscopy[24] is used to record diffractive patterns of the finite two-dimensional gratings with subwevelenght period containing multiple defects.

The recorded diffractive patterns are then post-processed to maximize the information representing interference from the multiple sub-wavelength slits. In parallel, theoretical calculations are used to generate a set of diffractive pattern from a set of almost-identical gratings whose openings openings have small ~10-nm variations in position and size. The resulting theoretical ensembles are represented in Fourier-Bessel space $\tilde{I}(k_r, \phi) \mu \sum_{m,j} C_{mj} J_m \left(\alpha_{mj} \frac{k_r}{k_0}\right) \cos(m\phi)$, and the coefficients C_{mj} are used to train AI-based classifiers. Finally, the theory-trained AI machines are utilized to dissent the original experimental structures. Our analysis indicates that the proposed novel approach allows to detect and characterize objects that are approximately 1/10-th of the free-space wavelength across.

In addition, our analysis provides the outlook at the relative importance of individual m, j combinations to successful image recovery and, as result, allows us to get an insight into information storage and into machine-learning dynamics.

Our results have been submitted to CLEO/QELS 2020 conference and are being finalized for submission to a peer-reviewed journal. Fig.7

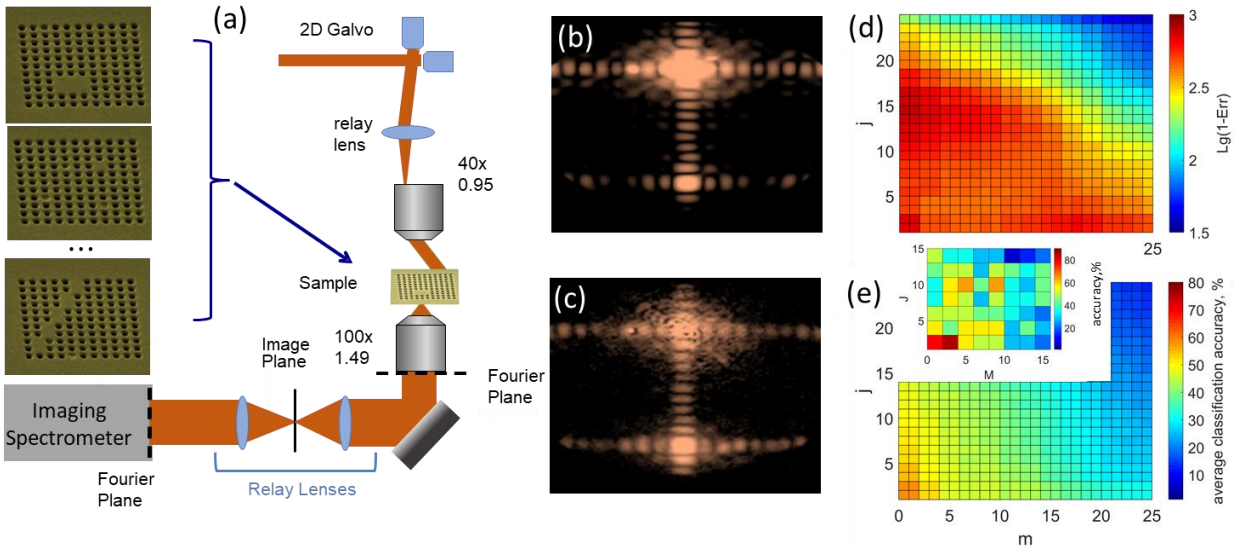

Fig.7: Panel (a) illustrates experimental setup (main figure) and several examples of the diffractive structures analyzed in our experiments (right insets); typical processed diffractive intensity patterns are shown in panels (b) (theory) and (c) (experiment); panels (d,e) illustrate the main result of this work, the average contribution of the information contained in a given m, j pair to the recovery accuracy, as indicated by analysis of theoretical (d) and experimental (e) data; both panels (d,e) represent averages of multiple recovery attempts with different combinations of Bessel harmonics. Inset in (e) illustrates one such individual study as described in the text

3 INTER-GROUP COMMUNICATION

No productive research is possible without efficient communication. Over the course of the program, the team members have extensively collaborated with each other; the following list summarizes some of these activities

- We regularly communicated via e-mail, and exchanged data via Dropbox and OneDrive services
- We held regular (approximately weekly) telecom conferences via Skype and/or phone
- Members of the two teams met during multiple conferences, including the Faraday discussions in London, UK, Metamorphose in Finland, and CLEO/QELS in San Jose, CA, US.

4 STUDENT TRAINING AND EDUCATION

The computational and analytical research, completed over the course of the project, formed the basis for PhD thesis of Bo Fan (UML) and for MS thesis of Paul Catalano (UML), in UK, nancone metamaterials fabrication and analysis of the optical properties were the basis for a PhD thesis of Ms Margoth Cordova Castro. Research on acousto-optical metamaterials and on diffractive microscopy has contributed to Ph.D. studies of Christopher Roberts and Abantika Ghosh (UML).

5 REFERENCES

1. C.Simovski, et.al. Adv.Mat 24 4229 (2012); J. Yao et al., Science 321, 930 (2008); P.A. Belov et.al. Phys. Rev. B 77, 193108 (2008) S. Thongrattanasiri and V.A. Podolskiy, Opt. Lett. 34, 890 (2009); J. Elser, R. Wangberg, V.A. Podolskiy, E.E. Narimanov Appl.Phys.Lett. 89, 261102 (2006); A. Kabashin, et.al., Nat.Mat., **8**, 867 (2009); G. A. Wurtz, et.al. Nat. Nanotech. **6**, 107 (2011)
2. Z. Jacob, I.I. Smolyaninov, E.E. Narimanov, Appl.Phys.Lett. 100, 161103 (2012); A.N. Poddubny, P.A. Belov, and Y.S. Kivshar, Phys. Rev. A 84, 023807 (2011); O. Kidwai, S.V. Zhukovsky, and J E. Sipe, Opt. Lett. 36, 2530 (2011); W.Yan, M.Wubs, N.A.Mortensen, Phys.Rev.B, 86, 205429 (2012)
3. P. Ginzburg, D. Roth, M.E. Nasir, P. Segovia Olvera, A.V. Krasavin, J. Levitt, L.M. Hirvonen, B. Wells, K. Suhling, D. Richards, V.A. Podolskiy, A.V. Zayats, *Spontaneous emission in nonlocal materials*, Nature Light: Science and Applications, **6**, e16273 (2017)
4. G. A. Wurtz, R. Pollard, W. Hendren, G. P. Wiederrecht, D. J. Gosztola, V. A. Podolskiy, and A. V. Zayats, "*Designed nonlocality-enhanced sub-picosecond nonlinearities in plasmonic nanorod metamaterial*", Nature Nanotechnology **6**, 107 (2011)
5. B. Wells, A.V. Zayats, V.A. Podolskiy, *Nonlocal optics of plasmonic nanowire metamaterials*, Phys Rev B **89**, 035111 (2014)
6. B. Fan, M. Nasir, A.V. Zayats, and V.A. Podolskiy, *Nonreciprocity and Faraday effect enhancement in magneto-optical metamaterials*, Adv.Opt.Mater. **2019**, 181420 (2019)
7. R. Yao, C-S Lee, V. Podolskiy, W. Guo, *Single-Transverse-Mode Broadband InAs Quantum Dot Superluminescent Light Emitting Diodes by Parity-time Symmetry*, Opt.Exp, **26**, 30588 (2018)
8. R. Yao, C.-S. Lee, V. Podolskiy, W.Guo *Electrically injected Parity-Time (PT) symmetric single transverse mode lasers*, Las. and Photonics Reviews, **13**, 1800154 (2019)
9. P. Catalano , validity of effective medium techniques for describing optics of nonlocal nanowire arrays, M.S. thesis, University of Massachusetts Lowell, 2017
10. Bo Fan, Engineered materials and structures for magneto-optics, long-wave plasmonics, and subwavelength imaging, Ph.D. thesis University of Massachusetts Lowell, 2018
11. Margoth Cordova Castro, Hyperbolic Plasmonic Materials, Ph.D. thesis, King's College London, 2019.
12. D.J. Roth, P. Ginzburg, L. Hirvonen, J. Levitt, M.E. Nasir, K. Suhling, D. Richards, V.A. Podolskiy, and A.V. Zayats, *Singlet-triplet transition rate enhancement inside hyperbolic metamaterials*, Laser&Photonic Reviews **13,** 1900101 (2019)
13. B. Wells, A. Yu. Bykov, G. Marino, M.E. Nasir, A.V. Zayats, V.A. Podolskiy *Structural second-order nonlinearity in metamaterials*, Optica, **5**, 1502 (2018); **[top 10 downloads in Dec. 2018, UML press release]**
14. B. Fan, D. Filonov, P. Ginzburg, V.A. Podolskiy *Low frequency Nonlocal and Hyperbolic Modes in Corrugated Wire Metamaterials*, Opt.Exp. **26** 17541 (2018) **[Opt.Exp Editor's Pick]**
15. E.K. Tanyi, S. Mashhadi, S.D. Bhattacharyya, T. Galfsky, V. Menon, E. Simmons, V.A. Podolskiy, N. Noginova, M.A. Noginov, *Directional emission of Rhodamine 6G on Top of a Silver Grating,* Opt. Lett. **43**, 2668 (2018)
16. B. Wells, Zh.A. Kudyshev, N. Litchinitser, V.A. Podolskiy, *Nonlocal effects in transition hyperbolic metamaterials*, ACS Photonics, **4**, 2470 (2017)
17. P. Ginzburg, D. Roth, M.E. Nasir, P. Segovia Olvera, A.V. Krasavin, J. Levitt, L.M. Hirvonen, B. Wells, K. Suhling, D. Richards, V.A. Podolskiy, A.V. Zayats, *Spontaneous emission in nonlocal materials*, Nature Light: Science and Applications, **6**, e16273 (2017) [previously reported research]

18. E. K. Tanyi, H. Thuman, N. Brown, S. Koutsares, V. Podolskiy, M. A. Noginov, *Control of the Stokes Shift with the Strong Coupling,* Advanced Optical Materials, **5**, 1600941 (2017);
19. S. Peruch, A. Neira, G.A. Wurtz, B. Wells, V.A. Podolskiy, A.V. Zayats, *Geometry defines ultrafast hot carrier dynamics and Kerr nonlinearity in plasmonic metamaterial waveguides and cavities*, Adv. Opt. Mat **5**, 1700299 (2017)
20. See http://faculty.uml.edu/vpodolskiy/codes
21. A. Bykov et al. Ultrafast carrier and lattice dynamics in nanocrystalline plasmonic covelite
22. R. M. Córdova-Castro , A.V Krasavin, M.E Nasir, A.V Zayats, and W. Dickson, *Nanocone-based plasmonic metamaterials*, Nanotechnology **30**, 055301 (2019)
23. B. Wells et.al. *Field enhancement and ultrafast plasmonics in nonlocal transitional metamaterials* CLEO/QELS 2019, paper FTh4M.3 (2019)
24. C.M. Roberts, N. Olivier, W.P. Wardley, S. Inampudi, W. Dickson, A.V. Zayats, and V.A. Podolsk*iy Interscale Mixing Microscopy: far field imaging beyond the diffraction limit*, Opti**ca 3**, 803 (2016)

6 APPENDICES:

6.1.1 Manuscripts published

1. D.J. Roth, P. Ginzburg, L. Hirvonen, J. Levitt, M.E. Nasir, K. Suhling, D. Richards, V.A. Podolskiy, and A.V. Zayats, *Singlet-triplet transition rate enhancement inside hyperbolic metamaterials*, Laser&Photonic Reviews **13,** 1900101 (2019)
2. B. Fan, M. Nasir, A. Zayats, V. Podolskiy, *Nonreciprocity and Faraday effect enhancement in magneto-optical metamaterials,* Adv.Opt.Mater. **7**, 1801420 (2019)
3. R. Yao, C.-S. Lee, V. Podolskiy, W.Guo *Electrically injected Parity-Time (PT) symmetric single transverse mode lasers*, Laser and Photonics Reviews, **13**, 1800154 (2019) **[cover manuscript]**
4. B. Wells, A. Yu. Bykov, G. Marino, M.E. Nasir, A.V. Zayats, V.A. Podolskiy *Structural second-order nonlinearity in metamaterials*, Optica, **5**, 1502 (2018); **[top 10 downloads in Dec. 2018]**
5. R. Yao, C-S Lee, V. Podolskiy, W. Guo, *Single-Transverse-Mode Broadband InAs Quantum Dot Superluminescent Light Emitting Diodes by Parity-time Symmetry*, Opt.Exp, **26**, 30588 (2018)
6. B. Fan, D. Filonov, P. Ginzburg, V.A. Podolskiy *Low frequency Nonlocal and Hyperbolic Modes in Corrugated Wire Metamaterials*, Opt.Exp. **26** 17541 (2018) **[Opt.Exp Editor's Pick]**
7. E. Tanyi, S. Mashhadi, S. Bhattacharyya, T. Galfsky, V. Menon, E. Simmons, V. Podolskiy, N. Noginova, M.A. Noginov, *Directional emission of Rhodamine 6G on Top of a Silver Grating,* Opt. Lett. **43**, 2668 (2018)
8. B. Wells, Zh.A. Kudyshev, N. Litchinitser, V.A. Podolskiy, *Nonlocal effects in transition hyperbolic metamaterials*, ACS Photonics, **4**, 2470 (2017)
9. P. Ginzburg, D. Roth, M.E. Nasir, P. Segovia Olvera, A.V. Krasavin, J. Levitt, L.M. Hirvonen, B. Wells, K. Suhling, D. Richards, V.A. Podolskiy, A.V. Zayats, *Spontaneous emission in nonlocal materials*, Nature Light: Science and Applications, **6**, e16273 (2017) [previously reported research]
10. E. K. Tanyi, H. Thuman, N. Brown, S. Koutsares, V. Podolskiy, M. A. Noginov, *Control of the Stokes Shift with the Strong Coupling,* Advanced Optical Materials, **5**, 1600941 (2017);
11. S. Peruch, A. Neira, G.A. Wurtz, B. Wells, V.A. Podolskiy, A.V. Zayats, *Geometry defines ultrafast hot carrier dynamics and Kerr nonlinearity in plasmonic metamaterial waveguides and cavities*, Adv. Opt. Mat **5**, 1700299 (2017)

6.1.2 Theses published

1. P. Catalano, Validity of effective medium techniques for describing optics of nonlocal nanowire arrays, M.S. thesis, University of Massachusetts Lowell, 2017
2. Bo Fan, Engineered materials and structures for magneto-optics, long-wave plasmonics, and subwavelength imaging, Ph.D. thesis University of Massachusetts Lowell, 2018
3. Margoth Cordova Castro, Hyperbolic Plasmonic Materials, Ph.D. thesis, King's College London, 2019.

6.1.3 Manuscripts accepted for publication and under review

1. None

6.1.4 Manuscripts in preparation (not attached)

1. B.Fan, et al, Unidirectional modes in magneto-optical metamaterials
2. A. Ghosh et.al, Subwavelength imaging with machine learning
3. A. Bykov et al. Ultrafast carrier and lattice dynamics in nanocrystalline plasmonic covelite

The table below summarizes the commitment of the team members involved in research on the current program, regardless of their funding source

Name	Role	yr1	yr2	yr3	extension (Aug 1-Oct 31)	total
		(person-months)				
Viktor Podolskiy	PI	4	3	3	1	**11**
Anatoly Zayats	co-PI	2	2	2		**6**
Anton Bykov	Postdoc	2	2	2	2	**8**
Mazhar Nasir	Postdoc	5	5	5		**15**
Diane Roth	Other Professional	2	2	2		**6**
Paul Catalano	Other Professional	2	2			**4**
RM Cordova-Castro	Other Professional	5	5	5		**15**
Bo Fan	Graduate Student (research assistant)	15	12	1		**28**
Abantika Ghosh	Graduate Student (research assistant)		2	12	3	**17**

Singlet–Triplet Transition Rate Enhancement inside Hyperbolic Metamaterials

Diane J. Roth, Pavel Ginzburg, Liisa M. Hirvonen, James A. Levitt, Mazhar E. Nasir, Klaus Suhling, David Richards, Viktor A. Podolskiy, and Anatoly V. Zayats*

The spontaneous emission process is known to be largely affected by the surrounding electromagnetic environment of emitters, which manifests itself via the Purcell enhancement of decay rates. This phenomenon has been extensively investigated in the case of dipolar transitions in quantum systems, commonly delivering fast decay rates in comparison to forbidden transitions such as high-order multipolar transitions or spin-forbidden, singlet–triplet phosphorescence processes. Here, a decay rate enhancement of almost 2750-fold is demonstrated for a ruthenium-based phosphorescent emitter located inside a plasmonic hyperbolic metamaterial. The standard electromagnetic local density of states description, typically employed for the Purcell factor analysis of dipolar transitions, is unable to account for a photoluminescence enhancement of this magnitude, which is attributed to the interplay between the local density of states and strongly inhomogeneous electromagnetic fields inside the metamaterial. The large available range of spontaneous emission lifetimes reported here enables application of phosphorescent emitters in novel, fast, and efficient light-emitting sources, beneficial for optical communications, quantum information processing, spectroscopy, or bio-imaging.

1. Introduction

The enhancement of the spontaneous emission rates of dipolar emitters, known as the Purcell effect,[1] has been demonstrated in many different material environments, owing to the modification of the local density of electromagnetic states (LDOS) available for the emitters' relaxation.[2] Photonic structures, such as photonic crystals[3] or microresonators,[4] have received a lot of interest in the past thanks to their high quality factors, but their use has been hindered by diffraction limited modal volumes, restricting the enhancement factors. Instead, the use of plasmonic structures, such as nanoantennas[5] or plasmonic cavities,[6] has enabled the confinement of light to subwavelength scales, delivering modal volumes far beyond the diffraction limit. Despite the limitation of the enhancement factors due to the inherent material losses[7] of the plasmonic structures, the resonant character of the enhancement process nonetheless led to rather narrow enhancement bandwidths. Recently, sizeable spontaneous emission rate enhancements using metamaterials, ordered nanostructured media with designed electromagnetic properties, have been achieved. A subclass of metamaterials, namely hyperbolic metamaterials (HMM),[8] has been shown to deliver broadband non-resonant Purcell enhancement, limited by microscopic factors, such as the composite granularity.[9–11] Most of the experimental studies involving hyperbolic metamaterials reported Purcell factors of several tens,[12–15] reaching ≈80 with additional structuring of a metal-dielectric multilayer metamaterial.[16] In nanorod-based hyperbolic metamaterials, decay rate enhancements of dipolar emitters reaching up to 100 were observed, depending on the positioning of the emitters in the unit cell as well as the material losses,[9] and led to emission in both free space and waveguided modes of the metamaterial slab.[15,17]

Spontaneous emission from other atomic transitions has, however, not been extensively investigated, mostly due to their conventionally forbidden character strictly controlled by selection rules. Electric-dipole-forbidden atomic transitions, such as magnetic-dipole transitions, multipolar transitions with orbital angular momentum changes, spin-flip-required, or singlet–triplet transitions, are typically orders of magnitude slower than regular dipolar transitions between selection-rule-allowed states, and therefore are hardly experimentally observable. However, it was recently shown that using highly confined plasmon modes of 2D materials or surface magnon polaritons, these forbidden emission processes can be significantly accelerated and may

Dr. D. J. Roth, Dr. L. M. Hirvonen, Dr. J. A. Levitt, Dr. M. E. Nasir, Prof. K. Suhling, Prof. D. Richards, Prof. A. V. Zayats
Department of Physics and London Centre for Nanotechnology
King's College London
Strand, London WC2R 2LS, UK
E-mail: diane.roth@kcl.ac.uk
Dr. P. Ginzburg
School of Electrical Engineering
Tel Aviv University
Tel Aviv 69978, Israel
Prof. V. A. Podolskiy
Department of Physics and Applied Physics
University of Massachusetts Lowell
One University Ave
Lowell, MA 01854, USA

The ORCID identification number(s) for the author(s) of this article can be found under https://doi.org/10.1002/lpor.201900101

DOI: 10.1002/lpor.201900101

compete with conventional dipolar transitions with emission primarily into plasmonic and polaritonic modes; while the increased local density of electromagnetic states plays an important role in the Purcell effect, strong gradients in highly confined electromagnetic fields are essential for the enhancement of forbidden transitions.[18–21]

In the specific case of phosphorescence, which is a second-order quantum process, emitters typically exhibit lifetimes in the range of milliseconds to seconds,[22] orders of magnitude longer than the common nanosecond lifetimes of fluorescent dyes. This comes from the forbidden nature of the transitions involved in the emission process, including transitions between states of different spin multiplicities such as singlet–triplet transitions. However, the phosphorescence process can be enhanced in organometallic complexes possessing a heavy transition-metal element, favoring spin–orbit coupling interactions. This therefore results in improved quantum yields and shorter lifetimes of the order of 100 s of ns to 10 s of µs,[22] making the phosphorescent transitions experimentally accessible. Here we report on the decay rate enhancement of a singlet–triplet transition in a long lifetime phosphorescent ruthenium-based complex (Ru(dpp)) inside a gold-nanorod-based hyperbolic metamaterial. Large enhancements of the transition rate are observed on smooth gold films and metamaterial-based structures, suggesting the inapplicability of the commonly used Purcell factor for pure dipolar transitions, based on the electromagnetic local density of states modifications only. Embedding the emitters within the hyperbolic metamaterial, realised as an array of vertically aligned gold nanorods, yields the record lifetime reduction of ≈2750-fold at the maximum peak of the measured lifetime distribution (an ≈4800-fold reduction can be estimated at the tail of the lifetime distribution). Theoretical predictions, relying on electromagnetic local density of states, fail to predict such an enormous rate acceleration, instead pointing to the role played by the electromagnetic field gradients between the nanorods forming the array.

2. Results and Discussion

In this study, the decay dynamics of ruthenium-tris(4,7-diphenyl-1,10-phenanthroline) dichloride complex (Ru(dpp), Sigma-Aldrich) dissolved in different solvents, were measured in the vicinity of various plasmonic substrates, employing a time-correlated single photon counting (TCSPC) technique (see Experimental Section). Ru(dpp) is a transition metal complex, which is constituted of a central Ru^{2+} ion surrounded by 3 diphenyl-phenanthroline ligand molecules. Due to the presence of the ligands, these complexes exhibit unique electronic transitions called metal-to-ligand charge-transfer (MLCT) states. These transitions involve a charge transfer from the d-orbitals of the metal (t_{2g}) to the unoccupied π^*_L orbital of the ligands, as represented in the simplified diagram of the molecular orbitals and states of the complex in **Figure 1**a. Following absorption from the ground state (S_0) to the ^{1}MLCT singlet state, fast and efficient intersystem crossing occurs (k_{isc}) and electrons relax to the triplet ^{3}MLCT state. Emission from this triplet state to a singlet ground state is classified as phosphorescence (k_r) and exhibits lifetimes of the order of several microseconds, shorter than usual phosphorescent state lifetimes.[22] This efficient intersystem crossing and reduced lifetime of the triplet excited state is due to the presence of the ruthenium transition-metal ion, inducing spin–orbit interactions and enhancing the probability of the theoretically spin-forbidden triplet to ground-state transitions, therefore increasing the efficiency of the phosphorescence process.[23]

The ruthenium-based emitter was first dissolved in water and then deposited on: a glass substrate; a smooth gold film of thickness 30 nm; and inside a gold-nanorod-based hyperbolic metamaterial (see scanning electron microscopy (SEM) image, Figure 1b). The nanorod array parameters used in this experimental study were ≈250 ± 5 nm length, 50 ± 2 nm diameter, and 100 ± 2 nm center-to-center spacing. More details on the fabrication process of the metamaterial structure are available in the Experimental Section. The extinction spectra of the free-standing nanorod array immersed in water for different angles of incidence of transverse magnetic (TM)-polarized light (Figure 1c) show the presence of two modes associated with the electron motion perpendicular (⊥) and parallel (//) to the nanorods, respectively centered around 530 and 585 nm.[24]

The decay dynamics of the emitters deposited on glass, the gold film, and the nanorod metamaterial are represented in **Figure 2**a. These decays were fitted using an inverse Laplace transform method described in the Experimental Section. In the case of the emitters deposited on glass, the experimental decay is mono-exponential with a component of the lifetime distribution centered around 770 ns (Figure 2b), in good agreement with values found in the literature.[25] The measurements on the gold film and inside the nanorod-based metamaterial exhibit much more complicated decay dynamics compared to that of glass. For emitters placed on the gold film, the dependence of the lifetime on the position and orientation of the emitters with regard to the gold surface led to a multi-exponential decay (Figure 2a,b). The gold-film-modified lifetime distribution is broadened compared to the case of glass and is dominated by a lifetime component centered on 3.7 ns, corresponding to an increase of the decay rate of ≈210. The large span of the lifetime distribution is mainly related to the distance and orientation-dependent distribution of the emitters with regard to the interface but can also be influenced by the level of noise in the experimental data.

In this case, it is shown that the observed decay rate enhancement cannot be explained with the help of the commonly accepted LDOS theory.[2] The dynamics of emitters, modified by the presence of nearby plasmonic surfaces, in particular those of noble metals, is a well understood process. The key contributions leading to the modification of the spontaneous emission lifetime are mainly mirror-reflected waves, the excitation of surface plasmons, and quenching.[26] All these effects can be taken into account in a semi-analytical formula for the spontaneous emission enhancement as described in the Experimental Section. Using this theoretical formulation and the experimentally measured lifetime distribution of the emitter on a glass coverslip, a theoretical prediction of the lifetime distribution on the gold film could be obtained for various depths of optical excitation above the surface. This method takes into account the position of the emitters with regard to the metallic surface and their spatial orientation. As can be seen from the theoretical predictions (Figure 2d), even for a small depth of excitation, the average lifetime enhancement does not even increase by as much as a factor of 10, which is more than an order of magnitude lower than the

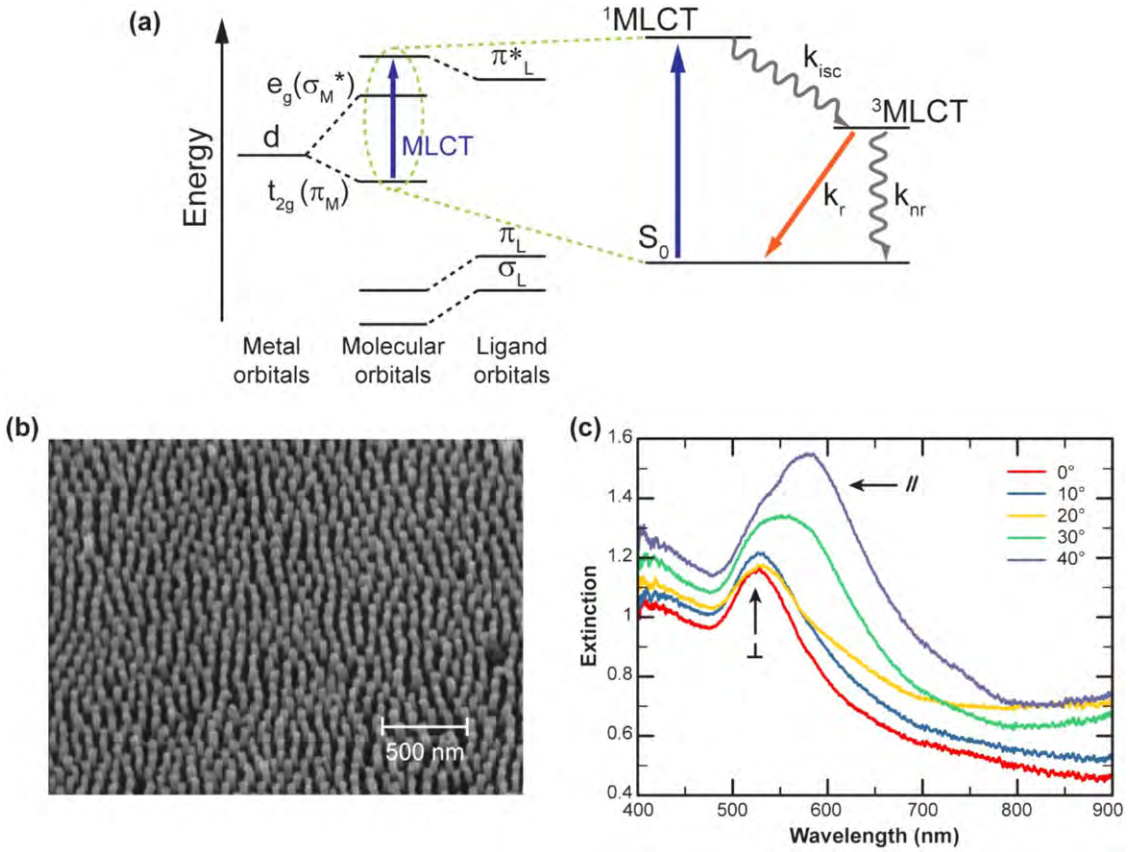

Figure 1. Properties of the ruthenium-based complex and the gold-nanorod-based metamaterial. a) Simplified molecular orbitals and state diagram of the ruthenium-based complex. Energy level positions are not to scale. MLCT stands for metal-to-ligand charge transfer. b) SEM image of a typical nanorod-based metamaterial sample (tilted at 45°). c) Experimental extinction spectra ($-\log T$) of the free-standing nanorod-based metamaterial in water ($n = 1.33$) taken for different angles of incidence of TM-polarized light.

experimentally observed value. It is worth noting that this same fitting procedure was conducted on the lifetime distributions of conventional fluorescent dyes (Alexa, Fluorescein, ATTO dyes) obtained using the same experimental setup, leading to an excellent agreement between theoretical and experimental data for a depth of excitation of 175 nm, verifying the validity of the method.[9]

When deposited inside the metamaterial, the phosphorescent emitter exhibits strongly accelerated decay dynamics, following a multi-exponential profile owing to the random position and polarization of the emitters within the metamaterial. The corresponding lifetime distribution is largely shifted toward shorter lifetimes and shows a maximum peak around 0.28 ns, corresponding to ≈2750-fold reduction of the spontaneous emission lifetime. A reduction of ≈4800-fold can be estimated at the tail of the main peak of the lifetime distribution. The homogenized properties of the metamaterial cannot be directly employed for calculation of the quantum dynamics of emitters, situated inside the structure, due to the finite size of the metamaterial unit cell.[27] However, a comprehensive analysis of the decay rates of emitters inside the nanorod-based metamaterial, taking into account spatial averages, local field corrections, interfaces, and spatial dispersion effects, which has been developed by us previously,[9] has been demonstrated to predict the correct decay rates for widely used dipolar emitters; this theory predicts an averaged spontaneous emission rate enhancement of about 30, also consistent with other reports. However, in the present case, as for a flat gold film, this theoretical description fails to predict the modification of the spontaneous emission lifetime. Therefore, this approach relying on the modification of the LDOS appears to be inapplicable in the case of phosphorescent emission. Photoluminescence spectroscopy of the emitter inside the metamaterial was also performed (Figure 2c), where a slight red-shift of the emission inside the metamaterial is observed with regard to the emitters deposited on glass.

Over the past decades, ruthenium-based emitters have extensively been used as efficient oxygen sensors.[28–30] In the presence of molecular oxygen, dynamic quenching occurring via collisions leads to the de-excitation of the emitter, ultimately reducing its spontaneous emission lifetime.[31] In order to minimize the effect of oxygen in our study, the same experiments were conducted in glycerol, exhibiting a higher viscosity than water and therefore limiting the dynamic quenching process. In this case, a nanorod-based metamaterial sample coated with a thin layer of polymer (7.5 nm), as described in the Experimental Section, was used as an additional material environment. This coating is expected to reduce the emission quenching due to the close proximity of the metallic nanorods to the emitters. The bare nanorod metamaterial sample was fabricated with the same geometrical parameters as the sample used for the emitter in water, while those

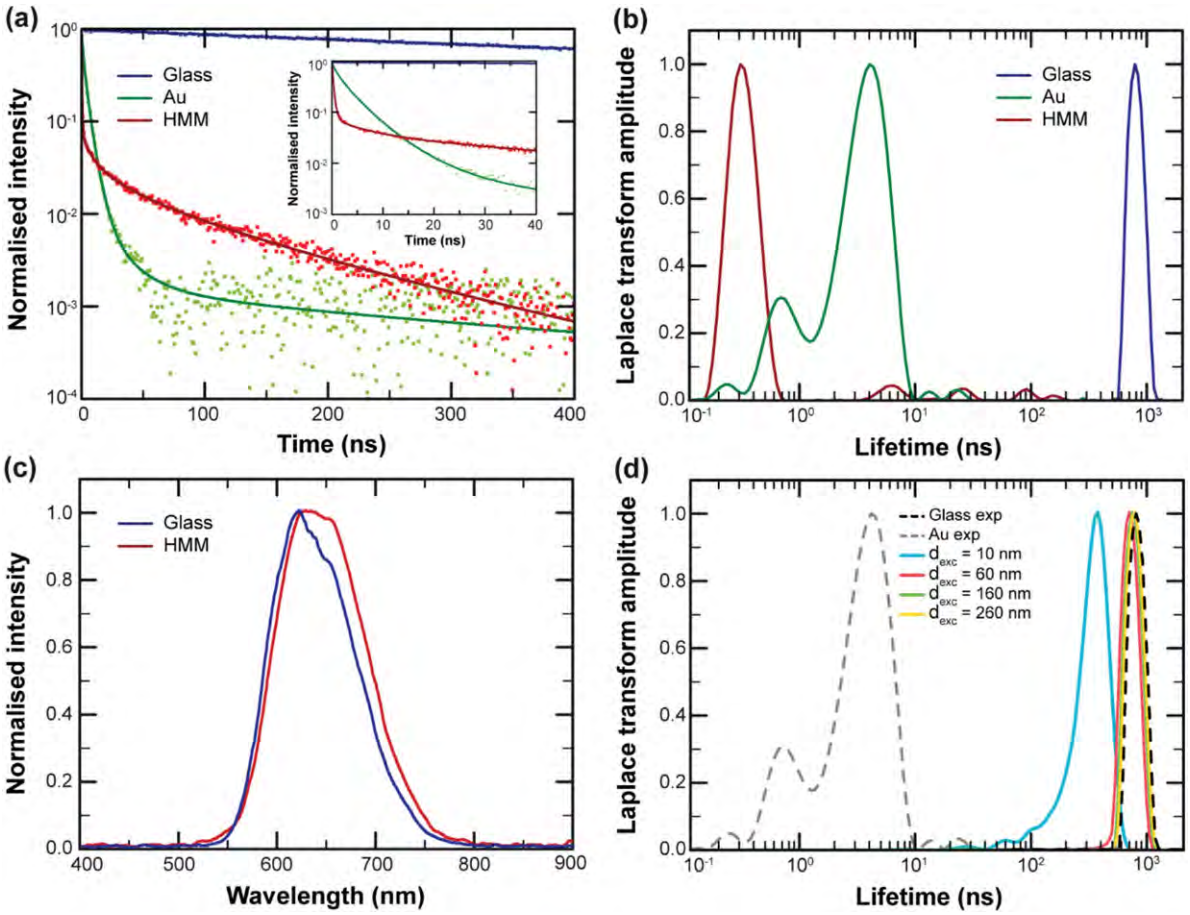

Figure 2. Ruthenium-based complex in water. a) Emission dynamics of Ru(dpp) in water on (blue) a glass substrate, (green) a 30 nm thick gold film, and (red) inside the nanorod-based metamaterial. The dotted lines correspond to the experimental data and the solid lines represent the fits performed using an inverse Laplace transform method. The inset shows the decays on gold and the hyperbolic metamaterial over a shorter timescale. b) Lifetime distributions corresponding to the fits in (a), with the same colour coding. c) Emission spectra of Ru(dpp) in water deposited (blue) on glass and (red) inside the nanorod-based metamaterial. d) Theoretical lifetime distributions above the smooth gold film recalculated from the measured lifetime distributions of the emitters deposited on glass for different depths of excitation (d_{exc}). Dashed lines are experimental data measured on glass and above the gold film, solid lines are the theoretical estimations.

of the coated nanorod metamaterial sample were ≈130 ± 5 nm length, 50 ± 2 nm diameter, and 100 ± 2 nm center-to-center spacing. The extinction spectra of both bare and polymer coated free-standing nanorods immersed in glycerol, for different angles of incidence of TM-polarized light, again show the presence of two peaks (**Figure 3**). In comparison with Figure 1c, an increased splitting between the two modes is observed due to the higher refractive index of glycerol to that of water.[24]

The analysis of the time-resolved measurements show that the decay dynamics of the emitters deposited on glass exhibits a mono-exponential profile, whereas the decay dynamics of the emitters in the cases of the gold film, the bare metamaterial, and the polymer coated metamaterial samples show here again more complicated profiles (**Figure 4**a). In the case of the emitters deposited on glass, the associated lifetime distribution of the complex is centered around 4.4 µs (Figure 4b), in good agreement with values found in the literature.[25] The lifetime distributions of the emitters placed on the gold film, the bare metamaterial, and the coated metamaterial are broadened and strongly shifted toward shorter lifetimes. Considering the position of the maximum of the dominant peak of the lifetime distribution, an ≈980-fold reduction of the lifetime is observed when the emitter is placed near the gold surface and about 2590-fold reduction in the case of the emitters inside the bare metamaterial. A reduction of ≈4600-fold can be estimated at the tail of the main peak of the lifetime distribution for the bare metamaterial. For the coated metamaterial sample, the presence of the polymer shell significantly reduces the decay rate enhancement of the ruthenium-based emitter compared to the bare metamaterial (Figure 4a). The corresponding distribution of lifetimes, represented in Figure 4b, exhibits a maximum around 3.9 ns, leading to a 1130-fold increase of the decay rate compared to the case of glass (an ≈2100-fold increase is observed at the tail of the main peak of the lifetime distribution). This more moderate rate enhancement can be related to the reduced access of the emitters to the field with strongest gradients and/or the prevention of nonradiative quenching typically occurring for emitters in very close proximity to metals, emphasizing the strong dependence of the decay rate on the positioning of the emitters within the metamaterial. Photoluminescence spectroscopy was performed for the emitters

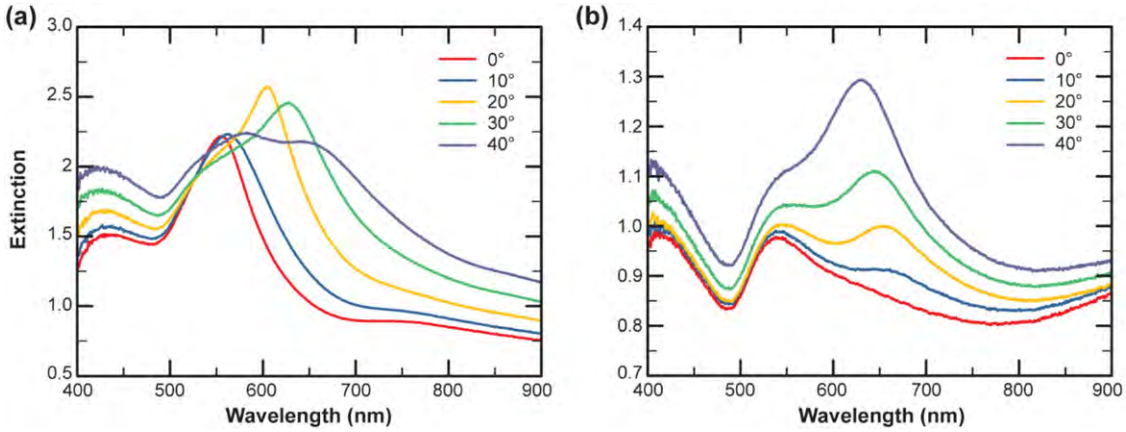

Figure 3. Optical properties of the metamaterial in glycerol. a,b) Experimental extinction spectra (−log*T*) of the bare (a) and the coated (b) free-standing nanorod-based metamaterial in glycerol ($n = 1.47$) taken for different angles of incidence of TM-polarized light.

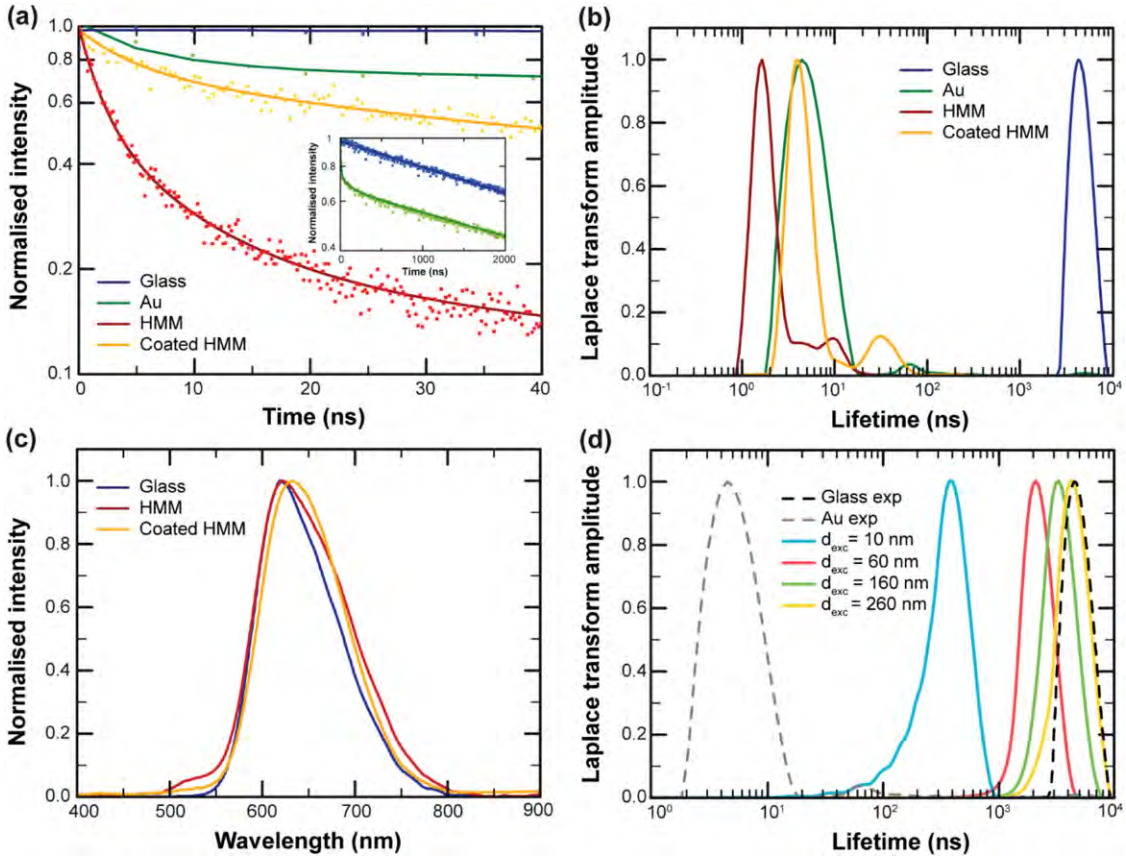

Figure 4. Ruthenium-based complex in glycerol. a) Emission dynamics of Ru(dpp) in glycerol on (blue) a glass substrate, (green) a 30 nm thick gold film, (red) inside the bare nanorod-based metamaterial, and (yellow) inside the polymer coated nanorod-based metamaterial. The dotted lines correspond to the experimental data and the solid lines represent the fits performed using an inverse Laplace transform method. The inset shows the decays on glass and gold on a longer timescale. b) Lifetime distributions corresponding to the fits in (a), with the same colour coding. c) Emission spectra of Ru(dpp) in glycerol deposited (blue) on glass, (red) inside the bare nanorod-based metamaterial, and (yellow) inside the polymer-coated nanorod-based metamaterial. d) Theoretical lifetime distributions above the smooth gold film recalculated from the measured lifetime distributions of the emitters deposited on glass for different depths of excitation (d_{exc}). Dashed lines are experimental data measured on glass and above the gold film, solid lines are the theoretical estimations.

on glass and inside the bare and coated metamaterials as shown in Figure 4c, where the emission spectra inside the metamaterial are here again slightly red-shifted compared to the emitter on glass, owing to the interaction with the nanorods. Using the same method as described in the case of the emitters dissolved in water, a theoretical prediction of the distribution on the gold film was obtained from the experimental distribution on glass for different depths of excitation (Figure 4d). The same conclusion as for the emitters in water can be observed and confirms the inapplicability of the conventional dipolar transition LDOS method for phosphorescence.

3. Conclusion

The decay dynamics of a phosphorescent ruthenium-based complex located in the vicinity of different electromagnetic environments were investigated. By combining the use of an emitter with large spin–orbit coupling and plasmonics, giant enhancements of the singlet–triplet transition rate were demonstrated in the vicinity of plasmonic substrates, including smooth thin gold films and gold-nanorod-based metamaterial structures, which cannot be simply described by the theory used for pure dipolar transitions. While the decay rate enhancement in the case of fluorescence processes has been proven to be theoretically predicted by the LDOS theory, we have shown that the description considering only the LDOS fails in the case of singlet–triplet transitions. For such transitions, the strong gradients of the electromagnetic field need to be taken into account.[18–21] These gradient effects are available in the near-field proximity to the gold film, due to the excitation of surface plasmons by the emitter's radiation, as well as between the nanorods forming the metamaterial. Decay rates up to two orders of magnitude higher than those predicted by the LDOS theory were observed both in the case of the emitter located near the smooth gold film and inside the metamaterial. Recently, several experimental studies on phosphorescent emission enhancement and decay rate manipulation with modified electromagnetic environments were reported. Among them, 320-fold luminescence enhancement in the vicinity of photonic crystals[32] was achieved and Purcell factors of more than 10^3 near plasmonic structures[33] were demonstrated, where the plasmonic systems investigated exhibit inherently strong field gradients related to the formed nanoscale gaps. It should be noted that a good agreement between experimental results and modeling using a theory based on standard dipolar transitions was obtained in ref. [33] for the investigation of a different ruthenium-based dye in a plasmonic gap antenna. Several factors may have however contributed to the dissimilar observations to those of our study, such as the extremely small gaps potentially leading to strong coupling to the gap modes of the system or the specific orientational characteristics of the dipole radiation in the simulations. In addition to these studies, the role of the field gradients and the differences between the rate modifications of dipolar and dipolar-forbidden transitions have also recently been shown theoretically.[34] A similar combination of a high LDOS and a nonuniform field distribution are likely responsible for the observations in this work and in the aforementioned papers. In nanorod-based metamaterials, additionally to the presence of strong field gradients, the interaction between the emitters and the optical orbital angular momentum of the cylindrical surface plasmons propagating along the nanorods might also play a role in the decay rate enhancement.[18] These results show the remarkable potential of hyperbolic metamaterials for the control of spontaneous emission rates over a large range, useful for the design of fast and enhanced light-emitting devices.

4. Experimental Section

Fabrication of the Metamaterial: The nanorod-based hyperbolic metamaterials were fabricated via electrodeposition of gold into a porous anodized aluminum oxide (AAO) template, as described in ref. [35]. Highly ordered pores were obtained using a two-step anodization process in 0.3 M oxalic acid at 40 V. After an initial anodization step, the porous layer formed was etched in a solution of H_3PO_4 (3.5%) and CrO_3 (20 g L^{-1}) at 70 °C, yielding an ordered, indented Al surface. The second step anodization was then performed under the same conditions as in the first step. An etching step in NaOH was then used to achieve pore widening and remove the barrier layer at the bottom of the pores. Gold electrodeposition was subsequently performed with a three-electrode system using a non-cyanide solution. The AAO template was subsequently removed using a mixed solution (1:1) of 0.3 M NaOH and 99.5% ethanol. The polymer coated nanorod sample was prepared using a layer-by-layer deposition of polyelectrolytes.[36] Each polyelectrolyte layer was prepared by alternating the deposition of poly(allylamine hydrochloride) and polystyrene sulfonate. For each deposition step, the plasmonic gold nanorod metamaterial was immersed in a polyelectrolyte solution (10 mg mL^{-1} in 1 mmol L^{-1} NaCl aqueous solution) for 30 min and washed with pure water (18 MΩ) to remove any unbound electrolyte. The layer-by-layer process was initiated with the cationic poly(allylamine hydrochloride) layer in order to facilitate the attachment of the first polyelectrolyte layer to the gold nanorods through amine–gold interactions. Gold films of 30 nm thickness sputtered on similar substrates were also used in these experiments.

Optical Characterization: Angle-resolved transmission spectroscopy was performed using light from a tungsten-halogen lamp polarized and collimated onto the sample. The transmitted light was then collected by an objective lens and coupled to a spectrometer equipped with a CCD camera via a multimode optical fiber.

Time-Resolved Photoluminescence Measurements: Time-correlated single photon counting (TCSPC) was employed to evaluate the decay dynamics of the ruthenium complex. A pulsed diode laser (Hamamatsu PLP-10 470, 200 kHz repetition rate) was used as the excitation source for the measurements on glass and on the gold film, while a pulsed laser beam from a supercontinuum laser (Fianium SC450-2, 20 MHz repetition rate), filtered with a 10 nm bandpass filter centered on 488 nm (ZET488/10×, Chroma) was used for the measurements in the metamaterial. The beam was focused on the sample using a high-numerical aperture oil-immersion objective (100×, NA = 1.3) and the PL signal was collected via the same objective. A 490 nm longpass dichroic mirror and a bandpass filter (620 nm, bandwidth 40 nm) centered on the emission peak of the complex were used for the lifetime measurements.

Photoluminescence Lifetime Data Analysis: Time-resolved measurements were analyzed using an inverse Laplace transform method,[9] allowing the determination of lifetime distributions in different material environments. This method does not require any preliminary estimation of the lifetime distribution and is based on the solution of the equation.

$$I(t) = \int_0^\infty F(\tau) e^{-t/\tau} d\tau \tag{1}$$

where $I(t)$ is the measured decay deconvoluted from the instrumental response function and $F(\tau)$ is the relative weight of the exponential decay components. An iterative fitting procedure was used to obtain stable results due to the ill-defined character of inverse methods.

Quantum Yield Measurements: Quantum yields of the ruthenium complex in water and glycerol were measured using a method developed by de Mello et al.[37] The samples, placed in an integrating sphere, were illuminated using a 470 ± 10 nm LED source. The emitted light was collected by a spectrometer (QE Pro, Ocean optics). Quantum yields of 0.099 and 0.81 were measured for the ruthenium complex in water and glycerol, respectively. This difference in the quantum yield may contribute to the stronger observed increase of the decay rate in the metamaterial for water than glycerol solvent.

Estimation of the Lifetime Distribution of the Ensemble of Emitters Near a Gold Film: A semi-analytical expression for the total decay rate enhancement of a point-like emitter near an interface between two materials was used in order to calculate the distribution of lifetimes near the gold surface, as developed in ref. [9]. Given the experimentally measured lifetime distributions of fluorophores near a glass substrate $F^{\text{exp}}_{\text{Glass}}(\tau)$, the corresponding distribution near a gold film can be derived as

$$F^{\text{Theor}}_{\text{Au}}(\tau) \sim \int_0^{d_{\text{exc}}} \left|\vec{E}_{\text{pump}}(z)\right|^2 Q_{\text{loc}}(z)\, n(z)\, F^{\text{exp}}_{\text{Glass}}\left(\frac{\tau}{\psi(z)}\right) dz \qquad (2)$$

where $\psi(z)$ is the position-dependent polarization-averaged total decay rate enhancement factor near the gold surface (relative to the case of emission near the glass substrate), $|\vec{E}_{\text{pump}}(z)|^2$ is the position-dependent intensity of the excitation light, $Q_{\text{loc}}(z)$ is the emitter's local quantum yield, and $n(z)$ is the distribution density of the emitters along the focal depth, which was assumed to be uniform. The depth of excitation d_{exc} was varied.

Acknowledgements

D.J.R., P.G., and L.M.H. contributed equally to this work. This research was sponsored in part by the US Army Research Office (ARO) (W911NF-12-1-0533 and W911NF-16-1-0261), the Binational Science Foundation (project 2016059), EPSRC (UK), and H2020 ERC project iPLASMM (321268).

Conflict of Interest

The authors declare no conflict of interest.

Keywords

hyperbolic metamaterials, phosphorescence, ruthenium complexes, singlet–triplet transitions, time-correlated single photon counting

Received: March 21, 2019
Revised: June 4, 2019
Published online:

[1] E. M. Purcell, *Phys. Rev.* **1946**, *69*, 37.
[2] L. Novotny, B. Hecht, *Principles of Nano-Optics*, Cambridge University Press, Cambridge, UK **2012**.
[3] P. Lodahl, A. F. Van Driel, I. S. Nikolaev, A. Irman, K. Overgaag, D. Vanmaekelbergh, W. L. Vos, *Nature* **2004**, *430*, 654.
[4] J. P. Reithmaier, G. Sek, A. Löffler, C. Hofmann, S. Kuhn, S. Reitzenstein, L. V. Keldysh, V. D. Kulakovskii, T. L. Reinecke, A. Forchel, *Nature* **2004**, *432*, 197.
[5] T. B. Hoang, G. M. Akselrod, C. Argyropoulos, J. Huang, D. R. Smith, M. H. Mikkelsen, *Nat. Commun.* **2015**, *6*, 7788.
[6] K. J. Russell, T.-L. Liu, S. Cui, E. L. Hu, *Nat. Photonics* **2012**, *6*, 459.
[7] J. A. Schuller, E. S. Barnard, W. S. Cai, Y. C. Jun, J. S. White, M. L. Brongersma, *Nat. Mater.* **2010**, *9*, 193.
[8] A. Poddubny, I. Iorsh, P. Belov, Y. Kivshar, *Nat. Photonics* **2013**, *7*, 948.
[9] P. Ginzburg, D. J. Roth, M. E. Nasir, P. Segovia, A. V. Krasavin, J. Levitt, L. M. Hirvonen, B. Wells, K. Suhling, D. Richards, V. A. Podolskiy, A. V. Zayats, *Light: Sci. Appl.* **2017**, *6*, e16273.
[10] Z. Jacob, I. I. Smolyaninov, E. E. Narimanov, *Appl. Phys. Lett.* **2012**, *100*, 181105.
[11] A. N. Poddubny, P. A. Belov, P. Ginzburg, A. V. Zayats, Y. S. Kivshar, *Phys. Rev. B* **2012**, *86*, 035148.
[12] T. Tumkur, G. Zhu, P. Black, Y. A. Barnakov, C. E. Bonner, M. A. Noginov, *Appl. Phys. Lett.* **2011**, *99*, 151115.
[13] M. Y. Shalaginov, V. V. Vorobyov, J. Liu, M. Ferrera, A. V. Akimov, A. Lagutchev, A. N. Smolyaninov, V. V. Klimov, J. Irudayaraj, A. V. Kildishev, A. Boltasseva, V. M. Shalaev, *Laser Photonics Rev.* **2015**, *9*, 120.
[14] H. N. S. Krishnamoorthy, Z. Jacob, E. Narimanov, I. Kretzschmar, V. M. Menon, *Science* **2012**, *336*, 205.
[15] D. J. Roth, A. V. Krasavin, A. Wade, W. Dickson, A. Murphy, S. Kéna-Cohen, R. Pollard, G. A. Wurtz, D. Richards, S. A. Maier, A. V. Zayats, *ACS Photonics* **2017**, *4*, 2513.
[16] D. Lu, J. J. Kan, E. E. Fullerton, Z. W. Liu, *Nat. Nanotechnol.* **2014**, *9*, 48.
[17] D. J. Roth, M. E. Nasir, P. Ginzburg, P. Wang, A. Le Marois, K. Suhling, D. Richards, A. V. Zayats, *ACS Photonics* **2018**, *5*, 4594.
[18] N. Rivera, I. Kaminer, B. Zhen, J. D. Joannopoulos, M. Soljacic, *Science* **2016**, *353*, 263.
[19] P. K. Jain, D. Ghosh, R. Baer, E. Rabani, A. P. Alivisatos, *Proc. Natl. Acad. Sci. USA* **2012**, *109*, 8016.
[20] J. Sloan, N. Rivera, J. D. Joannopoulos, I. Kaminer, M. Soljacic, *arXiv:1810.06761*, **2018**.
[21] A. Manjavacas, R. Fenollosa, I. Rodriguez, M. C. Jiménez, M. A. Miranda, F. Meseguer, *J. Mater. Chem. C* **2017**, *5*, 11824.
[22] J. R. Lakowicz, *Principles of Fluorescence Spectroscopy*, Springer Science & Business Media, Berlin, Germany **2013**.
[23] M. A. Baldo, D. O'Brien, Y. You, A. Shoustikov, S. Sibley, M. Thompson, S. R. Forrest, *Nature* **1998**, *395*, 151.
[24] N. Vasilantonakis, G. Wurtz, V. Podolskiy, A. Zayats, *Opt. Express* **2015**, *23*, 14329.
[25] L. M. Hirvonen, F. Festy, K. Suhling, *Opt. Lett.* **2014**, *39*, 5602.
[26] G. W. Ford, W. H. Weber, *Phys. Rep.* **1984**, *113*, 195.
[27] P. Ginzburg, A. V. Krasavin, A. N. Poddubny, P. A. Belov, Y. S. Kivshar, A. V. Zayats, *Phys. Rev. Lett.* **2013**, *111*, 036804.
[28] B. D. MacCraith, C. M. McDonagh, G. O'Keeffe, E. T. Keyes, J. G. Vos, B. O'Kelly, J. F. McGilp, *Analyst* **1993**, *118*, 385.
[29] B. Lei, B. Li, H. Zhang, S. Lu, Z. Zheng, W. Li, Y. Wang, *Adv. Funct. Mater.* **2006**, *16*, 1883.
[30] R. I. Dmitriev, D. B. Papkovsky, *Cell. Mol. Life Sci.* **2012**, *69*, 2025.
[31] K. J. Morris, M. S. Roach, W. Xu, J. Demas, B. DeGraff, *Anal. Chem.* **2007**, *79*, 9310.
[32] P. Zhou, D. Zhou, L. Tao, Y. Zhu, W. Xu, S. Xu, S. Cui, L. Xu, H. Song, *Light: Sci. Appl.* **2014**, *3*, e209.
[33] G. M. Akselrod, C. Argyropoulos, T. B. Hoang, C. Ciracì, C. Fang, J. Huang, D. R. Smith, M. H. Mikkelsen, *Nat. Photonics* **2014**, *8*, 835.
[34] A. Cuartero-González, A. I. Fernandez-Dominguez, *ACS Photonics* **2018**, *5*, 3415.
[35] P. Evans, W. R. Hendren, R. Atkinson, G. A. Wurtz, W. Dickson, A. V. Zayats, R. J. Pollard, *Nanotechnology* **2006**, *17*, 5746.
[36] C. Ciracì, R. Hill, J. Mock, Y. Urzhumov, A. Fernández-Domínguez, S. Maier, J. Pendry, A. Chilkoti, D. Smith, *Science* **2012**, *337*, 1072.
[37] J. C. de Mello, H. F. Wittmann, R. H. Friend, *Adv. Mater.* **1997**, *9*, 230.

Magneto-Optical Metamaterials: Nonreciprocal Transmission and Faraday Effect Enhancement

Bo Fan, Mazhar E. Nasir, Luke H. Nicholls, Anatoly V. Zayats, and Viktor A. Podolskiy**

Magneto-optical effects are at the heart of modern technologies providing opportunities for polarization control in laser physics and optical communications, metrology, and in high-density data storage. Here a new type of a hyperbolic magneto-optical metamaterial based on Au–Ni nanorod arrays is developed. The metamaterial exhibits an enhanced magneto-optical response with large rotation of the polarization plane and nonreciprocal light transmission. The effective medium model that incorporates both plasmonic and magneto-optical phenomena in complex multicomponent nanorod media is proposed and validated. The experimental and theoretical results indicate that the magneto-optical response of the nanostructured metamaterial is drastically enhanced and spectrally modified with respect to bulk ferromagnetic media due to interplay between strong anisotropy and magnetic field induced polarization rotation.

1. Introduction

Magneto-optical effects are at the core of polarization-control, telecommunications, sensing, and the emerging field of nonreciprocal photonics[1,2] where axial symmetry of the magnetic field is the enabling mechanism for the violation of parity-time symmetry of the optical response. Unfortunately, homogeneous materials available in nature exhibit relatively weak magneto-optical activity. Artificial magneto-optical behavior has been recently demonstrated in photonic-crystal-inspired structures and in waveguided geometries,[3,4] configurations known for their sensitivity to long-range order and, therefore, highly susceptible to fabrication imperfections. Planar multilayered and more complex geometries have been suggested theoretically.[5]

Here, we demonstrate that multicomponent nanostructured metamaterials can be used to significantly enhance magneto-optical response of their inclusions by combining field enhancement, enabled by plasmonic nanostructures, and the strong anisotropy of nanorod composites.[6,7] The metamaterial is fabricated using standard electrodeposition protocols[8] and operates in the effective medium regime, known for its tolerance to small-scale geometry variations.[9–13] We present comprehensive theoretical, experimental, and numerical analysis of the electromagnetic properties of the magneto-optical metamaterial, demonstrating both the rotation of the polarization plane and nonreciprocal transmission, two phenomena that can be controlled by the direction of the external magnetic field. This enhanced response is the result of the combination of the introduced magneto-optical properties and strong anisotropy of the metamaterial. We demonstrate rotation of the polarization plane with the effective Verdet constant equivalent of at least 10^5 rad m^{-1} T^{-1}, significant enhancement with respect to bulk ferromagnetic materials,[14] suggesting that nanostructured magnetic materials have much stronger magneto-optical response than their bulk counterparts. Overall, plasmonic magneto-optical nanorods combine the benefits of sub-wavelength light manipulation offered by metamaterials and of strong magneto-optics offered by plasmonic nanocomposites, leading to a promising material platform for integrated nanophotonic applications.

The magneto-optical metamaterial geometry and its optical response are illustrated in **Figure 1**. The composite is formed by an array of aligned plasmonic (gold) nanorods with magneto-optical (nickel) shells inside a dielectric (alumina) matrix (note that in the composites the Ni shells extend only part-way along the rod; see the Experimental Section). As follows from the geometry, in the absence of an external static magnetic field and in the limit when the unit cell is much smaller than the wavelength ($a \ll \lambda_0$), the optical response of the composite can be described by a diagonal permittivity tensor with Cartesian components $\hat{\epsilon} = \{\epsilon_\perp, \epsilon_\perp, \epsilon_{zz}\}$. Effective medium theory can be used to relate the components of the effective permittivity $\epsilon_\perp$ and ϵ_{zz} to the permittivity of the constituent materials as well as to the geometrical parameters of a metamaterial, such as a unit cell a, and radii of the rod r_1 and of the shells around the rod r_i, with $i = 2, \ldots, N$. Existing analytical and numerical tools allow calculations of the optical response of metamaterials composed of rods without shells, with plasmonic and magneto-optical material constituents and in the limit $r_1 \ll a$,[1,11,13,15] as well as shelled nanorod composites, comprising nonmagneto-optical materials with arbitrary rod concentration.[12,16] Here, we present a formalism that can incorporate magneto-optical response in the effective-medium description of shelled rod metamaterials and even in the limit $r_i \simeq \frac{a}{2}$. We consider a metamaterial with a = 64 nm, r_1 = 15 nm, and r_2 = 23 nm and assume that the

Dr. B. Fan, Prof. V. A. Podolskiy
Department of Physics and Applied Physics
University of Massachusetts Lowell
Lowell, MA 01854, USA
E-mail: viktor_podolskiy@uml.edu
Dr. M. E. Nasir, Dr. L. H. Nicholls, Prof. A. V. Zayats
Department of Physics and London Centre for Nanotechnology
King's College London
Strand, London WC2R 2LS, UK
E-mail: anatoly.zayats@kcl.ac.uk
The ORCID identification number(s) for the author(s) of this article can be found under https://doi.org/10.1002/adom.201801420.

DOI: 10.1002/adom.201801420

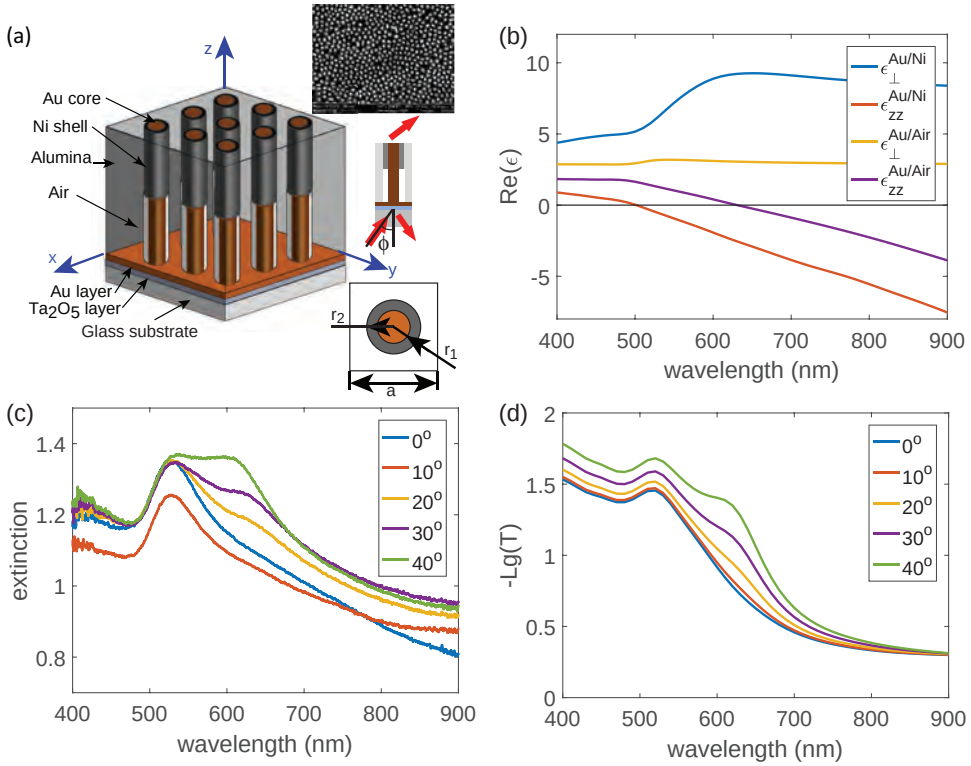

Figure 1. a) Schematic geometry and the electron microscope image (top inset) of the nanorod composite. b) Diagonal components of the effective permittivity tensor of Au/Ni/Al_2O_3 and Au/air/Al_2O_3 metamaterials. c,d) Optical extinction spectra of the Au/Ni/Al_2O_3 metamaterial excited with p-polarized light for different angles of incidence: (c) experiment and (d) EMT calculations.

height of each of Ni-clad and air-clad section of the nanorods is equal to 100 nm. Different combinations of geometrical parameters can potentially further optimize magneto-optical response beyond what is reported in this work.

The diagonal components of the effective permittivity (Figure 1b) are of different signs throughout visible (Au/Ni composites) and IR (Au composite) frequency ranges (see the Supporting Information for the details), with poles and resonances of the components of the effective permittivity resulting in the peaks of optical extinction of the composite (Figure 1c,d). Metamaterials with such strong anisotropy, also called hyperbolic metamaterials, are known to enable sub-wavelength light manipulation and modulation of the optical density of states.[9,10,17,18] This work extends the applications of hyperbolic metamaterials to magneto-optical media, potentially enabling strong magneto-optical activity in sub-wavelength optical waveguides.

Magneto-optical media are characterized by the changes in their optical response as a result of the applied external magnetic field. The details of these changes are related to the direction and the amplitude of the external magnetic field.[19] In particular, when the external field is perpendicular to the interface, the parallel slab of magneto-optical material rotates the plane of polarization of transmitted light and can be potentially used as an optical isolator.[1,2,19] When a magnetic field is parallel to the slab interface and perpendicular to the plane of incidence, a lossy magneto-optical material can result in asymmetric propagation, potentially enabling unidirectional transmission of light.[20,21] In both cases, optical properties of the magneto-optical materials can be related to the nonzero off-diagonal components of their permittivity tensor. For composite materials it becomes important to relate the optical response of the metamaterial constituents to the response of the metamaterial as a whole.

2. Effective Medium Response of Shelled Nanorod Metamaterials with Magneto-Optic Inclusions

The proposed approach is based on the Maxwell–Garnett-type formalism, extended to high concentration of inclusions.[12,15,16] In contrast to the previous studies, here we implement magneto-optical behavior in the effective medium response of the shelled nanorod composites. The procedure, applicable to the case of the anisotropic unit cell and to nanorod materials with multiple shells, is described below.

Since the dimensions of the unit cell are much smaller than the free space wavelength ($a \ll \lambda_0$), the quasi-static approximation can be used to calculate the distribution of the electric field across a unit cell of the metamaterial. As such, distribution of the electric field across the unit cell can be related to the solutions of the Laplace equation for the electric potential Φ. In an individual shell, these solutions are represented as

$$\Phi_i(r,\varphi) = \sum_{m=1,3,5,\ldots}^{M}\left(\alpha_{i,m}^{+}r^m + \alpha_{i,m}^{-}\frac{1}{r^m}\right)\cos(m\varphi) + \sum_{m=1,3,5,\ldots}^{M}\left(\beta_{i,m}^{+}r^m + \beta_{i,m}^{-}\frac{1}{r^m}\right)\sin(m\varphi) + \alpha_{i,0} + \beta_{i,0}\ln(r) \quad (1)$$

where (r,φ) are the cylindrical coordinates, the index i represents the shell number, the index m represents the Fourier index, and M represents the number of Fourier terms used in the expansion.

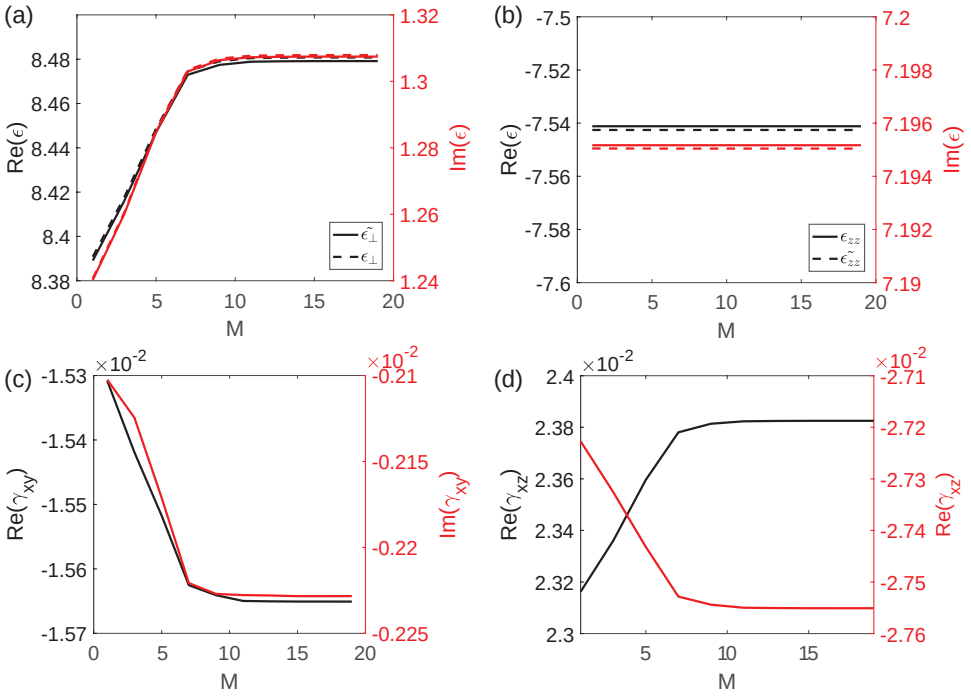

Figure 2. Convergence of the effective medium parameters as a function of a number of terms in Equation (1). Geometric parameters of the unit cell are $a = 64$ nm, $r_1 = 15$ nm, and $r_2 = 23$ nm, and the permittivity of the components are $\epsilon_1 = -34.47 + 7.94i$, $\epsilon_2 = -14.7 + 24.98i$, and $\epsilon_3 = 3.09$, with magneto-optical response of Ni given by $i\gamma_{Ni} = -0.36 + 0.126i$.

The problem of finding the effective permittivity of the nanorod composite is, therefore, reduced to the problem of calculating the coefficients of the expansions $\overline{\alpha_i^{\pm}}$ and $\overline{\beta_i^{\pm}}$ in each layer, based on the external excitation field that is parameterized by a coefficient $\alpha_{N,1}^{+}$. The procedure of calculating these coefficients is outlined in the Experimental Section.

The known potential is used to calculate the distribution of the electric field (in the ith layer $\vec{E}_i = -\vec{\nabla}\Phi_i$) and the displacement ($\vec{D}_i = \hat{\epsilon}_i \vec{E}_i$, where ϵ_i is the permittivity of the i-th layer, which maybe magneto-optically active) across the unit cell. The components of the effective permittivity tensor are then related to the field distributions via $\langle \vec{D} \rangle = \hat{\epsilon}_{\text{eff}} \langle \vec{E} \rangle$ with $\langle \cdots \rangle$ being the unit-cell average (note that due to linearity of the Maxwell equations, the effective parameters are independent of the incident electromagnetic field). In calculating the components of the effective permittivity tensor (see the Experimental Section), we use the following nonzero tensor components

$$\hat{\epsilon}_{\text{eff},y} = \begin{pmatrix} \epsilon_\perp & 0 & i\gamma_{xz} \\ 0 & \epsilon_\perp & 0 \\ -i\gamma_{xz} & 0 & \tilde{\epsilon}_{zz} \end{pmatrix} \tag{2a}$$

$$\hat{\epsilon}_{\text{eff},z} = \begin{pmatrix} \tilde{\epsilon}_\perp & i\gamma_{xy} & 0 \\ -i\gamma_{xy} & \tilde{\epsilon}_\perp & 0 \\ 0 & 0 & \epsilon_{zz} \end{pmatrix} \tag{2b}$$

for an external static magnetic field oriented along $\hat{y}$ and $\hat{z}$ directions, respectively. The diagonal components of the effective permittivity tensors $(\epsilon_\perp, \tilde{\epsilon}_\perp, \epsilon_{zz}, \tilde{\epsilon}_{zz})$ represent the material response with the induced polarization along the direction of the external electric field. The off-diagonal components (γ_{xz}, γ_{xy}), responsible for magneto-optical activity, represent the component of the displacement field which is perpendicular to the excitation field. In the absence of an external static magnetic field, we recover $\gamma_{xz} = \gamma_{xy} = 0, \epsilon_\perp = \tilde{\epsilon}_\perp, \epsilon_{zz} = \tilde{\epsilon}_{zz}$ with $\epsilon_\perp$ and ϵ_{zz} given by the (modified) Maxwell-Garnett formalism.[16]

The typical convergence of the effective parameters as a function of the number of the Fourier components is presented in **Figure 2**. It shows that about six to seven terms are sufficient to achieve stable solutions.

Once the effective medium parameters for the metamaterial are known, transmission and reflection through the magneto-optical metamaterial can be determined with a standard transfer matrix formalism.[22,23]

3. The Enhanced Faraday Effect

When an external static magnetic field is parallel to the nanorods (axis z in Figure 1) and the effective permittivity tensor of a metamaterial has symmetry shown in Equation (2b), the eigenmodes supported by the metamaterial represent a combination of elliptically polarized plane waves (see the Experimental Section). The dispersion of these modes (i.e. the dependence of the components of their wavevector $\vec{k} = \{k_x, k_y, k_z\}$ on angular frequency ω) is given by

$$k_z^2 = \tilde{\epsilon}_\perp \frac{\omega^2}{c^2} - \frac{k_x^2}{2}\left(\frac{\tilde{\epsilon}_\perp}{\epsilon_{zz}} + 1\right) \pm \sqrt{\frac{k_x^4}{4}\left(\frac{\tilde{\epsilon}_\perp}{\epsilon_{zz}} - 1\right)^2 + \gamma_{xy}^2 \frac{\omega^2}{c^2}\left(\frac{\omega^2}{c^2} - \frac{k_x^2}{\epsilon_{zz}}\right)} \tag{3}$$

where c is the speed of light in vacuum (here we use the geometry with (xz)-plane being the plane of incidence, resulting in $k_y = 0$). The elliptical polarization of these eigenmodes, combined with the difference of their propagating constants, implies that the metamaterial does not preserve the polarization of the linearly polarized incident waves. In general, transmitted monochromatic light has elliptical polarization. For the incident linearly polarized light, magneto-optical performance is often characterized by the rotation of the major axis of the polarization ellipse of the transmitted light with respect to the linear polarization of the incident light (the parameter known as rotation of polarization plane $\Delta\theta$; see the Experimental Section).

The spectral dependence of polarization rotation in the case of p-polarized incident light with the magnetic field directed along the light propagation has a nontrivial dependence on the angle of incidence (**Figure 3**). While the full-wave numerical solutions of the Maxwell equations largely reproduce the spectra of the polarization rotation seen in the experiment (cf. Figure 3a,b), the magnitude of the predicted response is several orders of magnitude below what is seen in the experiment. We believe that this disagreement stems from the difference in magneto-optical response between nanostructured and bulk Ni. Indeed, increasing the off-diagonal components of Ni by a factor of 50 with respect to the bulk tabulated data, which assumes saturating static magnetic field,[24] brings the results of the simulations in line with the rotation angles seen in the experiment (Figure 3c).

The effective medium theory developed in this work can be used to drastically reduce the complexity of the numerical solutions of the Maxwell equations. **Figure 4** illustrates the validity of this effective medium theory (EMT), described by Equations (2,3) in the case when the static magnetic field is directed along the nanorods (both the numerical and the EMT models assume that magneto-optical response of Ni is identical to the values exhibited in bulk samples[24]). The predictions of the EMT adequately describe the results of the full-wave simulations (cf. Figure 4a,b), at the same time providing drastic reductions in the calculation time and in memory requirements. The spectral dependence of the off-diagonal components of the effective medium polarizability of the Au–Ni-alumina composite for both bulk and the 50-times larger off-diagonal components of Ni susceptibility are shown in Figure 4c,d. The spectral dependencies of the off-diagonal components of the composite are significantly modified with respect to the spectra for bulk Ni, in terms of both amplitude and sign. This is the effect of the interplay between magneto-optical activity of the components and geometric anisotropy of the metamaterial. Notably, increasing the magneto-optical response of Ni beyond the tabulated data for a bulk Ni film yields better agreement between the simulated and experimental values for the polarization rotation. In order to avoid excessive fitting of the theoretical model, we limit the theoretical data to a 50-times increase of the off-diagonal response, which provides order-of-magnitude agreement with experimental data for both polarization rotation and nonreciprocal transmission. The comparison between experimental and theoretical results indicates that the magneto-optical response of nanostructured Ni is much stronger (approximately ten times)

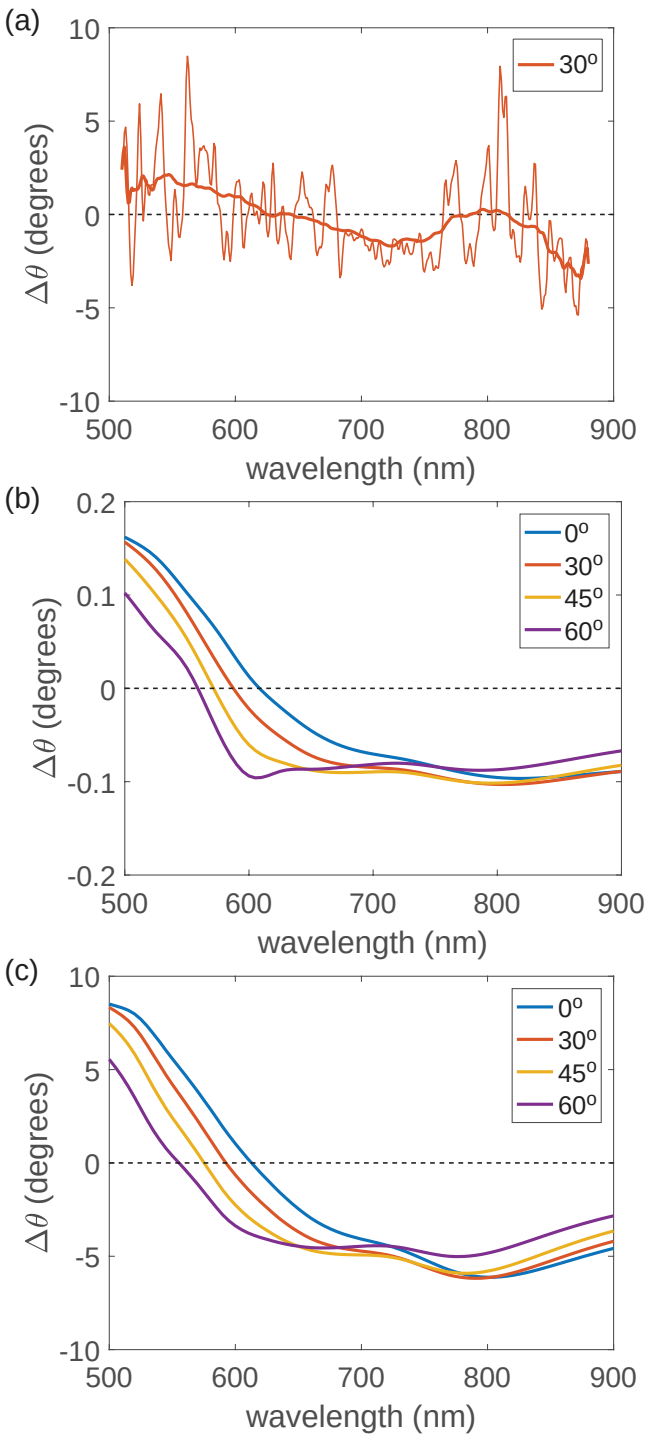

Figure 3. Rotation of the polarization plane of p-polarized light incident on the metamaterial at different angles of incidence when static magnetic field is directed along the direction of incident light. a) Experimental data for an angle of incidence of 30° averaged by applying Savitzky–Golay filter (thick line) to increase signal-to-noise ratio (note that due to the high extinction, the experimental signal is weak for wavelengths below ≈550 nm, preventing accurate reconstruction of polarization state). b,c) Numerical simulations for (b) bulk tabulated Ni permittivity and (c) the off-diagonal permittivity components increased 50 times.

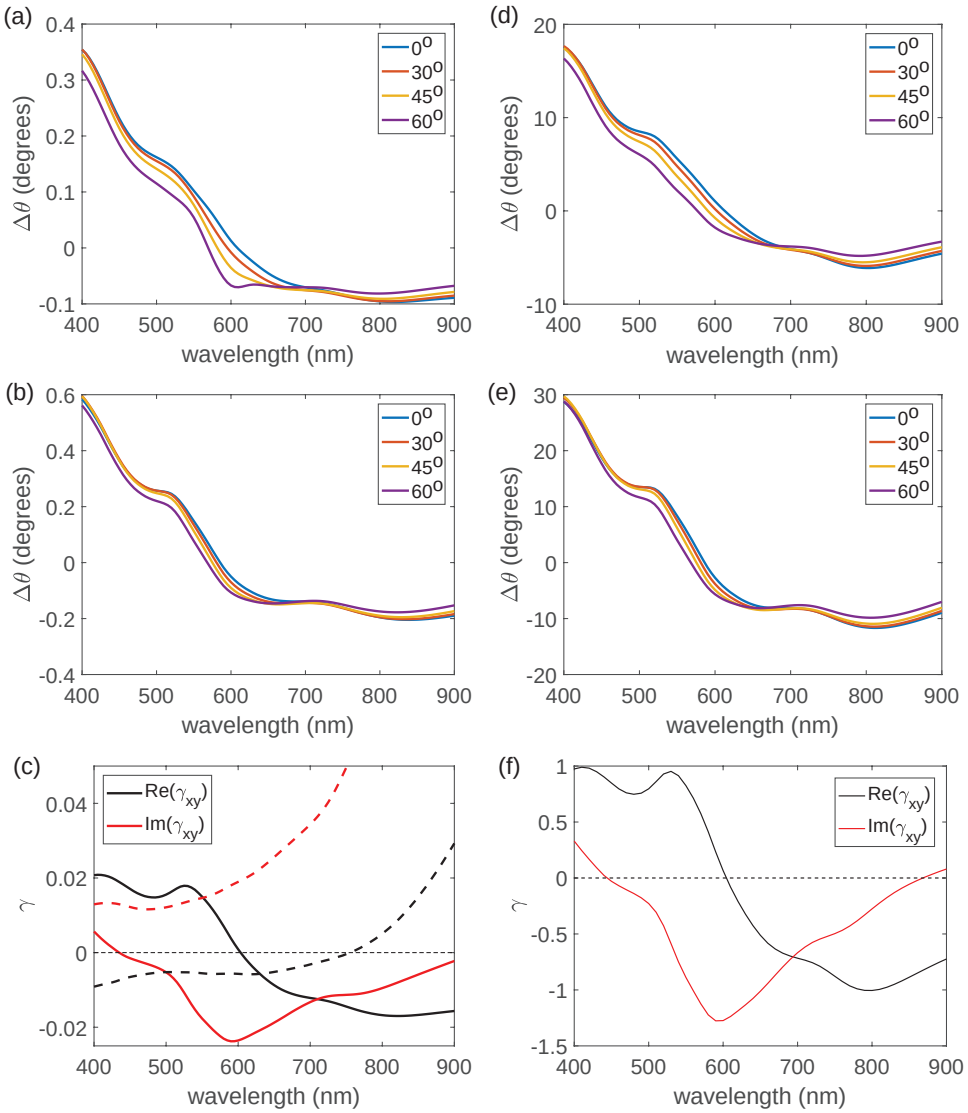

Figure 4. Rotation of the polarization plane for a p-polarized beam incident on the metamaterial at different angles of incidence when static magnetic field is along the nanorods: a,d) FEM and b,e) EMT simulations. c,f) The spectral dependences of the off-diagonal components γ_{xy} used in (b) and (e), respectively: (solid lines) the off-diagonal components of the effective permittivity tensor, (dashed lines) the off-diagonal components of Ni, scaled by the volumetric concentration of Ni in the composite. Tabulated data for Ni[24] are assumed in (a)–(c), while γ_{xy} for Ni increased 50 times with respect to the tabulated data is assumed in (d)–(f).

than that of its bulk counterpart. Similar increase has been previously reported in larger-diameter Ni nanowire media with the magneto-optical response approximately five times stronger than that expected from a bulk material response[13,25] and in ultrathin Iron Garnett films.[26] The results suggest that nanostructured Ni can provide further enhancement of magneto-optical response. This leads to the significant changes in the cross-polarized transmission due to magneto-optical activity of the composite (Figure 4e,f). Even in the case when optical response of Ni is described by the tabulated bulk material data, the metamaterial provides significant rotation of the polarization plane with the effective Verdet constant of the order of 10^5 rad m^{-1} T^{-1}, as estimated based on Figures 3b and 4a,b. This value of effective Verdet constant is three orders of magnitude larger than $\approx 10^2$ rad T^{-1} m^{-1} that can be achieved with typical bulk magneto-optical materials, like Terbium Gallium Garnet.[14]

4. Nonreciprocal Transmission

When a static magnetic field is perpendicular to the plane of incidence (y direction in geometry shown in Figure 1), the eigenmodes of the metamaterial recover linear polarization, commonly observed in uniaxial crystals. The two families of linearly polarized waves can be grouped in ordinary (*s*-, transverse-electric, TE-polarized) modes that have electric field along the $\hat{y}$ direction and have dispersion

$$k_z^2 = \epsilon_\perp \frac{\omega^2}{c^2} - k_x^2 \tag{4}$$

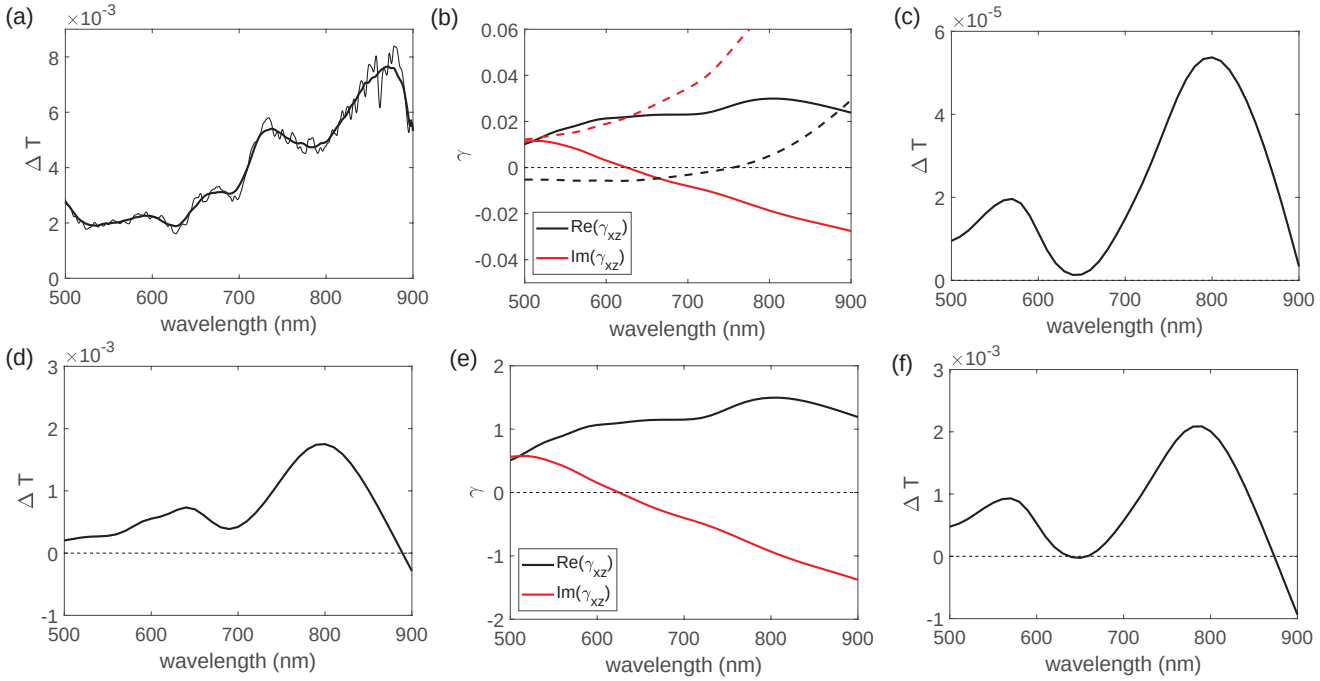

Figure 5. Nonreciprocal transmission of a p-polarized light incident at 30° when static magnetic field is perpendicular to the plane of incidence: a) experimental data for an angle of incidence of 30° averaged by applying Savitzky–Golay filter (thick line) to increase signal-to-noise ratio (note that due to the high extinction, the experimental signal is weak for wavelengths below ≈550 nm). c,f) EMT and d) FEM simulations for (c) the tabulated data for Ni[24] and (d,f) γ_{xz} increased 50 times with respect to the tabulated data. b,e) Spectra of the off-diagonal components γ_{xz} of the effective permittivity tensor used in (c) and (d), respectively. Dashed lines in (b) are the spectra of the off-diagonal components γ_{xz} of the permittivity tensor of Ni scaled by the volumetric concentration of Ni in the composite.

and extraordinary (*p*-, transverse-magnetic, TM-polarized) modes that have the electric field in the (*xz*)-plane and have the dispersion

$$k_z^2 = \left(\epsilon_\perp - \frac{\gamma_{xz}^2}{\tilde{\epsilon}_{zz}}\right)\frac{\omega^2}{c^2} - \frac{\epsilon_\perp}{\tilde{\epsilon}_{zz}}k_x^2 \tag{5}$$

Quadratic dependence of the dispersion of both TE and TM modes on the wavevector indicates that, even in the presence of magneto-optical response, the modes of the bulk nanorod metamaterial remain reciprocal. However, a combination of asymmetric geometry, anisotropy, and nonvanishing absorption is expected to yield nonreciprocal excitation of these modes, and, therefore, leads to nonreciprocal transmission of the p-polarized light through the planar slab of the metamaterial.[20,21] Such asymmetric transmission in the metamaterial structure is shown in **Figure 5**. Similar to the cross-polarized transmission described above, the nonreciprocity seen in the experimental data (Figure 5a) is much stronger than the signal expected from analytical calculations (Figure 5b).

The validity of the developed effective medium description is illustrated in Figure 5c,d. The results of the full-wave solutions of the Maxwell equations (Figure 5c) are compared with the EMT predictions (Figure 5d) for the magneto-optical response of Ni enhanced 50 times with respect to the tabulated data for bulk material. Once again, it is seen that such an enhancement of the Ni response brings the predictions of both the finite elements method (FEM) and EMT models to quantitative agreement with the experiment, further indicating the strong potential effect of nanostructuring of Ni on its magneto-optical properties.

5. Conclusions

We have designed and demonstrated magneto-optical properties of plasmonic shelled nanorod metamaterials. Theoretically, we have developed the effective medium technique for understanding the magneto-optical response of the composite and validated this technique via full-wave solutions of the Maxwell equations. Experimentally, we have demonstrated two hallmark phenomena enabled by the magneto-optical metamaterials, cross-polarization coupling and nonreciprocal transmission. In both cases, the experimental results indicate that the magneto-optical response of nanostructured Ni is significantly stronger than the tabulated response of its bulk counterpart. While this work focuses on Au/Ni/alumina metamaterials, we expect that qualitatively similar behavior can be obtained in plasmonic/magneto-optic/dielectric core–shell metamaterials with different plasmonic materials (including but not limited to Al, Cu, Ag), different magneto-optical components (Co, Fe), and different dielectrics (including polymers).

The metamaterial approach allows engineering of the magneto-optical response combining magnetic and geometric anisotropy in one metamaterial platform. Although the concentration of magnetic material is smaller in the metamaterial

compared to a continuous magnetic film, the lower absorption and the enhancement of the magnetic response provided by the metamaterial open up opportunities for developing new magneto-optical designs. Magneto-optical metamaterial platforms allow the combination of plasmonic and magneto-optical materials in a way to utilize the best qualities of both systems, opening the way for compact high-performance optical isolators and other magneto-optical components.

6. Experimental Section

Material Fabrication: Plasmonic magnetic metamaterials based on ordered Au-core/Ni-shell nanorod arrays have been fabricated on a glass substrate. Nanoporous anodic alumina oxide templates were synthesized by two-step anodization. An aluminum film of 600 nm thickness was deposited on a multilayer glass substrate by magnetron sputtering. The substrate comprised of a glass slide with 20 nm thick adhesive layer of tantalum oxide and a 7 nm thick Au film acting as a weakly conducting layer. Tantalum pentoxide is deposited by sputtering tantalum using a 20% oxygen/80% argon mixture. The porous alumina structures were obtained by a two step-anodization in 0.3 M sulfuric acid at 25 V. After an initial anodization process, the poorly ordered porous layer formed was removed by etching in a solution of H_3PO_4 (3.5%) and CrO_3 (20 g L^{-1}) at 70 °C. An ordered, patterned surface was obtained after removal of the porous layer formed during first step of anodization. Then the samples were anodized again under the same conditions as in the first step. The anodized samples were subsequently etched in 30×10^{-3} M NaOH to achieve pore widening and remove the barrier layer.

Gold electrodeposition was performed with a three electrodes system using a noncyanide solution. The length of the nanorods was controlled by the electrodeposition time. The sample was etched again in 30×10^{-3} M NaOH to form nanoshells around the Au nanorods. The thickness of the Ni shell around the Au nanorods was controlled by etching time. Nickel was electrodeposited in these nanoshells using a mixed solution of 0.2 M nickel sulfate and 0.1 M boric acid.

The structure used in these measurements has an Au core of ≈30 nm in diameter and a Ni shell ≈8 ± 2 nm thick. The period is ≈64 nm and length of nanorods is ≈200 nm.

Optical Characterization: The schematic diagram of the experimental setup for optical measurements is shown in **Figure 6**. It consists of a white-light source, collimation lenses, a polarizer, and an analyzer, with optical axes that can be adjusted with respect to each other and the plane of incidence, and a charge coupled device (CCD)-based spectrometer. The sample is mounted onto a nonmagnetic stage. Neodymium ring and disc magnets of 20 mm diameter and 10 mm thickness with magnetic field of 0.3 and 0.16 T, respectively, are used in the experiments to provide a magnetic field. The magnets are adjusted at the distance of 5 mm from the sample to maximize the magnetic field strength. The external magnetic field is applied horizontally along the direction of the incident light (the magnetic field has the components both along and perpendicular to the nanorods, along both ordinary and extraordinary axes of the metamaterial, the ratio of the components depends on the angle of incidence) or, alternatively, from the top of the sample perpendicular to the direction of the incident light (the magnetic field perpendicular to the nanorod axes, along the ordinary axis of the metamaterial). The size of the magnets is much larger than the diameter of the optical beam, so that uniform magnetic field can be assumed across the illuminated spot. The measurements are performed in transmission configuration in the saturated magnetic field. The samples are fully demagnetized for the baseline measurements.

In order to retrieve the polarization of the transmitted light, the intensity $P(\theta)$ of the light is measured at four different analyzer angles ($\theta = 0°$, 30°, 45°, and 60° with respect to the incident polarizer angle). These four measurements and the fact that $P(\theta) \propto |\boldsymbol{E} \cdot \boldsymbol{u}(\theta)|^2$, where $\boldsymbol{u}(\theta)$ is the unit vector along the analyzer direction, are used to determine the three unknown quantities of the transmitted polarization state $\mathrm{E} = (E_o^{re}, E_e^{re} + iE_e^{im})$ using a least-square error fit.[27] The rotation due to the introduction of the magnetic field can then be determined by comparing the angle of orientation of the major semiaxes of the polarization ellipses.

The Effective Medium Analysis: The effective permittivity is calculated in the quasi-static approximation, with the spatial distribution of the electric field given by the electric potential ($\vec{E} = -\vec{\nabla}\Phi$) that, in turn, is given by Equation (1). Symmetry of the problem dictates that only odd Fourier modes ($m = 1, 3, ..., M$) contribute to the solution.[29]

To find the amplitudes of coefficients $\vec{\alpha}_i$ and $\vec{\beta}_i$ boundary conditions are used at each intershell boundaries to relate the coefficients in the neighboring layers, using interface-specific scattering $\hat{S}$ and $\hat{T}$ transfer matrices

$$\begin{bmatrix} \overrightarrow{\alpha_i^-} \\ \overrightarrow{\beta_i^-} \end{bmatrix} = \hat{S}_i \begin{bmatrix} \overrightarrow{\alpha_i^+} \\ \overrightarrow{\beta_i^+} \end{bmatrix}$$

$$\begin{bmatrix} \overrightarrow{\alpha_{i-1}^+} \\ \overrightarrow{\beta_{i-1}^+} \end{bmatrix} = \hat{T}_i \begin{bmatrix} \overrightarrow{\alpha_i^+} \\ \overrightarrow{\beta_i^+} \end{bmatrix} \quad (6)$$

On the implementation level, the matrices depend on the direction of the external static magnetic field. In particular, for the case of B_z field, the $\hat{S}$ and $\hat{T}$ matrices for a particular interface, can be obtained by enforcing the boundary conditions for the electric field and the displacement at this interface. Given a general form of the potential [Equation (1)] as well as cylindrical symmetries of nanorod shells, the relevant boundary conditions reduce to continuity of tangential electric field (E_φ) and normal electric displacement (D_r). Cylindrical symmetry of nanorod shells allows one to decouple the coefficients related to the Fourier

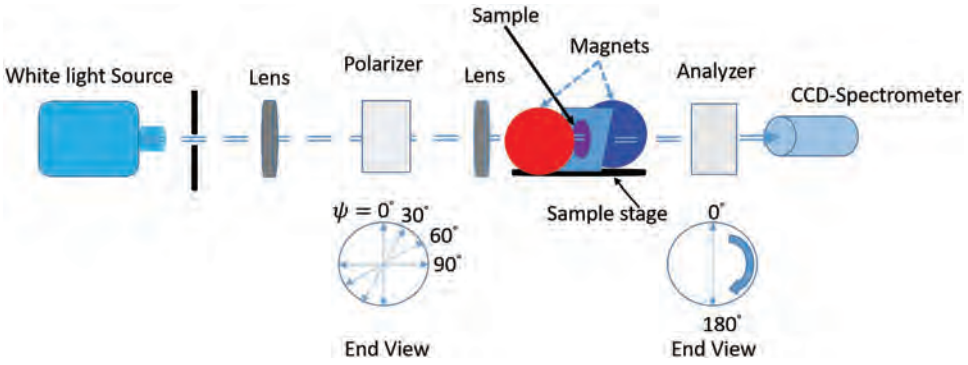

Figure 6. Experimental setup. Bottom diagrams shows the orientation of the polarizer and analyzer for magneto-optical measurements.

harmonics corresponding to different indices m from each other. It becomes convenient to represent the boundary conditions in a matrix form

$$\hat{F}_{i-1}(r_i)\begin{pmatrix}\overrightarrow{\alpha_{i-1}^{+}}\\ \overrightarrow{\beta_{i-1}^{+}}\\ \overrightarrow{\alpha_{i-1}^{-}}\\ \overrightarrow{\beta_{i-1}^{-}}\end{pmatrix}=\hat{F}_i(r_i)\begin{pmatrix}\overrightarrow{\alpha_{i}^{+}}\\ \overrightarrow{\beta_{i}^{+}}\\ \overrightarrow{\alpha_{i}^{-}}\\ \overrightarrow{\beta_{i}^{-}}\end{pmatrix} \tag{7}$$

where matrices $\hat{F}_i(r_j)$ have $4M$ rows and columns each. The mth $(2M+m)$th birows of the matrix represent the electric field (displacement) for the terms preserving particular $\sin(m\varphi)$, $\cos(m\varphi)$ terms in the ith layer at the position r_j. Equation (7) can be straightforwardly transformed into

$$\begin{pmatrix}\overrightarrow{\alpha_{i-1}^{+}}\\ \overrightarrow{\beta_{i-1}^{+}}\\ \overrightarrow{\alpha_{i-1}^{-}}\\ \overrightarrow{\beta_{i-1}^{-}}\end{pmatrix}=\widehat{M}_i\begin{pmatrix}\overrightarrow{\alpha_{i}^{+}}\\ \overrightarrow{\beta_{i}^{+}}\\ \overrightarrow{\alpha_{i}^{-}}\\ \overrightarrow{\beta_{i}^{-}}\end{pmatrix} \tag{8}$$

where $\widehat{M}_i=\hat{F}_{i-1}(r_i)^{-1}\hat{F}_i(r_i)$. As before, matrix $\widehat{M}$ is a $4M\times 4M$ matrix. It can be represented as four sub-matrices, $\widehat{M}_i^{jk}$ $2M\times 2M$ each, with $j, k = 1, 2$. It is now easy to represent the $\hat{S}_i$,$\hat{T}_i$ matrices in terms of the sub-matrices $\widehat{M}_i^{jk}$ and $\hat{S}_{i-1}$

$$\begin{aligned}\hat{S}_i&=-\left(\widehat{M}_i^{22}-\hat{S}_{i-1}\widehat{M}_i^{12}\right)^{-1}\left(\widehat{M}_i^{21}-\hat{S}_{i-1}\widehat{M}_i^{11}\right)\\ \hat{T}_i&=\widehat{M}_i^{11}+\widehat{M}_i^{12}\hat{S}_i\end{aligned} \tag{9}$$

Equation (9), combined with requirement to have finite field at the origin ($\hat{S}_1=\hat{0}$), solves the problem of finding the full set of interface-specific matrices $\hat{S}_i$ and $\hat{T}_i$ for the case when the external magnetic field is parallel to the nanorods.

In the complimentary case, when the static magnetic field is directed along the y-direction, symmetry of the permittivity of components of metamaterial is represented by Equation (2). Therefore, the $m = 1$ components of the in-plane fields are coupled to the z-field. The boundary conditions now require continuity of both E_φ and D_r (for all values of m) as well as continuity of E_z (for $m = 1$). With these additions, the procedure for calculating $\hat{S}_i$ and $\hat{T}_i$ matrices is similar to the one described above. The resultant set of matrices $\hat{S}_i$ and $\hat{T}_i$ can be used to calculate the response of the individual multishelled nanorod (or a set of periodic rods) to any quasi-static external electric field. To analyze the effective medium behavior of the metamaterial, a homogeneous excitation field $\left(\text{given by } \alpha_N^1=1\right)$ is assumed and periodic boundary conditions are imposed on the fields across the unit cell. To achieve the latter goal, a sufficiently large number of points (x_p,y_p) along the unit cell boundary are chosen (it can be shown that the symmetry imposed by the choice of the Fourier harmonics suffices to restrict these points to the first quadrant of the boundary where x_p, $y_p > 0$). We then calculate the matrix relationships between the distribution of the Cartesian component of the field $E_\xi(x_p, y_p)$ with $\xi = x, y$ and the coefficients $\overrightarrow{\alpha^{\pm}}$ and $\overrightarrow{\beta^{\pm}}$. In the limit $p > M$, this matrix reduces the field periodicity condition to an overdetermined least-square fit problem that is used to find all the coefficients $\overrightarrow{\alpha_i}$ and $\overrightarrow{\beta_i}$ except for α_N^1.

Dispersion and Polarization of Plane Waves in Magneto-Optical Materials: In nonmagnetic media (materials with relative magnetic permeability $\mu_r = 1$), the Maxwell's equations result in

$$\vec{\nabla}\times\vec{\nabla}\times\vec{E}=-\frac{1}{c^2}\frac{\partial^2}{\partial t^2}\hat{\epsilon}\vec{E} \tag{10}$$

Assuming plane-wave solution, $\vec{E}=\overrightarrow{E_0}\exp\left(i\vec{k}\cdot\vec{r}-i\omega t\right)$, the above equation reduces to eigen-value problem

$$\vec{k}\cdot\left(\vec{k}\cdot\overrightarrow{E_0}\right)-\left(\vec{k}\cdot\vec{k}\right)\overrightarrow{E_0}+\frac{\omega^2}{c^2}\hat{\epsilon}\,\overrightarrow{E_0}=0 \tag{11}$$

that can be used to find the dispersion (a dependence of the components of the wavevector $\vec{k}$ on a frequency ω) as well as the polarization (relationship between components of the field $\overrightarrow{E_0}$) of the eigenmodes of the system.[19] In particular, when the symmetry of the permittivity is given by Equation (2), Equation (14) for $\vec{k}=\{k_x,0,k_z\}$ yields

$$\begin{pmatrix}\epsilon_\perp\frac{\omega^2}{c^2}-k_z^2 & 0 & i\gamma_{xz}\frac{\omega^2}{c^2}+k_xk_z\\ 0 & \epsilon_\perp\frac{\omega^2}{c^2}-k_x^2-k_z^2 & 0\\ -i\gamma_{xz}\frac{\omega^2}{c^2}+k_xk_z & 0 & \tilde{\epsilon}_{zz}\frac{\omega^2}{c^2}-k_x^2\end{pmatrix}\begin{pmatrix}E_{0x}\\ E_{0y}\\ E_{0z}\end{pmatrix}=0 \tag{12}$$

The dispersion of the eigenmodes is given by Equations (4) and (5) for s-polarized waves $\overrightarrow{E_0}=\{0,1,0\}$ and Equation (4)] for p-polarized waves $\overrightarrow{E_0}=\left\{1,0,-\frac{\epsilon_\perp-k_z^2\,c^2/\omega^2}{i\gamma_{xz}+k_xk_z\,c^2/\omega^2}\right\}$. Note that both eigenmodes are linearly polarized.

Similarly, when the symmetry of the permittivity is given by Equation (2b), we obtain

$$\begin{pmatrix}\tilde{\epsilon}_\perp\frac{\omega^2}{c^2}-k_z^2 & i\gamma_{xy}\frac{\omega^2}{c^2} & k_xk_z\\ -i\gamma_{xy}\frac{\omega^2}{c^2} & \tilde{\epsilon}_\perp\frac{\omega^2}{c^2}-k_x^2-k_z^2 & 0\\ k_xk_z & 0 & \epsilon_{zz}\frac{\omega^2}{c^2}-k_x^2\end{pmatrix}\begin{pmatrix}E_{0x}\\ E_{0y}\\ E_{0z}\end{pmatrix}=0 \tag{13}$$

resulting in the dispersion described by Equation (3) and the amplitude of the eigenmodes given by $\overrightarrow{E_0^+}=\left\{-i\frac{\frac{\tilde{\epsilon}_\perp\omega^2}{c^2}-k_x^2-k_z^2}{\gamma_{xy}\frac{\omega^2}{c^2}},1,E_{0z}^+\right\}$, $\overrightarrow{E_0^-}=\left\{1,i\frac{\gamma_{xy}\frac{\omega^2}{c^2}}{\frac{\tilde{\epsilon}_\perp\omega^2}{c^2}-k_x^2-k_z^2},E_{0z}^-\right\}$, with $E_{0z}^\pm=-\frac{k_xk_z}{\tilde{\epsilon}_{zz}\frac{\omega^2}{c^2}-k_x^2}E_{0x}^\pm$. In the limit of vanishing magneto-optical response ($\gamma_{xy} = 0$), two linear s ($E_{0y}\neq 0$) and p (E_{0x}, $E_{0z}\neq 0$) polarized waves are recovered. When $\gamma_{xy}\neq 0$, both eigenmodes however are elliptically polarized.

Numerical Solutions of the Maxwell Equations: To verify the validity of the developed effective medium theory, transmission and reflection of the composites were calculated with 3D vectorial solutions of the Maxwell equations with a commercial FEM solver.[28] The model explicitly considers a single (finite height) unit cell of a metamaterial and implements the Floquet periodicity along x- and y-directions to mimic the infinite planar structure. In the z-direction, the geometry is terminated with two ports at the bottom and two ports at the top interfaces, assuring the reflection-less transmission of co- and cross-polarized light. A subwavelength unit cell of the metamaterial, along with wavelength-scale separation between the ports and the nanorods, ensures that no diffracted beam contributes to the field at the location of the ports. Transmission and reflection can be extracted directly from the FEM model using S-parameter calculations.

In separate calculations the metamaterial was approximated as a homogeneous slab with the effective permittivity tensor given by Equation (1), and the optical response of the planar metamaterial layer was calculated using the transfer-matrix-method (TMM) formalism. Our in-house implementation of the TMM is available in the Supporting Information.

In order to calculate rotation of the polarization plane, the transmitted part of a normally incident light is represented as a linear

combination of TE- and TM-polarized plane waves with amplitudes a_y and a_x, respectively. This combination describes, in general, elliptically polarized light. The rotation of polarization represents the direction of the major semiaxis of the ellipse, given by

$$\theta = \frac{1}{2}\arg\frac{a_x - ia_y}{a_x + ia_y} \tag{14}$$

Supporting Information

Supporting Information is available from the Wiley Online Library or from the author.

Acknowledgements

B.F. and M.E.N. contributed equally to this work. This research was supported by the US Army Research Office (Grant No. W911NF-16-1-0261), Engineering and Physical Sciences Research Council (UK) and the European Research Council iPLASMM project (No. 321268). A.V.Z. acknowledges support from the Royal Society and the Wolfson Foundation.

Conflict of Interest

The authors declare no conflict of interest.

Keywords

effective medium theory, Faraday effect, metamaterials, nonreciprocity

Received: October 17, 2018
Revised: February 20, 2019
Published online:

[1] *Magneto Optics* (Eds: S. Sugano, N. Kojima), Springer, Berlin **2000**.
[2] D. Jalas, A. Petrov, M. Eich, W. Freude, S. Fan, Z. Yu, R. Baets, M. Popović, A. Melloni, J. D. Joannopoulos, M. Vanwolleghem, C. R. Doerr, H. Renner, *Nat. Photonics* **2013**, *7*, 579.
[3] A. B. Khanikaev, G. Shvets, *Nat. Photonics* **2017**, *11*, 763.
[4] Z. Yu, G. Veronis, Z. Wang, S. Fan, *Phys. Rev. Lett.* **2008**, *100*, 023902.
[5] M. Sadatgol, M. Rahman, E. Forati, M. Levy, D. Ö. Güney, *J. Appl. Phys.* **2016**, *119*, 103105.
[6] P. Ginzburg, F. J. Rodríguez Fortuño, G. A. Wurtz, W. Dickson, A. Murphy, F. Morgan, R. J. Pollard, I. Iorsh, A. Atrashchenko, P. A. Belov, Y. S. Kivshar, A. Nevet, G. Ankonina, M. Orenstein, A. V. Zayats, *Opt. Express* **2013**, *21*, 14907.
[7] D. Vestler, I. Shishkin, E. A. Gurvitz, M. E. Nasir, A. Ben-Moshe, A. P. Slobozhanyuk, A. V. Krasavin, T. Levi-Belenkova, A. S. Shalin, P. Ginzburg, G. Markovich, A. V. Zayats, *Opt. Express* **2018**, *26*, 17841.
[8] M. E. Nasir, W. Dickson, G. A. Wurtz, W. P. Wardley, A. V. Zayats, *Adv. Mater.* **2014**, *26*, 3532.
[9] V. Drachev, V. A. Podolskiy, A. Kildishev, *Opt. Express* **2013**, *21*, 15048.
[10] A. Poddubny, I. Iorsh, P. Belov, Y. Kivshar, *Nat. Photonics* **2013**, *7*, 948.
[11] R. Wangberg, J. Elser, E. E. Narimanov, V. A. Podolskiy, *J. Opt. Soc. Am. B* **2006**, *23*, 498.
[12] W. T. Perrins, D. R. McKenzie, R. C. McPhedran, *Proc. R. Soc. A* **1979**, *369*, 207.
[13] S. Melle, J. Menendez, C. Armelles, D. Naas, M. Vazquez, K. Nielsch, *Appl. Phys. Lett.* **2003**, *83*, 4547.
[14] D. J. Dentz, R. C. Puttbach, R. F. Belt, *AIP Proc.* **1974**, *18*, 18954.
[15] P. M. Hui, D. Stroud, *Appl. Phys. Lett.* **1987**, *50*, 950.
[16] B. Wells, W. Guo, V. A. Podolskiy, *MRS Commun.* **2016**, *6*, 23.
[17] H. K. Krishnamoorthy, Z. Jacob, E. Narimanov, I. Kretzschmar, V. M. Menon, *Science* **2012**, *336*, 205.
[18] P. Ginzburg, D. Roth, M. E. Nasir, P. Segovia Olvera, A. V. Krasavin, J. Levitt, L. M. Hirvonen, B. Wells, K. Suhling, D. Richards, V. A. Podolskiy, A. V. Zayats, *Light: Sci. Appl.* **2017**, *6*, e16273.
[19] L. D. Landau, E. M. Lifshitz, L. P. Pitaevskii, *Electrodynamics of Continuous Media, Landau and Lifshitz Course of Theoretical Physics*, Vol. *8*, Reed Educational Publishing, Oxford, UK **1980**.
[20] V. A. Fedotov, P. L. Mladyonov, S. L. Prosvirnin, A. V. Rogcheva, Y. Chen, N. I. Zheludev, *Phys. Rev. Lett.* **2006**, *97*, 167401.
[21] A. Leviyev, B. Stein, A. Christofi, T. Galfsky, H. Krishnamoorthy, I. L. Kuskivsky, V. Menon, A. B. Khanikaev, *APL Photonics* **2017**, *2*, 076103.
[22] S. M. Rytov, *Sov. Phys. JETP* **1956**, *2*, 466.
[23] P. Yeh, A. Yariv, C.-S. Hong, *J. Opt. Soc. Am.* **1977**, *67*, 423.
[24] G. S. Krinchik, V. A. Artem'ev, *Sov. Phys. JETP* **1968**, *26*, 1080.
[25] A. A. Stashkevich, Y. Roussigné, A. N. Poddubny, S.-M. Chérif, Y. Zheng, F. Vidal, I. V. Yagupov, A. P. Slobozhanyuk, P. A. Belov, Y. S. Kivshar, *Phys. Rev. B* **2015**, *92*, 214436.
[26] M. Levy, A. Chakravarty, H.-C. Huang, R. M. Osgood Jr., *Appl. Phys. Lett.* **2015**, *107*, 011104.
[27] L. Nicholls, F. J. Rodríguez-Fortuño, M. E. Nasir, R. M. Cordova-Castro, N. Olivier, G. A. Wurtz, A. V. Zayats, *Nat. Photonics* **2017**, *11*, 628.
[28] Comsol Multiphysics, COMSOL AB.
[29] G. Milton, *Theory of Composites*, Cambridge University Press, Cambridge, UK **2002**.

Electrically Injected Parity Time–Symmetric Single Transverse–Mode Lasers

*Ruizhe Yao, Chi-Sen Lee, Viktor Podolskiy, and Wei Guo**

Dedicated to Dr. Ruizhe Yao, who regrettably passed away prior to issue publication of this work.

Single transverse–mode operation of broad area–coupled waveguide lasers enabled by parity-time (PT) symmetry is demonstrated. The PT-symmetric laser operates on coupled waveguide cavities with electrically tuned gain and loss. Such a counterintuitive waveguide design enables PT-symmetric breaking, causing unique mode selection and ultimately enables single-mode operation. By electrically tuning the loss in the loss region of the coupled waveguide cavity, several different PT-symmetric phases are analyzed theoretically, and the corresponding PT-symmetric phase transition is demonstrated experimentally in the coupled waveguide laser.

1. Introduction

In recent explorations, parity-time (PT) symmetry offers a unique pathway to advance laser science by incorporating counterintuitive gain and loss across the laser cavity.[1–10] Several promising experimental demonstrations of PT symmetry–based lasers have been reported.[11–20] For example, Feng et al.[21] and Hodaei et al.[22] have shown optically pumped single-mode microcavity and micro-ring lasers operated in the PT-symmetric broken phase, respectively, where the gain is achieved by optically pumping the active regions and loss is obtained from material absorption loss. Unfortunately, until now, applications of PT symmetry in lasers are mostly limited to optically injected devices.[23–27] In this context, here we report a coupled waveguide PT-symmetric laser with independently and electrically tuned gain and loss. Compared to its optically injected counterparts, the presented device provides more effective ways to dynamically adjust gain and loss in the cavities, which is necessary to reveal and fully utilize the rich physics of PT symmetry in optics. The PT-symmetric mode discrimination conditions are analyzed numerically and confirmed experimentally. Several distinct phases of PT symmetry breaking are identified and the corresponding cavity mode manipulation by PT symmetry is observed experimentally. Most importantly, we demonstrate an electrically injected single transverse–mode broad area–coupled waveguide lasers enabled by PT-symmetric mode selection.

Dr. Ruizhe Yao, Dr. Chi-Sen Lee, Prof. Viktor Podolskiy, Prof. Wei Guo
Department of Physics and Applied Physics
University of Massachusetts Lowell
Lowell, MA 01854, USA
E-mail: wei_guo@uml.edu

DOI: 10.1002/lpor.201800154

In the applications of high power lasers and tapered amplifier (TA) diodes, it is essential to utilize large-area waveguides while still maintaining single transverse–mode operations.[28] However, present design paradigms are accompanied by degraded laser performance, unstable single-mode operation at high output power, and extra fabrication complexity due to the tapered waveguide shapes.[29,30] In this context, PT symmetry provides a unique pathway to manipulate the laser cavity modes and realize a single transverse–mode operation without sacrificing the laser performance.

2. Experimental Section

Laser cavity used in this work comprised two electrically isolated quantum dots (QDs)–filled Fabry–Perot broad-area laser cavities. The two regions could be considered as two coupled (multimode) waveguides, due to the large width. The concept of PT symmetry–breaking mode manipulations in coupled waveguides was first theoretically discussed by Miri et al.[31] In the coupled waveguide cavities, a broad-area waveguide with gain g_m was coupled to its counterpart of loss α_m with coupling coefficient κ_{m}. It has been shown that the combination of $g_{\mathrm{m}}/\alpha_{\mathrm{m}}$ and κ_{m} determines the PT symmetry–breaking conditions. When $g_{\mathrm{m}} < \kappa_{\mathrm{m}}$, the modes of the coupled waveguide represent symmetric and anti-symmetric combination of the modes of the two waveguide components. The propagation constants of the two combinations were often degenerate featuring complete balance of gain and loss. However, when $g_{\mathrm{m}} > \kappa_{\mathrm{m}}$, the PT symmetry was spontaneously broken, and modes of the waveguide components became the modes of the combined waveguide. Most importantly, only one of the two supermodes exhibited gain. In Fabry–Perot cavities, the higher-order modes were typically of higher coupling coefficient than the one of the fundamental mode. Therefore, it was possible to design a coupled waveguide cavity to allow only the fundamental mode to reach the PT symmetry–breaking threshold; hence, only the fundamental mode could have net gain and lase.

Although ideal PT-symmetric cavities require equal gain and loss, semiconductor lasers generally exhibit gain clamping after lasing, a process that limits cavity gain at the threshold modal gain, g_{th}.[31,32] Therefore, it was essential to explore PT symmetry in coupled waveguides with fixed gain and varied loss configurations.

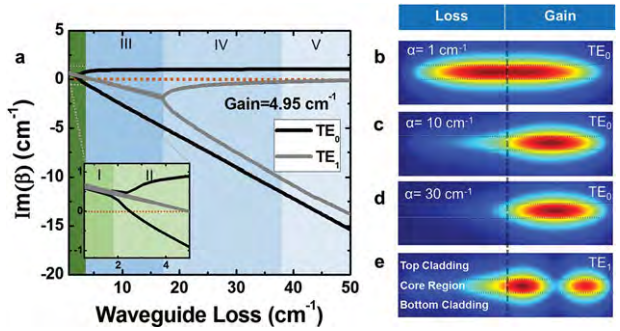

Figure 1. a) Imaginary part of the eigenfrequency versus loss in the loss waveguide. Inset: Enlarged region of $\alpha < 4.95$ cm^{-1}. The red dashed lines indicate zero propagation constant. In Phase I, all the modes are below their EPs. In Phase II, the first pair of supermodes has already reached their EP, but, since the total gain is still greater than loss, the broken supermodes as well as some non-broken modes have net gain. In Phase III, only one pair of the supermodes has net gain and the single-mode operation becomes possible. In Phase IV, the second pair of supermodes passes their EP. However, since the gain is not large enough to overcome loss in this phase, single-mode operation is still preserved. In Phase V, one of the second pair of the PT symmetry–broken supermodes has sufficient gain to overcome loss and single-mode operation becomes prohibited again. b,c) Electric field distribution of TE_0 mode with the loss of 1 cm^{-1} and 10 cm^{-1}. d,e) Electric field distribution of TE_0 and TE_1 mode with the loss of 30 cm^{-1} in the loss waveguide.

Here, the dependence of mode profiles and their eigenfrequency was analyzed with commercial finite element method solver of Maxwell equations, COMSOL Multiphysics. **Figure 1**a illustrates the dependence of imaginary part of the eigenfrequency as a function of modulation of loss in one half of the waveguide, while the gain of 4.95 cm^{-1} is fixed in the other half. Similar to the idealized PT symmetry–breaking studies,[33] a series of the exceptional points (EPs) could be identified.

As shown in Figure 1a, the coupled waveguide PT symmetric laser exhibits several phase transitions. The corresponding mode electric field distribution in each phase is shown in Figure 1b–e. In Phase I, $\alpha < 1.8$ cm^{-1}, all the modes were below their EPs. Due to the asymmetric gain and loss, the non-broken modes exhibited net gain in this phase, and the coupled waveguide cavity behaved as a conventional broad-area cavity supporting multiple transverse modes to lase. When the loss is between 1.8 and 4.95 cm^{-1} (Phase II), the first pair of supermodes had reached their EP, but, since the total gain was still greater than loss, the broken supermodes as well as some non-broken modes showed net gain, and single-mode operation was not yet obtained. When the loss was further increased from 4.95 to 16.9 cm^{-1}, only one pair of the supermodes showed net gain, making the single-mode operation possible, as indicated in Phase III. When the loss reached 16.9 cm^{-1}, Phase IV, the second pair of supermodes passed their EP. However, since the gain was not large enough to overcome loss in this phase, single-mode operation was still preserved. According to the PT-symmetric breaking conditions, the coupling efficiency κ_0 and κ_1 of the coupled waveguides were 4.95 and 16.9 cm^{-1}, respectively, from the numerical analysis. It is worth noting that the coupling efficiency, $\kappa_{m,}$ was dependent on the laser geometry alone and could be regarded as constant in any fabricated lasers. This also provided a new waveguide to calculate coupling coefficient in coupled waveguide structures. Finally, with further increment of the loss approaching to 44 cm^{-1}, one of the second pair of the PT symmetry–broken supermodes had sufficient gain to overcome loss, and single-mode operation was prohibited again, as shown in Phase V.

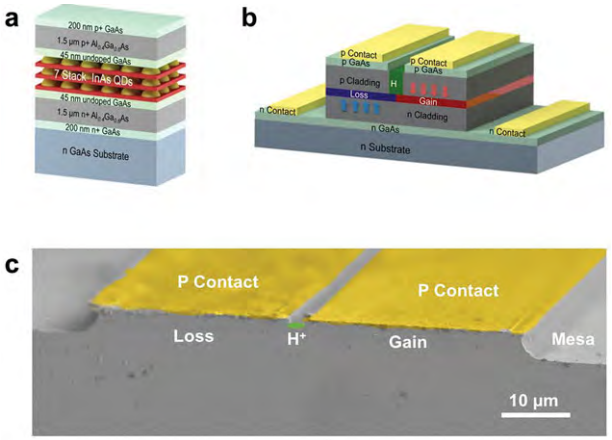

Figure 2. a) Heterostructures and b) schematic of the InAs QD PT symmetric coupled waveguide laser. c) SEM overview of the fabricated InAs QD–coupled waveguide laser.

The coupled waveguide PT symmetric laser was experimentally demonstrated as well. Shown in **Figure 2**a, the QD laser heterostructures were grown by molecular beam epitaxy (MBE). Figure 2b,c show the schematic and oblique view of the coupled waveguide laser, respectively. The coupled waveguides with total width of 60 μm were obtained and two p-type ohmic contacts were defined on top of the coupled waveguides to provide independent control of gain and loss in the waveguides.

3. Results and Discussion

The near- and far-field patterns of the coupled waveguide lasers are measured to characterize the cavity modes and laser output beam profile. **Figure 3**a–c show the near- and far-field patterns of the laser diodes with the gain bias current of 400 mA and loss bias current at 0, 50, and 120 mA, respectively. It is worth noting that $I_{th}(L = \infty)$ of the coupled waveguide lasers of 132 mA is fitted from independent experiments with the same waveguide geometry. Thus, although the loss waveguide is under small forward bias, it still exhibits loss in our cases. In the far-field pattern in Figure 3a, it is clearly seen that, with zero biased loss waveguide, the coupled waveguide laser exhibits clear signs of high-order modes as indicated by labels A and B, where the fundamental mode is labeled as C. The near-field pattern shows that the emission is from the gain waveguide facet. It is estimated that the total waveguide loss in the loss cavity is >50 cm^{-1} by considering the InAs QD absorption loss under zero bias.[34] Thus, due to the large loss and small gain, the coupled waveguide laser is operated in Phase V. When the bias current of the loss waveguide is increased to 50 mA, the peaks from the higher-order modes are successfully suppressed as shown in Figure 3b and near single-lobe far-field pattern is obtained in the broad area–coupled waveguide lasers. This indicates that the

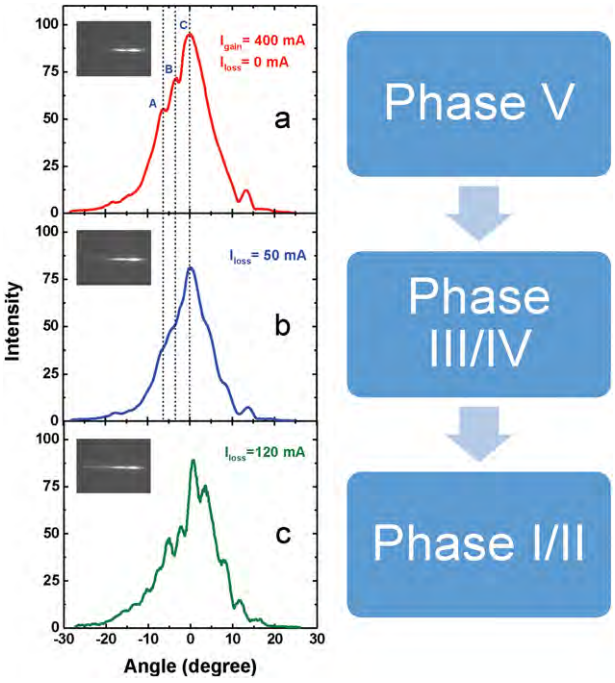

Figure 3. a–c) Far- and near-(inset)field patterns of coupled waveguide laser with I_{gain} = 400 mA, and I_{loss} varying from 0 to 120 mA. The higher order modes (A,B) and the fundamental mode (C) are labeled. It is seen that, with zero biased loss waveguide, the coupled waveguide laser exhibits clear signs of high-order modes as indicated by the label A and B. The near-field pattern shows that the emission is from the gain waveguide facet. The coupled waveguide laser is operated in Phase V where both the fundamental and first-order modes pass their PT symmetry EP. When the bias current of the loss waveguide is increased to 50 mA, the peaks from the high-order modes are successfully suppressed and near-single-lobe far-field pattern is obtained in the broad area–coupled waveguide lasers. This indicates that the laser is now operating in Phase III/IV. When the loss waveguide bias is further increased to 120 mA, high-order mode peaks reappear in the far-field pattern. The far-field pattern exhibits small shift toward the center of the coupled waveguide, and the multiple peaks imply that high-order unbroken modes start to lase. This implies that the laser is now operating in Phase I/II.

laser is now operating in Phase III or IV. In addition, the peak output power is reduced by 17%, which is due to the suppression of higher-order modes. Finally, when the loss waveguide bias is further increased to 120 mA, higher-order mode lobes reappear in the far-field pattern (Figure 3c). The far-field pattern exhibits small shift toward the center of the coupled waveguide, and multiple lobes in the pattern imply that higher-order unbroken modes start to lase compared to the case in Figure 3a. The near-field pattern shows that the laser emission pattern starts to shift toward the center of the coupled waveguides and a broken fundamental mode is still observed in the gain waveguide. This indicates that the device is now operating in Phase I/II, where both the broken fundamental mode and unbroken higher-order modes lase and the former has higher power due to larger gain compared to the remaining lasing modes. It is worth noting that the higher-order modes shown in Figure 3a are less profound than the ones in Figure 3c, this is due to the fact that the gain of higher-order modes is naturally suppressed and determined by the loss in the lossy waveguide in the PT symmetry–broken phase. This is fundamentally different from the traditional tapered waveguide lasers, where the gain of higher-order modes can still increase and exhibit lasing at higher bias conditions. Thus, it is anticipated that, if the proposed coupled waveguide PT symmetric lasers are further optimized, for example, more proper thermal management, the PT symmetric–coupled waveguide lasers can exhibit higher output power limits.

4. Conclusions

In summary, in this work, we have experimentally demonstrated a single transverse–mode broad area–coupled waveguide laser based on PT symmetry. By changing the loss in the waveguide, the supermode broken and phase transitions are experimentally observed and agree well with the theoretic predication. Further work is underway to optimize the device efficiencies and reduce the device Joule heating. Nevertheless, this work opens a pathway for the practical device applications of PT symmetry in optics.

Supporting Information

Supporting Information is available from the Wiley Online Library or from the author.

Acknowledgements

US Army Research Office (W911NF-16-1-0261); Commonwealth of Massachusetts. Note: A dedication was added on January 7th, 2019, following initial online publication in early view.

Conflict of Interest

The authors declare no conflict of interest.

Keywords

electrically injected, lasers, parity-time symmetry, phase transition

Received: June 2, 2018
Revised: August 30, 2018
Published online: October 19, 2018

[1] S. V. Suchkov, A. A. Sukhorukov, J. Huang, S. V. Dmitriev, C. Lee, Y. S. Kivshar, *Laser Photonics Rev.* **2016**, *10*, 177.
[2] L. Ge, R. El-Ganainy, *Sci. Rep.* **2016**, *6*, 24889.
[3] H. Jing, S. K. Ozdemir, J. Zhang, X.-Y. Lv, F. Nori, *Phys. Rev. Lett.* **2014**, *113*, 053604.
[4] H. Jing, S. Özdemir, X.-Y. Lü, J. Zhang, L. Yang, F. Nori, *Phys. Rev. Lett.* **2014**, *113*, 053604.
[5] L. Feng, Y.-L. Xu, W. S. Fegadolli, M.-H. Lu, J. E. B. Oliveira, V. R. Almeida, Y.-F. Chen, A. Scherer, *Nat. Mater.* **2013**, *12*, 108.
[6] H. Hodaei, M.-A. Miri, M. Heinrich, D. N. Christodoulides, M. Khajavikhan, presented at CLEO: 2014, San Jose, CA **2014**.
[7] R. El-Ganainy, M. Khajavikhan, L. Ge, *Phys. Rev. A* **2014**, *90*, 013802.
[8] C. Dai, Y. Wang, X. Zhang, *Opt. Express* **2014**, *22*, 29862.

[9] C. M. Bender, M. Gianfreda, Ş. K. Özdemir, B. Peng, L. Yang, *Phys. Rev. A* **2013**, *88*, 062111.
[10] M. Liertzer, L. Ge, A. Cerjan, A. D. Stone, H. E. Türeci, S. Rotter, *Phys. Rev. Lett.* **2012**, *108*, 173901.
[11] Z. Gu, N. Zhang, Q. Lyu, M. Li, S. Xiao, Q. Song, *Laser Photonics Rev.* **2016**, *10*, 697.
[12] W. Hayenga, M.-A. Miri, H. Hodaei, A. Ulhassan, M. Heinrich, D. N. Christodoulides, M. Khajavikhan, presented at CLEO: 2015, San Jose, CA **2015**.
[13] B. Peng, S. K. Ozdemir, F. Lei, F. Monifi, M. Gianfreda, G. L. Long, S. Fan, F. Nori, C. M. Bender, L. Yang, *Nat. Phys.* **2014**, *10*, 394.
[14] H. Hodaei, A. U. Hassan, W. E. Hayenga, M. A. Miri, D. N. Christodoulides, M. Khajavikhan, *Opt. Lett.* **2016**, *41*, 3049.
[15] H. Jing, Ş. K. Özdemir, Z. Geng, J. Zhang, X.-Y. Lü, B. Peng, L. Yang, F. Nori, *Sci. Rep.* **2015**, *5*, 9663.
[16] P. Miao, Z. Zhang, J. Sun, W. Walasik, S. Longhi, N. M. Litchinitser, L. Feng, *Science* **2016**, *353*, 464.
[17] M. Brandstetter, M. Liertzer, C. Deutsch, P. Klang, J. Schöberl, H. E. Türeci, G. Strasser, K. Unterrainer, S. Rotter, *Nat. Commun.* **2014**, *5*, 4034.
[18] B. Peng, Ş. K. Özdemir, S. Rotter, H. Yilmaz, M. Liertzer, F. Monifi, C. M. Bender, F. Nori, L. Yang, *Science* **2014**, *346*, 328.
[19] L. Feng, R. El-Ganainy, L. Ge, *Nat. Photonics* **2017**, *11*, 752.
[20] Z. Zhang, P. Miao, J. Sun, S. Longhi, N. M. Litchinitser, L. Feng, *ACS Photonics* **2018**, *5*, 3016.
[21] L. Feng, Z. J. Wong, R.-M. Ma, Y. Wang, X. Zhang, *Science* **2014**, *346*, 972.
[22] H. Hodaei, M.-A. Miri, M. Heinrich, D. N. Christodoulides, M. Khajavikhan, *Science* **2014**, *346*, 972.
[23] Z. Gao, S. T. M. Fryslie, B. J. Thompson, P. S. Carney, K. D. Choquette, *Optica* **2017**, *4*, 323.
[24] W. Liu, M. Li, R. S. Guzzon, E. J. Norberg, J. S. Parker, M. Lu, L. A. Coldren, J. Yao, *Nat. Commun.* **2017**, *8*, 15389.
[25] H. Zhao, P. Miao, M. H. Teimourpour, S. Malzard, R. El-Ganainy, H. Schomerus, L. Feng, *Nat. Commun.* **2018**, *9*, 981.
[26] Z. Gu, N. Zhang, Q. Lyu, M. Li, S. Xiao, Q. Song, *Laser Photonics Rev.* **2016**, *10*, 588.
[27] N. Zhang, Z. Gu, K. Wang, M. Li, L. Ge, S. Xiao, Q. Song, *Laser Photonics Rev.* **2017**, *11*, 1700052.
[28] R. Diehl, *High-Power Diode Lasers: Fundamentals, Technology, Applications*, Vol. *78*, Springer Science & Business Media, Heidelberg **2003**.
[29] M. Mikulla, in *High-Power Diode Lasers: Fundamentals, Technology, Applications: With Contributions by Numerous Experts* (Ed: R. Diehl), Springer, Berlin **2000**, pp. 265–288.
[30] M. T. Kelemen, J. Weber, M. Mikulla, G. Weimann, *SPIE* **2005**, *5723*, 198.
[31] M.-A. Miri, P. LiKamWa, D. N. Christodoulides, *Opt. Lett.* **2012**, *37*, 764.
[32] P. Bhattacharya, *Semiconductor Optoelectronic Devices*, Prentice-Hall, Inc., Upper Saddle River, NJ, USA **1994**.
[33] C. Huang, F. Ye, X. Chen, *Phys. Rev. A* **2014**, *90*, 043833.
[34] Y. C. Xin, H. Su, L. F. Lester, L. Zhang, A. L. Gray, S. Luong, K. Sun, Z. Zou, T. Whittington, J. Zilko, P. M. Varangis, *SPIE* **2005**, *5722*, 49.

Research Article Vol. 5, No. 12 / December 2018 / Optica 1502

Structural second-order nonlinearity in plasmonic metamaterials

Brian Wells,[1,2,†] Anton Yu. Bykov,[3,†] Giuseppe Marino,[3,4,†] Mazhar E. Nasir,[3] Anatoly V. Zayats,[3,5] and Viktor A. Podolskiy[1,6]

[1]Department of Physics and Applied Physics, University of Massachusetts Lowell, Lowell, Massachusetts 01854, USA
[2]Department of Physics, University of Hartford, Hartford, Connecticut 06117, USA
[3]Department of Physics and London Centre for Nanotechnology, King's College London, London WC2R 2LS, UK
[4]Matériaux et Phénoménes Quantiques, Université Paris Diderot-CNRS, F-75013 Paris, France
[5]e-mail: anatoly.zayats@kcl.ac.uk
[6]e-mail: viktor_podolskiy@uml.edu

Received 13 July 2018; revised 24 September 2018; accepted 2 October 2018 (Doc. ID 338796); published 26 November 2018

Nonlinear processes are at the core of many optical technologies whose further development require optimized materials suitable for nanoscale integration. Here we demonstrate the emergence of a strong bulk second-order nonlinear response in a plasmonic nanorod composite comprised of centrosymmetric materials. We develop an effective-medium description of the underlying physics, compare its predictions to the experimental results, and analyze the limits of its applicability. We demonstrate strong *tunable* generation of the *p*-polarized second-harmonic light in response to either *s*- or *p*-polarized excitation. High second-harmonic enhancement is observed for fundamental frequencies in the epsilon-near-zero spectral range. The work demonstrates emergence of structurally tunable nonlinear optical response in plasmonic composites and presents a new nonlinear optical platform suitable for integrated nonlinear photonics.

https://doi.org/10.1364/OPTICA.5.001502

1. INTRODUCTION

Second-harmonic generation (SHG), a phenomenon in which the incoming radiation of a frequency ω is converted into the signal at a double frequency 2ω, is a fundamental nonlinear optical process that enables high-resolution microscopy, laser technology, and surface studies [1–5]. Materials with strong second-order nonlinear response can further advance a broad class of photonic applications, including frequency conversion, optical information processing, sensing, security, and healthcare. Unfortunately, natural optical materials with strong second-order nonlinearity are few, and new solutions are needed to develop nonlinear optics in compact, wavelength-scale, and integrated systems.

Recent advances in nano- and microfabrication have brought into play a new class of composite media, often called metamaterials, whose optical properties are determined by shape and mutual arrangement of their components [6–10]. Metamaterials provide a flexible platform for engineering linear optical behavior that can range from isotropic [6,9] to anisotropic and hyperbolic [11,12] to chiral and bianisotropic [10]. As a rule, linear optical response of metamaterials can be related to averaged linear optical response of their components via the effective-medium theory (EMT) [9,10]. Similarly, the effective nonlinear susceptibility of the composite can be related to the nonlinear susceptibilities of constituent materials [13–16]. Recently, nonlinear metamaterials have been used for engineering third-order (Kerr-type) nonlinearity, achieving on-demand spectral response, including its sign and polarization control [17–21].

In this work, we show that re-shaping of electromagnetic fields in metamaterials with plasmonic components can be used to transform SHG from surface- to volume-dominated regime and engineer strong tunable bulk nonlinear response in plasmonic composites. We experimentally demonstrate tunable SHG from plasmonic nanorod metamaterials, develop a theoretical description of the observed phenomena, and prove that the nonlinear response can be engineered by changing structural parameters of the composite.

2. FABRICATION AND LINEAR OPTICAL RESPONSE

We consider SH response of the metamaterial comprising an array of gold nanorods in an alumina matrix [Fig. 1(a)]. When the nanorod radius r and inter-rod separation a are much smaller than the operating wavelength λ, such metamaterial behaves as a uniaxial crystal with an optical axis parallel to the nanorods [11,22,23].

The linear optical response of the metamaterial is described by a diagonal permittivity tensor $\hat{\epsilon}$ with components $\epsilon_{xx} = \epsilon_{yy} = \epsilon_{\perp}$ and $\epsilon_{zz} \neq \epsilon_{\perp}$. If the material absorption is not too small and $r \ll a \ll \lambda$, the effective-medium parameters can be related to the relative permittivity of the host ϵ_h and nanorod ϵ_{Au} materials, and the nanorod concentration $p = \pi r^2/a^2$ via

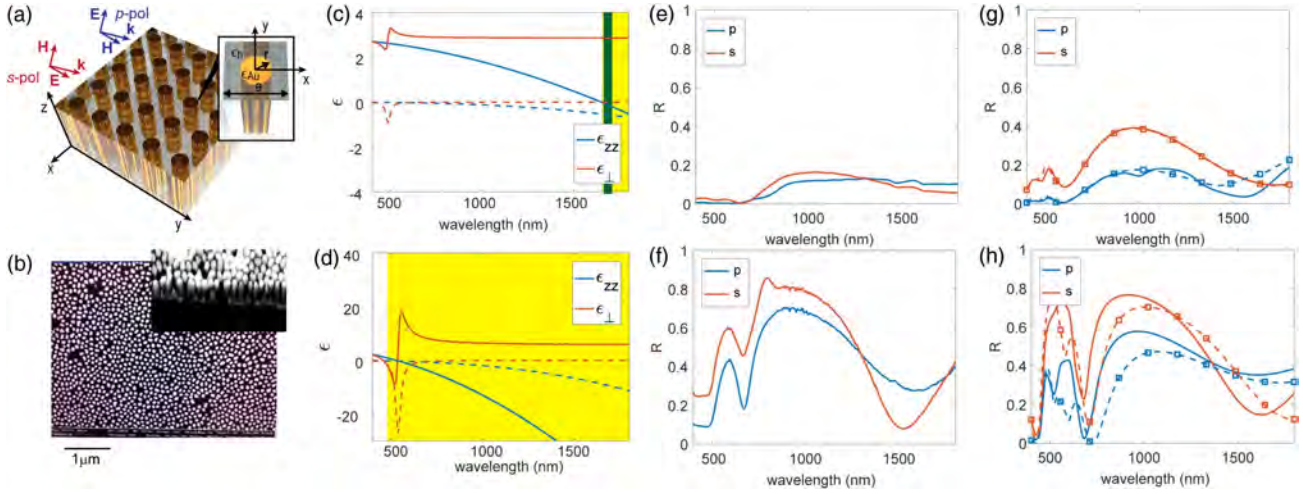

Fig. 1. (a) Schematic geometry of a metamaterial along with orientation of the fields and wavevectors considered in modeling and experiments. (b) SEM image of the nanorods after removal of the AAO matrix. (c), (d) Real (solid lines) and imaginary (dashed lines) parts of the effective permittivity of samples A (c) and B (d); green and yellow areas highlight the spectral ranges of the ENZ behavior for sample A and hyperbolic dispersion for both samples, repectively. (e)–(h) Linear reflection spectra for metamaterials A (e), (g) and B (f), (h): experiment (e), (f) and theoretical modeling (g), (h) using the full-wave finite-element simulations (solid lines) and the effective-medium theory (dashed lines). Angle of incidence in all figures is fixed at 45°.

$$\epsilon_\perp = \epsilon_h \frac{(1+p)\epsilon_{\mathrm{Au}} + (1-p)\epsilon_h}{(1+p)\epsilon_h + (1-p)\epsilon_{\mathrm{Au}}}, \quad \epsilon_{zz} = p\epsilon_{\mathrm{Au}} + (1-p)\epsilon_h. \quad (1)$$

In the limit of small absorption, long nanorods, or large unit cells, the deviations from the local EMT predictions can be quantitatively explained by incorporating retardation effects into nonlocal (wavevector-dependent) EMT [24–27].

Importantly, components of the effective permittivity tensor $\epsilon_\perp$ and ϵ_{zz} can be of different signs (Fig. 1), tuning the nanorod composite between anisotropic dielectric, epsilon near zero (ENZ) media, and a unique "hyperbolic metamaterial," which enables propagation of waveguided modes with subwavelength light confinement that in turn enhance light–matter interactions in the metamaterial [10,12,23,28].

Plasmonic nanorod metamaterials were fabricated via Au electrodeposition into nanoporous anodized aluminum oxide (AAO) templates on a glass substrate [29]. An Al film of 500 nm thickness was deposited on a substrate by magnetron sputtering. The substrate comprises a glass cover slip with a 10-nm-thick adhesive layer of tantalum pentoxide and a 7-nm-thick Au film acting as a weakly conducting layer. Highly ordered, nanoporous AAO was synthesized by a two-step anodization in 0.3M oxalic and 0.3M selenic acid at 40 V and 48 V, respectively. Gold electrodeposition was performed with a three-electrode system using a non-cyanide solution. The length of nanorods was controlled by the electrodeposition time. Fabricated metamaterials were ion-milled to smooth the top surface and ensure that the nanorods are of the same length [30]. We estimate that the variation of the nanorod height is on a few nm level, so that optical properties of the composites are not affected by surface roughness. In particular, SHG, which is very sensitive to surface roughness, exhibited neither an appreciable diffuse component nor unpolarized signal, which typically appear for rough surfaces. The samples were annealed at 300°C to improve Au optical properties.

Two samples were used in this study: sample A composed of 18-nm-diameter, 220-nm-long nanorods arranged in 110-nm period array, and sample B comprising 67-nm-diameter, 150-nm-long nanorods in the array of 100-nm period. Reflectivity and the effective-medium parameters of both samples are presented in Fig. 1. Sample A exhibits the effective plasma frequency at around $\lambda_0 \simeq 1500$ nm, while sample B operates in hyperbolic regime throughout visible and infrared spectral ranges. The linear reflection spectra of the composites are typical of anisotropic metamaterials, showing resonances due to the Fabry–Perot modes of the metamaterial slab [23,28]. The measured spectra correspond well to the numerical models for both the full-wave solutions of the Maxwell's equations using finite-element method (FEM) [31] and the transfer matrix formalism that approximates metamaterials as homogeneous layers with anisotropic permittivity given by Eq. (1).

Slight disagreement between the experiment and numerical calculations in the visible range is due to the interband transitions in gold that are not well described by the Drude model, $\epsilon_{\mathrm{Au}} = \epsilon_b - \omega_p^2/[\omega(\omega - i\tau)]$ with plasma frequency $\omega_p = (e^2 n_0/m_e\epsilon_0)^{1/2} = 1.36\times10^{16}\ \mathrm{s}^{-1}$, inelastic scattering frequency $\tau = 2.1\times10^{14}\ \mathrm{s}^{-1}$, parameter $\epsilon_b = 9.5$, and ϵ_0, e, m_e, and n_0 being the permittivity of free space, electron charge, electron mass, and free-electron density in gold, respectively [32].

3. NONLINEAR OPTICAL RESPONSE

SHG spectroscopy was performed using light from the optical parametric amplifier (200 fs pulse trains at the repetition rate of 200 kHz and average power up to 50 mW in near-IR wavelength range 1100–1800 nm). The laser light polarization was controlled to achieve *p*- or *s*-polarized fundamental light incident on the sample at an angle of incidence of 45° with a spot approximately 30–50 μm in diameter. The reflected *p*- or *s*- polarized SH light was spectrally selected using the set of short-pass optical filters and measured with the spectrometer and the cooled charged-coupled device (CCD) camera. In order to compensate for pulse energy and pulse duration fluctuations, the measured signal was normalized to a reference SHG measured in reflection from *β*-barium borate (BBO) crystal. Also, the SHG from each sample

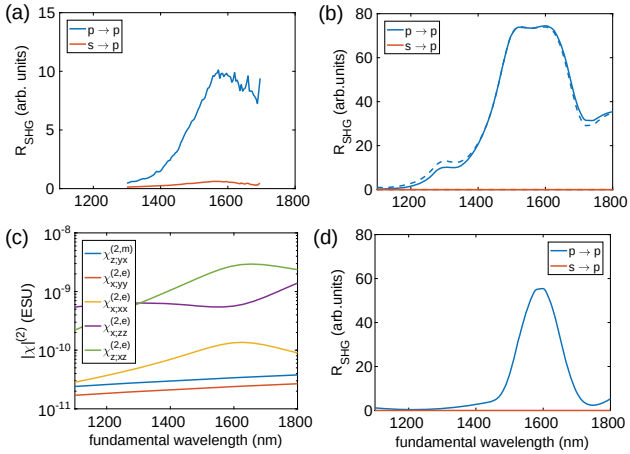

Fig. 2. SHG spectra for different polarization configurations from metamaterial A at an angle of incidence of 45°: (a) experimental spectra normalized with $s \rightarrow p$ SHG from z-quartz at $\lambda_0 = 1300$ nm; (b) spectra simulated using the full-wave numerical modeling with the nonlinear polarization described by Eq. (2) (solid lines) and by the simplified model Eq. (3) (dashed lines). (c) Spectral dependence of the non-vanishing components of the effective polarizability matrix. (d) SHG spectra simulated with the nonlinear EMT model [Eqs. (4) and (5)].

was compared to the signal from a z-quartz plate. As a result, the SHG data for samples A and B can be directly compared to each other.

SHG spectra of the two samples fundamentally differ from each other. Sample A exhibits strong *p*-polarized SHG emission in response to a *p*-polarized pump in the ENZ frequency range (Fig. 2). At the same time, SHG signal generated by sample B (Fig. 3) exhibits pronounced maxima associated with excitation of the metamaterial slab modes [28] for both *p*- and *s*-polarized excitation. Interestingly, the SHG intensity from sample B under *s*-polarized excitation is approximately four times stronger than under *p*-polarized pump, indicating the important role of local fields inside the metamaterial, as was observed previously for the nanoparticle composites [33].

The spectral and polarization dependences of the SHG are in a good agreement with the full-wave numerical simulations (Figs. 2 and 3) that implement the hydrodynamic model of the SHG in plasmonic media [28,34,35] (see Supplement 1) with the nonlinear polarization of gold given by

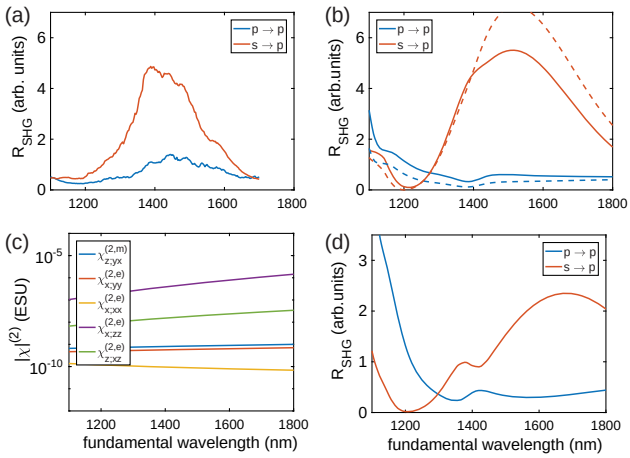

Fig. 3. Same as Fig. 2 but for sample B.

$$\mathbf{P}_{2\omega} = \frac{1}{2\omega(2\omega - i\tau)}\left\{\sum_{\alpha}\frac{\partial}{\partial r_\alpha}\left(\frac{\mathbf{j}_\omega j_{\omega;\alpha}}{en_0}\right) - \frac{e}{m_e}[\epsilon_0(\nabla\cdot\mathbf{E}_\omega)\mathbf{E}_\omega + \mathbf{j}_\omega \times \mathbf{B}_\omega]\right\}, \quad (2)$$

where ω and 2ω represent the fundamental and SH frequencies, respectively, index α represents the Cartesian coordinates, and $\mathbf{E}, \mathbf{B}, \mathbf{j}$ are the electric field, magnetic induction, and current density, respectively (the quantitative difference between numerical and experimental results for sample A can be explained by deviation of optical absorption of solution-derived gold from the Drude model used in this work [36]).

The detailed analysis shows that SHG efficiency and polarization dependencies are complex functions of the effective medium parameters, thickness of the metamaterial slab, and angle of illumination θ [28]. Nevertheless, in all cases, the nonlinear polarization, and, therefore, SHG, is dominated by the terms related to the components of the electromagnetic fields that have nonvanishing unit-cell averages [37] and to $\partial/\partial z$ derivatives of these components. These terms depend on polarization of the incident beam and are given by

$$P^{(p)}_{2\omega;x} = -\frac{1}{2\omega(2\omega - i\tau)}\left(\frac{e}{m}j_{\omega;z}B_{\omega;y} + \frac{1}{ne}\left[j_{\omega;z}\frac{\partial j_{\omega;x}}{\partial z} - j_{\omega;x}\frac{\partial j_{\omega;z}}{\partial z}\right]\right),$$

$$P^{(s)}_{2\omega;x} = \frac{1}{2\omega(2\omega - i\tau)}\frac{e}{m}j_{\omega;y}B_{\omega;z},$$

$$P^{(p)}_{2\omega;z} = \frac{1}{2\omega(2\omega - i\tau)}\left(\frac{e}{m}j_{\omega;x}B_{\omega;y} - \frac{2j_{\omega;z}}{ne}\frac{\partial j_{\omega;z}}{\partial z}\right),$$

$$P^{(s)}_{2\omega;z} = -\frac{1}{2\omega(2\omega - i\tau)}\frac{e}{m}j_{\omega;y}B_{\omega;x}. \quad (3)$$

This is illustrated in Figs. 2(b) and 3(b), which compare SHG predictions according to simplified Eq. (3) and full-wave solutions [Eq. (2)]. It is seen that Eq. (3) largely agrees with the full-wave solutions of the Maxwell's equations, while slightly overestimating the reflected SHG of sample B. At the same time, Eq. (3) underestimates the transmitted SHG for this sample (see Supplement 1), so that the total SHG predicted by the simplified model is in line with predictions of the full-wave calculations. Note that the simplified model predicts $P_{2\omega;y} = 0$, resulting in only *p*-polarized SHG signal, in line with the experiment as well as with the predictions of the full-wave calculations.

Using Eqs. (3) and the constituent relationship $\mathbf{j} = i\omega\epsilon_0\epsilon_{\mathrm{Au}}\mathbf{E}$, it becomes possible to represent the unit-cell-averaged nonlinear polarization in the metamaterial as a quadratic form of the (unit-cell-averaged) fields, introducing the effective *bulk* second-order nonlinear susceptibilities $\chi^{(2,e)}$ and $\chi^{(2,m)}$:

$$P_{2\omega;\alpha} = \sum_{\beta,\gamma}[\chi^{(2,e)}_{\alpha;\beta\gamma}E_{\omega;\beta}E_{\omega;\gamma} + \chi^{(2,m)}_{\alpha;\beta\gamma}E_{\omega;\beta}B_{\omega;\gamma}], \quad (4)$$

where the Greek subscripts represent the Cartesian coordinates x, y, and z.

Components of the effective nonlinear susceptibility were calculated in the limit of the validity of local EMT [Eq. (1)], which yields homogeneous fields across the cross section of the nanorods [10,24, and Supplement 1], by substituting explicit relationships between field components inside the nanorod, their unit-cell averages, frequency, and components of the wavevector, resulting in

$$\chi^{(2,e)}_{x;xx} = N^p L \epsilon_{\mathrm{Au}} k_x \frac{\epsilon_\perp}{\epsilon_{zz}},$$

$$\chi^{(2,e)}_{x;zz} = N^p \left(\frac{p\epsilon_{zz}\omega_p^2 + \epsilon_{zz}\epsilon_{\mathrm{Au}} L\omega^2}{k_x c^2} - \epsilon_{\mathrm{Au}} L k_x \right),$$

$$\chi^{(2,e)}_{z;xz} = -N^p/2 \left(L \frac{\omega_p^2 \epsilon_{zz}}{c^2 k_x} - 2pk_x \epsilon_{\mathrm{Au}} \frac{\epsilon_\perp}{\epsilon_{zz}} \right),$$

$$\chi^{(2,m)}_{z;yx} = -2L\epsilon_0 \epsilon_{\mathrm{Au}} \frac{e}{m} \frac{\omega^2}{\omega_p^2} [\epsilon_{\mathrm{Au}}(2\omega) - \epsilon_b],$$

$$\chi^{(2,e)}_{x;yy} = -\chi^{(2,m)}_{z;yx} \frac{k_x}{\omega}. \quad (5)$$

Here, $N^p = 2\epsilon_0 \epsilon_{\mathrm{Au}} (e/m)(\omega^3/\omega_p^4)(\epsilon_{\mathrm{Au}}(2\omega) - \epsilon_b)$ is the normalization parameter, $k_x = \omega \sin\theta/c$ is the transverse component of the wavevector, and $L = 2p\epsilon_b/[\epsilon_{\mathrm{Au}}(\omega) + \epsilon_b]$ represents the relationship between the E_x and E_y components of the electric field in the nanorod and its unit-cell-averaged values. The first three components describe SHG excitation due to *p*-polarized fundamental light, while the latter two represent the SH generated by the *s*-polarized light.

4. DISCUSSION

Equations (4) and (5) represent the main result of this work: the metamaterial as a whole exhibits dipolar-like nonlinear response even though its material constituents lack bulk dipolar $\chi^{(2)}$. The effective nonlinear susceptibilities of plasmonic nanorod composite are determined primarily by the structure of the local fields inside it [37]. Components of the effective nonlinear susceptibility depend on an angle of incidence so that the symmetry of the metamaterial is broken by the internal fields, except at normal incidence when the electric-dipole SHG is forbidden due to symmetry considerations. The explicit dependence of the effective nonlinear susceptibility on the wavenumber reflects the *structural* origin of the nonlinearity of a metamaterial.

The developed nonlinear EMT adequately predicts both spatial distribution of nonlinear polarization (Supplement 1) and spectral SH response [Figs. 2(d) and 3(d)] with exception of a small red shift of the SHG spectra for sample B, which is related to the red shift in a linear reflectivity observed in Fig. 1. Calculated values of an effective nonlinear response of the composite $\chi^{(2)} \sim 10^{-10}$–10^{-6} [electrostatic units, ESU] [Figs. 2(c), 3(c), and 4] indicate relatively strong nonlinearity, which favorably compares to common nonlinear-optical crystals, including quartz, potassium dihydrogen phosphate (KDP) ($\chi^{(2)} \sim 10^{-9}$ ESU), and $LiNbO_3$ ($\chi^{(2)} \sim 10^{-7}$ ESU) [1,2]. Experimental data are in line with calculated values for the nonlinear susceptibility for both studied metamaterials. SHG intensity from the composites can be further optimized by manipulating geometry and reducing losses.

The main limitation on the effective-medium nonlinear description, presented in this work, comes from the granularity of metamaterial. In particular, the local EMT that underpins the final expressions in Eq. (1) assumes local behavior of the constituents, dipolar quasistatic field between the nanorods, and does not account for propagation of cylindrical plasmons along the nanorods. Nonlocal response of a free-electron plasma [23,38] may become relevant for composites with ultra-thin nanorods ($r \ll 1/k_F \sim \lambda_0/100$, with k_F being the Fermi wavenumber). Contributions of retardation effects and spatial dispersion may affect field distribution in the composites with a nanorod concentrations $p \gtrsim 0.3$. In the limit $r \ll \lambda$, these effects can be taken into account by including retardation effects [24] in the nonlocal Maxwell–Garnett formalism. Excitation of cylindrical plasmons primarily affects composites with low loss operating across elliptic and ENZ regimes. This limitation can be addressed by including propagation of additional electromagnetic waves (with linear response described in Ref. [25]) into the developed formalism. Nonlocal EMT can be further developed to incorporate non-quasistatic effects. Granularity of the composite must also be considered when emission of SH light is calculated. We expect that including the high-index "longitudinal" modes through nonlocal EMT [25,39] may further improve predictive power of the formalism presented in this work.

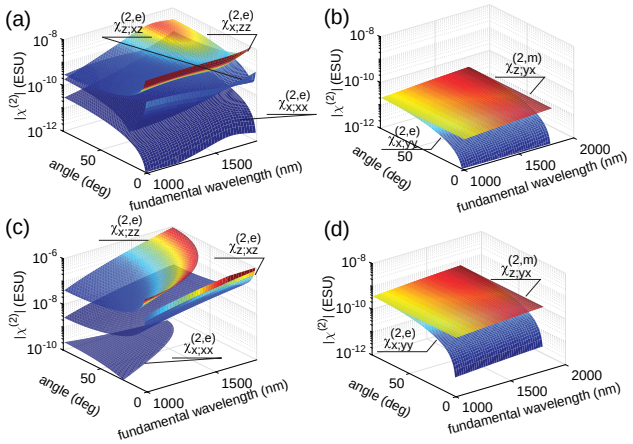

Fig. 4. Spectral and angular dependences of the components of the effective nonlinear polarizability for sample A (a), (b) and sample B (c), (d) for (a), (c) *p*- and (b), (d) *s*-polarized fundamental light.

In contrast to common nonlinear optical crystals with fixed optical properties, the structural origin of the second-order nonlinearity in metamaterials provides a platform for engineering not only spectral but also polarization properties of a nonlinear response. For example, the structural parameters of the nanorod metamaterials can be tuned to achieve dominant SHG contribution from either $p \to p$ (Fig. 2) or $s \to p$ (Fig. 3) polarization configurations [28,33].

In the former case, the metamaterial operates in the ENZ ($\epsilon_{zz} \simeq 0$) regime at a fundamental frequency $\lambda_0 \simeq 1600$ nm. The relatively weak effective nonlinear polarizability is compensated by the strong enhancement of *z* component of the electric field (a similar response has been predicted for bulk, nontunable, ENZ materials [20,40]). Interestingly, numerical calculations [Fig. 5(a)] suggest that material absorption in gold (which

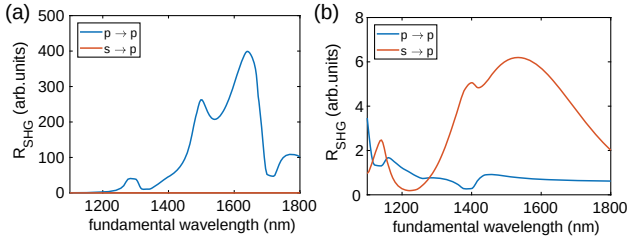

Fig. 5. Full-wave numerical modeling of the SHG spectra from low-loss analogs of sample A (a) and sample B (b). The loss is decreased by two times compared to Figs. 2(b) and 3(b).

effectively limits the value of $|\epsilon_{zz}|$) plays the role of the limiting factor in the SHG process in the ENZ regime. Reducing losses in the gold by a factor of 2 (achieved in calculations by reducing scattering frequency τ to the value that is in line with bulk Au $\tau = 1.05 \times 10^{-14}$ s [32]) has a potential to increase SHG efficiency in the metamaterial by an order of magnitude.

In another limit, the metamaterial operates in the hyperbolic regime so that the enhancement of the local field is attributed mainly to the Fabry–Perot modes of the metamaterial slab of a finite thickness [28]. This modest enhancement of a local field does not significantly depend on material absorption [Fig. 5(a)] and, being accompanied by a relatively strong nonlinear polarizability, once again results in a strong SH response of the metamaterial.

5. CONCLUSION

We have demonstrated the emergence of structural nonlinearity in composite metamaterials. The approach, presented here on the example of SHG from plasmonic nanorod metamaterials, can be extended to analyze nonlinear response of a broad class of composites, such as plasmonic nanoparticle metasurfaces [33] and metamaterials based on noncentrosymmetric, strongly nonlinear materials, such as AlGaAs nanopillars [41]. Structural nonlinearity opens the door to utilize composite media to engineer spectral and polarization nonlinear response beyond what is available with naturally occurring materials.

All the data supporting this research are presented in the article and in the supplementary material.

Funding. Army Research Office (ARO) (W911NF-12-1-0533, W911NF-16-1-0261); Engineering and Physical Sciences Research Council (EPSRC) (UK); H2020 European Research Council (ERC) iPLASMM project (321268); Royal Society; Wolfson Foundation.

See Supplement 1 for supporting content.

†These authors contributed equally to this work.

REFERENCES AND NOTES

1. R. W. Boyd, ed., *Nonlinear Optics*, 2nd ed. (Academic, 2003).
2. Y. Shen, *The Principles of Nonlinear Optics* (Wiley, 1984).
3. P. Campagnola and C.-Y. Dong, "Second harmonic generation microscopy: principles and applications to disease diagnosis," Laser Photon. Rev. **5**, 13–26 (2011).
4. M. Fiebig, V. V. Pavlov, and R. V. Pisarev, "Second-harmonic generation as a tool for studying electronic and magnetic structures of crystals: review," J. Opt. Soc. Am. B **22**, 96–118 (2005).
5. P. Segovia, G. Marino, A. V. Krasavin, N. Olivier, G. A. Wurtz, P. A. Belov, P. Ginzburg, and A. V. Zayats, "Hyperbolic metamaterial antenna for second-harmonic generation tomography," Opt. Express **23**, 30730–30738 (2015).
6. J. B. Pendry, "Negative refraction makes a perfect lens," Phys. Rev. Lett. **85**, 3966–3969 (2000).
7. N. Engheta, "Circuits with light at nanoscales: optical nanocircuits inspired by metamaterials," Science **317**, 1698–1702 (2007).
8. C. Kern, M. Kadic, and M. Wegener, "Experimental evidence for sign reversal of the hall coefficient in three-dimensional metamaterials," Phys. Rev. Lett. **118**, 016601 (2017).
9. G. W. Milton, *The Theory of Composites*, 1st ed. (Cambridge University, 2002).
10. M. A. Noginov and V. A. Podolskiy, eds., *Tutorials in Metamaterials* (CRC Press, 2012).
11. T. Dumelow and D. Tilley, "Optical properties of semiconductor superlattices in the far infrared," J. Opt. Soc. Am. A **10**, 633–645 (1993).
12. A. Poddubny, I. Iorsh, P. Belov, and Y. Kivshar, "Hyperbolic metamaterials," Nat. Photonics **7**, 948–957 (2013).
13. K. C. Rustagi and C. Flytzanis, "Optical nonlinearities in semiconductor-doped glasses," Opt. Lett. **9**, 344–346 (1984).
14. D. Stroud and P. M. Hui, "Nonlinear susceptibilities of granular matter," Phys. Rev. B **37**, 8719–8724 (1988).
15. D. J. Bergman, "Nonlinear behavior and 1/f noise near a conductivity threshold: effects of local microgeometry," Phys. Rev. B **39**, 4598–4609 (1989).
16. J. W. Haus, N. Kalyaniwalla, R. Inguva, M. Bloemer, and C. M. Bowden, "Nonlinear-optical properties of conductive spheroidal particle composites," J. Opt. Soc. Am. B **6**, 797–807 (1989).
17. M. Kauranen and A. Zayats, "Nonlinear plasmonics," Nat. Photonics **6**, 737–748 (2012).
18. N. N. Lepeshkin, A. Schweinsberg, G. Piredda, R. S. Bennink, and R. W. Boyd, "Enhanced nonlinear optical response of one-dimensional metal-dielectric photonic crystals," Phys. Rev. Lett. **93**, 123902 (2004).
19. A. Neira, N. Olivier, M. E. Nasir, W. Dickson, G. A. Wurtz, and A. V. Zayats, "Eliminating material constraints for nonlinearity with plasmonic metamaterials," Nat. Commun. **6**, 7757 (2015).
20. D. de Ceglia, S. Campione, M. A. Vincenti, F. Capolino, and M. Scalora, "Low-damping epsilon-near-zero slabs: nonlinear and nonlocal optical properties," Phys. Rev. B **87**, 155140 (2013).
21. L. Nicholls, F. J. Rodríguez-Fortuño, M. E. Nasir, R. M. Cordova-Castro, N. Olivier, G. A. Wurtz, and A. V. Zayats, "Ultrafast synthesis and switching of light polarization in nonlinear anisotropic metamaterials," Nat. Photonics **11**, 628–633 (2017).
22. R. Wangberg, J. Elser, E. E. Narimanov, and V. A. Podolskiy, "Nonmagnetic nanocomposites for optical and infrared negative-refractive-index media," J. Opt. Soc. Am. B **23**, 498–505 (2006).
23. N. Vasilantonakis, M. E. Nasir, W. Dickson, G. A. Wurtz, and A. V. Zayats, "Bulk plasmon-polaritons in hyperbolic nanorod metamaterial waveguides," Laser Photon. Rev. **9**, 345–353 (2015).
24. B. M. Wells, W. Guo, and V. A. Podolskiy, "Homogenization of nanowire-based composites with anisotropic unit-cell and layered substructure," MRS Commun. **6**, 23–29 (2016).
25. B. M. Wells, A. V. Zayats, and V. A. Podolskiy, "Nonlocal optics of plasmonic nanowire metamaterials," Phys. Rev. B **89**, 035111 (2014).
26. V. Agranovich and V. Kravtsov, "Notes on crystal optics of superlattices," Solid State Commun. **55**, 85–90 (1985).
27. Note that these nonlocal corrections originate from the composite nature of the plasmonic metamaterial and not from the optical response of its components, which is assumed to be described by local ϵ_{Au} and ϵ_h.
28. G. Marino, P. Segovia, A. V. Krasavin, P. Ginzburg, N. Olivier, G. A. Wurtz, and A. V. Zayats, "Second-harmonic generation from hyperbolic plasmonic nanorod metamaterial slab," Laser Photon. Rev. **12**, 1700189 (2018).
29. M. E. Nasir, S. Peruch, N. Vasilantonakis, W. P. Wardley, W. Dickson, G. A. Wurtz, and A. V. Zayats, "Tuning the effective plasma frequency of nanorod metamaterials from visible to telecom wavelengths," Appl. Phys. Lett. **107**, 121110 (2015).
30. A. V. Krasavin, M. E. Nasir, W. Dickson, and A. V. Zayats, "Reactive tunnel junctions in electrically-driven plasmonic nanorod metamaterials," Nat. Nanotechnol. **13**, 159–164 (2018).
31. The commercial software (COMSOL, www.comsol.com) implements a model of a periodic Au nanorod array with ϵ_{Au} given by Drude model, $\epsilon_{Al_2O_3} \approx 2.74$, and geometrical parameters (r, a) deduced from the structures used in the experiments.
32. P. B. Johnson and R. W. Christy, "Optical constants of the noble metals," Phys. Rev. B **6**, 4370–4379 (1972).
33. T. Stefaniuk, N. Olivier, A. Belardini, C. P. T. McPolin, C. Sibilia, A. A. Wronkowska, A. Wronkowski, T. Szoplik, and A. V. Zayats, "Self-assembled silver-germanium nanolayer metamaterial with the enhanced nonlinear response," Adv. Opt. Mater. **5**, 1700753 (2017).
34. Y. Zeng, W. Hoyer, J. Liu, S. W. Koch, and J. V. Moloney, "Classical theory for second-harmonic generation from metallic nanoparticles," Phys. Rev. B **79**, 235109 (2009).
35. A. V. Krasavin, P. Ginzburg, and A. V. Zayats, "Free-electron optical nonlinearities in plasmonic nanostructures: a review of the hydrodynamic description," Laser Photon. Rev. **12**, 1700082 (2017).

36. R. Pollard, A. Murphy, W. Hendren, P. Evans, R. Atkinson, G. A. Wurtz, A. V. Zayats, and V. A. Podolskiy, "Optical nonlocalities and additional waves in epsilon-near-zero metamaterials," Phys. Rev. Lett. **102**, 127405 (2009).
37. We assume that the fields propagate in xz plane; s-polarized light has non-zero components of E_y, H_x, H_z, while the p-polarized light has components of E_x, E_z, H_y fields. We limit our study to the regime when the metamaterial is excited by a single electromagnetic wave that is either p or s polarized. The detailed investigation of more complicated excitation geometries and the analysis of tensorial properties of $\chi^{(2)}_{\alpha;\beta\gamma}$ will be the subject of future work.
38. M. Scalora, M. A. Vincenti, D. de Ceglia, and J. W. Haus, "Nonlocal and quantum-tunneling contributions to harmonic generation in nanostructures: electron-cloud-screening effects," Phys. Rev. A **90**, 013831 (2014).
39. P. Ginzburg, D. Roth, M. E. Nasir, P. Segovia, A. V. Krasavin, J. Levitt, L. M. Hirvonen, B. Wells, K. Suhling, D. Richards, V. A. Podolskiy, and A. V. Zayats, "Spontaneous emission in non-local materials," Light Sci. Appl. **6**, e16273 (2017).
40. M. A. Vincenti, D. de Ceglia, and M. Scalora, "Nonlinear dynamics in low permittivity media: the impact of losses," Opt. Express **21**, 29949–29954 (2013).
41. L. Carletti, D. Rocco, A. Locatelli, C. D. Angelis, V. F. Gili, M. Ravaro, I. Favero, G. Leo, M. Finazzi, L. Ghirardini, M. Celebrano, G. Marino, and A. V. Zayats, "Controlling second-harmonic generation at the nanoscale with monolithic AlGaAs-on-AlOx antennas," Nanotechnology **28**, 114005 (2017).

Research Article | Vol. 26, No. 23 | 12 Nov 2018 | OPTICS EXPRESS 30588
Optics EXPRESS

Single-transverse-mode broadband InAs quantum dot superluminescent light emitting diodes by parity-time symmetry

RUIZHE YAO, CHI-SEN LEE, VIKTOR PODOLSKIY, AND WEI GUO*

Physics and Applied Physics Department, University of Massachusetts Lowell, Lowell, MA 01854, USA
**wei_guo@uml.edu*

Abstract: Parity-time (PT) symmetry breaking in counterintuitive gain/loss coupled waveguide designs is numerically and theoretically investigated. The PT symmetry mode selection conditions are determined theoretically. Single-transverse-mode broadband InAs quantum dot (QD) superluminescent light emitting diodes (SLEDs) are fabricated and characterized; the PT symmetric broad-area SLEDs contain laterally coupled gain and loss PT- symmetric waveguides. Single-transverse-mode operation is achieved by parity-time symmetry breaking. The broadband SLEDs exhibit a uniform Gaussian-like emission spectrum with the 3-dB bandwidth of 110 nm. Far-field characteristics of the coupled waveguide SLEDs exhibit a single-lobe far-field pattern when the gain and loss waveguides are biased at the injection current of 600 mA and 60 mA, respectively.

1. Introduction

Parity-time (PT) symmetry is originally discovered in quantum mechanics for non-Hermitian Hamiltonians [1]. Due to the similarity between Schrodinger and Maxwell equations, optics have become an ideal platform to investigate non-Hermitian systems, where the non-Hermiticity is denoted by optical gain and loss. Several novel behaviors have been theoretically and experimentally discovered in the PT symmetry optics, such as mode discrimination and non-reciprocity in optical waveguides [2–9]. Particularly, the mode discrimination in PT-symmetric waveguides has been employed to realize single mode PT symmetric lasers [10,11]. Such devices are mostly limited to optical injection [12,13], and they are mainly focused on laser devices. However, laser devices exhibit gain clamping after lasing and limit the further exploration of physics in PT-symmetric devices. In this context, we report a novel application of PT symmetry in the electrically driven broadband superluminescent light emitting diodes (SLEDs) where the mode discrimination based on PT symmetry is utilized in the coupled waveguides to achieve single-transverse-mode operation in tunable gain/loss configuration. In the SLED devices, both the gain and loss can be tuned and the broadband emission provide another challenge to investigate the frequency dependence of PT-symmetric conditions, which is studied theoretically in this work.

As an important category of the optoelectronic devices, SLED devices have found applications in several areas. For example, owing to the recent development of optical coherence tomography (OCT) systems for biomedical imaging, broadband SLEDs in the telecommunication wavelength regime have drawn great interest [14,15], as the key components in OCT. The inhomogeneous gain spectrum broadening of InAs quantum dot (QD) materials has made it a supreme candidate for broadband light sources [16–19]. Despite being considered as a promising candidate, it remains challenging to achieve high-performance, highly focused beam and high power, broadband QD SLEDs for OCT applications [20–25]. There are two major reasons hindering the further development of QD SLEDs, non-uniform gain spectrum and smaller gain compared with their quantum well (QW) counterparts. The former issue has been largely investigated and several unique

#334813 https://10.1364/OE.26.030588
Journal © 2018 Received 13 Jun 2018; revised 29 Aug 2018; accepted 12 Sep 2018; published 12 Nov 2018

Optics EXPRESS

structures and techniques have been employed to obtain a Gaussian-like broadband gain spectrum [26]. To improve the device output power, it is natural to use broad-area waveguide design, while mode filters, such as tapered waveguide design, has to be employed to maintain single-transverse-mode output for efficient fiber coupling and diffraction limit focus [27]. However, the device performance is largely scarified, since the mode filter techniques often introduce large loss to the fundamental modes. In this context, the reported PT-symmetric SLEDs provide a unique pathway to achieve single-transverse-mode operation in broad-area coupled waveguide configurations. In addition to the device applications, the presented PT-symmetric SLED devices also provide a platform to investigate PT symmetry with both tunable gain and loss.

2. PT-symmetric waveguide design

The optical response of any active optical system, including lasers and LEDs, can be related to the interplay between the active (gain) material that generates photons and the encompassing waveguide or resonator structure that provides spectral and spatial feedback to the gain medium. In this work the active region is incorporated in the coupled gain/loss planar waveguides running parallel to each other. A schematic of the waveguide structure is illustrated in Fig. 1. The waveguide core and cladding layers consist of GaAs and $Al_{0.4}Ga_{0.6}As$ with the thickness of 300 nm and 1.5 μm, respectively. The coupled waveguides have identical geometry and conjugate refractive index, representing gain and loss in the core region and total width of 60 μm.

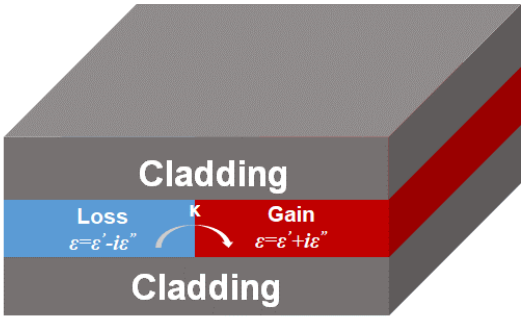

Fig. 1. Schematic of the gain/loss coupled waveguide structure, where ε' and ε'' represents the real and imaginary part of the permittivity in the waveguide region, respectively and κ is the coupling coefficient; time dependence $\propto \exp i\omega t$ is assumed

Monochromatic electromagnetic radiation propagating in the waveguide structure can be represented as a linear combination of waveguide modes, with each mode characterized by its spatial profile, as well as its overall gain/loss coefficient. The overall modal gain coefficient can be related to the imaginary part of permittivity of the (active) waveguide core. The parity (P) and time (T) symmetries of a particular mode can be related to its behavior under reflection of the geometry and gain/loss conjugation, respectively.

The compound nature of the waveguide in our SLED implies that modes of the compound waveguide can be represented as a combination of the modes of its components. Analytically, the propagation constant of the compound mode can be related to the properties of the modes in the components via coupled-mode theory. Alternatively, the properties of the modes of the compound waveguide can be calculated numerically.

Optics EXPRESS

3. Coupled mode theory

In two coupled waveguides with conjugate imaginary index, the modal amplitudes a_m and b_m of the m_{th} modes in these two guides is described through the coupled mode theory as follow;

$$\frac{da_m}{dz} = i\beta_m a_m + ik_m b_m + g_m a_m \tag{1}$$

$$\frac{db_m}{dz} = i\beta_m b_m + ik_m a_m + g_m b_m \tag{2}$$

where β_m is their respective propagation constant, κ_m is coupling coefficient between these modes, and g_m stands for the modal gain or loss in the m_{th} mode. The solution of the coupled wave equations is depending on the ratio of $R_m = \frac{g_m}{k_m}$, and described as follow;

$$\begin{pmatrix} a_m \\ b_m \end{pmatrix} = \begin{cases} \begin{pmatrix} 1 \\ \mp\exp(\mp i\theta_m) \end{pmatrix} \exp\left(\mp ikcos(\theta_m) z\right) \ \exp(iR_m z) & R_m < 1 \\ \begin{pmatrix} 1 \\ \mp\exp(\mp\theta_m) \end{pmatrix} \exp\left(\mp ksinh(\theta_m) z\right) \ \exp(iR_m z) & R_m > 1 \end{cases} \tag{3}$$

where $\cosh\theta_m = R_m$, as shown by Christodoulides et. al. and Miri et. al. [5,28]. As result, the threshold condition for PT-symmetric breaking in conjugate gain/loss coupled waveguides is $\kappa_m = g_m$. When $g_m < \kappa_m$, the modes of the coupled waveguide represent symmetric and anti-symmetric combinations of the two waveguide modes. The propagation constants of these modes are often degenerated featuring a complete balance of gain and loss. However, when $g_m > \kappa_m$, PT symmetry is spontaneously broken, and the waveguide modes become the modes of the combined waveguide; most importantly, only one of the two supermodes exhibits gain and the other experiences loss. In waveguide cavities, higher order modes are typical of larger coupling coefficient than the one of the fundamental mode. Therefore, it is possible to design a coupled waveguide device to allow only the fundamental mode to reach the PT-symmetric breaking threshold and exhibit gain.

Even though PT-symmetric breaking can be achieved in conjugate gain/loss coupled waveguide configurations, it is almost impossible to maintain the conditions of equal gain and loss in practical devices. Thus, it is preferable to operate the devices with varied gain while the loss is fixed. It has been shown by Christodoulides et. al. and Li et. al. that, in unbalanced gain/loss conditions, the PT symmetry conditions can significantly deviate from their exact PT balance [28,29]. The PT symmetry breaking threshold becomes $k_m = \frac{|g_m| + |\alpha_m|}{2}$, where κ_m, g_m, and α_m are the coupling coefficient, gain and loss of the m_{th} order mode, respectively. With a fixed loss of α_m, the thresholdless PT symmetry breaking condition becomes $\alpha_m = 2\kappa_m$.

4. Waveguide simulation

The PT-symmetric waveguides described above are investigated with a 2-dimensional (2D) model by commercial Maxwell equation solver, COMSOL Multiphysics, to simulate the mode profile and effective mode index. Wavelength of 1.3 μm is considered in the simulation. Transverse electric (TE) modes are calculated in the simulations, since only the

Optics EXPRESS

TE modes are supported in Fabry-Perot waveguides with QD active materials [30]. Figure 2(a) shows the imaginary part of the mode propagation constant vs. g/α, gain/loss of the waveguide. It is calculated that, in the balanced gain/loss waveguide configuration, the PT symmetry exceptional point (EP) of TE_0 mode is at $\alpha_0 = g_0 = 6.2$ cm^{-1}, and, by further increasing the gain/loss in the waveguide, higher order TE_1 supermodes subsequently reach their EP and break their PT symmetry. The coupled mode theory therefore implies that the effective coupling coefficient of TE_0 mode, $\kappa_0 = g_0 = 6.2$ cm^{-1}, is determined. In addition, we further investigate the PT-symmetric breaking conditions in coupled waveguide containing fixed loss and varied gain. In typical InAs quantum dots, the modal loss can be adjusted in the range of 0 to 50 cm^{-1} by changing the biasing conditions in the loss waveguide. Figures 2(b)-2(d) illustrate the simulated imaginary part of the mode propagation constant vs. gain of the gain waveguide, where the loss in the loss waveguide is fixed at 8.2 cm^{-1}, 20 cm^{-1}, and 37 cm^{-1}, respectively. Our simulation results have shown that PT-symmetric breaking, and similar behaviors can be obtained in the fixed loss and varied gain configurations as well, and the exceptional points of the supermodes in the coupled waveguides is largely depending on the fixed loss. Figure 2(e) illustrates the EP of TE_0 and TE_1 modes as a function loss, where it is shown that the EP is decreasing at increased loss. When the loss is at $\alpha_0 = = 2*\kappa_0 = 11.4$ cm^{-1}, the coupled PT symmetric waveguides exhibit thresholdless PT-symmetric broken of TE_0 mode, EP = 0 cm^{-1}. The thresholdless PT-symmetric broken condition agrees well with the coupled model theory.

In addition, we discuss the mode selections for single-transverse-mode operation in the couple waveguide cavity. Single-transverse-mode operation is achieved when there is only one pair of supermode break their PT symmetry and exhibit net gain. The gray areas in Figs. 2(b)-2(d) illustrate the window meeting the aforementioned conditions. It is worth noting that, as shown in Fig. 2(b), since the loss is small, the single-transverse-mode operation is prohibited before TE_1 supermodes reach their EP, since the non-broken supermodes start to exhibit net gain. Figure 2(f) shows the required gain vs. different fixed loss in gain and loss coupled waveguide for single-transverse-mode output. It is found that the single transverse mode operation exhibits largest window if the loss in the loss waveguide is tuned to ~10 cm^{-1}.

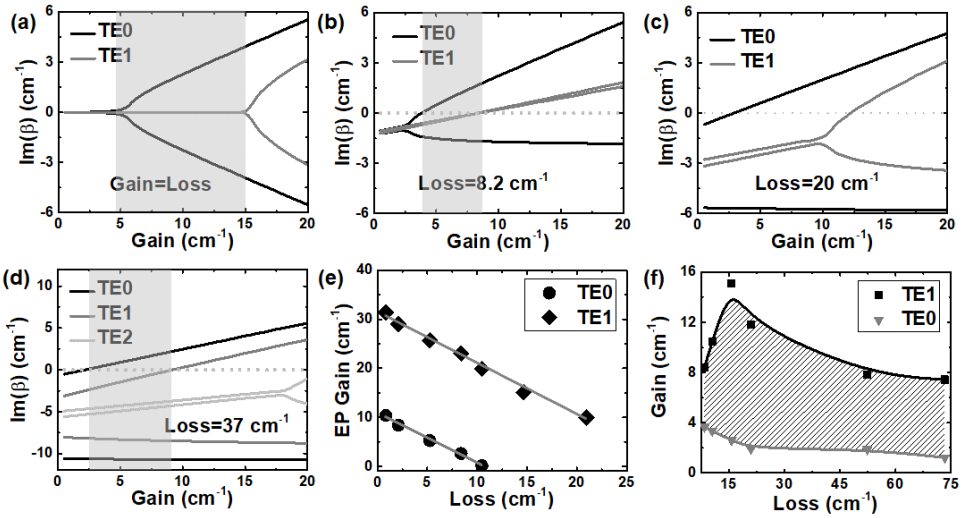

Fig. 2. (a) Imaginary part of the mode propagation constant vs. g/α, gain/loss of the waveguide. (b)-(d) the simulated imaginary part of the mode propagation constant vs. gain of the gain waveguide in the coupled waveguide configurations, where the loss in the loss waveguide is fixed at 8.2 cm^{-1}, 20 cm^{-1}, and 37 cm^{-1}, respectively (e) EPs of TE_0 and TE_1 modes as a function loss. (f) Required gain vs. fixed loss for single-transverse-mode operation.

Optics EXPRESS

Since the broadband SLEDs exhibit emissions across a broad-spectrum range, it is essential to investigate the frequency dependence of EPs and single-transverse-mode operation conditions. Figure 3 illustrates the EP of TE_0 (square) and lower (dot) and upper (triangle) boundaries of the single mode operation windows vs. wavelength, where the loss of 20 cm^{-1} is fixed in the loss waveguide. It is found that the single mode operation window, shaded area in Fig. 3, exhibits weakly dependence on the wavelength, which is favorable for PT symmetric devices with broadband emissions.

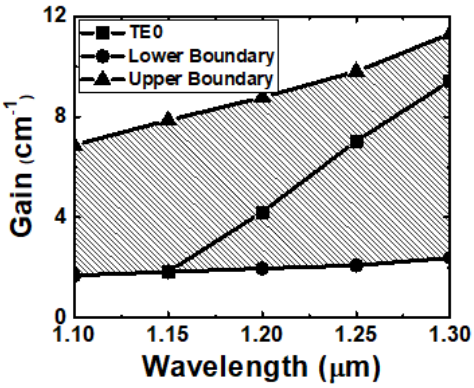

Fig. 3. EP of TE_0 (square) and lower (dot) and upper (triangle) boundaries of the single-mode-operation windows vs. wavelength.

5. SLED fabrication process

Shown in Fig. 4(a), the QD SLED heterostructures is grown by a Veeco Gen-II molecular beam epitaxy (MBE) system. The top and bottom GaAs and $Al_{0.4}Ga_{0.6}As$ layers are doped with beryllium and silicon, respectively, to provide the electrical contacts and carrier injections. To achieve broadband output emission spectrum, chirped QD active region with a varied $In_xAl_{1-x}As$ strain reducing layers is used. This technique has been previously demonstrated by us to effectively improve the QD SLED emission bandwidth and reduce the spectrum dip [26]. The coupled waveguide PT symmetric SLEDs are fabricated by standard photolithography, wet chemical etching and metallization. As shown in Fig. 4(b), the coupled waveguides with a total width of 60 μm are obtained and two p-type Ohmic contacts are defined on top of the coupled waveguides to provide independent control of the gain and loss in the waveguides, where the electrical isolation between them are achieved by three-step deep H^+ ion implantation process. The ion implanted region has the width of 3 μm and depth of 1.5 μm. In addition, the top 200 nm p^+ GaAs contact region is removed by wet chemical etching to assure a good electrical isolation. The oblique view of the fabricated device is shown in scanning electron microscope (SEM) image in Fig. 4(c). The facets are roughened on purpose to increase the mirror loss of the SLED cavity and suppress gain clamping.

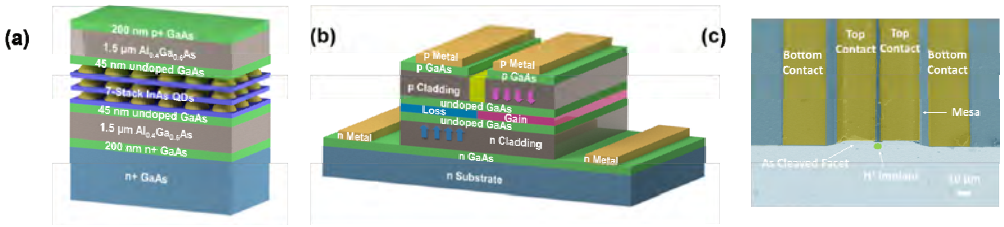

Fig. 4. Heterostructures (a), schematic (b) and SEM image (c) of the InAs QD PT symmetric coupled waveguide SLEDs

6. Experiment results and discussions

To minimize the heating effect, the coupled waveguide PT-symmetric SLEDs are characterized under pulse current injection conditions with the pulse width and duty cycle of 1 μs and 1%, respectively, at room temperature. To characterize the cavity modes and output beam profile, near-field and far-field patterns are measured. Figures 5(a) and 5(b) show the near- and far-field patterns of the SLED under gain and loss bias current of 600 mA and 60 mA, respectively. It is found that near single-lobe far-field pattern is obtained from the PT-symmetric SLEDs, and the SLED emission is from the gain waveguide, which implies that the coupled waveguide is operating in the PT-symmetric broken regime. Finally, it is also measured that the SLED far-field pattern remains single-lobe with the gain bias current varied from 300 to 800 mA.

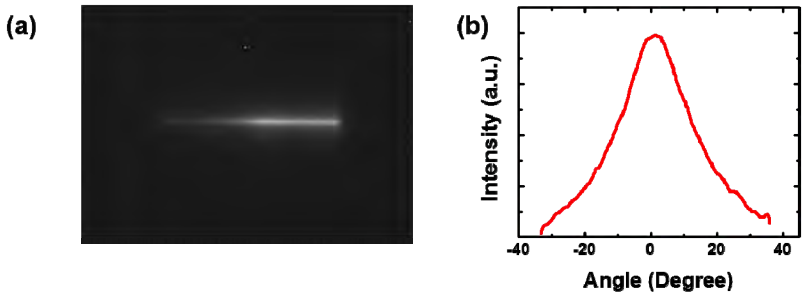

Fig. 5. PT-symmetric SLED near-field (a) and far-field (b) patterns with the basing condition of I_{gain} = 600 mA and I_{loss} = 60 mA.

Finally, Fig. 6 shows the emission spectrum of the QD SLEDs, where the 3-dB bandwidth > 100 nm is obtained. More importantly, the emission spectrum shows no obvious spectrum dip with a near Gaussian-like shape.

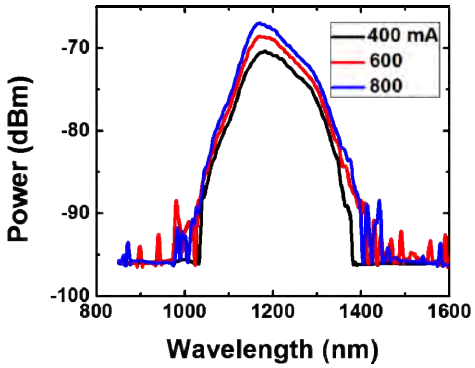

Fig. 6. EL spectra of the PT symmetric SLED at I_{gain} = 400, 600 and 800 mA and I_{loss} = 60 mA.

7. Summary

In summary, in this work, we have numerically investigated the PT-symmetric breaking conditions in gain/loss coupled waveguides, where the supermode EPs in varied both gain and fixed loss configurations are studied. The single-transverse-mode operation window is determined numerically as well. In addition, we have experimentally demonstrated a single-transverse-mode broadband QD SLED based on PT symmetry. By introducing the gain and loss in the coupled waveguide and concept of PT symmetry, single transverse mode can be achieved in the broad-area waveguides, which has the potential to significantly improve the

SLED output power while still maintaining the preferred mode profile. Further work is underway to optimize the device efficiencies and reduce the device Joule heating. Nevertheless, this work opens a pathway for practical device applications of PT symmetry in optics. It is argued that the PT symmetric QD SLEDs can play a significant role in biomedical imaging applications after further optimizing the cavity design for the broadband.

Funding

US Army Research Office (W911NF-16-1-0261); Commonwealth of Massachusetts.

References

1. C. M. Bender, S. Boettcher, and P. N. Meisinger, "PT-symmetric quantum mechanics," J. Math. Phys. **40**(5), 2201–2229 (1999).
2. C. E. Rüter, K. G. Makris, R. El-Ganainy, D. N. Christodoulides, M. Segev, and D. Kip, "Observation of parity–time symmetry in optics," Nat. Phys. **6**(3), 192–195 (2010).
3. A. Regensburger, C. Bersch, M.-A. Miri, G. Onishchukov, D. N. Christodoulides, and U. Peschel, "Parity-time synthetic photonic lattices," Nature **488**(7410), 167–171 (2012).
4. Z. Lin, H. Ramezani, T. Eichelkraut, T. Kottos, H. Cao, and D. N. Christodoulides, "Unidirectional invisibility induced by PT-symmetric periodic structures," Phys. Rev. Lett. **106**(21), 213901 (2011).
5. M.-A. Miri, P. LiKamWa, and D. N. Christodoulides, "Large area single-mode parity–time-symmetric laser amplifiers," Opt. Lett. **37**, 764–766 (2012).
6. L. Feng, M. Ayache, J. Huang, Y.-L. Xu, M.-H. Lu, Y.-F. Chen, Y. Fainman, and A. Scherer, "Nonreciprocal light propagation in a silicon photonic circuit," Science **333**(6043), 729–733 (2011).
7. L. Feng, Y.-L. Xu, W. S. Fegadolli, M.-H. Lu, J. E. Oliveira, V. R. Almeida, Y.-F. Chen, and A. Scherer, "Experimental demonstration of a unidirectional reflectionless parity-time metamaterial at optical frequencies," Nat. Mater. **12**(2), 108–113 (2013).
8. P. Miao, Z. Zhang, J. Sun, W. Walasik, S. Longhi, N. M. Litchinitser, and L. Feng, "Orbital angular momentum microlaser," Science **353**(6298), 464–467 (2016).
9. M. Brandstetter, M. Liertzer, C. Deutsch, P. Klang, J. Schöberl, H. E. Türeci, G. Strasser, K. Unterrainer, and S. Rotter, "Reversing the pump dependence of a laser at an exceptional point," Nat. Commun. **5**(1), 4034 (2014).
10. L. Feng, Z. J. Wong, R.-M. Ma, Y. Wang, and X. Zhang, "Single-mode laser by parity-time symmetry breaking," Science **346**(6212), 972–975 (2014).
11. H. Hodaei, M.-A. Miri, M. Heinrich, D. N. Christodoulides, and M. Khajavikhan, "Parity-time-symmetric microring lasers," Science **346**(6212), 975–978 (2014).
12. W. Liu, M. Li, R. S. Guzzon, E. J. Norberg, J. S. Parker, M. Lu, L. A. Coldren, and J. Yao, "An integrated parity-time symmetric wavelength-tunable single-mode microring laser," Nat. Commun. **8**, 15389 (2017).
13. Z. Gao, S. T. Fryslie, B. J. Thompson, P. S. Carney, and K. D. Choquette, "Parity-time symmetry in coherently coupled vertical cavity laser arrays," Optica **4**(3), 323–329 (2017).
14. H. Hodaei, M. A. Miri, A. U. Hassan, W. E. Hayenga, M. Heinrich, D. N. Christodoulides, and M. Khajavikhan, "Single mode lasing in transversely multi-moded PT-symmetric microring resonators," Laser Photonics Rev. **10**(3), 494–499 (2016).
15. W. Drexler and J. G. Fujimoto, *Optical coherence tomography: Technology and applications* (Springer Science & Business Media, 2008).
16. S. Haffouz, P. J. Barrios, R. Normandin, D. Poitras, and Z. Lu, "Ultrawide-bandwidth, superluminescent light-emitting diodes using InAs quantum dots of tuned height," Opt. Lett. **37**(6), 1103–1105 (2012).
17. P. D. Greenwood, D. T. Childs, K. Kennedy, K. M. Groom, M. Hugues, M. Hopkinson, R. A. Hogg, N. Krstajić, L. E. Smith, S. J. Matcher, M. Bonesi, S. MacNeil, and R. Smallwood, "Quantum Dot Superluminescent Diodes for Optical Coherence Tomography: Device Engineering," IEEE J. Sel. Top. Quantum Electron. **16**(4), 1015–1022 (2010).
18. L. Li, M. Rossetti, A. Fiore, L. Occhi, and C. Velez, "Rail-to-rail super class AB CMOS operational amplifiers," Electron. Lett. **41**, 1 (2005).
19. Z. Zhang, R. Hogg, X. Lv, and Z. Wang, "Self-assembled quantum-dot superluminescent light-emitting diodes," Adv. Opt. Photonics **2**(2), 201–228 (2010).
20. F. Ginovart, J. C. Simon, and I. Valiente, "Gain recovery dynamics in semiconductor optical amplifier," Opt. Commun. **199**(1-4), 111–115 (2001).
21. M. L. Nielsen, J. Mørk, R. Suzuki, J. Sakaguchi, and Y. Ueno, "Experimental and theoretical investigation of the impact of ultra-fast carrier dynamics on high-speed SOA-based all-optical switches," Opt. Express **14**(1), 331–347 (2006).
22. I. O'Driscoll, T. Piwonski, J. Houlihan, G. Huyet, R. J. Manning, and B. Corbett, "Phase dynamics of InAs⁄GaAs quantum dot semiconductor optical amplifiers," Appl. Phys. Lett. **91**(26), 263506 (2007).
23. X. Li, P. Jin, Q. An, Z. Wang, X. Lv, H. Wei, J. Wu, J. Wu, and Z. Wang, Nanoscale Res. Lett. **6**, 1–5 (2011).
24. W.-S. Wang, M.-L. Zhang, and Z.-D. Chen, "Influence of a phonon bath in a quantum dot cavity QED system: Dependence of the shape," Chin. Phys. B **23**(9), 094205 (2014).

Optics EXPRESS

25. Q. An, P. Jin, Z. C. Wang, X. K. Li, and Z. G. Wang, "Lightwave Technology," Journalism **30**, 2684–2688 (2012).
26. R. Yao, N. Weir, C.-S. Lee, and W. Guo, IEEE Photonics J. **8**, 1–7 (2016).
27. Z. Zhang, R. Hogg, P. Jin, T. Choi, B. Xu, and Z. Wang, "High-Power Quantum-Dot Superluminescent LED With Broadband Drive Current Insensitive Emission Spectra Using a Tapered Active Region," IEEE Photonics Technol. Lett. **20**(10), 782–784 (2008).
28. H. Hodaei, A. U. Hassan, J. Ren, W. E. Hayenga, M. A. Miri, D. N. Christodoulides, and M. Khajavikhan, "Design Considerations for Single-Mode Microring Lasers Using Parity-Time-Symmetry," IEEE J. Sel. Top. Quantum Electron. **22**(5), 12–18 (2016).
29. L. Ge and L. Feng, "Optical-reciprocity-induced symmetry in photonic heterostructures and its manifestation in scattering PT -symmetry breaking," Phys. Rev. A (Coll. Park) **94**(4), 043836 (2016).
30. D. Bimberg, M. Grundmann, and N. N. Ledentsov, *Quantum Dot Heterostructures* (John Wiley & Sons, 1999).

Research Article | Vol. 26, No. 13 | 25 Jun 2018 | OPTICS EXPRESS 17541
Optics EXPRESS

Low-frequency nonlocal and hyperbolic modes in corrugated wire metamaterials

Bo Fan,[1] Dmitry Filonov,[2] Pavel Ginzburg,[2] and Viktor A. Podolskiy[1,*]

[1]*Department of Physics and Applied Physics, University of Massachusetts Lowell, Lowell, MA 01854, USA*
[2]*School of Electrical Engineering, Tel Aviv University, Tel Aviv, 69978, Israel*
**viktor_podolskiy@uml.edu*

Abstract: Metamaterials based on arrays of aligned plasmonic nanowires have recently attracted significant attention due to their unique optical properties that combine tunable strong anisotropy and nonlocality. These optical responses provide a platform for implementation of novel sensing, imaging, and quantum optics applications. Basic building blocks, used for construction of those peculiar composites, are plasmonic metals, such as gold and silver, which have moderate negative values of permittivities at the optical spectral range. Scaling the plasmonic behavior to lower frequencies remains a longstanding challenge also owing to the emergence of strong spatial dispersion in homogenized artificial composites. At lower THz and GHz frequencies, the electromagnetic response of noble metals approaches that of perfect electric conductors, preventing straightforward scaling of visible-frequency plasmonics to the frequency domains that are important for a vast range of applications, including wireless communications, microwave technologies and many others. Here we demonstrate that both extreme anisotropy (so-called hyperbolicity) and nonlocality of artificial composites can be achieved and designed in arrays of corrugated perfectly conducting wires at relatively low GHz frequencies. The key concept is based on hybridization of spoof plasmon polariton modes that in turn emulate surface polariton waves in systems with corrugated interfaces. The method makes it possible to map the recent developments in the field of plasmonics and metamaterials to the domain of THz and RF photonics.

OCIS codes: (250.5403) Plasmonics; (160.3918) Metamaterials.

References and links

1. P. A. Belov, Y. Zhao, S. Sudhakaran, A. Alomainy, and Y. Hao, "Experimental study of the subwavelength imaging by a wire medium slab," Appl. Phys. Lett. **89**(26), 262109 (2006).
2. E. E. Narimanov, H. Li, Y. A. Barnakov, T. U. Tumkur, and M. A. Noginov, "Reduced reflection from roughened hyperbolic metamaterial," Opt. Express **21**(12), 14956–14961 (2013).
3. A. V. Kabashin, P. Evans, S. Pastkovsky, W. Hendren, G. A. Wurtz, R. Atkinson, R. Pollard, V. A. Podolskiy, and A. V. Zayats, "Plasmonic nanorod metamaterials for biosensing," Nat. Mater. **8**(11), 867–871 (2009).
4. V. V. Yakovlev, W. Dickson, A. Murphy, J. McPhillips, R. J. Pollard, V. A. Podolskiy, and A. V. Zayats, "Ultrasensitive nonresonant detection of acoustic waves (ultrasound) with plasmonic metamaterials," Adv. Mater. **25**(16), 2351–2356 (2013).
5. G. A. Wurtz, R. Pollard, W. Hendren, G. P. Wiederrecht, D. J. Gosztola, V. A. Podolskiy, and A. V. Zayats, "Designed nonlocality-enhanced sub-picosecond nonlinearities in plasmonic nanorod metamaterial," Nat. Nanotechnol. **6**, 107 (2011).
6. J. Yao, Z. Liu, Y. Liu, Y. Wang, C. Sun, G. Bartal, A. M. Stacy, and X. Zhang, "Optical negative refraction in bulk metamaterials of nanowires," Science **321**(5891), 930 (2008).
7. A. S. Shalin, S. V. Sukhov, A. A. Bogdanov, P. A. Belov, and P. Ginzburg, "Optical pulling forces in hyperbolic metamaterials," Phys. Rev. A **91**(6), 063830 (2015).
8. P. Ginzburg, D. J. Roth, M. E. Nasir, P. Segovia, A. V. Krasavin, J. Levitt, L. M. Hirvonen, B. Wells, K. Suhling, D. Richards, V. A. Podolskiy, and A. V. Zayats, "Spontaneous emission in nonlocal materials," Light Sci. Appl. **6**(6), e16273 (2017).
9. J. B. Pendry, A. J. Holden, W. J. Stewart, and I. Youngs, "Extremely low frequency plasmons in metallic mesostructures," Phys. Rev. Lett. **76**(25), 4773–4776 (1996).

#328511 https://doi.org/10.1364/OE.26.017541
Journal © 2018 Received 19 Apr 2018; revised 14 May 2018; accepted 15 May 2018; published 21 Jun 2018

10. V. Kuzmiak, A. A. Maradudin, and F. Pincemin, "Photonic band structures of two-dimensional systems containing metallic components," Phys. Rev. B Condens. Matter **50**(23), 16835–16844 (1994).
11. P. A. Belov, R. Marques, S. I. Maslovski, I. S. Nefedov, M. Silveirinha, C. R. Simovski, and S. A. Tretyakov, "Strong spatial dispersion in wire media in the very large wavelength limit," Phys. Rev. B **67**(11), 113103 (2003).
12. J. B. Pendry, L. Martín-Moreno, and F. J. Garcia-Vidal, "Mimicking surface plasmons with structured surfaces," Science **305**(5685), 847–848 (2004).
13. A. I. Fernandez-Dominguez, L. Martin-Moreno, F. J. Garcia-Vidal, S. R. Andrews, and S. A. Maier, "Spoof plasmon polariton modes propagating along periodically corrugated wires," IEEE J. Sel. Top. Quantum Electron. **14**(6), 1515–1521 (2008).
14. A. Rusina, M. Durach, and M. I. Stockman, "Theory of spoof plasmons in real metals," Appl. Phys., A Mater. Sci. Process. **100**(2), 375–378 (2010).
15. B. Wells, A. V. Zayats, and V. A. Podolskiy, "Nonlocal optics of plasmonic nanowire metamaterials," Phys. Rev. B **89**(3), 035111 (2014).
16. S. Maier, Plasmonics: Fundamentals and applications (Springer, New York, 2007).
17. I. Avrutsky, I. Salakhutdinov, J. Elser, and V. A. Podolskiy, "Highly confined optical modes in nanoscale metal-dielectric multi-layers," Phys. Rev. B **75**(24), 241402 (2007).
18. J. C. Maxwell Garnett, "Colours in metal glasses, in metallic films and in metallic solutions," Roy. Proc. A **205**, 237 (1906).
19. M. A. Noginov and V. A. Podolskiy, eds., Tutorials in Metamaterials (CRC, Boca Raton, 2012).
20. M. A. Kats, D. Woolf, R. Blanchard, N. Yu, and F. Capasso, "Spoof plasmon analogue of metal-insulator-metal waveguides," Opt. Express **19**(16), 14860–14870 (2011).
21. COMSOL AB, www.comsol.com

1. Introduction

Plasmonics is a rapidly developing field of nanophotonics focusing on optical phenomena with noble metals. These materials, having negative permittivities at optical and infrared (IR) spectral ranges, introduce frontier possibilities in tailoring and designing peculiar electromagnetic interactions between light and matter, which can be utilized in a range of practical applications. Apart from intriguing responses of individual metal elements, structured arrays of plasmonic components form a flexible platform for metamaterials - composite media with engineered optical responses unavailable in nature. In particular, metamaterials formed by arrays of aligned plasmonic nanowires grown in dielectric matrices operating at visible and near-infrared frequencies, have been recently used to demonstrate super resolution imaging [1], and super-absorbers [2], achieve record-high performances of bio- and acousto-optical sensors [3,4], to enable novel nonlinear optical platforms [5], realize negative refraction of light [6], achieve optical attraction forces [7], and record-enhancement of density of states [8]. These phenomena are enabled by extreme optical anisotropy (also known as hyperbolicity) in combination with strong nonlocality of nanowire composites.

Unfortunately, due to materials dispersion, advances in visible-frequency plasmonics can be rarely reproduced at lower, GHz and THz frequencies. Attempts to mimic electron plasma behavior at GHz frequencies with arrays of ultra-thin wires [9] faced challenges even at extremely long wavelength limit [10,11]. Nevertheless, the behavior of individual surface plasmon polariton waves, propagating along a metal-dielectric surface, can be mimicked with spoof plasmons, electromagnetic modes supported by structured perfectly conducting interfaces [12–14].

Here we propose a novel metamaterial platform that relies on hybridized spoof plasmons to realize hyperbolic and nonlocal modes in low-frequency systems. We analyze numerically the dispersion of these modes and demonstrate the analytical mapping between the low-frequency response of corrugated wire systems and the formalism, proposed in Ref [15]. by Wells et.al. for high-frequency response of plasmonic nanowire media. The rest of the manuscript is organized as follows: Sections 2 and 3 introduce important concepts of the nonlocal plasmonic wire media and of spoof plasmons and provides a brief review of relevant recent results. Section 4 presents the spoof wire media and outlines the results of exact numerical solutions of Maxwell equations. in these materials. The analytical mapping between optical response of plasmonic wires and low-frequency behavior of spoof wire metamaterials is presented in Section 5. Section 6 concludes the manuscript.

2. Nonlocal nanowire metamaterials in the optical domain

Optical response of metals is dominated by the dynamics of their free electrons. At visible and near-IR frequencies, this plasma-like dynamics causes permittivity of metals to become negative, enabling excitation of sub-wavelength plasmons resulting from coupling between free-space photons and electrons. Photon-plasmon interaction enable a special optical mode, known as surface plasmon polariton, a guided wave that propagates at the boundary between plasmonic and dielectric media and exponentially decays away from the interfaces into both of surrounding materials [16].

When multiple structures supporting surface plasmon polaritons are brought to close proximity to each other, individual polariton modes hybridize with each other, often enabling new types of guided waves [17]. Specifically, in metamaterial composites formed by arrays of aligned plasmonic wires (Fig. 1), hybridization of cylindrical surface plasmons supported by individual metallic yields the formation of bulk modes. The dispersion of the resulting optical modes can be described in terms of effective permittivity tensor, whose diagonal components $\hat{\epsilon} = \{\epsilon_\perp, \epsilon_\perp, \epsilon_z\}$ are given by:

$$\epsilon_\perp = \epsilon_\perp^{mg}; \epsilon_z(k_z) = \xi\left[k_z^2 - \left(k_z^l\right)^2\right]\frac{c^2}{\omega^2} \tag{1}$$

where $\hat{\epsilon}^{mg}$ represent the components of the effective permittivity obtained in quasi-static limit using Maxwell Garnett formalism [18],

$$\epsilon_\perp^{mg} = \epsilon_d\frac{(1+p)\epsilon_m + (1-p)\epsilon_d}{(1+p)\epsilon_d + (1-p)\epsilon_m};\ \epsilon_z^{mg} = p\epsilon_m + (1-p)\epsilon_d \tag{2}$$

p represents the volume-fraction of the wires in the system, ϵ_m and ϵ_d represent the permittivity of the metal wires and dielectric matrix, k_z^l represents the wavenumber of the collective plasmon-polariton mode propagating along the nanowires and the parameter ξ can be determined via $\xi = p\frac{\epsilon_m + \epsilon_d}{\epsilon_d - n_\infty^2}$, with $n_\infty = \lim_{\epsilon_m \to -\infty} k_z^l c/\omega$.

Note that the component of the permittivity in the direction along the wires is nonlocal (it explicitly depends on the wavevector). As result of nonlocality, the composite supports three waves, one TE-polarized "ordinary" wave and two TM-polarized "extraordinary" modes [or one TM and one longitudinal (additional) wave]. Explicitly, dispersion of the TE wave is given by:

$$k_x^2 + k_z^2 = \epsilon_\perp\frac{\omega^2}{c^2} \tag{3a}$$

and the dispersion of the extraordinary modes is given by

$$\frac{k_x^2}{\epsilon_z(k_z)} + \frac{k_z^2}{\epsilon_\perp} = \frac{\omega^2}{c^2} \tag{3b}$$

When $k_x = 0$ and the modes propagate parallel to optical axis of metamaterial, the dispersion of one of extraordinary modes is identical to that of TE wave; the second extraordinary mode, formally described by $\epsilon_{zz}(k_z) = 0$, represents longitudinal-like electromagnetic wave.

The dispersion of optical modes in plasmonic nanowires depend on multiple (often, interdependent) parameters including wavelength, material permittivity, and geometry. However, regardless of the exact parameter variation, this dispersion exhibits universal

behavior. To illustrate this behavior, we follow the approach of Ref [15]. and consider the hypothetical situation when the geometry of metamaterial and excitation wavelength are fixed and vary relative permittivity of wires.

The effective indices and the field distributions of transverse and longitudinal modes supported by the wire composites are summarized in Fig. 1. It is seen that the transverse waves represent oscillations of electron plasma perpendicular to wires, while longitudinal mode represents plasmonic oscillations along the nanowires. Note that since the polarizations of the two types of modes are orthogonal to each other, their dispersions are allowed to intersect at some point on the diagram [no anti-crossing phenomenon is observed in Fig. 1(c)].

However, when $k_x \neq 0$, "transverse" oscillations of electrons do couple to their "longitudinal" counterparts. As result of this coupling, the dispersion of the two TM modes exhibit a typical avoided crossing ehavior with wavenumber k_x playing the role of the effective coupling strength. Therefore, as the coupling strength is increased, the (square of) one of the effective modal indices grows and the other one decays. Mathematically [see Eq. (3)b)], evolution of the first mode can be mapped to hyperbola in k_x, k_z space, while the behavior of second mode is described by an ellipse. Hyperbolic-like modes, characterized by growing $k_z(k_x)$ behavior, has been utilized to postpone the onset of diffraction limit, to engineer optical density of states, and novel type of nonlinearities [2–8,19].

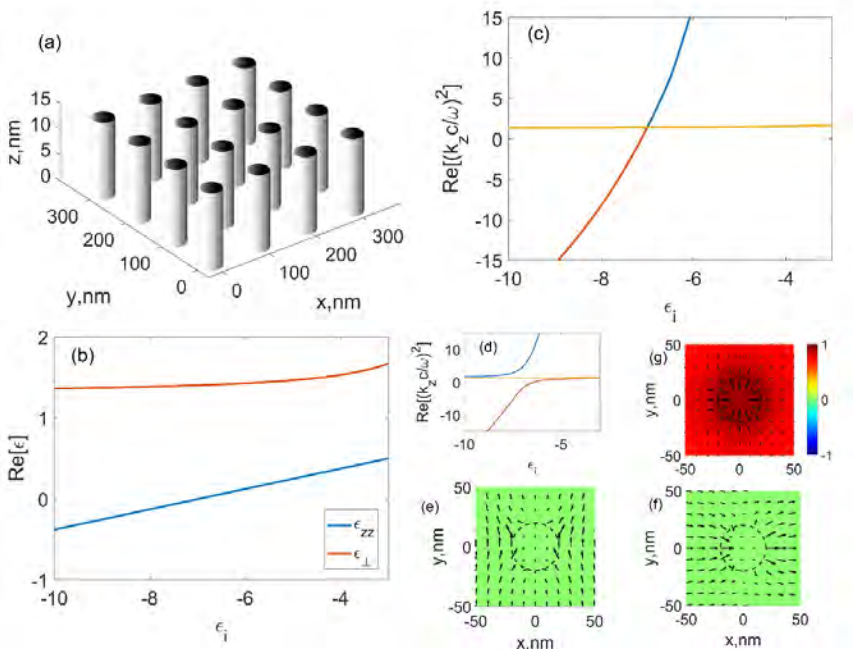

Fig. 1. (a) Schematic of the plasmonic nanowire composite; $a = 100nm, r = 20nm, \epsilon_d = 1$; vacuum wavelength $\lambda_0 = 1.5\mu m$; (b) effective medium parameters, according to the Maxwell-Garnett approximation; (c) effective modal index of the transverse (orange, $k_z c/\omega \approx 1$) and strongly dispersive longitudinal (red, blue) modes propagating parallel to the wires; panel (d) illustrates dispersion of the TM (red, blue lines) and TE (orange) modes propagating obliquely $[k_x = 0.3\omega/c]$ to the wires; panels (e,f,g) illustrate the distribution of electric field in the unit cell of the TE, TM, and longitudinal modes, respectively; in the limit $k_x \to 0$ propagation of transverse mode converges to predictions of Maxwell-Garnett effective medium theory [15]

Optics EXPRESS

Interestingly, effective out-of-plane permittivity of the "transverse" extraordinary wave in the limit $k_x \to 0$ converges to ϵ_{zz}^{mg} [15]. This wave has elliptic behavior at relatively high (visible) frequencies where $\epsilon_{zz}^{mg} > 0$, and switches to hyperbolic response at lower frequencies where $\epsilon_{zz}^{mg} < 0$. The "additional" extraordinary wave operates in hyperbolic regime when $\epsilon_{zz}^{mg} > 0, \epsilon_m < -\epsilon_d$ and becomes exponentially decaying mode when $\epsilon_{zz}^{mg} < 0$. At ultra-low frequencies where $|\epsilon_m| \gg 1$, electromagnetic response of metamaterial approaches epsilon-near-infinity limit that can be used for high-resolution imaging [1] but that does not provide the benefits of modulation of density of optical states associated with nonlocal epsilon-near-zero or hyperbolic systems [19].

3. Spoof plasmons

The concept of spoof plasmon was first introduced in Ref [12]. by Pendry et.al. In contrast to surface plasmon polaritons that propagate at the smooth metal-dielectric interface, spoof plasmons propagate at the interface between a dielectric and structured perfectly conducting metal and can be thought to result from coupling between cavity modes supported by the individual corrugations [14]. Similar to surface plasmon polaritons, electromagnetic fields in spoof plasmons exponentially decay away from the structured interface. Importantly, spoof plasmons can be used to realize relatively large effective modal indices, and as such, can be used to enhance interaction between matter and low-frequency (GHz…THz) electromagnetic waves.

Hybridization of few artificial plasmons has been demonstrated in flat structures [20]. However, the emergence of new electromagnetic waves as result of spoof plasmon hybridization has not been demonstrated so far. Here we show that such hybridization provides a powerful tool for developing GHz-optical mapping that can be used for design and development of practical antenna devices.

Of particular interest to this work are the spoof plasmons supported by the corrugated wires [13], schematically shown in Fig. 2(a). Figure 2(b) shows dispersion of the fundamental spoof plasmon mode in the structure with radii $r_1 = 15mm$ and $r_2 = 10mm$ and corrugation period $d = 2mm$, calculated with finite-element-method (FEM) numerical solver of Maxwell equations [21]. It is seen that the behavior of this mode is similar to the one of the surface plasmon polariton with effective plasma frequency of 12 GHz. Note that, as it is often the case with spoof plasmon structures, the period of corrugation is deeply subwavelength $(d \ll \lambda_0)$ so that corrugated wire essentially operates in "effective medium" regime [14].

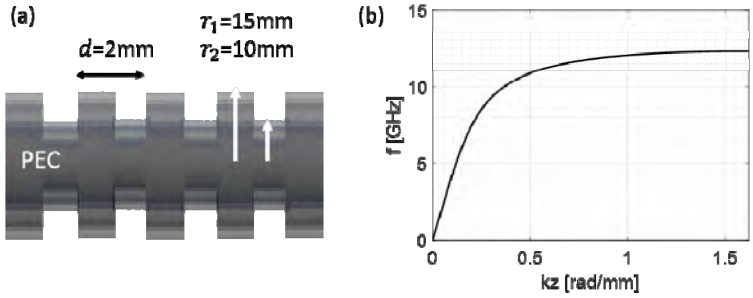

Fig. 2. (a) Schematic geometry of a corrugated wire, (b) dispersion relationship of the spoof-plasmon mode supported by the wire

4. Spoof wire metamaterials

As described above, the unique optical response of nonlocal hyperbolic nanowire composites can be related to hybridization of natural plasmonic modes. The main hypothesis, to be

verified in this work is whether hybridized spoof plasmons can be utilized to mimic nonlocality and hyperbolicity at the low frequency (GHz) regime.

Geometry of the proposed metamaterial is schematically shown in Fig. 3(a). The metamaterial represents a collection of aligned corrugated wires with subwavelength corrugation and subwavelength period a (here we use wires described in Fig. 2 arranged in square lattice with $a = 50mm$). As shown in Fig. 2, individual wires support propagation of spoof plasmon modes.

The modes of the corrugated wire composite are analyzed with commercial finite-element-method (FEM) solver, COMSOL multiphysics. In these calculations, we solve for the eigen frequency of the modes based on the values of the components of the (quasi-) wavevector $\vec{k}$. Figure 3(b…e) represents dispersion and field distribution of the three lowest-frequency modes supported by the metamaterial propagating parallel to its optical axis.

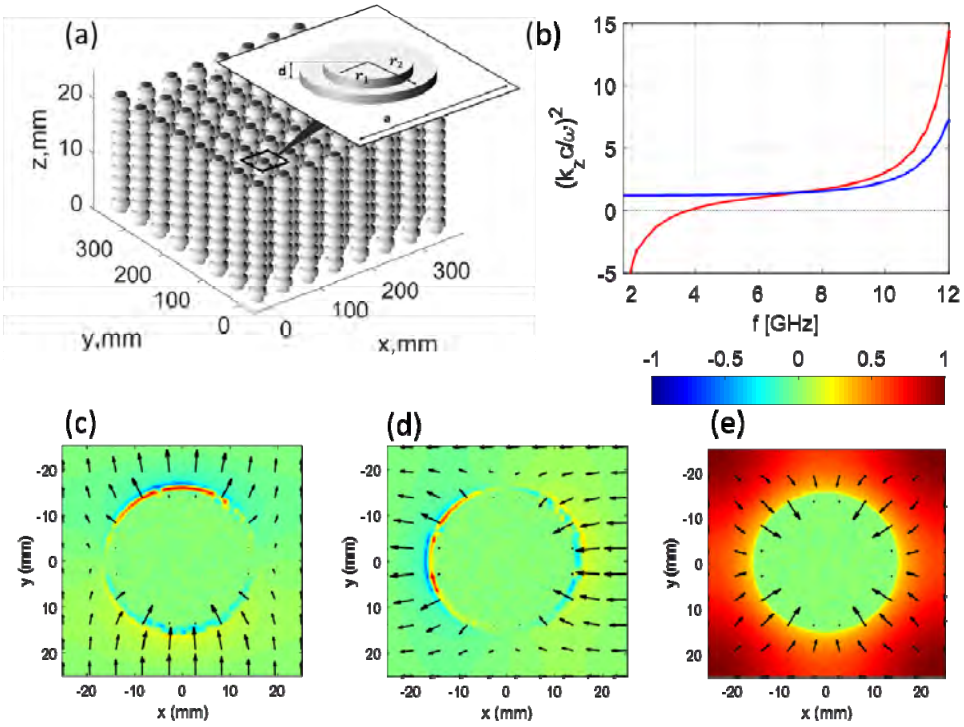

Fig. 3. (a) Schematic geometry of corrugated-wire metamaterial; (b) dispersion of the transverse (blue line) and longitudinal (red line) modes; panels (c,d,e) illustrate the field profiles in TE- polarized, TM-polarized, and longitudinal wave in the composite; compare to Fig. 1

From the homogenized metamaterial perspective [when the fields are averaged over the unit cell], these two of these modes have non-vanishing components of in-plane electric and magnetic fields, while the third mode has non-vanishing averaged E_z component. Therefore, similar to the case of plasmonic wires (see Fig. 1), these modes can be called ordinary (TE), and extraordinary (TM/longitudinal) waves. Notably, in further similarity to optical response of plasmonic wire metamaterials, two transverse modes of corrugated wire composites have identical dispersion, while dispersion of longitudinal wave resembles that of its smooth wire counterpart.

Optics EXPRESS

Dispersion and the field profiles of the three modes was analyzed for a range of in-plane (k_x) and out-of-plane (k_z) wavenumbers. These studies show that oblique propagation ($k_x \neq 0$) removes degeneracy between the two transverse waves and introduces avoided crossing between the two extraordinary modes (typical dispersion is shown in Fig. 4).

All in all, we note the drastic similarity between the field profiles and dispersions of the modes in spoof-wire systems and the optical behavior of plasmonic smooth-wire composites. These similarities motivate the application of the effective medium theory of nonlocal optical response of nanowire systems [15] to describe low-frequency electromagnetism of spoof wire metamaterials.

5. Effective medium description of nonlocal spoof wire composites

Successful application of effective medium theory requires knowledge of the frequency-dependent effective medium parameters $\epsilon_\perp, \epsilon_{zz}$, and ξ. While in the limit of plasmonic wires these parameters can be directly related to permittivity of metal and host matrix, these expressions cannot be used in the case of corrugated highly-conductive wires. Therefore, in order to test the applicability of the Eqs. (3), we extracted the frequency-dependent effective medium parameters by least-square fitting numerical data to Eqs. (3). Spectral response of effective medium parameters is illustrated in Fig. 4. The same figure presents nonlocal effective medium permittivity of the system.

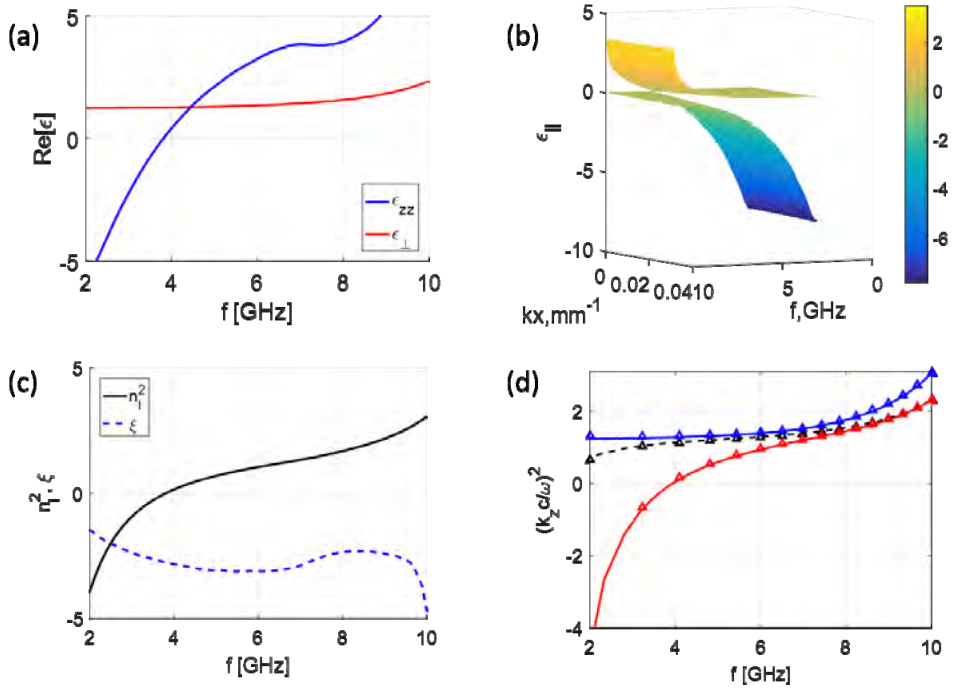

Fig. 4. Panels (a,b,c) illustrate effective medium parameters of the spoof-wire composite; panel (d) shows dispersion of the TM (solid lines) and TE (dashed line) polarized modes propagating obliquely ($k_x = \pi a / 2 \approx 0.03 mm^{-1}$) to the wires; lines represent analytical Eqs. (3), symbols correspond to FEM solutions of Maxwell equations.

Figure 4(d) demonstrate the validity of the proposed effective medium description comparing the predictions of Eq. (3) and exact numerical solutions of Maxwell equations. It is clearly seen that Eq. (3) adequately describes electromagnetism in corrugated wire systems.

Optics EXPRESS

Importantly, the corrugated wire composite provides complete map of optics of nonlocal hyperbolic wires to low (GHz) frequencies. The composite supports three waves, comprising one ordinary wave with spherical dispersion and two extraordinary modes, one with elliptical/epsilon-near-zero dispersion and one with hyperbolic-like dispersion.

6. Conclusions

To conclude, we demonstrated a new metamaterial based on arrays of corrugated wires that is capable of realizing nonlocal hyperbolic and epsilon-near-zero electromagnetism in low-frequency systems. We also demonstrated a quantitative map of the electromagnetic properties of such corrugated wire composite on high-frequency (optical) response of plasmonic nanowire composites.

By appropriately scaling geometric parameters of corrugated wire structures, the optical response of the composite can be engineered throughout far-IR…THz…GHz frequency ranges where propagation of spoof plasmons has been already demonstrated in few-interface structures.

Applicability of the effective medium description, proposed in this work is limited to $|k_x| \lesssim \pi / a$. The range of applicability of the proposed formalism can be significantly extended by designing metamaterials with deep subwavelength period that can be realized when the space between corrugations is filled with high-index media.

The proposed new class of corrugated wire metamaterials brings new avenues of engineering refractive response and optical density of states to the low-frequency (far IR…GHz) electromagnetic domain. Engineered nonlocality and hyperbolicity can be utilized to optimize detection and generation of low-frequency radiation, high resolution imaging, and enhancement of nonlinerities.

Funding

US Army Research Office (W911NF-16-1-0261); Binational Science Foundation (project 2016059); PAZY Foundation

Optics Letters

Directional emission of rhodamine 6G on top of a silver grating

E. K. Tanyi,[1] S. Mashhadi,[1] S. D. Bhattacharyya,[2] T. Galfsky,[2] V. Menon,[2] E. Simmons,[3] V. A. Podolskiy,[3] N. Noginova,[1] and M. A. Noginov[1,*]

[1]Center for Materials Research, Norfolk State University, Norfolk, Virginia 23504, USA
[2]City College, City University of New York, New York, New York 10031, USA
[3]University of Massachusetts Lowell, Lowell, Massachusetts 01854, USA
*Corresponding author: mnoginov@nsu.edu

Received 1 February 2018; revised 23 April 2018; accepted 23 April 2018; posted 2 May 2018 (Doc. ID 321044); published 30 May 2018

We have observed directional spontaneous emission of rhodamine 6G dye deposited on top of a silver grating and found that its angular distribution patterns were very different in TE and TM polarizations. The latter was related to the dispersion curves determined based on the polarized reflection spectra measured at multiple incidence angles. The most intriguing finding of this Letter was a resonance, which was coupled with TE-polarized light and determined the characteristic double-crescent patterns in the TE-polarized spontaneous emission. This observation, as well as nearly similar resonance observed in TM polarization, was tentatively explained in terms of leaky waveguide modes supported by a film of dye-doped polymer.

OCIS codes: (160.3918) Metamaterials; (310.6860) Thin films, optical properties.

https://doi.org/10.1364/OL.43.002668

Metamaterials, engineered composite materials composed of rationally designed sub-wavelength building blocks (meta-atoms) [1,2], have unparalleled responses to electromagnetic (in particular, light) waves and enable unprecedented functionalities, including a negative index of refraction [3–8] and optical cloaking [9,10], as well as sub-diffraction focusing [5] and imaging [5,11–15]. Moreover, metamaterials with hyperbolic dispersion [13–16], whose effective dielectric permittivities in orthogonal directions have opposite signs, have a broadband singularity in the photonic density of states (PDOS), [16] enabling control of the rate [17,18], quantum yield, and directionality of spontaneous emission [16,19–21].

Most metamaterials are lossy. Therefore, the efforts of the last several years [22–28] have been aimed at the development of low-loss nano-patterned metasurfaces, which do not require propagation of light through multiple layers of the metamaterial's volume and are relatively easy to fabricate. Of particular interest are hyperbolic metasurfaces which, similar to their bulk counterparts, have been claimed to possess large PDOS [16,29,30], allowing them to control spontaneous emission [30]. The prototype of a metasurface is a familiar diffraction grating [31], whose period and depth of the modulation can be much larger than the wavelength, much smaller than the wavelength, or comparable to the wavelength [32]. While the former two cases are reasonably well studied [31], the latter [32] is still not fully researched, keeping a promise of fascinating surprises, such as the relatively recently explored class of high contrast gratings (HCGs) [32,33].

Many unique responses of photonic metamaterials and metasurfaces to light waves are due to surface plasmons (SPs), which are either localized or propagating oscillations of a free electron density coupled to incident and scattered light and, in the latter case, surface waves propagating at the interface between metal and dielectric [34]. As wave-vectors of propagating SPs (also known as surface plasmon polaritons [SPPs]) are larger than those of photons in an adjacent dielectric, SPPs cannot be excited by an incident light falling from a dielectric onto a flat metallic surface. However, if a grating is patterned on a metallic surface, its wave-vector, G, can be added to the parallel (to the surface) component of the photon wave-vector $k_{\|}$, eliminating the wave-vector mismatch and allowing SPPs to be excited by TM- (p) [but not TE- (s)] polarized light [34]; see Fig. 1(a). More generally, the wave-vector of a surface wave, k_{sw}, is related to $k_{\|}$ and G via the following equation:

$$k_{sw} = \pm k_{\|} \pm mG, \tag{1a}$$

where m is an integer number.

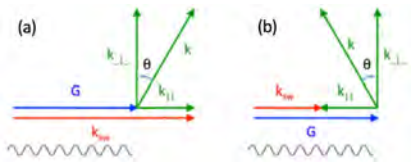

Fig. 1. (a) Addition of $k_{\|}$ and G allows one to match k_{sw}. (a) and (b) Two most likely combinations of the wave-vectors corresponding to the emission maximum at angle θ. k is the photon wave-vector, and $k_{\perp}$ is its perpendicular (to the surface) component.

Anomalies in the reflection of metallic gratings, manifested by dips (Wood anomaly [35]) or peaks (Rayleigh anomaly [36,37]) observed in angular or spectral scans of reflectance, are known for over a century. They have been explained in terms of SPPs, which can couple to incident and reflected far-field TM-polarized waves [38,39,40] or be in resonance with a grating (Bragg resonances). If gratings are coated by luminescent molecules, angular distribution patterns of spontaneous emission are related to characteristic dispersion curves of SPPs on a grating. As the anomalies in the grating reflectance were associated with propagation of SPPs, the majority of optical measurements were limited to TM (p) polarization, and nothing interesting was observed or searched for in TE (s) polarization.

In this Letter, we have studied angular distribution of spontaneous emission of rhodamine 6G (R6G) dye molecules deposited on top of a silver grating metasurface and observed two distinctly different luminescence patterns in TE and TM polarizations. The latter was in good agreement with the dispersion curves plotted based on the series of reflectance spectra collected at multiple incidence angles.

The grating sample was fabricated using a combination of the holographic lithography, thermal deposition, and spin coating techniques. The glass substrates (2.5 cm × 2.5 cm) were cleaned ultrasonically in a three-step process, using soap water, acetone, and iso-propanol, for 5 min each. The glass slides were air dried and baked on a heating plate at 120°C for 1 min. The positive S-1803 photoresist was spin coated (using the Spincoat G3P-8 instrument from Specialty Coating Systems) onto the glass substrate and pre-baked for 60 s at 110°C. After that, the sample was exposed (for 30 s) to an interference pattern created by two He-Cd laser beams ($\lambda = 325$ nm) of equal power (~2.5 mW), which were initially split with a beam splitter and then recombined on the sample. The sample was then developed in a basic solution of the developer (MF 319) for 30 s, rinsed in distilled water, and baked at 110°C for 60 s. As a result of this process, a grating of dielectric photoresist strips, forming the basis of the grating metasurface, has been created; see Figs. 2(a) and 2(b).

The metallic grating was fabricated by depositing ~45 nm of silver (using the NANO 36 thermal evaporator from Kurt J. Lesker) on top of the grating of photoresist strips described above. The depth of the grooves approximated ~45 nm. Finally, a 70 nm thin film of poly(methyl methacrylate) (PMMA) doped by R6G dye in concentration 2.2×10^{-4} mol/L (in solid state) was conformally deposited by spin coating on top of the silver grating; see Figs. 2(a) and 2(b). Note that a comparable concentration of R6G in PMMA was sufficient for a strong coupling of dye molecules with SPPs [41].

The period of the grating, evaluated by measuring the angle to the first order of diffraction, was equal to 478 ± 5 nm.

The directional spontaneous emission of the sample was measured using the setup of Fig. 3(a). The grooves of the grating were oriented vertically. The dye molecules were excited with a cw radiation of an Ar^+ laser at $\lambda = 514.5$ nm, through the silver film, from the side of the glass substrate. The spontaneously emitted light was intercepted by a white screen (with grids), which was held at 8.8 cm in front of (and parallel to) the grating sample. The spontaneous emission pattern was recorded using a CCD camera equipped with a photo camera objective. A polarizer and a series of notch, long-pass, and bandpass filters were used to block scattered pumping light, transmit spontaneous emission (with the maximum at ~565 nm), and control its polarization.

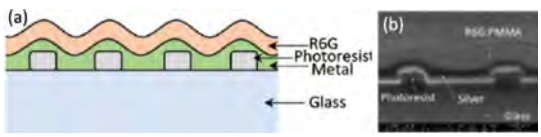

Fig. 2. (a) Schematics of the sample. (b) Scanning electron microscope image of the sample's cross section cut with a focused ion beam.

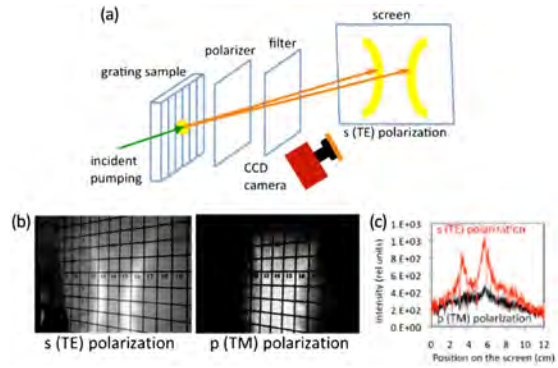

Fig. 3. (a) Experimental setup. (b) Experimental patterns of spontaneous emission in TE polarization (left panel) and TM polarization (right panel). (c) Profiles of intensity distribution in the horizontal plane in TM and TE polarizations.

The emission patterns in vertical (TE) and horizontal (TM) polarizations are depicted in Fig. 3(b), and the corresponding intensity profiles, recorded in the horizontal plane, are shown in Fig. 3(c). The vertically (TE) polarized spontaneous emission displays a double-crescent pattern, with the maximum emission intensity at $\theta \approx 6.5°$ to the normal of the screen; see Fig. 3(b) (left panel). At the same time, the pattern of the horizontally (TM) polarized emission [Fig. 3(b), right panel], showing a single maximum at nearly normal direction, was very different from that at the vertical (TE) polarization. The corresponding intensity profiles are depicted in Fig. 3(c).

The two most likely combinations of the wave-vectors (in a horizontal plane), leading to the emission maxima at the angle θ, depicted in Figs. 1(a) and 1(b), can be described by the following equation:

$$k_{sw} = G \pm k_{\|}, \tag{1b}$$

where the positive (negative) sign corresponds to the schematics of Fig. 3(a) [Fig. 3(b)]:

$$k_{\|} = k \sin\theta = \frac{\omega}{c} \sin\theta = \frac{2\pi}{\lambda_0} \sin\theta, \tag{2}$$

$$k_{sw} = \frac{\omega}{c} n_{sw} = \frac{2\pi}{\lambda_0} n_{sw}, \tag{3}$$

and

$$G = \frac{2\pi}{\Lambda}, \tag{4}$$

where k is the photon wave-vector in vacuum (or air), λ_0 is the vacuum wavelength, ω is the angular frequency, c is the speed of light, n_{sw} is the effective refractive index of a surface wave,

and Λ is the grating period. Substituting Eqs. (2)–(4) into Eq. (1b), one gets

$$n_{sw} = \pm \sin\theta + \frac{\lambda_0}{\Lambda}. \quad (5)$$

By substituting to Eq. (5), experimental values λ_0, Λ, and $\theta = 6.5°$ (for TE polarization), one obtains $n_{sw} = 1.30$ and $n_{sw} = 1.07$. (At $\theta = 0°$, corresponding to TM polarization, $n_{sw} = 1.18$.)

In order to understand the nature of the observed spontaneous emission patterns, the reflectance spectra of the samples, in both TM and TE polarizations, were measured at multiple incidence angles (between 5° and 80°, with 5° increments) inside the integrating sphere in the Lambda 900 spectrophotometer (PerkinElmer). The multiple dips in the reflectance spectra formed branches that were translated into the branches of the dispersion curves. (Note that the positions of the dips in the reflectance spectra allowed us to calculate $k_{||}$. The respective values k_{sw} were calculated by choosing proper signs in Eq. (1a), which corresponded to the positive slopes of the asymptotes crossing the origin.) The spectra and the corresponding dispersion curves in TE polarization are depicted in Figs. 4(a) and 4(b). The most intriguing feature of the dispersion plot is the branch whose effective index of refraction, $n_{sw} = 1.03$, is very close to that determined from the emission measurements, $n_{sw} = 1.07$.

In TM polarization, the reflectance spectra and the dispersion plot feature the branch characterized by the refractive index $n_{sw} = 1.05$ (very close to that in TE polarization); see Figs. 5(a) and 5(b). However, at this time, this dispersion branch features the splitting at the wave-vector approximately equal to G (the Bragg condition for the second harmonic of the grating [42]). Probably coincidently, the energy position of the splitting corresponds to that of the R6G absorption band. Two other branches of the dispersion curve, represented in Figs. 5(a) and 5(b) by green diamonds ($n_{sw} = 1.31$) and blue triangles ($n_{sw} = 1.65$), are tentatively ascribed to SPPs propagating at the top (Ag/R6G:PMMA/air) and the bottom (Ag/photoresist/glass) sides of the silver diffraction grating.

Note that the branches represented by red circles in Fig. 4(a) and purple circles in Fig. 5(a) are the measurement artifacts. Their wave-vectors are equal to G/2—the condition at which

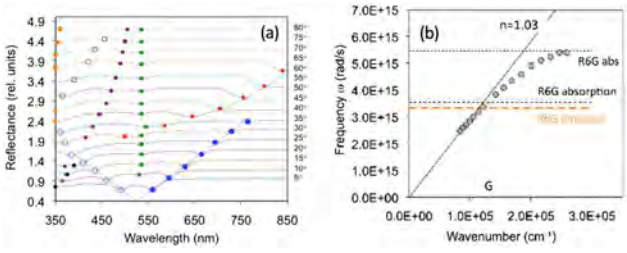

Fig. 4. TE polarization. (a) Reflectance spectra taken at different incidence angles. The dips are marked with characters. The dashed lines are guides for the eye. (b) Dispersion curve corresponding to two branches in (a) (marked with closed and open blue circles). The horizontal dashed and dotted lines show the energy positions of the absorption and emission bands of R6G [$S_0 \rightarrow S_1$ transition at $\sim 3.6 \times 10^{15}$ rad/s (524 nm) and $S_0 \rightarrow S_2$ transition at $\sim 5.5 \times 10^{15}$ rad/s]. The vertical dashed line marks wave-vector G. The slope of the diagonal line corresponds to $n_{sw} = 1.03$.

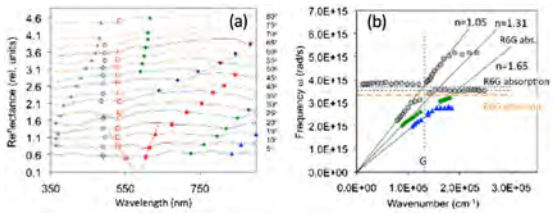

Fig. 5. TM polarization. (a) Reflectance spectra taken at different incidence angles. The dips are marked with characters. The dashed lines are guides for the eye. (b) Dispersion curves corresponding to multiple branches in (a). The horizontal dashed and dotted lines show the energy positions of the absorption and emission bands of R6G. The vertical dashed line marks wave-vector G. The slopes of the diagonal lines correspond to n_{sw} equal to 1.05, 1.31, and 1.65.

the −1st order of diffraction counter-propagates along the incident beam and leaves the integrating sphere without being detected.

The angular positions of the dips composing some of the branches in TM and TE polarizations are plotted versus wavelength in Fig. 6 (characters and extrapolating lines). The horizontal black line marks the angle $\theta = 6.5°$ corresponding to the direction of the crescent in the TE-polarized emission pattern. The thick vertical gray line represents the bandwidth of the spontaneous emission. One can see that one dispersion line in TE polarization (the one characterized by the index of refraction $n = 1.03$, closed blue circles) intersects the vertical gray line at the angle $\theta \approx 6.5°$, suggesting that the surface wave corresponding to this dispersion branch is responsible for the double-crescent pattern in the TE-polarized spontaneous emission. At the same time, in TM polarization, the very different branch (open red squares) intersects with the gray vertical line at the angle ~0°. This explains the angular distribution of spontaneous emission in TM polarization.

The most important experimental findings can be summarized as follows. (1) Two distinctly different patterns of spontaneous emission (of R6G-doped polymer deposited onto silver grating) have been observed in TE and TM polarizations. The former one had a double-crescent shape, while the latter had a single broad maximum centered at the normal to the surface; see Figs. 3(b) and 3(c). (2) Surface waves characterized by a surprisingly low effective refractive index, $n_{sw} = 1.03$ and $n_{sw} = 1.05$, have been found in both TE and TM polarizations in the series of reflection spectra taken at multiple incidence angles and the corresponding dispersion curves; see Figs 4 and 5. (3) The latter dispersion curve in TE polarization enabled coupling/decoupling of the 565 nm light at $\theta \approx 6.5°$

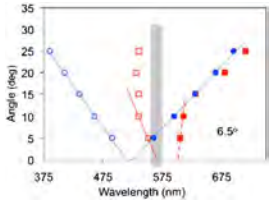

Fig. 6. Angular positions of the reflectance dips plotted as the function of the wavelength (characters). Open and filled circles, two branches in TE polarization; open and filled squares, two branches in TM polarization.

and was related to the double-crescent emission pattern. Likewise, a different dispersion curve was identified to correspond to the emission pattern in TM polarization.

As the most intriguing experimental feature, the surface wave characterized by the effective refractive index close to 1, is observed in both TE and TM polarizations; the explanation of the phenomenon should not involve SPPs. This rules out many scenarios extensively discussed in the literature [35,36,43,44]. We infer that the surface wave of interest is supported by a waveguide formed by the silver grating on one side and the outer surface of the R6G:PMMA polymer on the other side. Since the thickness of such a waveguide, ~70 nm, is significantly smaller than the cutoff value, ~190 nm, such a waveguide is expected to be very leaky. However, even at a relatively short propagation length, a substantial absorption loss with a dip in the reflectance spectrum. Simple calculations, neglecting the mode structure of a waveguide, which is assumed to be thick, show that if the first diffraction order is scattered parallel to the grating surface (or at least above the angle of the total internal refraction), the corresponding dispersion curve is a straight line with the slope ranging from c to c/n, in good agreement with the experimental result. (Here n is the refractive index of the polymer.) The TM-polarized wave may hybridize with the SPP, which is evidenced by a split in the dispersion curve in Fig. 5(b). Alternatively, the sandwich structure of Fig. 2 can be related to an HCG [32,33] (supporting surface waves having both TM and TE electric field components) or propagate Dyakonov-like plasmons (also with both TM and TE electric field components) similar to those described in Ref. [45]. The detailed study of the surface waves supported by complex multi-layered gratings will be published elsewhere.

Funding. National Science Foundation (NSF) (PREM DMR 1205457, RISE 1646789, DMREF 1629330); Air Force Office of Scientific Research (AFOSR) (FA9550-14-1-0221); Army Research Office (ARO) (W911NF-14-1-0639, W911NF-16-1-0256); MRSEC—CPHOM (DMR 1120923).

REFERENCES

1. W. Cai and V. Shalaev, *Optical Metamaterials: Fundamentals and Applications* (Springer, 2009).
2. M. A. Noginov and V. A. Podolskiy, eds., *Tutorials in Metamaterials, Series in Nano-Optics and Nanophotonics* (CRC Press, 2011).
3. A. Schuster, *An Introduction to the Theory of Optics* (Edward Arnold, 1904).
4. V. G. Veselago, Sov. Phys. Usp. **10**, 509 (1968).
5. J. B. Pendry, Phys. Rev. Lett. **85**, 3966 (2000).
6. D. R. Smith, W. J. Padilla, D. C. Vier, S. C. Nemat-Nasser, and S. Schultz, Phys. Rev. Lett. **84**, 4184 (2000).
7. R. A. Shelby, D. R. Smith, and S. Schultz, Science **292**, 77 (2001).
8. D. R. Smith, J. B. Pendry, and M. C. K. Wiltshire, Science **305**, 788 (2004).
9. J. B. Pendry, D. Schurig, and D. R. Smith, Science **312**, 1780 (2006).
10. W. Cai, U. K. Chettiar, A. V. Kildishev, and V. M. Shalaev, Nat. Photonics **1**, 224 (2007).
11. X. Zhang and Z. Liu, Nat. Mater. **7**, 435 (2008).
12. Z. Jacob, L. V. Alekseyev, and E. Narimanov, Opt. Express **14**, 8247 (2006).
13. A. Salandrino and N. Engheta, Phys. Rev. B **74**, 075103 (2006).
14. Z. Liu, H. Lee, Y. Xiong, C. Sun, and X. Zhang, Science **315**, 1686 (2007).
15. I. I. Smolyaninov, Y.-J. Hung, and C. C. Davis, Science **315**, 1699 (2007).
16. Z. Jacob, I. I. Smolyaninov, and E. E. Narimanov, Appl. Phys. Lett. **100**, 181105 (2012).
17. M. A. Noginov, H. Li, Y. A. Barnakov, D. Dryden, G. Nataraj, G. Zhu, C. E. Bonner, M. Mayy, Z. Jacob, and E. E. Narimanov, Opt. Lett. **35**, 1863 (2010).
18. Z. Jacob, J.-Y. Kim, G. V. Naik, A. Boltasseva, E. E. Narimanov, and V. M. Shalaev, Appl. Phys. B **100**, 215 (2010).
19. L. Gu, J. E. Livenere, G. Zhu, T. U. Tumkur, H. Hu, C. L. Cortes, Z. Jacob, S. M. Prokes, and M. A. Noginov, Sci. Rep. **4**, 7327 (2014).
20. S. Thongrattanasiri and V. A. Podolskiy, Opt. Lett. **34**, 890 (2009).
21. E. F. Kuester, M. A. Mohamed, M. Piket-May, and C. L. Holloway, IEEE Trans. Antennas Propag. **51**, 2641 (2003).
22. C. L. Holloway, M. A. Mohamed, E. F. Kuester, and A. Dienstfrey, IEEE Trans. Electromagn. Compat. **47**, 853 (2005).
23. Y. Zhao, N. Engheta, and A. Alù, Metamaterials **5**, 90 (2011).
24. D. M. Pozar, S. D. Targonski, and H. D. Syrigos, IEEE Trans. Antennas Propag. **45**, 287 (1997).
25. D. Sievenpiper, L. Zhang, R. F. J. Broas, N. G. Alexopolous, and E. Yablonovitch, IEEE Trans. Microwave Theory Tech. **47**, 2059 (1999).
26. C. G. M. Ryan, M. R. Chaharmir, J. Shaker, J. R. Bray, Y. M. M. Antar, and A. Ittipiboon, IEEE Trans. Antennas Propag. **58**, 1486 (2010).
27. M. Caiazzo, S. Maci, and N. Engheta, IEEE Antennas Wireless Propag. Lett. **3**, 261 (2004).
28. C. L. Holloway, D. C. Love, E. F. Kuester, A. Salandrino, and N. Engheta, IET Microwave Antennas Propag. **2**, 120 (2008).
29. A. V. Kildishev, A. Boltasseva, and V. M. Shalaev, Science **339**, 1232009 (2013).
30. Z. Jacob and V. M. Shalaev, Science **334**, 463 (2011).
31. F. Hopkinson and D. Rittenhouse, Trans. Am. Philos. Soc. **2**, 201 (1786).
32. C. J. Chang-Hasnain and W. Yang, Adv. Opt. Photonics **4**, 379 (2012).
33. C. F. R. Mateus, M. C. Y. Huang, Y. Deng, A. R. Neureuther, and C. J. Chang-Hasnain, IEEE Photonics Technol. Lett. **16**, 518 (2004).
34. H. Raether, *Surface Plasmons on Smooth and Rough Surfaces and on Gratings* (Springer-Verlag, 1988).
35. R. W. Wood, Philos. Mag. **4**(21), 396 (1902).
36. L. Rayleigh, Philos. Mag. **14**(79), 60 (1907).
37. U. Fano, J. Opt. Soc. Am. **31**, 213 (1941).
38. J. Feng, T. Okamoto, and S. Kawata, Appl. Phys. Lett. **87**, 241109 (2005).
39. M. Toma, K. Toma, P. Adam, J. Homola, W. Knoll, and J. Dostalek, Opt. Express **20**, 14042 (2012).
40. G. Lozano, D. J. Louwers, S. R. K. Rodriguez, S. Murai, O. T. A. Jansen, M. A. Verschuuren, and J. Gomez Rivas, Light Sci. Appl. **2**, e66 (2013).
41. V. N. Peters, T. U. Tumkur, J. Ma, N. A. Kotov, and M. A. Noginov, Opt. Express **24**, 25653 (2016).
42. A. Giannattasio, S. Wedge, and W. L. Barnes, J. Mod. Opt. **53**, 429 (2006).
43. P. Lalanne, J. P. Hugonin, H. T. Liu, and B. Wang, Surf. Sci. Rep. **64**, 453 (2009).
44. L. Aigouy, P. Lalanne, J. P. Hugonin, G. Julié, V. Mathet, and M. Mortier, Phys. Rev. Lett. **98**, 153902 (2007).
45. E. E. Narimano and Z. Jacob, Appl. Phys. Lett. **93**, 221109 (2008).

ACS Photonics

Article

Cite This: ACS Photonics 2017, 4, 2470-2478

pubs.acs.org/journal/apchd5

Nonlocal Effects in Transition Hyperbolic Metamaterials

B. Wells,*[,†,#,§] Zh. A. Kudyshev,[‡,⊥,§] N. Litchinitser,[‡] and V. A. Podolskiy[†]

[†]Department of Physics and Applied Physics, UMass Lowell, Lowell, Massachusetts 01854, United States

[‡]EE Department, University at Buffalo, SUNY, Buffalo, New York 14260, United States

ABSTRACT: Light−matter interactions at a particular point in a material may be dominated by properties of the medium at this point, or they could be affected by the electromagnetic properties of the medium in the surrounding regions. In the former case, the medium is said to be local, while in the latter, it is nonlocal. Recent studies of light−matter interactions in composite optical metamaterials showed that nonlocal effects enable new optical phenomena that are not acounted for by the conventional, local effective medium description. Up until now the majority of studies focused on metamaterials with spatially uniform material parameters. However, optical metamaterials with electromagnetic material parameters gradually changing from positive to negative values, so-called transition materials, have been predicted to induce a strong enhancement of the local electric or magnetic field in the vicinity of the zero refractive index point. This opens new opportunities for sensing and low-intensity nonlinear optical applications. Here, we analyze the field enhancement in realistic transition metamaterials consisting of an array of plasmonic cone-shaped rods embedded in a dielectric matrix and demonstrate that optical nonlocality is required to adequately describe this optical response. This work enables the design and practical applications of this new emerging metamaterial platform.

KEYWORDS: *spatial dispersion, nonlocality, nanowire metamaterials, transition metamaterials, epsilon-near-zero, field enhancement*

Engineered optical materials with a refractive index gradually changing from positive to negative values, often called transition materials, have attracted significant attention in the past few years due to a strong enhancement of the local electric field under oblique incidence in the vicinity of the zero referactive index point.[1−7] Such resonant enhancement can be used in the realization of efficient nonlinear optical phenomena at reduced intensities in ultracompact volumes and may therefore enable applications in microwave, terahertz, and optical spectral ranges. Recently, strong second-harmonic generation at significantly reduced pump wave intensities was predicted in such a transition layer with dielectric permittivity and magnetic permeability gradually changing from positive to negative values.[8] However, practical realization of low-loss double negative transition layers is a rather challenging task at optical frequencies.

On the other hand, the predicted field enhancement in a transition layer can be realized in strongly anisotropic metamaterials with gradually changing effective parameters, such that their dispersion changes from elliptical to hyperbolic.[9] Electromagnetic properties of these metamaterials are described by a diagonal dielectric permittivity tensor. In the case of elliptical dispersion, all the components of this tensor are positive, but differ in magnitude, while hyperbolic metamaterials are characterized by the dielectric permittivity tensor with the components that are different in sign.[10−18] This class of metamaterials has attracted significant interest due to their low losses, simplicity of fabrication as compared to double-negative resonance-based metamaterials, and tolerance to fabrication imperfections. Strongly anisotropic metamaterials with elliptical or hyperbolic dispersion have been realized in two different configurations: structures consisting of metal nanorods embedded in a dielectric host and those consisting of periodic metal−dielectric layers. In this work, we focus on the plasmonic nanorod structures that can be straightforwardly fabricated using electroplating,[19] resulting in nanorod composites consisting of dielectric substrates noble metal [gold (Au) or silver (Ag)] nanowires.[20,21]

From an effective medium standpoint, the electromagnetic response of these metamaterials can be described by using a uniaxial permittivity tensor. It was shown that incorporating nonlocal corrections to conventional effective medium theory (EMT) is required for adequate description of new optical phenomena in wire composites.[22−29] Granularity significantly affects the optical response of the wire media, leading to the excitation of additional electromagnetic waves whose properties can be incorporated in the effective medium description by introducing spatial dispersion of the effective permittivity. In total, wire-based metamaterials support propagation of one "ordinary" TE wave and either two or one "extraordinary" TM or longitudinal waves.[22,27,28,30,31] Here, for the first time, we consider the enhancement of electromagnetic waves in nonmagnetic transition hyperbolic media, taking into account the composite structure of the metamaterial. We show that granularity significantly affects the field enhancement in transition metamaterials and demonstrate that the nonlocal

Received: June 29, 2017
Published: September 19, 2017

DOI: 10.1021/acsphotonics.7b00690
ACS Photonics 2017, 4, 2470−2478

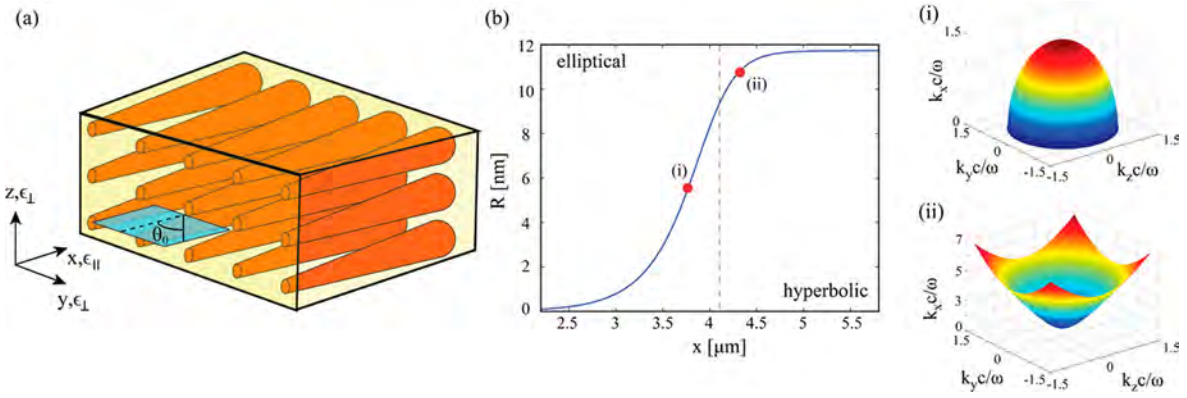

Figure 1. (a) Schematics of a transition hyperbolic layer that consists of metallic cones embedded in the dielectric matrix. (b) Radius of the metallic cones as a function of the x coordinate; dashed line represents the zero refractive index point, $x \approx 4.1$ μm. Insets (i) and (ii) show elliptical and hyperbolic dispersions at $f = 0.021$ and $f = 0.09$, respectively.

effective permittivity model adequately describes the observed optical response.

THEORY

The transition metamaterial considered in this work consists of an array of plasmonic cone-shaped rods embedded into a dielectric matrix, as shown in Figure 1(a). Both the radius of the wire $R(x)$ and the separation between the rods a are assumed to be much smaller than the wavelength λ. Here we use $\lambda = 731$ nm, $a = 60$ nm, and assume that the radius changes from $0 < R(x) < 12$ nm according to

$$R(x) = a\sqrt{\frac{0.12(1 + \tanh(a_1(b_1x + c_1)))}{2\pi}} \tag{1}$$

with $a_1 = 0.0018$, $b_1 = 1.5 \times 10^9$ m^{-1}, and $c_1 = 6000$, with wires occupying space between $2.3\ \mu\text{m} \le x \le 5.3\ \mu\text{m}$. Permittivity of dielectric and plasmonic components of the metamaterial are given by $\epsilon_d = 2$ and $\epsilon_m(\omega) = \omega_p^2/\omega(\omega + i\Gamma)$, where $\omega_p = 2.068 \times 10^{15}$ Hz and $\Gamma = 4.449 \times 10^{12}$ Hz are plasma and collision frequencies. For the particular operating wavelength of interest, $\epsilon_m = -24.42 + 0.2761i$, representing Ag nanorods.[32]

Following the approach used in refs 21 and 22 permittivity of the nanowire composite is given by a diagonal tensor $\hat{\epsilon} = \{\epsilon_{\|}, \epsilon_{\perp}, \epsilon_{\perp}\}$ with components

$$\epsilon_{\perp} = \epsilon_d \frac{(1+f)\epsilon_m + (1-f)\epsilon_d}{(1-f)\epsilon_m + (1+f)\epsilon_d};$$
$$\epsilon_{\|}(k_x) = f\frac{\epsilon_m + \epsilon_d}{\epsilon_d - (n_\infty^1)^2}\frac{c^2}{\omega^2}(k_x^2 - k_x^{1^2}) \tag{2}$$

where $f = \frac{\pi R^2}{a^2}$ is the filling fraction of metal inside a dielectric, k_x is the component of the wavevector in the direction of the wires, k_x^1 is the wavevector of the longitudinal wave in the wire media, and the parameter $n_\infty^1 = \lim_{\epsilon_m \to -\infty} k_x^1 c/\omega$ describes the behavior of a longitudinal wave in a PEC wire medium. As shown in ref 22, dispersion $k_x^1(\omega)$ can be calculated by solving an eigenvalue-type problem with exact dependence governed by geometrical parameters of the composite as well as by permittivity of the wires and the matrix media. In the majority of practical metamaterials, eq 2 can be approximated as

$$\epsilon_{\|}(k_x) \simeq f\epsilon_m + (1-f)\epsilon_d + \delta_x\frac{k_x^2c^2}{\omega^2} \tag{3}$$

with the first two terms representing the local permittivity (given by Maxwell–Garnett effective medium theory[33]) and δ_x being a nonlocality parameter, respectively. This parameter can be approximated as $\delta_x = f\frac{\epsilon_m + \epsilon_d}{\epsilon_d - (n_\infty^1)^2}$. The extent of the nonlocal interwire interaction has been analyzed in ref 34, concluding that the bulk properties of the mematerial emerge from a ~10 × 10 array of wires.

Note that the spatial dispersion of the effective permittivity of nanowire arrays takes into account material granularity. Similar to our previous works,[21,22] we consider permittivity of the components of the metamaterial to be local. In composites that have ultrasmall (or ultrasharp) plasmonic inclusions permittivity of components themselves may become nonlocal,[35−41] requiring further development of effective medium theories.

The crucial difference between previous works and this work, for investigating the optics of hyperbolic composites, is the fact that here we consider nanorods with an increasing radius along the transverse position x (see Figure 1(b)); that is, the fill fraction f changes as a function of spatial coordinate x. Since in plasmonic metals across the visible spectrum $\epsilon_m < 0$, the modulation of the fill fraction causes the material's response to change from elliptical to hyperbolic, Figure 1. It has been a long-standing question as to how to accurately describe the material response and the electromagnetic wave propagation in the transition region where the elliptical medium transitions into the hyperbolic one.

By analyzing the dependence of dispersion for the modes in a transition metamaterial composed of cone-shaped nanorods, we find that within the elliptical regime the transition layer supports two propagating TM waves, commonly known as the main and additional TM modes. The main TM mode has elliptic-like dispersion, while its additional counterpart has hyperbolic-like behavior. When the fill fraction becomes large enough and the material transitions to the hypebolic response, the elliptic mode cuts off (exponentially decays along the wires), while the hyperbolic TM wave takes the role of the main TM mode. As a result, we expect to see interference between the main and additional TM waves from the positive side of the transition layer and only one propagation main mode in the hyperbolic region. In addition to TM-polarized waves, the composite supports propagation of the "ordinary" TE-polarized mode. The dispersion of the three waves is given by[22]

DOI: 10.1021/acsphotonics.7b00690
ACS Photonics 2017, 4, 2470−2478

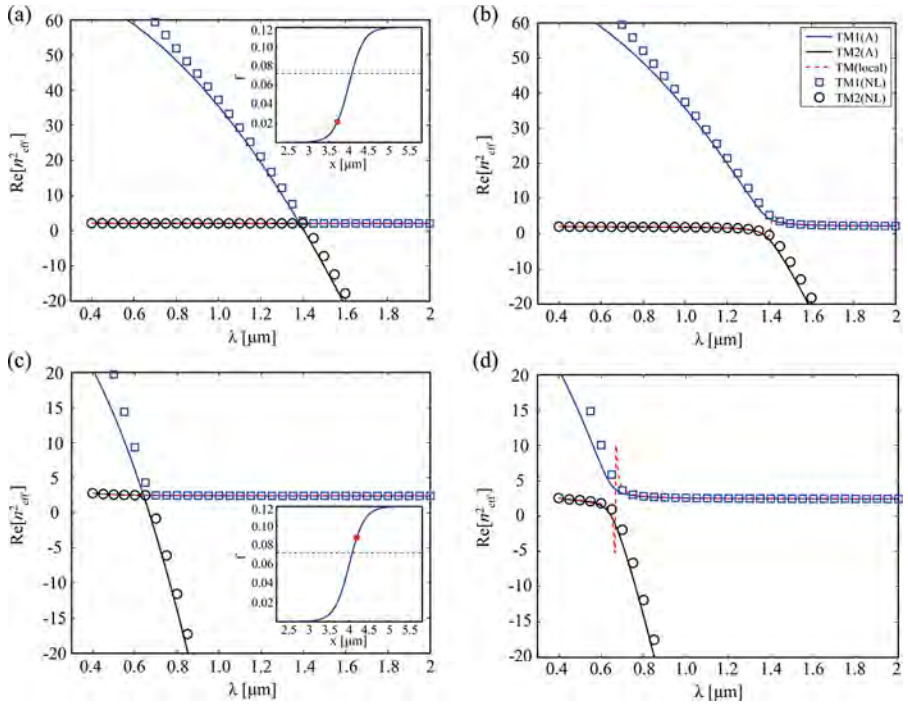

Figure 2. Dispersion of main and additional TM modes for two different cases: (a, b) $f = 0.021$ with $\delta = 0.027-0.0004i$ and (c, d) $f = 0.09$ with $\delta = 0.064-0.001i$ at 0° and 20°. The solid lines represent the approximate dispersion using the nonlocality parameter, the dashed line is the local EMT, and the symbols represent exact nonlocal EMT. Insets show the fill-fraction gradient along the sample, and the dashed line shows the boundary between the elliptical and hyperbolic regions of the transition layer.

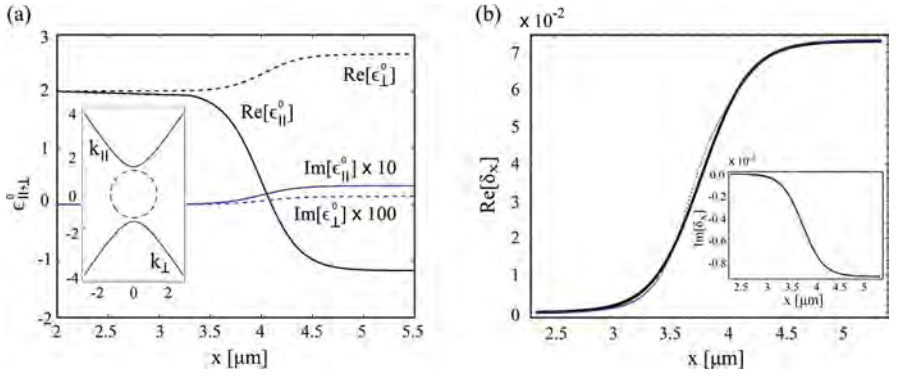

Figure 3. (a) Spatial distribution of local permittivity tensor components $\epsilon_{\parallel}$ and $\epsilon_{\perp}$. (b) Real and imaginary parts of nonlocality parameter δ_x along the transition layer. The dots correspond to the data obtained using the nonlocal TMM approach, while solid curves show an interpolation used within the FDTD simulations.

$$k_x^2 + k_y^2 + k_z^2 = \epsilon_{\perp}\frac{\omega^2}{c^2}$$

$$(k_x^2 - k_x^{1^2})\left(k_x^2 - \epsilon_{\perp}\frac{\omega^2}{c^2}\right) = -f\frac{\epsilon_m + \epsilon_d}{\epsilon_d - (n_{\infty}^1)^2}\epsilon_{\perp}(k_y^2 + k_z^2) \quad (4)$$

Figure 2 shows the behavior of the square of modal index $\mathcal{R}(n^2) = \mathcal{R}(k_x^2c^2/\omega^2)$ corresponding to the TM modes in the case of local (dashed curve), nonlocal approximation using eq 3 with the nonlocality parameter (solid curves), and exact nonlocal (symbols)[22] effective medium theory. It can be seen that the TM mode obtained using the local effective medium approximation overlaps with different TM modes obtained from using the nonlocal theory on the left and on the right of the so-called longitudinal (L) resonance (that coinsides with epsilon-near-zero [ENZ] condition). Following the notation introduced in ref 22 the TM mode that overlaps with the local TM mode is called the main mode, while the other mode is the additional TM mode. It is also worth noting that in the range of wavelengths shorter than the L resonance the main and additional TM waves simultaneously propagate inside the nanocone structure, while for the longer wavelengths, only the main mode propagates inside the medium while the additional mode exponentially decays.

The (avoided) crossing between dispersion of the two TM-polarized waves predicted by the nonlocal EMT reveals the true nature of the electromagnetic response of this unique class of metamaterials. Similar to the majority of plasmonic structures, the modes of the nanowire composite represent collective oscillations of electrons coupled to electromagnetic radiation. When the composite is excited by the normally indident light [Figure 2(a,c)] these two modes represent transverse plasmon

DOI: 10.1021/acsphotonics.7b00690
ACS Photonics 2017, 4, 2470−2478

(electrons oscillating perpendicular to wires) and longitudinal plasmon polaritons (electrons oscillating along the wires). When the metamaterial is excited by obliquely incident light [Figure 2(b,d)], the two modes "couple" to each other, resulting in avoided splitting of their dispersion curves. Equation 4 provides an analytical description of this process, with its left-hand side representing the plasmon excitations and its right-hand side playing the role of the effective coupling strength.[22] Here we characterize the direction of light propagation using the angle of incidence in a vacuum via $k_y = 0$, $k_z = \frac{\omega}{c}\sin\theta$.

Since the metamaterial exhibits a position-dependent fill fraction f, it is therefore important to analyze the dependence of dispersion for the main and additional TM modes at different points within the metamaterial. The inset in Figure 2 illustrates the fill-fraction gradient along the sample with the dashed line corresponding to the ENZ condition at our operating frequency, 731 nm. When the fill fraction is below this critical value, the metamaterial supports two propagation TM waves, as illlustrated in Figure 2(a,b): the main TM mode, which has a lower modal index, and an additional mode, which has a higher modal index. When the fill fraction becomes large enough to transition the composite into the hyperbolic regime, only one propagating TM mode remains, as shown in Figure 2(c,d). Therefore, we expect to see the interference between the main and additional TM waves for relatively small fill fractions, converting to a single propagating mode for areas with larger radii of the transition layer.

Figure 3(a) summarizes the spatial dependence of the effective medium parameters of the composite, which further illustrates the modal behavior explained above. Figure 3(b) shows the spatial distribution of the nonlocality parameter. The dashed line represents the optimal results obtained by eq 3, while solid lines represent the analytical approximation of the dashed lines that is required for FDTD solutions of Maxwell equations (see below).

METHODS

Three different numerical techniques providing full-wave solutions of Maxwell equations were used to analyze field distribution in transition metamaterials. First, we utilized the finite-difference time-domain (FDTD) method that incorporates the approximate dispersion model, given by eq 3. Second, a more accurate description of nonlocal EMT (eq 4) was used to solve Maxwell's equations in the frequency domain with nonlocal transfer matrix formalism. Finally, the commercial finite-element method (FEM) was used to calculate the field distribution in the composite and thus to assess the validities of the effective medium description of this complex media. The FEM calculations take into account the full 3D structure of the composite and do not assume any homogenization. On the implementation side, FEM results use significantly more memory and time to calculate field distribution than local or nonlocal EMTs. However, since FEM considers the full structure of the metamaterial, FEM results can be used as a "gold standard" against which results of different homogenization techniqeus can be compared.

In all calculations, the excitation beam was assumed to be TM-polarized with components $H = \{0, 0, H_z\}$ and $E = \{E_x, E_y, 0\}$. In FDTD calculations, the spatial dependence of the nonlocality parameter δ_x was interpolated by an inverse tangent function; the agreement between such interpolation and the values deduced from eq 3 is shown in Figure 3(b).

First, Maxwell's equations,

$$\nabla \times \vec{E} = -\frac{\partial \vec{B}}{\partial t},\ \nabla \times \vec{H} = \frac{\partial \vec{D}}{\partial t},\ \vec{B} = \mu_0 \vec{H} \tag{5}$$

are solved using the finite-difference time-domain method within the auxiliary differential equation approach.[42] The system of auxiliary differential equations is derived with the help of inverse Fourier transform of material equations $\tilde{D}_\perp = \epsilon_0\epsilon_\perp\tilde{E}_\perp$ and $\tilde{D}_\parallel = \epsilon_0\epsilon_\parallel\tilde{E}_\parallel$ and reads

$$\begin{aligned}
&\frac{1}{\varepsilon_0}\left(\frac{\partial^3 D_x}{\partial t^3} + \Gamma\frac{\partial^2 D_x}{\partial t^2}\right) \\
&\quad = A_1\frac{\partial^3 E_x}{\partial t^3} + \Gamma\frac{\partial^2 E_x}{\partial t^2} + f\omega_p^2\frac{\partial E_x}{\partial t} \\
&\qquad - c^2\frac{\partial^2}{\partial x^2}\left[\delta_x\frac{\partial E_x}{\partial t} + \delta_x\Gamma E_x\right] \\
&\frac{1}{\varepsilon_0}\left(A_2\frac{\partial^2 D_y}{\partial t^2} + A_2\Gamma\frac{\partial D_y}{\partial t} + (1-f)\omega_p^2 D_y\right) \\
&\quad = \varepsilon_d A_3\frac{\partial^2 E_y}{\partial t^2} + \varepsilon_d A_3\Gamma\frac{\partial E_y}{\partial t} + \varepsilon_d(1+f)\omega_p^2 E_y
\end{aligned} \tag{6}$$

here ϵ_0 and μ_o are the permittivity and permeability of free space, $A_1 = (1-f)\epsilon_d + f$, $A_2 = 1 - f(x) + (1+f)\epsilon_d$, and $A_3 = A_1 + 1$. We note that the difference between the local and nonlocal approach originates from the last term of the first equation in eq 6, which is proportional to the spatial second-order derivative. Using the FDTD code, we considered propagation of an obliquely incident TM-polarized wave in the transition layer within the local and nonlocal approximation.

In separate studies, propagation of electromagnetic waves through metamaterials was solved in the frequency domain with (i) the nonlocal transfer matrix method (TMM), reported previously in refs 43−45 and with (ii) the finite-element solver. The combination of three techniques allows us to (i) assess the validity of nonlocal effective medium theory and of its approximate version, given by eq 3, (ii) assess the validity of additional boundary conditions that are required to develop the nonlocal transfer matrix formalism, and finally and most importnatly to (iii) understand the optical response of realistic transition metamaterials.

To solve for light propagation through conical media with the nonlocal transfer matrix, the conical wires were represented as arrays of stacked cylindrical disks with thickness h with their diameter gradually changing from 3 nm to ∼24 nm. The transition metamaterial was represented as a multilayer composite with the permittivity of each layer given by (nonlocal) effective medium theory that represents the average value of the fill fraction at the location of the layer. Understanding the reflection and refraction of light through the interface between local and nonlocal layers requires one additional boundary condition (ABC). As shown in ref 22, continuity of E_z and D_x can be used to introduce such ABCs from the first principles. To complete this task, we first extend the technique originally introduced in ref 22 and represent the fields of the two waves propagating in the wire media as

DOI: 10.1021/acsphotonics.7b00690
ACS Photonics 2017, 4, 2470−2478

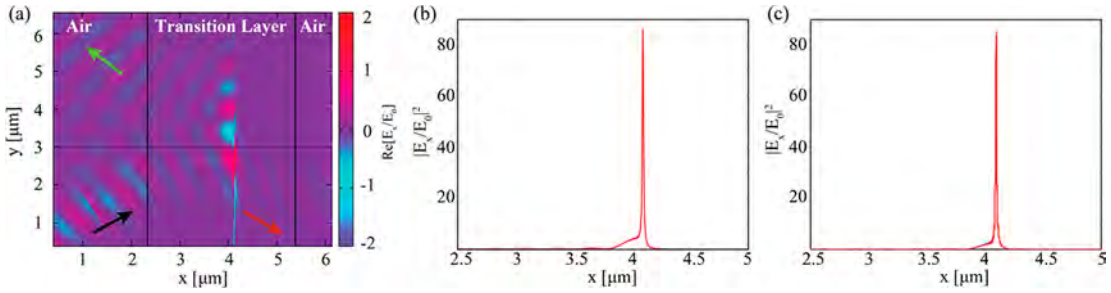

Figure 4. (a) Spatial distribution of the normalized real part of x components of the electric field in the case of oblique incidence with the incidence angle $\theta_0 = 20°$ within the local effective medium approximation at the cross section from (a) indicated by dashed line; (b) intensity distribution profile of E_x along the transition layer within the local response function approximation; (c) local EMT usng the TMM approach.

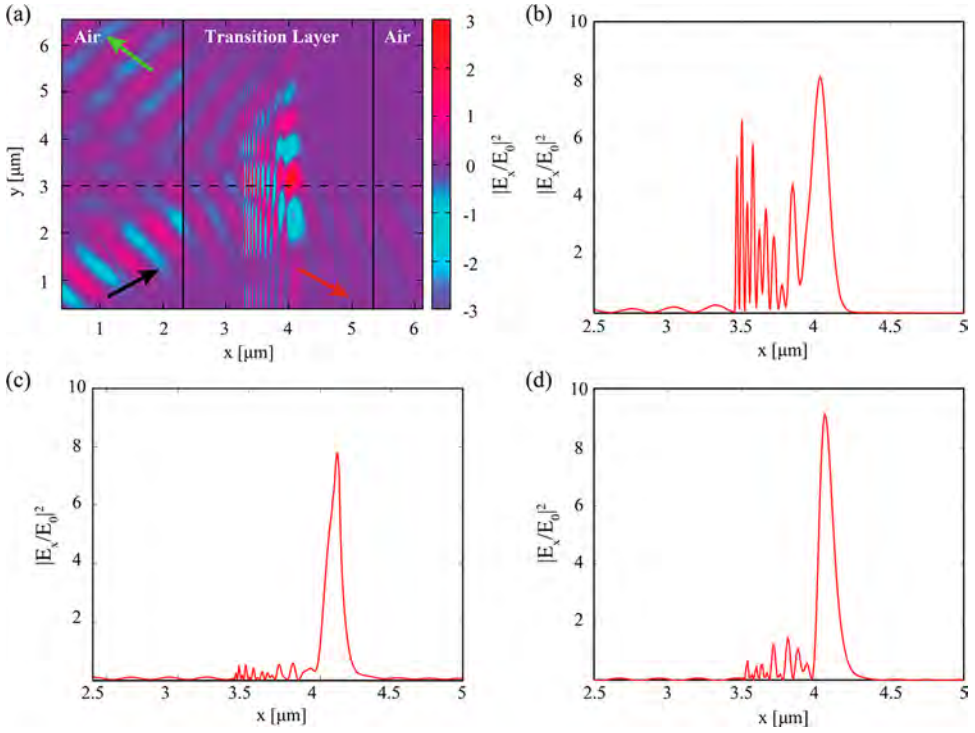

Figure 5. (a) Spatial distribution of normalized real part of x components of the electric field in the case of oblique incidence with incidence angle $\theta_0 = 20^o$ within the nonlocal effective medium approximation; (b) intensity distribution profile of E_x along the transition layer within the nonlocal response function approximation at the cross section from (a) indicated by a dashed line. (c) Nonlocal EMT using TMM and (d) finite-element method calculations.

$$E_z(y, z) = E_z^{\mathrm{mg}} + (\gamma^{\mathrm{mg}} + \gamma^{l})E_z^{l}|_{(x=0)}$$

$$E_x(y, z) = \gamma^{\mathrm{mg}}E_x^{\mathrm{mg}} + \gamma^{\mathrm{l}}E_x^{\mathrm{l}}|_{(x=0)} \quad (7)$$

where $\gamma^{\mathrm{mg}} = -\frac{\epsilon_\perp^{\mathrm{mg}} k_z}{\epsilon_x k_x} \frac{\epsilon_x - \epsilon^{\mathrm{l}}}{\epsilon_x^{\mathrm{mg}} - \epsilon^{\mathrm{l}}}$ and $\gamma^{\mathrm{l}} = -\frac{\epsilon_\perp^{\mathrm{mg}} k_x}{\epsilon_z k_z} \frac{\epsilon_z - \epsilon_z^{\mathrm{e}}}{\epsilon^{\mathrm{l}} - \epsilon_z^{\mathrm{e}}}$.

We then introduce the moment-averaged fields via

$$\mathbb{E}^n = \langle e^{2\pi i n z/a} E_z \rangle, \mathbb{D}^n = \langle e^{2\pi i n z/a} D_x \rangle \quad (8)$$

and follow ref 22 to use continuity $\mathbb{E}^0$ and $\mathbb{D}^0$ as "local" boundary conditions, continuity of $\mathbb{D}^1$ as first ABC, and continuity of $\mathbb{E}^1$ as the second ABC, required to analyze the interface between two nonlocal layers. As we reduce the disk thickness h, the resulting field distribution in the composite converges to the distribution that agrees with results of FDTD calculations. However, digitization of the smoothly varying radius introduces corner-scattering artifacts in the overal field distribution in the limit $h \to 0$. Such artifacts have been previosly observed in TMM-based solutions of light propagation in conical waveguides;[46] here, these artifacts appear when disk thickness h is reduced below ∼2 nm. In order to avoid numerical artifacts in TMM calculations, the layer thickness was fixed at $h = 8$ nm.

Finally, Maxwell equations have been solved with the commercial finite-element-based PDE solver.[45] In these calculations, the size of the individual mesh element was kept consistently below 1.5 nm. Despite small meshing size, our studies indicate that the resulting field distribution is significantly affected by the geometry (and, as a result, meshing) of the system, particularly in the spatial domain where the wire radius is small. As a result, we estimate the accuracy of the FEM solutions to be ∼10%.

In all studies, after solving Maxwell's equations, we characterize the enhancement of the field by considering the ratio of the component of the electric field along the axis of the nanowire E_x and the total electric field of the incident wave E_0.

DOI: 10.1021/acsphotonics.7b00690
ACS Photonics 2017, 4, 2470−2478

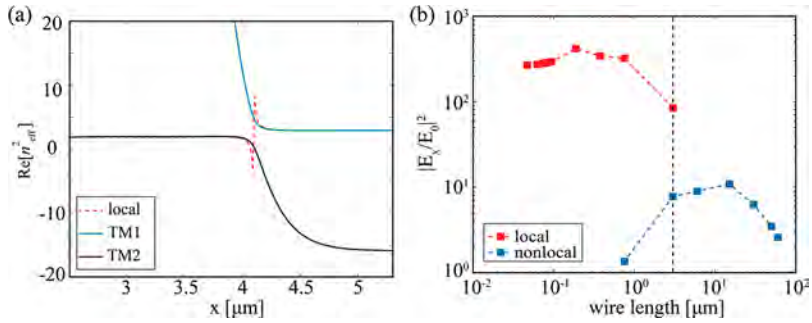

Figure 6. (a) Dependence of dispersion curves on wire position when λ = 731 nm. The solid lines represent main and additional TM modes calculated using nonlocal EMT, while the dashed line represents local EMT. (b) Dependence of maximal enhancement as a function of transition region width. The dashed vertical line coincides with the width of the transition region used throughout this study.

RESULTS

The strong enhancement of the electric field under oblique incidence, predicted in the vicinity of the zero refractive index point for the *local* transition HMM, is shown in Figure 4. Figure 4(a) shows the spatial distribution of the normalized real part of x components of the electric field in the case of oblique incidence with incidence angle $\theta_0 = 20°$. The field is normalized to the amplitude of the incident wave E_0. Incident wave (black arrow) propagates from air into the transition layer with the boundary shown with solid lines. It is partially refracted (red arrow) after passing the transition region and partially reflected from the first boundary (green arrow). Figure 4(b) shows the intensity distribution profile of E_x along the dashed line in Figure 4(a) and (c) using the local EMT approach and TMM with the fixed layer thickeness mentioned above with the same incident angle. We see almost exact agreement between these two approaches. On the left side of the transition region where $\mathcal{R}(\varepsilon_{\|}) = 0$, the interference pattern between incident and reflected waves can be clearly seen. On the right side, where the transition layer possesses hyperbolic dispersion, the field decays due to material absorption and is refracted in the negative direction as expected. In the vicinity of the $\varepsilon_{\|}$-zero region there is an enhancement of the x component E_x, similar to that previously shown in double-negative transition layer.[1] It is important to note that this field enhancement occurs only in the case of oblique incidence and only for the component of electric field perpendicular to the transition layer. This behavior can be explained by the fact that since electric displacement must be continuous at the $\varepsilon_{\|}$-zero region, the corresponding electric field component E_x anomalously increases as the permittivity component tends to zero.

Figure 5(a,b) show the spatial distribution of the normalized real part of x components of the field enhancement obtained with FDTD calculations within nonlocal effective medium approximations. Figure 5(c) shows the predictions of nonlocal EMT with the nonlocal transfer matrix formalism, and Figure 5(d) shows the numerical solutions of Maxwell's equations using FEM. To reduce the numerical artifacts, in all EMT calculations we assume that the local cone occupies the space $x \in [2.31, 3.4]$ μm, while the nonlocal region extends from $x \in [3.4, 5.3]$ μm.

It is clearly seen that material nonlocality drastically changes the predicted field distribution through the composite and reveals the signature of interference of the two TM-polarized waves in addition to the field enhancement in the vicinity of the transition region. Notably, the field profiles derived by effective medium theories are in agreement with results of full-wave 3D solutions of Maxwell's equations (that do not assume any effective medium response) throughout the majority of the nonlocal region.

Similar to other conventional transition metamaterials, hyperbolic transition materials offer a platform for a significant enhancement of the electric field. Importantly, the field enhancement is expected even in the presence of realistic material losses and taking into account the actual structure of the metamaterial.

Our study shows that the conventional effective medium description does not adequately predict the field enhancement. Local response calculations (Figure 4) drastically overestimate the enhancement, while the nonlocal EMT approach is in agreement with what is observed with full-vectorial numerical solutions of Maxwell's equations (Figure 5). Comparing the distribution of field intensities obtained within the local and nonlocal approximation we can see that taking into account nonlocal effects significantly reduces the value of the field enhancement and leads to the broadening of the peak in the vicinity of the transition region. In addition, realistic (nonlocal) nanorod arrays yield significant reflection of light into an additional mode. As this reflected mode propagates toward the apex of the cone, its effective index is increased, resulting in a pattern of highly oscillatory field peaks that may potentially be beneficial for surface-enhanced optical phenomena. The amplitudes of these peaks will likely be limited by the deviation of optical properties of nanostructured metallic wires from the predictions of the Drude model.[36]

The difference between predictions of local and nonlocal EMTs can be understood by comparing the behavior of the TM-polarized waves predicted by the two models, illustrated in Figure 6(a). The figure analyzes the behavior of the square of the effective modal index. The sign of this parameter can be used to understand the nature of the mode:[47] conventional propagating waves correspond to the positive square of the effective index; evanescent modes are described by the negative square of the effective index.

According to local EMT, the modes entering the transtition metamaterial are gradually slowed down, stopping at the vicinity of the $\epsilon_{xx} \simeq 0$ point (also known as epsilon-near-zero, ENZ point). The mode then tunnels through the remaining region of the elliptical response and leaves the system through the hyperbolic region. The maximal field enhancement is achieved at the ENZ point. The dynamics of the slow-down process, along the distance separating the turning point and the ENZ point, and material absorption define the maximal enhancement.[4] This effect is illustrated in Figure 6(b), which

DOI: 10.1021/acsphotonics.7b00690
ACS Photonics 2017, 4, 2470−2478

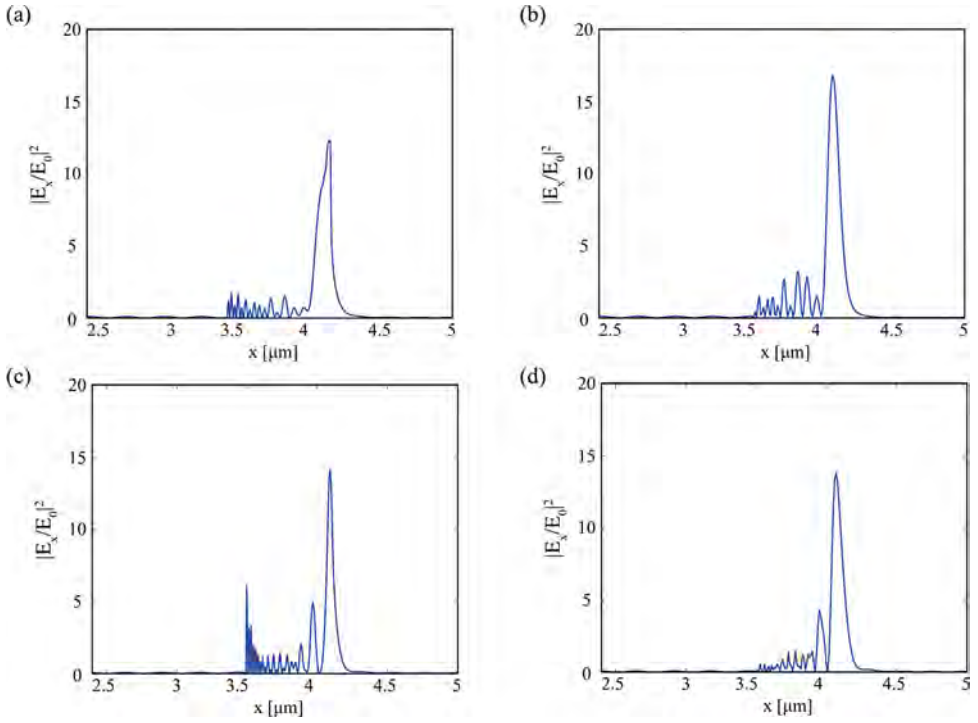

Figure 7. (a and b) Enhancement profile in a system with a hypothetical 10-fold loss reduction calculated using nonlocal EMT (a) and finite-element method (b), respectively. (c and d) Enhancement profile in a system with a = 30 nm, representing a 2-fold unit cell size reduction, obtained using nonlocal EMT (c) and finite-element method (d) calculations, respectively.

shows estimated maximal enhancement as a function of the width of the transition region. In these studies, we assumed that the radius profile shown in Figure 1 is linearly stretched or compressed. Note that while the local EMT predicts higher field enhancement in the shorter metamaterials, this field is concentrated in the increasingly small ENZ region (see Figure 6a).

In contrast, according to nonlocal EMT, the metamaterial operating in the elliptic regime supports two propagating TM-polarized modes. While one of these modes stops and becomes evanescent, the second mode never slows down to a stop. In addition, true (nonlocal) permittivity of the composite never reaches zero for obliquely incident light. The absence of the stopping point combined with larger permittivity explains the apparent reduction of the field enhancement. However, the decreased reduction is accompanied by a longer spatial region where this ehancement can be observed. Similar to the case of local EMTs, enhancement predicted by nonlocal EMT is affected by both material absorption and length of the transition region [Figure 6(b)].

Interestingly, in contrast to idealized metamaterials,[4] material absorption does not play the role of the main limiting factor in the field enhancement. In fact, hypothetical 10-fold reduction of losses yields rather incremental, ∼50% improvement in field enhancement, as predicted by both nonlocal EMT and full-wave numerical solutions of Maxwell's equations, [Figure 7(a,b)]. Similar improvement can be achieved by a 2-fold reduction of the unit cell of the metamaterial, in effect making the composite more local, [Figure 7(c,d)]. The consistent agreement between predictions of nonlocal EMT and full-wave calculations confirm that nonlocal EMT adequately describes the physics behind metamaterial response.

SUMMARY

In this work we considered propagation of the electromagnetic wave through a hyperbolic transition layer using local and nonlocal effective medium approximation. It is shown to correctly predict that the field enhancement nonlocality must be considered. This leads to the formation of additional interference between the main and additional modes inside the transition layer. The results predicted using the nonlocal effective medium theory are in agreement with those obtained in full-wave 3D numerical simulations of Maxwell's equations throughout the majority of the nonlocal region. From these studies, we conclude that nonlocal effects significantly affect the field behavior inside a transition hyperbolic layer. Having a model that can accurately predict the field behavior through these materials will lead to the design and practical applications of this new emerging metamaterial platform.

AUTHOR INFORMATION

Corresponding Author

*E-mail: brwells@hartford.edu.

ORCID

B. Wells: 0000-0002-0717-7648

N. Litchinitser: 0000-0002-3855-0927

Present Addresses

#University of Hartford, West Hartford, Connecticut 016117, United States.

⊥Purdue University, West Lafayette, Indiana 47907, United States.

Author Contributions

§B. Wells and Zh. A. Kudyshev contributed equally.

Notes

The authors declare no competing financial interest.

DOI: 10.1021/acsphotonics.7b00690
ACS Photonics 2017, 4, 2470−2478

■ ACKNOWLEDGMENTS

This research has been supported by ARO grants W911NF-12-1-0533, W911NF-16-1-0261, and W911NF-15-1-0146

■ REFERENCES

(1) Litchinitser, N. M.; Maimistov, A. I.; Gabitov, I. R.; Sagdeev, R. Z.; Shalaev, V. M. Metamaterials: electromagnetic enhancement at zero-index transition. *Opt. Lett.* **2008**, *33*, 2350−2352.
(2) Dalarsson, M.; Tassin, P. Analytical solution for wave propagation through a graded index interface between a right-handed and a left-handed material. *Opt. Express* **2009**, *17*, 6747−6752.
(3) Kim, K.; Lee, D.-H.; Lim, H. Resonant absorption and mode conversion in a transition layer between positive-index and negative-index media. *Opt. Express* **2008**, *16*, 18505−18513.
(4) Mozjerin, I.; Gibson, E. A.; Furlani, E. P.; Gabitov, I. R.; Litchinitser, N. M. Electromagnetic enhancement in lossy optical transition metamaterials. *Opt. Lett.* **2010**, *35*, 3240.
(5) Gibson, E. A.; Pennybacker, M.; Maimistov, A. I.; Gabitov, I. R.; Litchinitser, N. M. Resonant absorption in transition metamaterials: parametric study. *J. Opt.* **2011**, *13*, 024013.
(6) Gibson, E. A.; Gabitov, I. R.; Maimistov, A. I.; Litchinitser, N. M. Transition metamaterials with spatially separated zeros. *Opt. Lett.* **2011**, *36*, 3624.
(7) Alali, F.; Litchinitser, N. M. Gaussian beams in near-zero transition metamaterials. *Opt. Commun.* **2013**, *291*, 179.
(8) Kudyshev, Zh.A.; Gabitov, I. R.; Maimistov, A. I.; Sagdeev, R. Z.; Litchinitser, N. M. Second harmonic generation in transition metamaterials. *J. Opt.* **2014**, *16*, 114011.
(9) Sun, J.; Liu, X.; Zhou, J.; Kudyshev, Z.; Litchinitser, N. M. Experimental demonstration of anomalous field enhancement in all-dielectric transition magnetic metamaterials. *Sci. Rep.* **2015**, *5*, 16154.
(10) Smith, D. R.; Kolinko, P.; Schurig, D. Negative refraction in indefinite media. *J. Opt. Soc. Am. B* **2004**, *21*, 1032−1043.
(11) Podolskiy, V. A.; Narimanov, E. E. Strongly anisotropic waveguide as a nonmagnetic left-handed system. *Phys. Rev. B: Condens. Matter Mater. Phys.* **2005**, *71*, 201101.
(12) Jacob, Z.; Alekseyev, L. V.; Narimanov, E. E. Optical hyperlens: far-field imaging beyond the diffraction limit. *Opt. Express* **2006**, *14*, 8247−8256.
(13) Liu, Z.; Durant, S.; Lee, H.; Pikus, Y.; Fang, N.; Xiong, Y.; Sun, C.; Zhang, X. Far-field optical superlens. *Nano Lett.* **2007**, *7*, 403.
(14) Liu, Z.; Lee, H.; Xiong, Y.; Sun, C.; Zhang, X. Far-field optical hyperlens magnifying sub-diffraction-limited objects. *Science* **2007**, *315*, 16861686.
(15) Smolyaninov, I. I.; Hung, Y. J.; Davis, C. C. Magnifying superlens in the visible frequency range. *Science* **2007**, *315*, 16991701.
(16) Kabashin, A. V.; Evans, P.; Pastkovsky, S.; Hendren, W.; Wurtz, G. A.; Atkinson, R.; Pollard, R.; Podolskiy, V. A.; Zayats, A. V. Plasmonic nanorod metamaterials for biosensing. *Nat. Mater.* **2009**, *8*, 867871.
(17) Wurtz, G. A.; Pollard, R.; Hendren, W.; Wiederrecht, G. P.; Gosztola, D. J.; Podolskiy, V. A.; Zayats, A. V. Designed ultrafast optical nonlinearity in a plasmonic nanorod metamaterial enhanced by nonlocality. *Nat. Nanotechnol.* **2011**, *6*, 107111.
(18) Ferrari, L.; Wu, C.; Lepage, D.; Zhang, X.; Liu, Z. Hyperbolic metamaterials and their applications. *Prog. Quantum Electron.* **2015**, *40*, 1−40.
(19) Yao, J.; Liu, Z.; Liu, Y.; Wang, Y.; Sun, C.; Bartal, G.; Stacy, A. M.; Zhang, X. Optical negative refraction in bulk metamaterials of nanowires. *Science* **2008**, *321*, 930.
(20) Tsai, K. T.; Wurtz, G. A.; Chu, J. Y.; Cheng, T. Y.; Wang, H. H.; Krasavin, A. V.; Wells, B. M.; Podolskiy, V. A.; Wang, J. K.; Wang, Y. L. Looking into meta-atoms of plasmonic nanowire metamaterial. *Nano Lett.* **2014**, *14*, 4971.
(21) Pollard, R. J.; Murphy, A.; Hendren, W. R.; Evans, P. R.; Atkinson, R.; Wurtz, G. A.; Zayats, A. V.; Podolskiy, V. A. Optical nonlocalities and additional waves in epsilon-near-zero metamaterials. *Phys. Rev. Lett.* **2009**, *102*, 127405.
(22) Wells, B. M.; Zayats, A. V.; Podolskiy, V. A. Nonlocal optics of plasmonic nanowire metamaterials. *Phys. Rev. B: Condens. Matter Mater. Phys.* **2014**, *89*, 035111.
(23) Elser, J.; Podolskiy, V. A.; Salakhutdinov, I.; Avrutsky, I. Nonlocal effects in effective-medium response of nanolayered metamaterials. *Appl. Phys. Lett.* **2007**, *90*, 191109.
(24) Belov, P. A.; Marqués, R.; Maslovski, S. I.; Nefedov, I. S.; Silveirinha, M.; Simovski, C. R.; Tretyakov, S. A. Strong spatial dispersion in wire media in the very large wavelength limit. *Phys. Rev. B: Condens. Matter Mater. Phys.* **2003**, *67*, 113103.
(25) Silveirinha, M. G. Nonlocal homogenization model for a periodic array of ϵ-negative rods. *Phys. Rev. E* **2006**, *73*, 046612.
(26) Lagarkov, A. N.; Sarychev, A. K. Electromagnetic properties of composites containing elongated conducting inclusions. *Phys. Rev. B: Condens. Matter Mater. Phys.* **1996**, *53*, 6318.
(27) Hanson, G. W.; Forati, E.; Silveirinha, M. G. Modeling of spatially-dispersive wire media: transport representation, comparison with natural materials, and additional boundary conditions. *IEEE Trans. Antennas Propag.* **2012**, *60*, 4219−4232.
(28) Hanson, G. W.; Silveirinha, M. G.; Burghignoli, P.; Yakovlev, A. B. Non-local susceptibility of the wire medium in the spatial domain considering material boundaries. *New J. Phys.* **2013**, *15*, 083018.
(29) Ginzburg, P.; Roth, D. J.; Nasir, M. E.; Segovia, P.; Krasavin, A. V.; Levitt, J.; Hirvonen, L. M.; Wells, B. M.; Suhling, K.; Richards, D.; Podolskiy, V. A.; Zayats, A. V. *Light: Sci. Appl.* **2016**, *6*, e16273.
(30) Elser, J.; Wangberg, R.; Podolskiy, V. A.; Narimanov, E. E. Nanowire metamaterials with extreme optical anisotropy. *Appl. Phys. Lett.* **2006**, *89*, 261102.
(31) Orlov, A. A.; Voroshilov, P. M.; Belov, P. A.; Kivshar, Y. S. Engineered optical nonlocality in nanostructured metamaterials. *Phys. Rev. B: Condens. Matter Mater. Phys.* **2011**, *84*, 045424.
(32) Johnson, P. B.; Christy, R. W. Optical constants of the noble metals. *Phys. Rev. B* **1972**, *6*, 4370−4379.
(33) Garnett, M. Colors in metal glasses and in metallic films. *Philos. Trans. R. Soc., A* **1904**, *3*, 385−420.
(34) Slobozhanyuk, A. P.; Ginzburg, P.; Powell, D. A.; Iorsh, I.; Shalin, A. S.; Segovia, P.; Krasavin, A. V.; Wurtz, G. A.; Podolskiy, V. A.; Belov, P. A.; Zayats, A. V. Purcell effect in Hyperbolic Metamaterial Resonators. *Phys. Rev. B: Condens. Matter Mater. Phys.* **2015**, *92*, 195127.
(35) Yan, W.; Wubs, M.; Mortensen, N. A. Hyperbolic metamaterials: nonlocal response regularizes broadband supersingularity. *Phys. Rev. B: Condens. Matter Mater. Phys.* **2012**, *86*, 205429.
(36) Wiener, A.; Fernández-Domínguez, A. I.; Horsfield, A. P.; Pendry, J. B.; Maier, S. A. Nonlocal effects in the nanofocusing performance of plasmonic tips. *Nano Lett.* **2012**, *12*, 3308−3314.
(37) Ginzburg, P.; Zayats, A. V. Localized surface plasmon resonances in spatially dispersive nano-objects: phenomenological treatise. *ACS Nano* **2013**, *7*, 4334−4342.
(38) Krasavin, A. V.; Ginzburg, P.; Wurtz, G. A.; Zayats, A. V. Nonlocality-driven supercontinuum white light generation in plasmonic nanostructures. *Nat. Commun.* **2016**, *7*, 11497.
(39) Marinica, D. C.; Kazansky, A. K.; Nordlander, P.; Aizpurua, J.; Borisov, A. G. Quantum plasmonics: nonlinear effects in the field enhancement of a plasmonic nanoparticle dimer. *Nano Lett.* **2012**, *12*, 1333−1339.
(40) Haus, J. W.; de Ceglia, D.; Vincenti, M. A.; Scalora, M. Quantum conductivity for metal−insulator−metal nanostructures. *J. Opt. Soc. Am. B* **2014**, *31*, 259−269.
(41) Zhu, W.; Esteban, R.; Borisov, A. G.; Baumberg, J. J.; Nordlander, P.; Lezec, H. J.; Aizpurua, J.; Crozier, K. B. Quantum mechanical effects in plasmonic structures with subnanometre gaps. *Nat. Commun.* **2016**, *7*, 11495.
(42) Taflove, A. *Computational Electrodynamics: The Finite-Difference Time-Domain Method*; Artech House: Norwood, MA, 1995.
(43) Rytov, S. M. Electromagnetic properties of a finely stratified medium. *Sov. Phys. JETP* **1956**, *2*, 466−475.

DOI: 10.1021/acsphotonics.7b00690
ACS Photonics 2017, 4, 2470−2478

(44) Yeh, P.; Yariv, A.; Hong, C. Electromagnetic propagation in periodic stratified media. II. Birefringence, phase matching, and x-ray lasers. *J. Opt. Soc. Am.* **1977**, *67*, 423−438.
(45) *COMSOL Multiphysics*; COMSOL AB, 2013.
(46) Govyadinov, A. A.; Podolskiy, V. A. Metamaterial photonic funnels for subdiffraction light compression and propagation. *Phys. Rev. B: Condens. Matter Mater. Phys.* **2006**, *73* (15), 155108.
(47) Our studies indicate that n_{eff}^2 is dominated by its real part.

DOI: 10.1021/acsphotonics.7b00690
ACS Photonics 2017, 4, 2470−2478

OPEN

Light: Science & Applications (2017) 6, e16273; doi:10.1038/lsa.2016.273
Official journal of the CIOMP 2047-7538/17
www.nature.com/lsa

ORIGINAL ARTICLE

Spontaneous emission in non-local materials

Pavel Ginzburg[1,2,*], Diane J Roth[1,*], Mazhar E Nasir[1,*], Paulina Segovia[1], Alexey V Krasavin[1,*], James Levitt[1], Liisa M Hirvonen[1], Brian Wells[3,4], Klaus Suhling[1], David Richards[1], Viktor A Podolskiy[3] and Anatoly V Zayats[1]

Light–matter interactions can be strongly modified by the surrounding environment. Here, we report on the first experimental observation of molecular spontaneous emission inside a highly non-local metamaterial based on a plasmonic nanorod assembly. We show that the emission process is dominated not only by the topology of its local effective medium dispersion, but also by the non-local response of the composite, so that metamaterials with different geometric parameters but the same local effective medium properties exhibit different Purcell factors. A record-high enhancement of a decay rate is observed, in agreement with the developed quantitative description of the Purcell effect in a non-local medium. An engineered material non-locality introduces an additional degree of freedom into quantum electrodynamics, enabling new applications in quantum information processing, photochemistry, imaging and sensing with macroscopic composites.

Light: Science & Applications (2017) **6,** e16273; doi:10.1038/lsa.2016.273; published online 2 June 2017

Keywords: composite electromagnetic materials; non-local optical properties; plasmonic metamaterials; quantum electrodynamics; spontaneous emission

INTRODUCTION

When the behavior of a physical system at a given point depends on its state at another spatially separated region, the system is described as being non-local. Quantum states of light and matter are inherently non-local, reflecting the fundamental wave-particle duality[1]. Quantum entanglement is one of the most fascinating examples of non-localities in nature[2,3]. Its successful demonstration in optics with photons[4,5] is enabled by inherently weak photon-photon interactions. Material systems, on the other hand, suffer from various decoherence effects, such as electron-electron, electron-phonon and other scattering mechanisms that virtually eliminate optical non-locality in homogeneous room-temperature media[6]. However, electromagnetic non-locality may re-emerge in engineered composites, metamaterials[7], where coherent surface plasmons mediate coupling between unit cells of artificial electromagnetic crystals.

Here, we analyze both experimentally and theoretically the process of spontaneous emission in a non-local environment using a plasmonic nanorod metamaterial platform that has been recently demonstrated to enable a topological transition between elliptic and hyperbolic dispersions. Experimentally, we demonstrate a broadband, macroscopically averaged lifetime reduction of the order of 30 for several fluorophores, while microscopic reductions in lifetime are orders of magnitude higher, as estimated from the experimental data. We develop new theoretical and numerical approaches capable of calculating the local density of photonic states in non-local media. Although non-local effects are known to have a weak impact on linear reflection and transmission through the metamaterial[7], the situation is completely different in the quantum optical regime where non-locality results in an additional propagating mode inside the metamaterial, fundamentally altering the density of photonic states[8]. The dynamics of emitters' decay, and other quantum optical processes, inside a nanorod metamaterial are essentially dominated by the non-local response of the composite, as shown in this work.

The paper is organized as follows. In the Materials and methods section, we describe fabrication of the nanorod metamaterials and a flow-cell-based introduction of fluorophores inside the metamaterials. The details of fluorescence lifetime measurements are presented together with the lifetime distribution analysis based on the Laplace transform, which is paramount for understanding multi-exponential decay of an ensemble of emitters in a structured environment. This Laplace approach is verified by recovering the spontaneous emission lifetime distribution near a smooth Au film. The local and non-local models of the effective medium theory (EMT) for a composite metamaterial are then described. Subsequently, the analytical evaluation of the spontaneous emission lifetime is derived based on the EMT approach. Finally, the numerical model for the spontaneous emission inside the nanorod metamaterials is presented and compared with the EMT and experimental results. In the Results and discussion section,

[1]Department of Physics, King's College London, Strand, London WC2R 2LS, UK; [2]Present address: School of Electrical Engineering, Tel Aviv University, Tel Aviv 69978, Israel; [3]Department of Physics and Applied Physics, University of Massachusetts Lowell, One University Ave, Lowell, MA 01854, USA and [4]Present address: Department of Physics, University of Hartford, West Hartford, CT 06117, USA
*These authors contributed equally to this work
Correspondence: P Ginzburg, Email: pginzburg@post.tau.ac.il
Received 10 June 2016; revised 28 November 2016; accepted 13 December 2016; accepted article preview online 19 December 2016

the mode structure of the metamaterials is derived in the local and non-local EMT approximations. The role of non-locality and losses is elucidated on the topology of the isofrequency surfaces in elliptic and hyperbolic regimes of dispersion. Spontaneous emission rates are evaluated for the emitters inside the composite in the local and non-local EMT descriptions. The dependence of the mode dispersion and the photoluminescence (PL) lifetime on the scaling of the elementary cell of the nanorod composite is then shown, which is absent in the local EMT description and is a purely non-local effect. These analytical results are confirmed with full-vectorial numerical simulations. The spontaneous emission lifetimes of different fluorophores emitting at different wavelengths, falling within elliptical, epsilon-near-zero (ENZ), and hyperbolic dispersion regimes of the metamaterial are measured and analyzed. The results are in excellent agreement with the numerical solutions of Maxwell equations and analytical model, confirming an important role of non-locality for spontaneous emission inside the metamaterial.

MATERIALS AND METHODS

Metamaterial fabrication

Plasmonic nanorod metamaterials were fabricated by Au electrodeposition into highly ordered nanoporous anodic alumina oxide (AAO) templates on glass cover slips. An Al film of 700 nm thickness was deposited on a substrate by magnetron sputtering. The substrate comprised a glass cover slip with a 10 nm thick adhesive layer of tantalum pentoxide and a 7 nm thick Au film, acting as a weakly conducting layer. Highly ordered, nanoporous AAO was synthesized by a two step-anodization in 0.3 M oxalic acid at 40 V. After an initial anodization process, the formed porous layer was partly removed by etching in a solution of H_3PO_4 (3.5%) and CrO_3 (20 g L^{-1}) at 70 °C, which resulted in an ordered pattern. At the next step, the sample was anodized again under the same conditions as in the first step. The anodized AAO was subsequently etched in 30 mM NaOH to achieve pore widening. Gold electrodeposition was performed with a three electrode system, using a non-cyanide solution. The length of nanorods was controlled by the electrodeposition time. Free standing gold nanorod metamaterials were obtained after dissolving the nanoporous alumina template in a mix solution of 0.3 M NaOH and 99.50% ethanol. The nanorod array parameters used in the reported experiments are 50 ± 2 nm diameter, 100 nm period and 250 ± 5 nm height (Figure 1a). The optical properties and the extinction spectra of the metamaterial for various illumination angles are shown in Figure 1b–1d, respectively.

Fluorescence lifetime measurements

Four dye molecules, D1 (fluorescein), D2 (Alexa 514), D3 (ATTO 550) and D4 (ATTO 647N) with the emission wavelengths 514, 550, 575 and 670 nm, respectively, were used to probe local density of states of the metamaterial. For D1 and D2 dyes, the solvent was ethanol and the concentration was 2.5×10^{-5} mol L^{-1}. For D3 and D4 dyes, the solvent was made of 10 mM of Tris-HCL, 1 mM of EDTA, 30 mM of NaCl and NaOH to adjust the pH of the solution to 7.85, and the concentration of 10^{-6} mol L^{-1} was chosen. The dye solutions were introduced in the metamaterial using a flow cell, which was positioned on a confocal microscope for fluorescence measurements. In order to ensure a correct comparison between the lifetime measurements for different emitters, the same metamaterial was used for the measurements of all four dyes. For repeated measurements, the dyes' solution was washed out and the sample was plasma cleaned before changing emitters.

Time-resolved PL measurements were performed using time-correlated single photon counting (TCSPC)[9] based on a SPC-150 (Becker–Hickl) system. The wavelength of the TM-polarized excitation light from a Fianium super-continuum laser (< 10 ps pulse duration, 20 MHz repetition rate) was selected (525 nm for ATTO 550, 633 nm for ATTO 647N, 470 nm for Alexa 514 and 470 nm for fluorescein). The excitation light was focused on the sample with a 100×, numerical aperture = 1.49 oil-immersion objective and the resulting PL signal collected by the same objective. Appropriate band-pass filters centered on the peak emission wavelength of each dye were used to collect the PL signal and prevent any laser contribution to the measured light. For each dye, three sets of measurements were carried out on a metamaterial, a thin (50 nm) gold film, and a glass substrate. The PL spectra of the different dyes on glass and inside the metamaterial are shown in Supplementary Fig. S1.

Fluorescence lifetime data analysis

In order to analyze the time-dependence PL data, the inverse Laplace transform was used[10], which does not rely on any preliminary assumption on emission process and adequately reproduces the distribution of the lifetimes present in the experimental data. This procedure is implemented by solving the integral equation

$$I(t) = \int_0^\infty F(s) e^{-st} \mathrm{d}s \qquad (1)$$

where $I(t)$ is the time dependent fluorescence intensity (measured quantity), deconvoluted from the instrumental response function (measured in a separate experiment), and $F(s)$ is the relative weight of different single exponential decay components. The deconvolution was performed by applying Tikhonov regularization technique, also introducing low pass filtering, reducing the noise of the decay tail. Since the inverse Laplace transform is known to be an ill-defined problem (especially for analysis of noisy data), an iterative fitting procedure was applied in order to achieve stable results. This type of analysis assumes that the fluorophores are in the weak coupling regime of interaction with the surrounding environment.

Lifetime analysis of the ensemble of emitters near a gold film

A semi-analytical expression for decay rate modification of a point-like emitter near an interface between two dielectric materials relies on the knowledge of the electromagnetic Green's function[11] and its classical quantum correspondence to the spontaneous emission rate (proportionality to the imaginary part of the Green's function)[12,13]. Hence, given the lifetime distributions of fluorophores near a glass substrate $F^{\mathrm{exp}}_{\mathrm{Glass}}(s)$, the corresponding distribution near a gold film can be derived as

$$F^{\mathrm{Theor}}_{\mathrm{Au}}(s) \sim \int_{d_{\min}}^{d_{\max}} \left|\vec{E}_{\mathrm{pump}}(z)\right|^2 Q_{\mathrm{loc}}(z) n(z) F^{\mathrm{exp}}_{\mathrm{Glass}}(s/P(z)) \mathrm{d}z, \qquad (2)$$

where $P(z)$ is the position dependent polarization-averaged Purcell factor near the Au surface, $\left|\vec{E}_{\mathrm{pump}}(z)\right|^2$ is the position-dependent intensity of the excitation light, $Q_{\mathrm{loc}}(z)$ is the fluorophore local quantum yield, and $n(z)$ is the distribution density of the fluorophores along the focal depth, which was assumed to be uniform. The depth of focus ($d_{max} - d_{min}$) was taken to be ~175 nm for the best fit to the experimental data. Slight deviations between the fitting and experiment may arise due to sensitivity of the Laplace transform to noise in experimental data, and the assumption on $n(z)$, which in principle, may encapsulate stochastic inhomogeneity of the solution.

doi:10.1038/lsa.2016.273

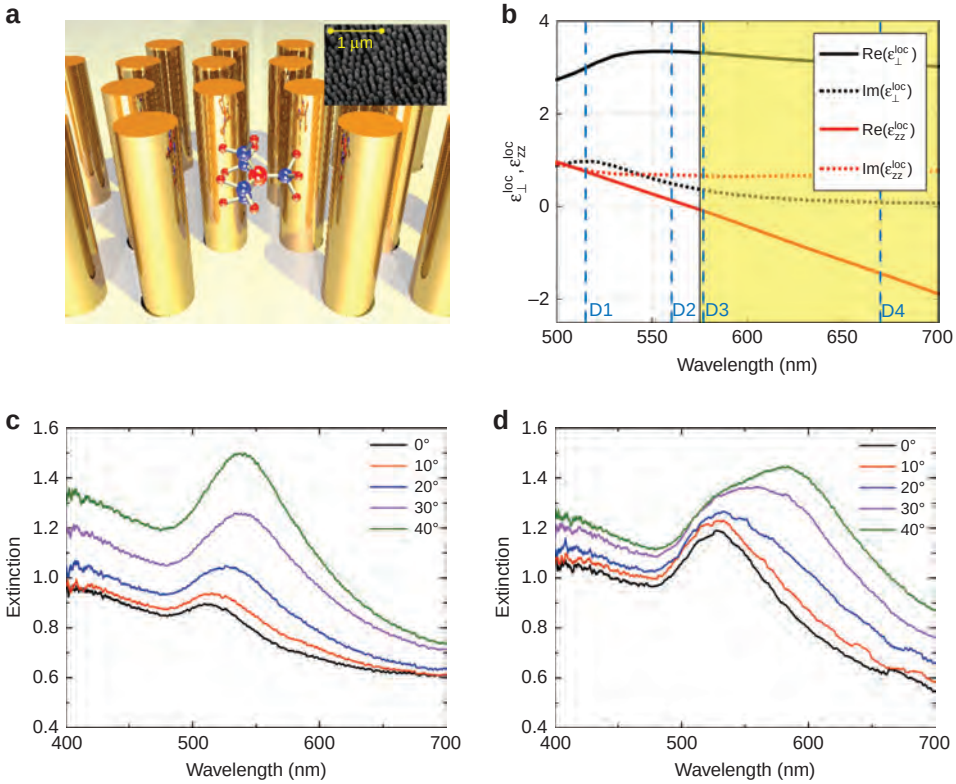

Figure 1 (**a**) Schematics of a nanorod metamaterial with a fluorescent molecule inside. Inset shows SEM image of the metamaterial comprised of Au nanorods in air (scale bar is 1 μm). (**b**) Local effective medium parameters of the metamaterials (Au nanorods in ethanol) determined from the geometry of the nanorod metamaterial 50 ± 2 nm diameter, 100 nm period and 250 ± 5 nm height) which reproduce the experimental extinction spectra in **c**. Vertical dashed lines indicate the emission wavelengths of the dyes for the PL lifetime measurements. (**c**, **d**) Extinction spectra of the metamaterials consisting of free standing nanorods for different angles of incidence of p-polarized light in **c** air and **d** ethanol.

Effective medium models of the metamaterial

For light wavelengths much larger than all the characteristic sizes of the composite, such as nanorod diameter and their period, the optical properties of the metamaterial can be described with the effective permittivity, which can be used to calculate transmission, reflection and absorption spectra of the composite. Due to symmetry, the optical properties of a nanorod metamaterial resemble those of an homogeneous uniaxial anisotropic medium with optical axis parallel to the nanorods (z-direction in Figure 1b). Macroscopically, these optical properties are described by a diagonal permittivity tensor $\hat{\epsilon}$ with $\epsilon_{xx} = \epsilon_{yy} \equiv \epsilon_{\perp} \neq \epsilon_{zz}$. In analytical calculations, a layer of a metamaterial was represented as a homogeneous layer described by either local[14] or non-local[15] effective medium theories.

Local EMT. In a conventional, local effective medium description, the permittivity of the metamaterial is given by the Maxwell Garnett theory:

$$\epsilon_{\perp}^{\mathrm{mg}} = \epsilon_h \frac{(1+p)\epsilon_{\mathrm{Au}} + (1-p)\epsilon_{\mathrm{h}}}{(1+p)\epsilon_{\mathrm{h}} + (1-p)\epsilon_{\mathrm{Au}}};\ \epsilon_{zz}^{\mathrm{mg}} = p\epsilon_{\mathrm{Au}} + (1-p)\epsilon_{\mathrm{h}} \qquad (3)$$

with ϵ_{h} and ϵ_{Au} being the permittivities of the host material and gold, respectively, and $p = \pi(r/a)^2$ is the fill factor of the metal inside the matrix (r is the nanorod radius and a is the period of the array). The Drude model, with corrections for restricted mean free path of electrons[16], previously shown to be in quantitative agreement with experimental results[7,16], was used to describe the permittivity of electrochemically deposited gold. The spectral behavior of the components of effective permittivity tensor of the metamaterial used in the experiments is shown in Figure 1b.

Non-local EMT. When optical losses in Au nanorods are small, a local effective medium description of metamaterial becomes invalid, and a more complex, non-local effective medium response must be considered[7]. In non-local EMT, the components of the permittivity tensor perpendicular to the optical axis are still described by the Maxwell Garnett theory ($\epsilon_{xx} = \epsilon_{yy} = \epsilon_{\perp}^{\mathrm{MG}}$), while the component of the permittivity tensor along the optical axis becomes explicitly dependent on the wave vector,

$$\epsilon_{zz}(k_z) = \xi\left(k_z^2\frac{c^2}{\omega^2} - \left(n_z^{\mathrm{l}}\right)^2\right);\ \xi = p\frac{\epsilon_{\mathrm{Au}} + \epsilon_{\mathrm{h}}}{\epsilon_{\mathrm{h}} - \left(n_{\infty}^{\mathrm{l}}\right)^2} \qquad (4)$$

where n_z^{l} is the effective refractive index of the cylindrical surface plasmons that propagate in a nanorod composite with the nanorod permittivity ϵ_{Au} and n_{∞}^{l} represents the limit of n_z^{l} for perfectly conducting nanorods[17]. These parameters can be calculated either numerically or by solving an eigenvalue-type problem.

The transfer matrix method[17], was used to calculate transmission and reflection of a planar slab of the metamaterial for a given excitation frequency and angle of incidence.

The effective medium model adequately describes the extinction spectra observed in experiment (cf. Figure 1c and 1d and Supplementary Fig. S2). The two spectral features, seen in extinction spectra at $\lambda \simeq 525$ nm (for all incident angles) and at $\lambda \simeq 575$ nm (for larger incident angles) correspond to the Maxwell Garnett

resonance ($\epsilon_{\perp}^{mg} \gg 1$) and the ENZ regime ($\epsilon_{zz}^{mg} \simeq 0$), respectively. For very long wave vectors that approach the edge of the Brillouin zone of the nanorod array, both local and non-local EMTs break down and should not be used. Similar behavior was recently observed in layered composites when the wave vector in the direction perpendicular to the layers becomes comparable to the period[15].

Fluorescence decay rate calculations from EMT formulation

A Green's function formalism was used to analyze the emission rate modification[18]. In this approach, the emission rate is proportional to the imaginary part of the Green's function, representing the electric field $\vec{E}$ generated by the point dipole $\vec{d}$ at the location of the dipole[8,11,18]

$$\frac{\Gamma}{\Gamma_0} \simeq \frac{3c^3 \,\mathrm{Im}\left(\vec{E} \cdot \vec{d}\right)}{2\omega^3 \quad |W_0|^2} \tag{5}$$

where Γ_0 is the emission rate in the free space, while Γ is the rate modified due to surrounding environment, and W_0 is the power radiated by the dipole in free space, which serves as a normalization constant. $\hat{z}$- polarized and in-plane polarized dipoles were considered separately, and the total emission rate was calculated as the weighted-average of the two dipole directions. This assumption is related to a completely random distribution of dye molecules inside the solution. The transfer matrix formalism was used to take into account the effect of multiple reflections of the dipole's emission inside the composite layer[19]. In order to avoid singularities caused by placing the dipole inside a lossy medium, the dipole was placed inside a 1 nm thin layer of lossless medium, cut out inside the lossy metamaterials (the technique known as extraction of a depolarization volume). In the non-local case, two TM-polarized modes were considered as independent emission channels; however, the obtained results suggest that the hyperbolic-like mode dominates emission in both elliptic and hyperbolic regimes, similar to what has been previously reported in emission inside an infinite idealized metamaterial[20].

Fluorescence decay rate calculation from numerical modeling

Numerical modeling was performed using the finite element method (FEM) implemented in Comsol Multiphysics software. The Purcell factor at various locations inside the nanorod metamaterial was calculated as a ratio of power flow from a point dipole placed at a given position and the corresponding value for a dipole in vacuum. In order to cross-check reliability of the numerical results, two independent methods were used for the power flow estimation: 1) via a Poynting vector flux through a small sphere (5 nm radius) enclosing the point dipole and 2) via the energy dissipation rate of the dipole, $W(\vec{r}) = -\frac{1}{2}\mathrm{Re}\left[\vec{E}^{*}(\vec{r}) \cdot \vec{J}(\vec{r})\right]$, where $\vec{E}(\vec{r})$ is the electric field produced by the dipole at the point of its location and $\vec{J}(\vec{r})$ is the dipole current. Both methods showed excellent agreement with each other. To take into account the arbitrary orientation of an emitting dipole, the power flow was calculated separately for emitters aligned with each coordinate axis, and the overall enhancement was calculated as the average $\Gamma(\vec{r}) = \frac{1}{3}\Gamma_x(\vec{r}) + \frac{1}{3}\Gamma_y(\vec{r}) + \frac{1}{3}\Gamma_z(\vec{r})$[21]. The results of these classical electromagnetic calculations can be directly mapped onto the quantum decays of emitters, by employing the classical quantum correspondence of radiation reaction forces[18]. In order to simulate an infinite number of nanorods in the metamaterial, the number of rods in the finite-size arrays was gradually increased with periodic boundary conditions on the sides of the nanorod patch. The convergence of the Purcell factor with the number of the nanorods within the simulation domain (Supplementary Fig. S3) confirms that a 10×10 nanorod array with periodic boundary conditions can be used to analyze the behavior of a dipole in infinite metamaterial. The averaging over the dipole position within the unit cell of the array of the metamaterial was performed, assuming a uniform distribution of the emitters with a position-dependent decay rate and local excitation efficiency, by an excitation light illuminating the metamaterial from the substrate side: $I(t) \propto \int_{e-c} \left|\vec{E}_{\mathrm{pump}}(\vec{r})\right|^2 Q_{\mathrm{loc}}(\vec{r}) n(\vec{r}) \exp\left(-P(\vec{r}) \cdot \Gamma_0 t\right) d^3\mathrm{r}$, where the integration is performed over the dye-filled volume within the elementary cell (e–c), taking into account the distance dependent number of emitters $n(\mathbf{r})$. $Q_{\mathrm{loc}}(\mathbf{r})$ is the local quantum efficiency defining how much of the emitted power is measured in the far-field (the internal quantum yield of the emitters was taken to be 1 in all the simulations). The local pump intensity was found to vary by only 8% between 470 and 633 nm excitation wavelength used in the experiment and was averaged for these values. Since this equation yields a multi-exponential decay, a procedure equivalent to the inverse Laplace transform was applied in order to recover the theoretically predicted lifetime distribution, in a manner similar to analysis of the experimental measurements.

RESULTS AND DISCUSSION

Electromagnetic waves in the metamaterial and topology of isofrequency surfaces

Homogeneous anisotropic media support the propagation of two types of waves that differ by their polarization. Ordinary waves (TE modes) that have electric field normal to the metamaterial's optical axis $\vec{E} \perp \hat{z}$ (Figure 1a) do not experience an anisotropy of dielectric permittivity. On the other hand, extraordinary waves (TM modes) that have magnetic field $\vec{H} \perp \hat{z}$ are strongly affected by material anisotropy. The dispersion of the extraordinary waves, the relationship between components of the wave vector $\vec{k}$, angular frequency ω, and speed of light c, is given by

$$\frac{k_x^2 + k_y^2}{\epsilon_{zz}} + \frac{k_z^2}{\epsilon_{\perp}} = \frac{\omega^2}{c^2} \tag{6}$$

The isofrequency surface, which is defined as the locus of points with coordinates $\{k_x(\omega), k_y(\omega), k_z(\omega)\}$, forms either an ellipsoid or a hyperboloid, depending on the relationship between the signs of $\epsilon_{\perp}$ and ϵ_{zz} which, in turn, are wavelength-dependent. The geometrical properties of this isofrequency surface are often referred to as the optical topology of a metamaterial[22]. The effective permittivity of the metamaterials used in this study (Figure 1b) shows that the composite operates in the elliptic regime for wavelengths below the 575 nm, exhibits ENZ response at around 575 nm, corresponding to the effective plasma frequency[23] and operates in the hyperbolic regime for longer wavelengths. Optical topology predicted by Equation (6) exhibits typical ellipsoidal isofrequencies for TE modes in both elliptic and hyperbolic regimes (Figure 2a and 2b). The dispersion of TM modes in the hyperbolic regime is described by a hyperboloid (Figure 2d). Dispersion of TM modes in the elliptic regime is strongly affected by material losses (*cf.* Supplementary Fig. S4g–i) and represents an ellipsoid in the center of the Brillouin zone which is increasingly deformed for higher wavenumbers (Figure 2c).

The optical topology of metamaterials has a marked effect on their quantum optical properties, leading, theoretically, to a singularity in the local density of optical states in homogeneous hyperbolic media[24] (this effect is limited by granularity in metamaterials[8]). The density of optical states affects the rate of spontaneous emission[25], nonradiative energy transfer between molecules[26], and other processes. Recent

doi:10.1038/lsa.2016.273

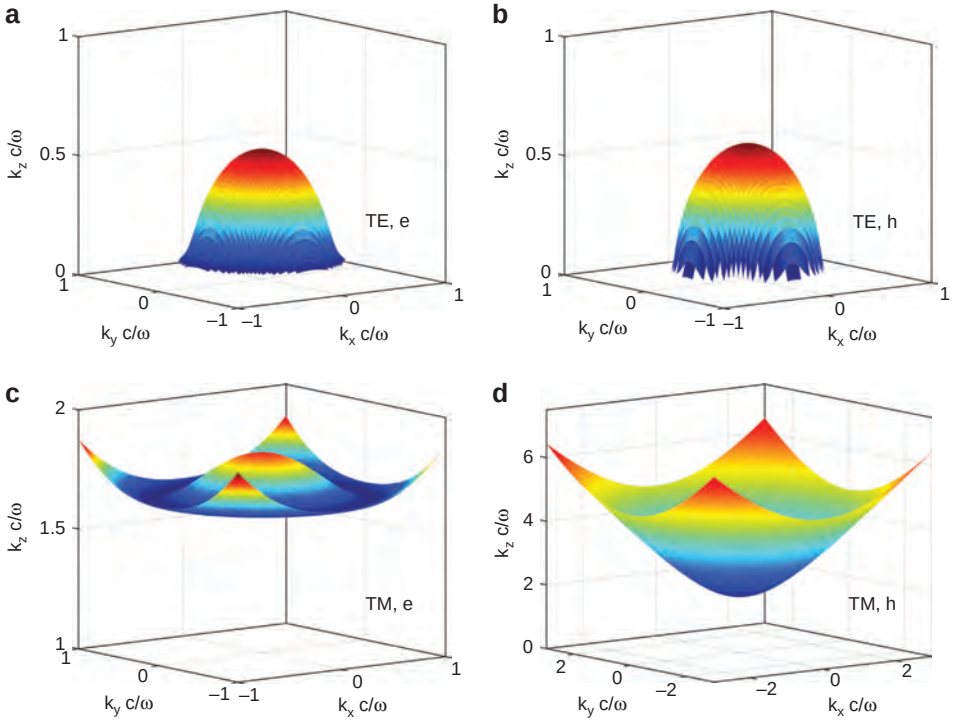

Figure 2 Isofrequency surfaces describing the dispersion of the propagating modes in the metamaterial with parameters as in Figure 1b, calculated with the local EMT: (**a**, **c**) elliptic (denoted e) regime ($\lambda = 550$ nm), (**b**, **d**) hyperbolic (denoted h) regime ($\lambda = 650$ nm) for (**a**, **b**) TE- and (**c**, **d**) TM-polarized modes. The non-monotonic behavior of the TM-polarized mode in the elliptical regime (**c**) is a direct consequence of the material absorption (Supplementary Fig. S2).

experimental studies, mostly focused on emitters near a layered metamaterial design, have demonstrated relatively modest 5–10 fold enhancements of the decay rate in the hyperbolic dispersion case and smaller enhancements in the elliptic dispersion regime[22]. Similar results were reported for emitters on top of hyperbolic plasmonic nanorod metamaterials[27]. Magnetic hyperbolic metamaterials provided a possibility to probe magnetic-dipole transitions[28]. However, the geometry of these previous studies prevented a test of emission dynamics in the non-local metamaterial regime, most pronounced inside nanorod metamaterials operating in the elliptical regime[7,17,29,30] (corresponding to $\lambda < 575$ nm for the metamaterials used in this work).

Optical non-localities in nanorod media

There exists a frequency range in which the nanorod metamaterial supports the propagation of not two, but three different modes[7,30]. One of these modes is a TE-polarized ordinary wave (Figure 3a and 3b), while the other two waves have identical (TM) polarization, but different effective indices. The dispersion of TM-polarized waves is given by

$$\left(k_z^2 - \left(n_z^{\mathrm{l}}\right)^2\frac{\omega^2}{c^2}\right)\left(k_z^2 - \epsilon_{\perp}^{\mathrm{mg}}\frac{\omega^2}{c^2}\right) = -\frac{\epsilon_{\perp}^{\mathrm{mg}}\omega^2}{\xi\ c^2}k_x^2 \qquad (7)$$

The topology of these waves is shown in Figure 3c and 3d). Comparing Figure 2 and Figure 3, it is seen that while in the hyperbolic regime the differences are minimal, the behavior in the elliptic regime is drastically different. The isofrequency of one of the TM polarized waves now qualitatively agrees with an ellipsoid, predicted by Equation (6). The second, additional TM polarized mode which is absent in the local effective medium theory, has a hyperbolic-like topology (Figure 3c).

Transmission spectra of the slab of the metamaterial, calculated with the local and non-local permittivity models for the metamaterial parameters used in this work, are almost identical with small deviations at the larger angles of incidence (Supplementary Fig. S2), with the non-local EMT providing better correspondence to the shape of the experimentally measured spectra (Figure 1c and 1d). Nevertheless, there is a drastic disagreement between predictions of the two approaches for the evaluation of emission properties of the dipole embedded inside the metamaterial. The additional wave described in the non-local EMT represents a collective excitation of cylindrical surface plasmons propagating on metallic nanorods[17]. This mode is a metamaterial analog of collective light–matter excitations, exciton-polaritons, that are known to enable additional waves in homogeneous semiconductors[6]. In both homogeneous and composite media, properties of additional waves can be successfully described by introducing non-locality, that is, a wave vector dependence of the permittivity of the material. However, although the permittivity of homogeneous media is essentially fixed by nature, the electromagnetic response of composites can be engineered.

Engineering non-local response by scaling metamaterial's unit cell and losses

The dispersion of modes in plasmonic nanorod composites can be controlled by scaling the unit cell, a process that does not change the local effective medium response, but does affect the non-local one. The predicted changes in the dispersion of optical modes as a result of geometry scaling are summarized in Figure 3e and 3f. Material losses can be controlled by the choice of plasmonic metal or by fabrication (for example, annealing) and serve as an additional degree of freedom for engineering the optical properties of a metamaterial.

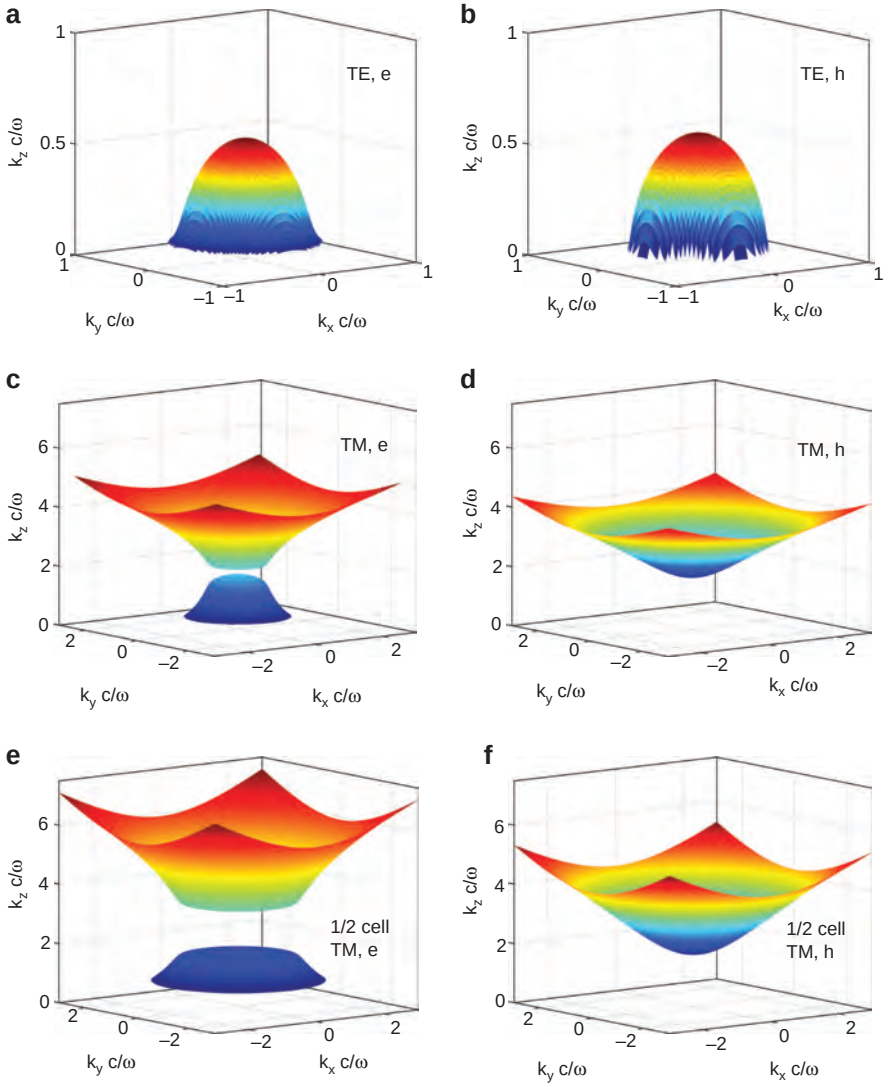

Figure 3 Dispersion of the modes supported by the nanorod metamaterial calculated using the *non-local* effective medium theory: (**a**, **c**, **e**) elliptic (denoted e) regime ($\lambda = 550$ nm) and (**b**, **d**, **f**) hyperbolic (denoted h) regime ($\lambda = 650$ nm) in the case of (**a**, **b**) TE- and (**c**–**f**) TM-modes for (**a**–**d**) the metamaterial considered in experiments (as in Figure 1b) and (**e**, **f**) metamaterial with 50% unit cell and nanorod diameter (25 nm diameter, 50 nm period). The scaling does not change the local effective medium parameters of the composite (Figure 2a–d).

The dispersion of the modes supported by the nanorod composite, predicted by local and non-local effective medium theories clearly shows that dispersion of TE polarized modes does not significantly depend on materials absorption or unit cell size and is close to those presented in Figure 2a and 2b. On the other hand, when the metamaterial operates in the elliptical regime, absorption, along with unit cell configuration, plays an important role in defining the topology of TM-polarized modes (Supplementary Fig. S4). When losses are small, the two TM polarized modes represent well-separated branches in the wave vector space, with the lower branch having elliptical behavior and the upper branch exhibiting hyperbolic-like dynamics (Supplementary Fig. S4a and S4d). As the unit cell becomes smaller, the behavior of the elliptic branch approaches predictions of the local effective medium theory (Supplementary Fig. S4g), while the upper branch moves 'up', increasing the effective index of the mode. As losses increase, the two TM-polarized modes approach each other (Supplementary Fig. S4b and S4c). Scaling the size of the unit cell of metamaterial still drastically affects the topology of these waves (Supplementary Fig. S4e and S4f). Note that when losses are high, the local EMT converges to the upper (hyperbolic) wave (Supplementary Fig. S4i); however, in the regime of moderate losses, realized in our work, the local EMT becomes invalid, predicting the response that does not match the properties of either of the two modes of the metamaterial (Supplementary Fig. S4h). When the metamaterial operates in the hyperbolic regime, the elliptical branch of the TM-dispersion cuts off, and the propagation of light is dominated by the hyperbolic branch (Supplementary Fig. S5). The effect of the spatial dispersion is now essentially limited to a quantitative correction of the dispersion. Decreasing the unit cell size or reducing losses causes the dispersion to approach a 'perfect' hyperboloid, while decreasing the unit cell alone causes the response to approach predictions of the local effective medium theory.

From the point of view of a quantum emitter, an additional electromagnetic wave represents a separate emission decay channel

doi:10.1038/lsa.2016.273

that, in turn, affects its radiation dynamics, and drastically increases the density of optical states in the elliptic regime.

Experimental studies

The analysis of decay dynamics of four fluorescent dyes with different emission wavelengths spanning elliptic and hyperbolic regimes and placed inside the metamaterial is summarized in Figure 4. Although all the studied emitters show nearly single-exponential fluorescence decays in a homogeneous environment, the presence of plasmonic surfaces and nanostructures makes the dynamics multi-exponential. This effect does not represent the strong coupling regime of interaction[31], but rather is the direct result of many emitters contributing to the signal, with each individual emitter having its own position- and polarization-dependent decay rate in the structured environment.

Here we have used the inverse Laplace transform[10], which does not rely on any preliminary assumptions and provides the distribution of the lifetimes present in the observations. Emitters situated above a glass substrate show smooth localized lifetime distributions peaked around their standard values of a few nanoseconds (Figure 5). The comparison of emission for glass and Au interfaces reveals the expected behavior, caused by the presence of the metal, and related plasmonic excitations[11]. Once the dependence of the lifetime on the emitter's spatial position is taken into account, an almost perfect agreement between theoretical predictions and experimental measurements of lifetime distributions is achieved for the emitters near the metal interface (Figure 5). The overall peak to peak rate enhancement is less than 2. For example, the lifetime distribution for D1 emitters (Figure 5a) is peaked at 3.9 ns, representing the reduction of the macroscopically averaged lifetime by a factor of ~ 1.2. Spatial averaging takes into account the random distribution of molecules inside the sample volume. The excellent agreement between the experimental data and the model indicates that, various possible collective effects which could affect the dynamics, such as super-fluorescence[32,33], can be ruled out.

The dynamics measured for the emitters inside the metamaterial exhibits even faster decay with an even broader distribution (7–100 times) of the lifetimes than for a single metal interface (Figure 5 and Supplementary Fig. S3). The span of the lifetime distributions reflects a strong position-dependent decay rate enhancement for the emitters inside the nanorod array unit cell[34]. Substantial lifetime reduction was observed for all wavelengths, possibly limited by the instrument function of the measurements.

The spectral dependence of the enhancement of the emission rates observed in experiments and obtained from direct numerical solutions of the Maxwell equations have similar features of a broad spread of the lifetimes at all emission wavelengths and weak wavelength dependence

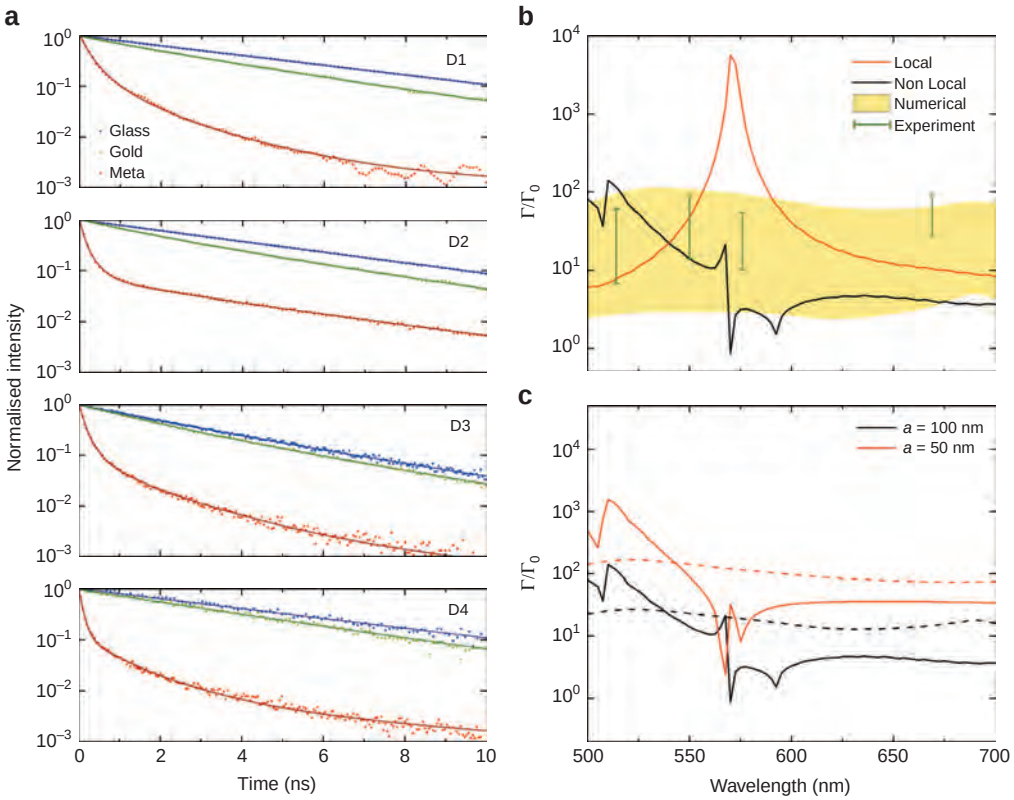

Figure 4 (**a**) Fluorescence dynamics of the emitters with the emission wavelength in different dispersion regimes of the metamaterial: (blue) on a glass surface, (green) on an Au film, (red) inside the metamaterial. The studied emitters are D1 (fluorescein), D2 (Alexa 514), D3 (ATTO 550) and D4 (ATTO 647N) with the emission wavelengths 514 nm, 550 nm, 575 nm and 670 nm, respectively. Solid lines present dynamics recovered by applying an inverse Laplace transform to the experimental data (dots). (**b**) Spectral dependence of the lifetime averaged over the dipole orientation: (red) local theory, (black) non-local theory, (bars) experimental data corresponding to the width of the lifetime distribution at 10% of the modal amplitude (Figure 5), (shaded area) the width of the simulated lifetime distribution at 10% of the modal amplitude obtained applying the inverse Laplace transform to the decay curves after the averaging over the dipole position within the elementary cell of the metamaterial (Supplementary Fig. S3a), (**c**) Spectral dependence of the rate enhancement obtained with the non-local theory (solid lines) and the full-wave numerical modeling at one position within the metamaterial (dashed lines, position 3 in Supplementary Fig. S3a): (black) the metamaterial as in b used in the experiments ($d = 50$ nm; $a = 100$ nm) and (red) the metamaterial with 50% unit cell ($d = 25$ nm; $a = 50$ nm) that yields an identical local effective medium response.

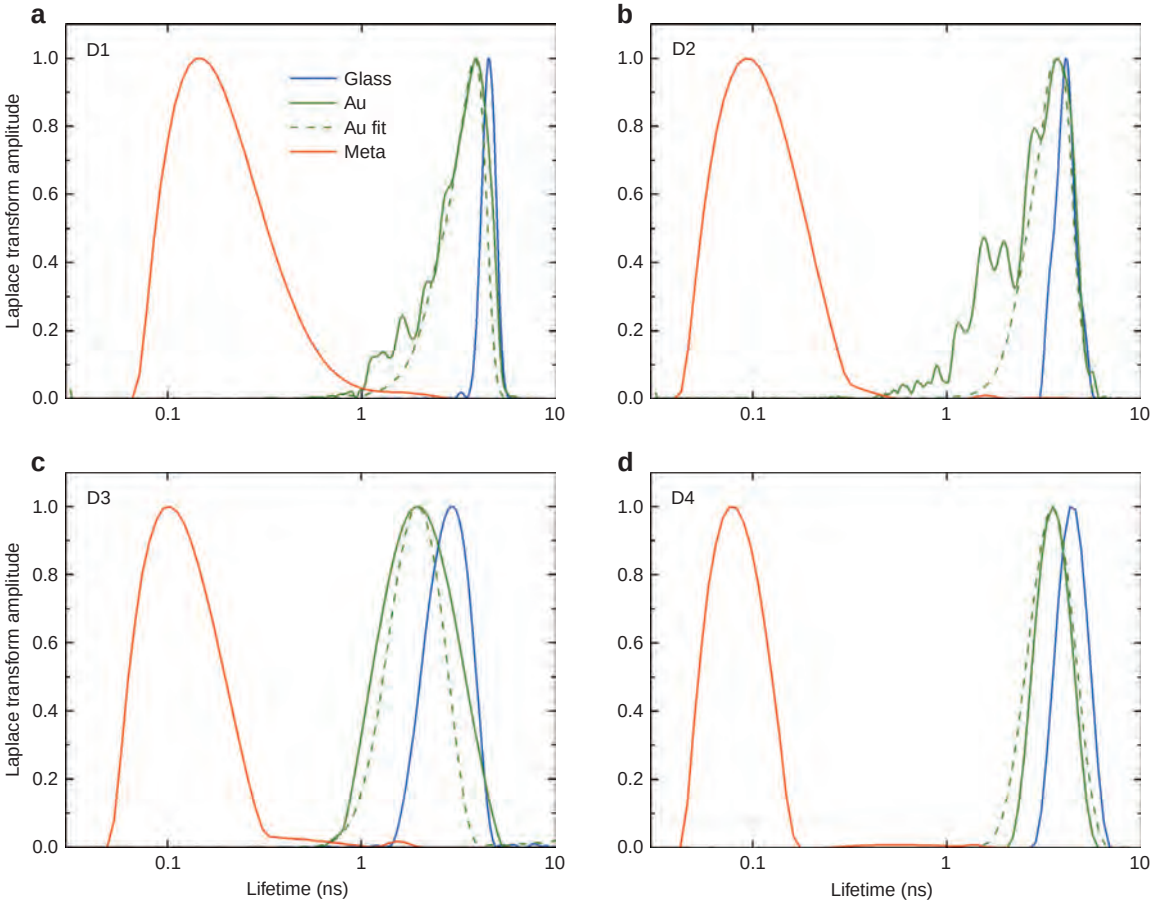

Figure 5 Experimental fluorescence lifetime (1/*s*) distribution of the emitters in different environments extracted using a Laplace transform method (Equation (1)) from the time-resolved PL measurements: (blue) glass substrate, (green) Au film, and (red) inside the metamaterial. Dashed green lines represent the lifetime distributions above the smooth Au surface recalculated from the measured lifetime distributions in the dielectric environment shown with blue lines. (**a**) D1: Fluorescein, (**b**) D2: Alexa 514, (**c**) D3: ATTO 550 and (**d**) D4: ATTO 647N.

of this distribution (Figure 4b). The experimental data show that the distribution of decay rate enhancements, from 10 to 100 (for the high and low-lifetime cut-offs, respectively, at 10% of the modal lifetime contribution), is almost independent of the wavelength across the elliptic, ENZ and hyperbolic regimes (Figure 4b). Local EMT predicts a strong enhancement of the decay rate in the ENZ regime, in sharp contrast with the observed behavior. At the same time, the experimental data are in closer agreement with predicted wavelength dependence of the decay rate given by non-local EMT. The remaining quantitative difference between the predictions of non-local effective medium theory (that averages the response of the composite) and experimental data stems from strong dependence of density of optical states on the position of the dipole within the unit cell[10]. Numerical modelling of a dipole emission inside the nanorod composites (Supplementary Fig. S3) confirms this position dependence and is also in agreement with the experimental data and the non-local theory. It should be noted that neither local nor non-local effective medium calculations allow discrimination of the emitter position in the unit cell of the array. Therefore, both EMTs provide an estimate of the average lifetime. Nevertheless, the transfer matrix-based mode-matching formalism allows additional averaging of the lifetime over emitter position along the nanorod length.

It is important to underline that both local and non-local effective medium theories predict almost identical transmission and reflection spectra of metamaterials (Supplementary Fig. S2), as the plane wave, incident from vacuum, only weakly couples to high-index additional waves inside the metamaterial. At the same time, point dipoles emitting from within the composite can successfully couple to these high-index modes, enabled by spatial dispersion. In fact, emission into additional waves dominates the decay dynamics while the metamaterial operates in the elliptical regime.

Engineering emission lifetime with metamaterial nonlocality

Adjusting the geometry and/or composition of a metamaterial opens the door for engineering quantum optical effects inside the composites. This is illustrated in Figure 4c where the lifetime dynamics in the composites studied above are compared with dynamics of emission in a similar metamaterial with nanorod diameter and unit cell dimension scaled by 50%. It is interesting to note that the reduction of the unit cell does not make the optical response of metamaterial appear more local; i.e., it does not lead to the enhancement of local density of states at ENZ and hyperbolic frequencies. Rather, 3D numerical simulations and non-local effective medium theory predict that the reduction of unit cell size yields a further, order of magnitude, broadband enhancement of decay rate (Figure 4c and Supplementary Fig. S3c and S3d), despite the local effective medium parameters of the metamaterial being the same.

doi:10.1038/lsa.2016.273

In order to check the stability of the non-local EMT approach to the lifetime modification estimations, we have varied the metamaterial geometrical parameters near the nominal parameters of the metamaterial used in the experiments (Supplementary Fig. S6). The obtained lifetime modifications are close to each other with similar spectral variations and all fall within the range of lifetimes predicted by the numerical simulations (Figure 4b).

Note that both non-local EMT and numerical solutions of Maxwell equations predict comparable enhancement of decay rate as a result of the unit cell reduction. As before, the quantitative difference between predictions of non-local EMT and numerical solutions reflects the limitation of an effective medium response, that nevertheless reveals the important physics and provides a relatively fast estimate of the radiation decay enhancement. Numerical solutions of Maxwell equations enable one to calculate the detailed optical response at any location at the expense of computational complexity and time.

Non-local homogenization theory for designs of large-scale hybrid optical sources

Understanding and predicting light–matter interactions can be drastically improved with the help of adequate homogenization theory. Local effective medium theories, under some conditions, provide an avenue to understand and design transmission and reflection of composite media. However, as shown above, a local EMT drastically fails when applied to calculations of a macroscopic Purcell effect. At the same time, a non-local EMT can be used to calculate Purcell enhancement in nanorod composites. From the fundamental science standpoint, non-local EMT provides a quantitative description light-mater interaction processes inside composite and identifies the dominant decay channels for the molecules, and can be used to engineer these channels. From the applications standpoint, non-local EMT allows one to avoid complex and extremely time- and memory-consuming numerical solutions of Maxwell equations for applications that rely on macroscopic number of fluorophores, distributed throughout the composite. In applications that require analysis of a position-dependent Purcell effect, numerical solutions of Maxwell equations cannot be avoided.

CONCLUSION

In summary, spontaneous radiation of an emitter inside nanorod-based metamaterials exhibiting non-local electromagnetic behavior was experimentally demonstrated and analyzed theoretically and numerically. It was shown that the effect of structural non-locality which results in the so-called additional electromagnetic modes in the metamaterial has significant impact on the density of photonic states inside the composite media and, as the result, quantum electrodynamic processes. The modal structure of a non-local composite material has a major impact on spontaneous decay dynamics, setting a fundamental limit on the overall emission rate enhancement and determines its spectral behavior. Careful consideration of structural non-locality allows the design of the density of optical states with geometrical parameters of the metamaterial composite beyond the limitations of the standard effective medium model, thus opening new opportunities for engineering and tailoring quantum optical processes inside metamaterials.

CONFLICT OF INTEREST

The authors declare no conflict of interest.

ACKNOWLEDGEMENTS

This work has been funded in part by ESPRC (UK), the ERC iPLASMM project (321268), and the US Army Research Office (Grant No. W911NF-12-1-0533). AZ acknowledges support from the Royal Society and the Wolfson Foundation. PG acknowledges TAU Rector Grant and German-Israeli Foundation (GIF, grant number 2399). The data access statement: all the data supporting this research are presented in full in the results section and the supplementary information.

1 de Broglie L. XXXV. A tentative theory of light quanta. *Philos Mag Lett* 2006; **86**: 411–423.
2 Einstein A, Podolsky B, Rosen N. Can quantum-mechanical description of physical reality be considered complete? *Phys Rev* 1935; **47**: 777–780.
3 Bell JS. On the problem of hidden variables in quantum mechanics. *Rev Mod Phys* 1966; **38**: 447–452.
4 Freedman SJ, Clauser JF. Experimental test of local hidden-variable theories. *Phys Rev Lett* 1972; **28**: 938–941.
5 Aspect A, Grangier P, Roger G. Experimental realization of einstein-podolsky-rosen-bohm *gedankenexperiment*: a new violation of Bell's inequalities. *Phys Rev Lett* 1982; **49**: 91–94.
6 Agranovich VM, Ginzburg VL. *Crystal Optics with Spatial Dispersion, and Excitons* 2nd edn. Pergamon Press: New York, USA, 1984.
7 Pollard RJ, Murphy A, Hendren WR, Evans PR, Atkinson R *et al.* Optical nonlocalities and additional waves in epsilon-near-zero metamaterials. *Phys Rev Lett* 2009; **102**: 127405.
8 Poddubny AN, Belov PA, Ginzburg P, Zayats AV, Kivshar YS. Microscopic model of Purcell enhancement in hyperbolic metamaterials. *Phys Rev B* 2012; **86**: 035148.
9 Lakowicz JR. *Principles of Fluorescence Spectroscopy* 3rd edn. Springer: USA, 2006.
10 Provencher SW. Inverse problems in polymer characterization: Direct analysis of polydispersity with photon correlation spectroscopy. *Die Makromol Chemie* 1979; **180**: 201–209.
11 Ford GW, Weber WH. Electromagnetic effects on a molecule at a metal surface. *Surf Sci* 1981; **109**: 451–481.
12 Vogel W, Welsch DG. *Quantum Optics* 3rd edn. Wiley-VCH: Weinheim, Germany, 2006.
13 Ginzburg P. Cavity quantum electrodynamics in application to plasmonics and metamaterials. *Rev Phys* 2016; **1**: 120–139.
14 Wangberg R, Elser J, Narimanov EE, Podolskiy VA. Nonmagnetic nanocomposites for optical and infrared negative-refractive-index media. *J Opt Soc Am B* 2006; **23**: 498–505.
15 Zhukovsky SV, Andryieuski A, Takayama O, Shkondin E, Malureanu R *et al.* Experimental demonstration of effective medium approximation breakdown in deeply subwavelength all-dielectric multilayers. *Phys Rev Lett* 2015; **115**: 177402.
16 Lissberger PH, Nelson RG. Optical properties of thin film Au-MgF_2 cermets. *Thin Solid Films* 1974; **21**: 159–172.
17 Wells BM, Zayats AV, Podolskiy VA. Nonlocal optics of plasmonic nanowire metamaterials. *Phys Rev B* 2014; **89**: 035111.
18 Novotny L, Hecht B. *Principles of Nano-Optics* 2nd edn. Cambridge University Press: Cambridge, UK, 2012.
19 Brueck SRJ. Radiation from a dipole embedded in a dielectric slab. *IEEE J Sel Top Quantum Electron* 2000; **6**: 899–910.
20 Podolskiy VA, Ginzburg P, Wells B, Zayats A. Light emission in nonlocal plasmonic metamaterials. *Faraday Discuss* 2015; **178**: 61–70.
21 Atre AC, Brenny BJM, Coenen T, García-Etxarri A, Polman A *et al.* Nanoscale optical tomography with cathodoluminescence spectroscopy. *Nat Nanotechnol* 2015; **10**: 429–436.
22 Krishnamoorthy HNS, Jacob Z, Narimanov E, Kretzschmar I, Menon VM. Topological transitions in metamaterials. *Science* 2012; **336**: 205–209.
23 Vasilantonakis N, Wurtz GA, Podolskiy VA, Zayats AV. Refractive index sensing with hyperbolic metamaterials: strategies for biosensing and nonlinearity enhancement. *Opt Express* 2015; **23**: 14329–14343.
24 Jacob Z, Smolyaninov II, Narimanov EE. Broadband Purcell effect: Radiative decay engineering with metamaterials. *Appl Phys Lett* 2012; **100**: 181105.
25 Purcell EM. Spontaneous emission probabilities at radio frequencies. *Phys Rev B* 1946; **69**: 674.
26 Tumkur TU, Kitur JK, Bonner CE, Poddubny AN, Narimanov EE *et al.* Control of Förster energy transfer in the vicinity of metallic surfaces and hyperbolic metamaterials. *Faraday Discuss* 2015; **178**: 395–412.
27 Tumkur T, Zhu G, Black P, Barnakov YA, Bonner CE *et al.* Control of spontaneous emission in a volume of functionalized hyperbolic metamaterial. *Appl Phys Lett* 2011; **99**: 151115.
28 Kruk SS, Wong ZJ, Pshenay-Severin E, O'Brien K, Neshev DN *et al.* Magnetic hyperbolic optical metamaterials. *Nat Commun* 2016; **7**: 11329.
29 Wurtz GA, Pollard R, Hendren W, Wiederrecht GP, Gosztola DJ *et al.* Designed ultrafast optical nonlinearity in a plasmonic nanorod metamaterial enhanced by nonlocality. *Nat Nanotechnol* 2011; **6**: 107–111.

30 Tsai KT, Wurtz GA, Chu JY, Cheng TY, Wang HH *et al*. Looking into meta-atoms of plasmonic nanowire metamaterial. *Nano Lett* 2014; **14**: 4971–4976.
31 Scully MO, Zubairy MS. *Quantum Optics*. Cambridge University Press: Cambridge, UK, 1997.
32 Bonifacio R, Lugiato LA. Cooperative radiation processes in two-level systems: Superfluorescence. *Phys Rev A* 1975; **11**: 1507–1521.
33 Martín-Cano D, Martín-Moreno L, García-Vidal FJ, Moreno E. Resonance energy transfer and superradiance mediated by plasmonic nanowaveguides. *Nano Lett* 2010; **10**: 3129–3134.
34 Slobozhanyuk AP, Ginzburg P, Powell DA, Iorsh I, Shalin AS *et al*. Purcell effect in hyperbolic metamaterial resonators. *Phys Rev B* 2015; **92**: 195127.

Supplementary Information for this article can be found on the *Light: Science & Applications*' website (http://www.nature.com/lsa).

ADVANCED OPTICAL MATERIALS
www.advopticalmat.de

Control of the Stokes Shift with Strong Coupling

*Ekembu K. Tanyi, Hannah Thuman, Nicolas Brown, Samantha Koutsares, Viktor A. Podolskiy, and Mikhail A. Noginov**

Strong coupling of excitons in macroscopic ensembles of quantum emitters and cavities (or surface plasmons) can lead to dramatic change of the optical properties and modification of the dispersion curves, characterized by the normal mode splitting of the order of 1 eV. Such gigantic alteration of the hybrid energy states enables scores of unparalleled physical phenomena and functionalities, ranging from enhancement of electrical conductivity to control of chemical reactions. While coupling of single emitters to a cavity is a pure quantum mechanical phenomenon, the origin of the strong coupling involving large ensembles of molecules is the subject of controversy. In this work, the strong coupling of rhodamine 6G dye molecules with silver Fabry–Perot cavities is studied and the significant increase of the Stokes shift between the excitation and the emission bands of hybridized molecules is demonstrated. The proposed empirical model of the underlying physics calls for the quantum mechanical parity selection rule.

1. Introduction

It is known that absorption and emission properties of molecules can be modified by inhomogeneous dielectric environments.[1–4] (Here we use the term molecules, in a broader sense, to refer to a variety of absorbing and emitting centers.) In the simplest case, the vicinity to a mirror can modify the spontaneous emission rate of a molecule;[1] however, it does not affect its energy eigenvalues. This is an example of a weak coupling of a molecule with its electromagnetic environment.

E. K. Tanyi, S. Koutsares, Prof. M. A. Noginov
Center for Materials Research
Norfolk State University
Norfolk, VA 23504, USA
E-mail: mnoginov@nsu.edu
H. Thuman, N. Brown
Summer Research Program
Center for Materials Research
Norfolk State University
Norfolk, VA 23504, USA
H. Thuman
Department of Materials Science and Engineering
Cornell University
Ithaca, NY 14853, USA
Prof. V. A. Podolskiy
Department of Physics
University of Massachusetts Lowell
Lowell, MA 01854, USA

DOI: 10.1002/adom.201600941

A stronger coupling can be achieved if a molecule is placed into a small resonant Fabry–Perot cavity or to a vicinity of a nanostructure supporting surface plasmon (SP) resonance. The time evolution of the two coupled oscillators, e.g., a cavity and a molecule, can be described as a linear superposition of their normal hybrid modes.[4] The even (odd) oscillation mode has the higher (lower) frequency, $\omega_{\pm} = \omega_0 \pm \Delta$, and corresponds to the upper (lower) branch of the dispersion curve. (Here Δ is the coupling frequency and the frequencies of uncoupled oscillators ω_0 are assumed to be the same.) If Δ exceeds all relaxation rates in the system, the dispersion curve features the avoided crossing and the well-resolved energy gap known as the normal mode splitting or the Rabi splitting[4,5] (**Figure 1**a,b). This criterion does not require the coupling to be large,[3,4] e.g., ≈5 meV,[6] as long as all relaxation processes of importance are sufficiently slow. This is often the case of single quantum emitters coupled to cavities.[7,8] We also propose in Figure 1c,d a model to explain this splitting behavior, which shall be discussed in detail shortly.

On the other hand, as the splitting energy 2Δ is getting comparable to ω_0, one enters the so-called ultrastrong coupling regime.[9] This is the case of large ensembles of dye molecules coupled to plasmonic nanostructures and resonant cavities, which routinely leads to the normal mode splitting (proportional to the square root of the molecular number density $\sqrt{N/V}$)[4] of the order of 1 eV.[10] Such a large change in the eigenvalues of the hybrid modes paves the way to unprecedented control of electrical conductivity,[11] excitation transport,[12] surface potential,[13] and rates of chemical reactions.[9]

Early research of the strong coupling was focused on quantum wells in resonant Bragg cavities.[5] In more recent years, this phenomenon has been studied at low and high (room) temperatures in multiple quantum and classical systems, including quantum dots,[7] single molecules,[8] and large molecular ensembles[14,15] interacting with localized and propagating SPs,[15,16] and cavities.[8,9,17]

In spite of large-scale theoretical and experimental efforts, some fundamental aspects of the strong coupling remain to be unexplored. One of them is the debated applicability of the quantum mechanical model to large ensembles of molecules, which may be possible if the latter act as one "giant atom,"[4] providing for coherent spontaneous emission,[18,19] and energy oscillations.[20] This fundamental question and the intriguing

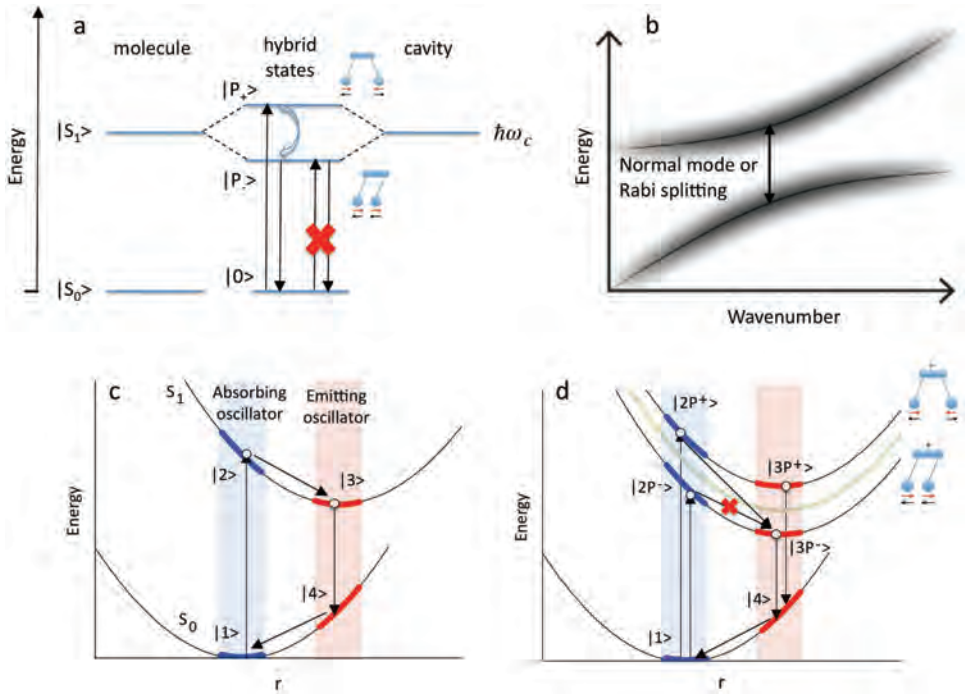

Figure 1. Spectroscopic model. a) Energy diagram of the strong coupling of a molecule with the cavity. $|S_0\rangle$ and $|S_1\rangle$ are the ground and the excited states of a molecule; $\hbar\omega_c$ is the resonance energy of a cavity; $|0\rangle$ is the ground state and $|P_+\rangle$ and $|P_-\rangle$ are the two (split) excited states of the strongly coupled system. The arrows show the allowed and forbidden absorption and emission transitions. b) Dispersion curve of a strongly coupled system, plotted in the {energy} versus {wavevector} coordinates, featuring the avoided crossing and the normal mode (or Rabi) splitting. The fuzziness of the traces indicates the spectral widths of the energy bands. Adopted and modified from ref. [2]. c) Energy diagram of a dye molecule depicting energy states $|S_0\rangle$ and $|S_1\rangle$ as parabolas and showing the interstate ($|1\rangle \rightarrow |2\rangle$ and $|3\rangle \rightarrow |4\rangle$) and the intrastate ($(|2\rangle \rightarrow |3\rangle$ and $|4\rangle \rightarrow |1\rangle)$) transitions. d) Energy diagram for a molecule in (c) coupled with the cavity. The molecular excited state $|S_1\rangle$ is transformed into two polariton states $|P_+\rangle$ and $|P_-\rangle$.

underlying physics of the strong coupling phenomenon motivated our current study.

2. Results

The experimental samples in our work were silver Fabry–Perot cavities filled with the poly(methyl methacrylate) (PMMA) polymer impregnated with the rhodamine 6G (R6G) dye (**Figure 2**a). The reflectance spectra of such cavities were collected using the setup in Figure 2b, while the emission and excitation spectra were collected using Figure 2c. The back mirror was highly reflective, while the front mirror was semi-transparent. The dye-doped polymer (deposited on glass) has the absorption maximum at ≈530 nm and the emission maximum at ≈570 nm (**Figure 3**a), with the tendency of a red shift and line broadening with the increase of the dye concentration (Figure 3b). As emission in strongly coupled systems was of primary interest to this research, the thickness of the R6G:PMMA film was chosen for the cavity to be resonant with the emission transition (Figure S1a, Supporting Information). The design, optimization, and fabrication of the dye-filled cavities are discussed in the Experimental Section.

The reflectance spectra $R(\lambda)$ of the cavities have been studied as the function of the incidence angle in p and s polarizations

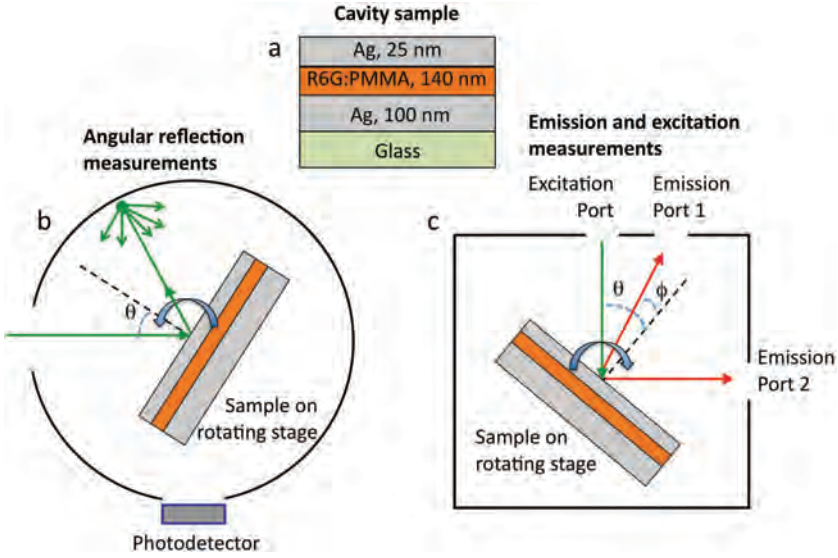

Figure 2. Experimental cavity samples and setups. Schematics of the a) cavity sample, b) angularly resolved reflectance measurement, and c) angularly resolved emission and excitation measurements. All angles are measured from the normal to the sample (dashed line).

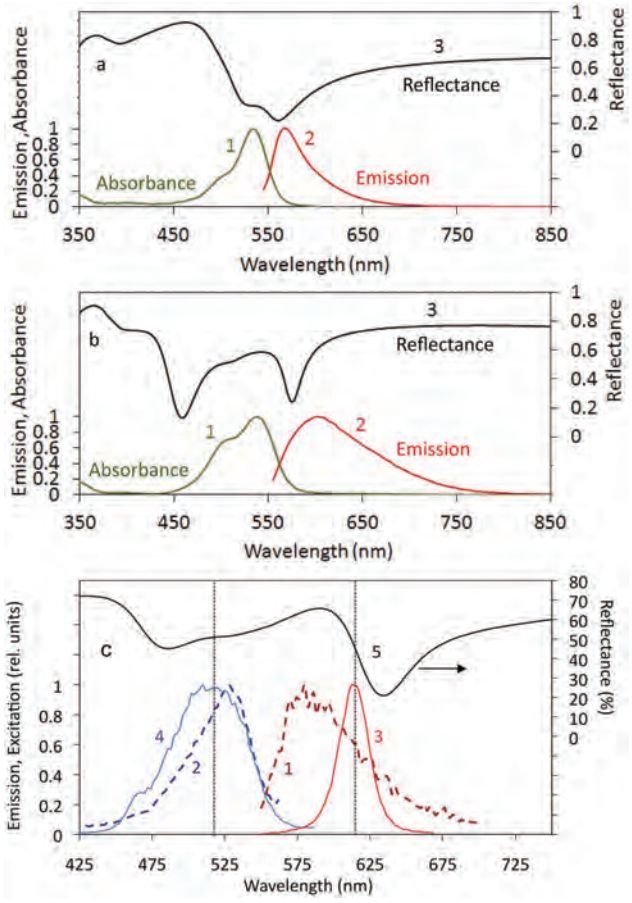

Figure 3. Spectroscopic properties of R6G:PMMA with and without cavity. a,b) Absorbance (1) and emission (2) of R6G:PMMA deposited on glass and reflection of the R6G:PMMA filled resonant cavity at nearly normal incidence (3); a) $n = 2.9 \times 10^{19}$ cm^{-3} and b) $n = 4.3 \times 10^{20}$ cm^{-3}. c) Emission spectrum (1) and excitation spectrum (2) of the R6G:PMMA film deposited on glass ($n = 5.2 \times 10^{20}$ cm^{-3}). Emission spectrum (3) and excitation spectrum (4) of the same R6G:PMMA film in the cavity. Reflection spectrum of the cavity at near normal incidence (5); (d = 140 nm, from comparison with the COMSOL modeling). All absorbance, emission and excitation spectra are normalized to unity.

(Figure 2b). At small dye concentration, $n \leq 1 \times 10^{19}$ cm^{-3} (in solid state), the reflectance spectrum has one pronounced dip, corresponding to the $\lambda/2$ cavity resonance (Figures SI1b and SI1c, Supporting Information). With increase of the dye concentration ($n \geq 3 \times 10^{19}$ cm^{-3}), the dip in the cavity's reflectance spectrum develops a shoulder (Figure 3a), and at $n \geq 1 \times 10^{20}$ cm^{-3} it splits into two, as expected in the strong coupling regime[4,5] (Figure 3b).

At $n = 5.2 \times 10^{20}$ cm^{-3} and small incidence angle (3°), the reflection spectrum had two minima, at $\lambda_1 = 638$ nm ($\omega_1 = 2.95 \times 10^{15}$ rad s^{-1}) and $\lambda_2 = 492$ nm ($\omega_2 = 3.83 \times 10^{15}$ rad s^{-1}) (**Figure 4**a). At inclined incidence, both reflection dips shifted to shorter wavelengths, in agreement with the theoretical predictions (see the Experimental Section) (Figure 4b). Figure 4 also depicts the angular dependencies of emission (Figure 4c) and excitation (Figure 4d). The positions of the minima plotted in the {frequency} versus {wavenumber} coordinates resulted in the dispersion curve featuring the lower and the upper polariton branches, which were slightly different in p and s polarizations (**Figure 5**). The energy (frequency) difference between the two branches, $2\Delta = \omega_2 - \omega_1$, which was close to its minimum at nearly normal incidence, was only four times smaller than the central frequency, $\omega_0 = (\omega_1 + \omega_2)/2$ ($2\Delta/\omega_0 \approx 0.26$). Therefore, at $n = 5.2 \times 10^{20}$ cm^{-3} the exciton-cavity interaction was nearing the ultrastrong coupling regime.

The emission and excitation spectra of the R6G:PMMA film on glass, $n = 5.2 \times 10^{20}$ cm^{-3}, are depicted in Figure 3c. In line with the literature,[21] they are asymmetrical and appear to be mirror images of each other. When the same highly doped R6G:PMMA film was placed inside the 140 nm cavity that was resonant with the R6G emission band: (i) the excitation and the emission spectral bands became more symmetrical (Figure 3c) and (ii) the excitation (emission) band shifted to the shorter (longer) wavelengths, thus increasing the molecule's Stokes shift. The latter finding is among the central results of this study. (Note that the excitation and the emission bands of the R6G dye in the cavity cannot be obtained by mere multiplication of the respective spectral bands of the dye on glass and the cavity's absorption, calculated as $(1 - R) \times 100\%$).

Emission spectra recorded at multiple orientations of the sample relative to the detector demonstrate blue shift with increase of the detection angle (Figure 4c). Although the emission was not intentionally polarized, the p polarized component was nearly ten times larger than the s polarized component (due to strongly different transmission of the vertically and horizontally polarized light by the monochromator). When the positions of the emission maxima were plotted on top of the dispersion curve in Figure 5, they formed the branch, which was reasonably close to that obtained from the reflection measurements. The difference between the dispersion curves measured in the emission and reflection experiments suggests (in line with ref. [22]) that excited and ground state molecules couple to the cavity differently.

The polarized emission spectra, recorded at the angle $\varphi = 63°$ (Figure 2c) had noticeable shift between p and s polarizations. The ordering of the corresponding emission maxima matched that of the p polarized and s polarized low polariton branches of the dispersion curves deduced from the reflectance measurements (Figure 5).

Surprisingly, with increase of the incidence angle θ (Figure 2c), the excitation spectrum shifted toward longer wavelength (Figure 4d), resulting in the negative slope of the corresponding dispersion curve (Figure 5). Therefore, with increase of the excitation and collection angles, the Stokes shift is getting smaller, becoming closer to that in R6G:PMMA deposited on glass.

3. Discussion

To explain the observed behavior, we follow the spectroscopic model of a dye molecule that is comprised of two parabolas, plotted in the {energy} versus {interatomic distance} coordinates, representing the ground state S_0 and the excited state S_1 (Figure 1c).[23] The parabolas are slightly shifted relative to each other, signifying different equilibrium interatomic distances r for S_0 and S_1. The absorption $|1\rangle \rightarrow |2\rangle$ and emission $|3\rangle \rightarrow |4\rangle$

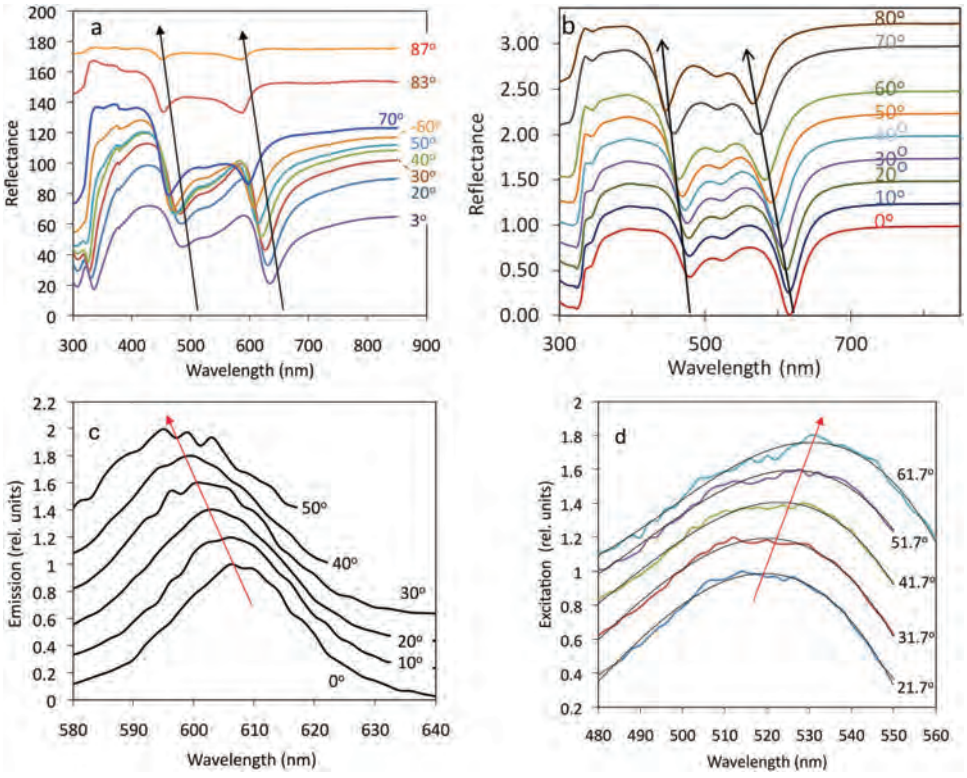

Figure 4. Angularly resolved spectra. a) Experimental p polarized reflectance spectra of the cavity ($d = 140$ nm, from comparisons with COMSOL modeling, $n = 5.2 \times 10^{20}$ cm^{-3}) measured at different incidence angles. The spectra are normalized to 100% in the maximum and shifted relative to each other for easier observation. b) Same spectra calculated with COMSOL. Qualitatively similar experimental and calculated spectra have been obtained for s polarization. c) Nominally unpolarized emission and d) excitation spectra of the same cavity measured at multiple collection and incidence angles.

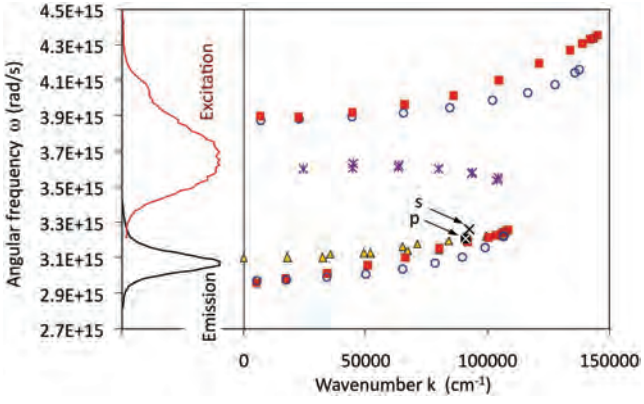

Figure 5. Dispersion curves. (Right) The dispersion curves for the upper and lower polaritonic branches in p polarization (open dark blue circuits) and s polarization (solid red squares) obtained by mapping the minima in the reflection spectra recorded at multiple incidence angles. Yellow triangles: the dispersion curve obtained by mapping the maxima in the emission spectra recorded at multiple orientation of the sample relative to the detector (nominally not polarized, with prevailing p polarization). Purple crosses (✳): the dispersion curve obtained by mapping maxima in the excitation spectra recorded at multiple incidence angles. Crosses ✕ and ✖: data obtained from the polarized emission spectra collected at $\varphi = 63°$. (Left) Normalized emission and excitation spectra of the R6G:PMMA film on glass ($n = 5.2 \times 10^{20}$ cm^{-3}).

transitions are so fast that they occur without change of r,[23–27] while the following energy relaxation to the bottom of each parabola is accompanied by the modification of r. This model is commonly used to illustrate the Stokes shift between the emission and the absorption and explain the quasi four-level laser action in a nominally two-level gain medium.[23–25]

To explain the increase of the Stokes shift in dye-doped cavities (as compared to that in uncoupled molecules on glass), we propose the heuristic model combining the two concepts illustrated in Figure 1a,c. We infer that when the molecule (Figure 1c) is strongly coupled with the cavity (Figure 1a), the excited state parabola splits into two hybrid polariton branches (Figure 1d). This gives rise to two absorption transitions, $|1\rangle \rightarrow |2P+\rangle$ and $|1\rangle \rightarrow |2P-\rangle$, and two emission transitions, $|3P+\rangle \rightarrow |4\rangle$ and $|3P-\rangle \rightarrow |4\rangle$. Assuming that the energy separation between the hybrid states $|P+\rangle$ and $|P-\rangle$ is not too large, depopulation of the state $|3P+\rangle$ is dominated by the nonradiative decay $|3P+\rangle \rightarrow |3P-\rangle$, and the quantum yield of the $|3P+\rangle \rightarrow |4\rangle$ emission is small.[21,28] Therefore, only one emission transition, $|3P-\rangle \rightarrow |4\rangle$ (Figure 1d), which is red shifted in comparison with the $|3\rangle \rightarrow |4\rangle$ transition in uncoupled molecules (Figure 1c), remains possible.

When excitation of the state $|2P+\rangle$ (at the transition $|1\rangle \rightarrow |2P+\rangle$) is followed by the intracentral relaxation $|2P+\rangle \rightarrow |3P-\rangle$, the state $|3P-\rangle$ becomes populated and the $|3P-\rangle \rightarrow |4\rangle$

emission can be observed. Since the polariton branches $|P+\rangle$ and $|P-\rangle$ have different parity, the transition $|2P+\rangle \rightarrow |3P-\rangle$ is parity allowed. On the other hand, when the hybrid state $|2P-\rangle$ is excited (at the transition $|1\rangle \rightarrow |2P-\rangle$), the intracentral relaxation $|2P-\rangle \rightarrow |3P-\rangle$ is parity forbidden, the state $|3P-\rangle$ is not populated, and no luminescence originating from this state is expected. Correspondingly, the only transition, $|1\rangle \rightarrow |2P+\rangle$, observed in the excitation spectrum of luminescence is blue shifted in comparison with that in uncoupled molecules $|1\rangle \rightarrow |2\rangle$, compare Figure 1c,d. (Note that the transition $|2P+\rangle \rightarrow |3P+\rangle$ is also parity forbidden. This is another reason why no emission originating from the state $|3P+\rangle$ is predicted.)

The proposed heuristic model qualitatively explains why the Stokes shift in resonant cavities filled with R6G:PMMA is larger than that in the same dye-doped films deposited on glass. It may also explain the seemingly paradoxical result of ref. [29]—that in resonant cavities strongly coupled with dye molecules, the emission originating from the low polariton state $|P-\rangle$ can be observed at optical excitation of the upper polariton state $|P+\rangle$ (at the transition $|0\rangle \rightarrow |P+\rangle$) but not at direct pumping of the low polariton state $|P-\rangle$ (at the transition $|0\rangle \rightarrow |P-\rangle$) (Figure 1a).

Exploring the proposed model even further, we infer that while the cavity is resonant with the emission band in the normal direction (see the Experimental Section), it loses the resonance (and, thus, the strong coupling-related phenomena) for the emission propagating (or excited) in an inclined direction. Therefore, with increase of the emission collection (or excitation) angle, the Stokes shift between the emission and the excitation bands is expected to decrease, returning to its value in uncoupled dye molecules on glass. Correspondingly, the emission (excitation) band is predicted to shift to shorter (longer) wavelengths—the behavior observed in our experiment.

Lastly, although the detailed analysis of the spectral lineshapes is beyond the scope of this paper, one can infer that some ensembles of dye molecules, contributing to the inhomogeneously broadened emission and excitation bands, are coupled to the cavity better than others. This may explain reshaping of the excitation and emission spectra in the cavity, which became more symmetrical (Figure 3b), and narrowing of the emission band, which was better coupled to the cavity (closer to the cavity resonance) than the excitation band.

4. Summary

To summarize, we have demonstrated strong coupling of excitons in the dye-doped polymer (R6G:PMMA) and silver Fabry–Perot cavities, which were made to be resonant with the dye's emission band. At dye concentration $n \geq 3 \times 10^{19}$ cm^{-3}, the samples' reflection spectra featured two dips, whose spectral positions depended on n as well as the reflection angle and the polarization. At $n = 5.2 \times 10^{20}$ cm^{-3}, the positions of the reflectance dips, plotted in the {frequency} versus {wavenumber} coordinates, resulted in the dispersion curve comprised two polariton branches, whose splitting, 0.57 eV, was 26% of the central energy, 2.23 eV, suggesting that the system neared the ultrastrong coupling regime. The experimental reflectance spectra were in a good agreement with the classical electrodynamics model (see the Experimental Section).

The behavior of emission was even more exciting. Thus, in the cavity strongly coupled with dye molecules, the emission and the excitation bands changed their shapes and became more symmetrical. Furthermore, in the cavity, the dye's emission (excitation) band experienced the red (blue) shift, increasing the Stokes shift in the strongly coupled system. When the emission was excited and/or collected in inclined directions, the emission band experienced the blue shift, closely following the low polariton branch obtained in the reflectance experiment. At the same time, the excitation band experienced the red shift, moving toward its position in uncoupled molecules on glass. This led to the negative slope of the excitation dispersion curve and the reduction of the Stokes shift. This intriguing behavior of the emission and the excitation bands as well as the Stokes shift are explained in terms of the phenomenological spectroscopic model taking into account (i) hybridization and splitting of the excited state parabolas, (ii) odd and even parity of the wave functions corresponding to the low and high polariton branches, and (iii) parity forbidden transitions within the same polariton branch.

5. Experimental Section

Cavity Design: Modeling and Calculations—Material Parameters: PMMA was assumed to have the index of refraction $n = 1.5$[30] throughout the spectral range of interest (300–1000 nm), while the spectrum of the complex dielectric permittivity of Ag was adopted from literature.[31] The absorption spectrum of the Rhodamine 6G dye has the maximum at $\lambda \approx 530$ nm and the shoulder at $\lambda \approx 490$ nm; the latter is particularly pronounced at high dye concentration (Figure 3b). Therefore, the spectrum of dielectric permittivity of the dye-doped polymer was modeled as a sum of two Lorentz oscillators[32] embedded in the PMMA host matrix.[33] The strengths, the spectral positions and the line-widths of the Lorentzian spectral bands were used as fitting parameters to match the experimentally measured absorption spectrum.

Resonance Frequency of the Cavity without Dye: Since coupling of excitons and a cavity is strongest when the two resonance frequencies match, the authors first calculated the dependence of the resonant frequency on the size of the cavity filled with undoped PMMA. The cavity consisted of the 100 nm silver film deposited on glass (nearly 100% reflective back mirror), PMMA films of varied thickness, and 25 nm silver film on the top (semi-transparent mirror) (Figure 2a). The solutions of the Maxwell equations were performed with the transfer matrix based calculator[34] for the normal incidence of light. The dependence of the resonance wavelength on the cavity size d is depicted in Figure SI1a in the Supporting Information, while Figures SI1b and SI1c in the Supporting Information show the field distribution within cavity. The $d = 122$ nm cavity was predicted to be in resonance with the R6G absorption band ($\lambda = 530$ nm), while $d = 138$ nm approximately corresponds to the emission band ($\lambda = 580$ nm), which is of primary interest to this study.

Numerical Solutions of Maxwell Equations: Maxwell equations were solved with commercial finite-element-method (FEM) solver, COMSOL Multiphysics. Schematic geometry of the Fabry–Perot cavities in the model was identical to the one described in Figure 2a. To mimic plane wave excitation of the sample, periodic boundary conditions were used on the left and right boundaries, while plane-wave ports were used for horizontal boundaries. To minimize possible near-field artifacts, excitation port was positioned 1 μm away from the dielectric layer. The reflectance spectra were calculated for both p and s polarizations and multiple angles of incidence.

The authors first calculated the series of normal incidence reflectance spectra for the cavities of different size d (Figure SI2a, Supporting Information). Dye concentration in the model corresponded to $n = 5.2 \times 10^{20}$ cm^{-3}. Besides the two expected dips corresponding to the upper and the lower hybrid states, the calculated spectra featured the relatively minor middle dip, which was due to the fact that the absorption spectrum of R6G:PMMA consisted of two partly overlapping bands. (Similar middle dips, although of smaller scale, have been observed in the experimental reflectance spectra, Figure 4a.) The positions of the dips in the reflectance spectra, plotted in the {frequency} versus {inverse cavity size} coordinates, resulted in the three branches of the dispersion curve depicted in Figure SI2b in the Supporting Information. The upper and the lower polariton branches had the minimal energy splitting, corresponding to the strongest coupling between the cavity and the dye-doped polymer, at $d \approx 120$ nm (Figure SI2c, Supporting Information). The same optimal size was predicted (above) to provide for the resonance of the PMMA-filled cavity at the frequency of the R6G absorption band (Figure SI1a, Supporting Information).

Similar FEM model was used to calculate the spectra of reflectance at multiple incidence angles (Figure 4b) and compare the result with the experimental data (Figure 4a). The best agreement between the theory and the experiment was observed at $d = 140$ nm—the targeted cavity size supporting the resonance at the frequency of the R6G emission band. The corresponding calculated and experimental dispersion curves are depicted in Figures SI3a and SI3b in the Supporting Information.

Fabrication: The design and the targeted dimensions of the Fabry–Perot cavities are depicted in Figure 2a. Silver films were fabricated using the thermal vapor deposition technique (Edwards 306 Evaporator).

To prepare R6G:PMMA films with the desired concentration of the R6G dye, the authors first dissolved m_{R6G} g of rhodamine 6G chloride (R6G, $M_{R6G} = 464.98$ g mol^{-1})[35] in dichloromenthane (DCM) and then dissolved in the same solution m_{PMMA} g of poly(methyl methacrylate) (PMMA, m.w. = 120 000 a.u.). The dissolution was done in an ultrasonic bath at room temperature, ≈5 min for R6G and ≈15 min for PMMA. The viscosity of the solution was regulated by the amount of the solvent.

Knowing the density of R6G, $\rho_{R6G} = 1.26$ g cm^{-3},[36] and PMMA, $\rho_{PMMA} = 1.18$ g cm^{-3},[30] the authors evaluated, in the first approximation, the concentration of R6G molecules in the solid R6G:PMMA compound (without solvent) as $n[\text{cm}^{-3}] = \frac{m_{R6G}}{M_{R6G}} N_A \left(\frac{m_{R6G}}{\rho_{R6G}} + \frac{m_{PMMA}}{\rho_{PMMA}}\right)^{-1}$, where N_A is the Avogadro number. The corresponding molar concentration is $c[\text{mol L}^{-1}] = 1000 n N_A^{-1}$ and the mass of R6G per liter (cubic decimeter) of the solid compound is $\eta[\text{g L}^{-1}] = 1000 M_{R6G} n N_A^{-1}$.

In formulation of the highly doped R6G:PMMA polymer used in the majority of the experiments, $m_{R6G} \approx 0.03$ g of R6G and $m_{PMMA} \approx 0.06$ g of PMMA were dissolved in ≈10 mL of DCM, resulting in $n = 5.2 \times 10^{20}$ cm^{-3} ($c = 0.86$ mol L^{-1} and $\eta = 4.2 \times 10^2$ g L^{-1}).

The prepared solutions were spin coated onto silver films (using the Model 6800 and the Spincoat G3P-8 spin coaters from Specialty Coating Systems) employing the optimized three-step recipe.

To determine the thickness of the deposited silver and polymeric layers, the films were scratched in several locations, after which the thickness was measured using the DekTak XT profilometer (from Bruker). The results were averaged over several tests. In the calibration measurements performed on metallic and polymeric test samples, the film thickness measured with the profilometer was compared with that measured with scanning electron microscope (SEM) on the focused ion beam (FIB)-cut cross-section of the multilayered stack. The good agreement between the results of the two measurements (Ag: 44 nm measured with the profilometer and 45 nm measured with SEM; polymer: 69 nm measured with the profilometer and 75 nm measured with SEM) guaranteed high accuracy of the thickness measurements.

Spectroscopic Measurements: The reflectance spectra of the cavity samples were studied as the function of the incidence angle in p and s polarizations in the spectrophotometer setup equipped with the 150 mm integrating sphere (Lambda 900 from PerkinElmer) (Figure 2b).

The emission and excitation spectra have been studied in the spectrofluorimeter setup (Fluorolog 3 from Horiba Jobin Yvon). The sample chamber had one excitation (pumping) port and two emission (collection) ports (Figure 2c). By rotating the sample and switching between two emission ports, one could span a broad range of excitation, θ, and emission, φ, angles. In the majority of measurements, the emission was not intentionally polarized. However, the signal in the horizontal p polarization was nearly an order of magnitude larger than that in the vertical s polarization (due to strongly different transmission of the vertically and horizontally polarized light by the monochromator).

Note that three nominally identical cavity samples with the dye concentration $n = 5.2 \times 10^{20}$ cm^{-3} have been fabricated and studied experimentally. While the optical properties of one representative sample are reported below, those of the other two samples were nearly the same.

Supporting Information

Supporting Information is available from the Wiley Online Library or from the author.

Acknowledgements

This work was supported by the NSF PREM grant DMR 1205457, NSF IGERT grant DGE 0966188, NSF RISE grant F1040058, AFOSR grant FA9550-14-1-0221, ARO grant W911NF-14-1-0639, and ARO grant W911NF-16-1-0261.

Received: November 12, 2016
Revised: February 3, 2017
Published online: March 29, 2017

[1] K. H. Drexhage, *Prog. Opt.* **1974**, *12*, 163.
[2] Z. Jacob, I. I. Smolyaninov, E. E. Narimanov, *Appl. Phys. Lett.* **2012**, *100*, 181105.
[3] M. A. Noginov, H. Li, Y. A. Barnakov, D. Dryden, G. Nataraj, G. Zhu, C. E. Bonner, M. Mayy, Z. Jacob, E. E. Narimanov, *Opt. Lett.* **2010**, *35*, 1863.
[4] P. Törmä, W. L. Barnes, *Rep. Prog. Phys.* **2015**, *78*, 013901.
[5] G. Khitrova, H. M. Gibbs, M. Kira, S. W. Koch, A. Scherrer, *Nat. Phys.* **2006**, *2*, 81.
[6] F. Jahnke, M. Kira, S. W. Koch, G. Khitrova, E. K. Lindmark, T. R. Nelson Jr., D. V. Wick, J. D. Berger, O. Lynges, H. M. Gibbs, K. Tai, *Phys. Rev. Lett.* **1996**, *77*, 5257.
[7] T. Yoshie, A. Scherer, J. Hendrickson, G. Khitrova, H. M. Gibbs, G. Rupper, C. Ell, O. B. Shchekin, D. G. Deppe, *Nature* **2004**, *432*, 200.
[8] R. Chikkaraddy, B. de Nijs, B. Benz, S. J. Barrow, O. A. Scherman, E. Rosta, A. Demetriadou, P. Fox, O. Hess, J. J. Baumberg, *Nature* **2016**, *535*, 127.
[9] J. A. Hutchison, T. Schwartz, C. Genet, E. Devaux, T. W. Ebbesen, *Angew. Chem., Int. Ed.* **2012**, *51*, 1592; *Angew. Chem.* **2012**, *124*, 1624.
[10] T. Schwartz, J. A. Hutchison, C. Genet, T. W. Ebbesen, *Phys. Rev. Lett.* **2011**, *106*, 196405.
[11] E. Orgiu, J. George, J. A. Hutchison, E. Devaux, J. F. Dayen, B. Doudin, F. Stellacci, C. Genet, J. Schachenmayer, C. Genes, G. Pupillo, P. Samorì, T. W. Ebbesen, *Nat. Mater.* **2015**, *14*, 1123.
[12] J. Feist, F. J. Garcia-Vidal, *Phys. Rev. Lett.* **2015**, *114*, 196402.
[13] J. A. Hutchison, A. Liscio, T. Schwartz, A. Canaguier-Durand, C. Genet, V. Palermo, P. Samori, T. W. Ebbesen, *Adv. Mater.* **2013**, *25*, 2481.
[14] I. Pockrand, A. Brillante, D. Möbius, *J. Chem. Phys.* **1982**, *77*, 6289.

[15] J. Bellessa, C. Bonnand, J. C. Plenet, J. Mugnier, *Phys. Rev. Lett.* **2004**, *93*, 036404.
[16] N. T. Fofang, T.-H. Park, O. Neumann, N. A. Mirin, P. Nordlander, N. J. Halas, *Nano Lett.* **2008**, *8*, 3481.
[17] D. G. Lidzey, D. D. C. Bradley, M. S. Skolnick, T. Virgili, S. Walker, D. M. Whittaker, *Nature* **1998**, *395*, 53.
[18] S. A. Guebrou, C. Symonds, E. Homeyer, J. C. Plenet, Yu. N. Gartstein, V. M. Agranovich, J. Bellessa, *Phys. Rev. Lett.* **2012**, *108*, 066401.
[19] L. Shi, T. K. Hakala, H. T. Rekola, J. P. Martikainen, R. J. Moerland, P. Törmä, *Phys. Rev. Lett.* **2014**, *112*, 153002.
[20] P. Vasa, W. Wang, R. Pomraenke, M. Lammers, M. Maiuri, C. Manzoni, G. Cerullo, C. Lienau, *Nat. Photonics* **2013**, *7*, 128.
[21] P. Venkateswarlu, M. C. George, Y. V. Rao, H. Jagannath, G. Chakrapani, A. Miahnahri, *J. Phys.* **1987**, *28*, 59.
[22] T. U. Tumkur, G. Zhu, M. A. Noginov, *Opt. Express* **2016**, *24*, 3921.
[23] S. Forget, S. Chénais, *Organic Solid-State Lasers, Springer Series in Optical Sciences*, Vol. *175*, Springer-Verlag, Berlin, Germany **2013**, p. 30.
[24] R. C. Powell, *Physics of Solid-State Laser Materials (Atomic, Molecular, and Optical Physics Series)*, Vol. 1, AIP Press, New York **1998**, p. 107.
[25] O. Svelto, *Principles of Lasers*, 5th ed., Springer, New York **2010**, pp. 390–394.
[26] J. Franck, *Trans. Faraday Soc.* **1926**, *21*, 536.
[27] E. Condon, *Phys. Rev.* **1928**, *32*, 858.
[28] J. George, S. Wang, T. Chervy, A. Canaguier-Durand, G. Schaeffer, J-M. Lehn, J. A. Hutchison, C. Geneta, T. W. Ebbesen, *Faraday Discuss.* **2015**, *178*, 281.
[29] Note that many dyes, including R6G, have multiple excited states (above the lowest excited singlet state S_1), which can be pumped optically. However, "regardless of the state to which they are originally excited, the dye molecules relax through fast nonradiative transitions to the lowest excited singlet state S_1, where the thermalization is established in a time much shorter than the radiative lifetime of that state."
[30] J. E. Mark, *Physical Properties of Polymers Handbook*, 2nd ed., Springer, NY **2007**, p. 825.
[31] P. B. Johnson, R. W. Christy, *Phys. Rev. B* **1972**, *6*, 4370.
[32] R. W. Boyd, *Nonlinear Optics*, 3rd ed.,Elsevier, Oxford **2008**, p. 439.
[33] M. Szczurowski, Database with refractive index of various organic polymers, http://refractiveindex.info/?shelf=organic&book=poly%28methyl_methacrylate%29&page=Szczurowski (accessed March 2017).
[34] S. Ishii, U. K. Chettiar, X. Ni, A. V. Kildishev, *PhotonicsRT: Wave Propagation in Multilayer Structures*, NICT & Purdue University, www.nanohub.org (accessed March 2017).
[35] Exciton's product sheet for Rhodamine 6G 590, http://exciton.com/pdfs/RH590.pdf (accessed March 2017).
[36] Density of Rhodamine 6G ($C_{27}H_{29}ClN_2O_3$), http://www.chemnet.com/cas/en/113162-02-0/O-(4-chlorobenzoyl)hydroquinidine.html (accessed March 2017).

Geometry Defines Ultrafast Hot-Carrier Dynamics and Kerr Nonlinearity in Plasmonic Metamaterial Waveguides and Cavities

Silvia Peruch, Andres Neira, Gregory A. Wurtz, Brian Wells, Viktor A. Podolskiy, and Anatoly V. Zayats*

Hot carrier dynamics in plasmonic nanorod metamaterials and its influence on the metamaterial's optical Kerr nonlinearity is studied. The electron temperature distribution induced by an optical pump in the metallic component of the plasmonic metamaterial leads to geometry-dependent variations of the optical response and its dynamics as observed in both the transmission and reflection properties of the metamaterial slab. Thus, the ultrafast dynamics of a metamaterial's optical response can be controlled via modal engineering. Both the transient response relaxation time and magnitude of the nonlinearity are shown to depend on the modal-induced spatial profile of the electron temperature distribution and the hot-electron diffusion in nanorods. The nonlocal effects, depending on the excitation-induced losses in the metal, are shown to dictate the modal structure of the metamaterial slab and the associated dynamics of its nonlinear response. The opportunity of controlling the electron temperature profile induced in the plasmonic nanorods by changing the metamaterial's geometry and/or excitation conditions paves the way to achieve controllable dynamics of the nonlinear optical response for free-space as well as integrated nanophotonic applications involving nonequilibrium electrons.

1. Introduction

The dynamics of excited, nonequilibrium carriers in plasmonic materials determines many interesting and important phenomena, such as hot-electron-induced photochemical transformations and catalysis, nanoscale photodetectors, as well as nonlinear optical response of plasmonic nanostructures and its temporal dynamics.[1] Illumination of a material containing free electrons results in a redistribution of the electrons between allowed energy states within the conduction band either due to interband transitions and/or intraband transitions facilitated by phonons or surface plasmons, depending on the illumination wavelength. The excitation by a short light pulse, generally results in the nonthermalized distribution of free electrons in the conduction band (or holes in the valence bands, depending on the excitation wavelength and band structure of the material). Relatively fast electron–electron and electron-phonon scattering processes establish the thermalized electron distribution described by the increased temperature, before the residual electron energy is transferred to lattice.

A reliable way to probe the electron distribution modifications and its dynamics is based on optical pump–probe spectroscopy, allowing to trace in time nonlinear optical modifications of the permittivity of the material induced by the absorption of a strong short pulse with a weak probe light. The excitation of nonequlibrium electrons results in the modifications of the permittivity of plasmonic metals, which leads to nonlinear changes of absorption and scattering of plasmonic nanoparticles. When such nanoparticles are assembled in metamaterials—composite nanostructured media that exhibit effective optical properties at the macroscopic level—controlling the interaction between the metamaterial's constituents affects both linear optical properties and nonlinear response as well as its dynamics associated with the excitation and relaxation of the electron gas.[2]

Plasmonic metamaterials can be understood considering "meta-atoms" capable of supporting coherent electron gas excitations with high light–matter interaction strength. They are widely used for engineering refraction and reflection properties, as bio and chemical sensing components as well as for actively controlling light.[3] The strong field enhancement provided by plasmonic modes facilitates nonlinear light–matter interactions at relatively low light intensities, including the optical Kerr effect which leads to light-induced nonlinear changes in

Dr. S. Peruch, Dr. A. Neira, Dr. G. A. Wurtz, Prof. A. V. Zayats
Department of Physics
King's College London
Strand, London WC2R 2LS, UK
E-mail: silvia.peruch87@gmail.com
Dr. G. A. Wurtz
Department of Physics
University of North Florida
Jacksonville, FL 32224, USA
Dr. B. Wells, Prof. V. A. Podolskiy
Department of Physics and Applied Physics
University of Massachusetts Lowell
One University Ave
Lowell, MA 01854, USA

DOI: 10.1002/adom.201700299

the effective refractive index, so that the optical response of plasmonic metamaterial can be dynamically modified by control light illumination, achieving modulation and switching of signal light.[4,5]

Two-photon absorption was identified as the mechanism driving the nonlinear response of a gold film patterned with split-ring resonators. This metamaterial has been reported to achieve a modulation of up to 40% with a fluence of the optical control pulse of 270 μJ cm^{-2} when both the signal and control wavelengths are around the plasmonic resonance of the metamaterial.[6] Au thin films nanostructured with gratings can provide ultrafast modulation of surface plasmon polariton (SPP) excitation using interband electron transitions.[7] Nonlinear effects in ultrathin long-range plasmonic waveguides have been demonstrated in the spectral range of intraband absorption.[8] Due to its inherent nature related to the hot-electron distribution within a nanosctructured conductor in both geometrical space and within the conduction band, the dynamics of free-electron nonlinearity depends on the excitation pulse duration as well as on the geometry of the nanostructured system. In a simple smooth-film geometry, these dependences can be described via the nonlinear Schrodinger equation,[8] and thus inherently depend on the absorption of the system.

The optical properties of plasmonic metamaterials with hyperbolic dispersion are strongly sensitive to the changes of the refractive index of their constituents, thus providing an excellent platform for studies of Kerr-type nonlinear functionalities and their dynamics.[2,3c,9] Hyperbolic dispersion is the signature of anisotropic metamaterials in the spectral range where the components of the effective permittivity tensor have opposite signs. In this frequency range, the metamaterial supports bulk plasmon polaritons with large wavevectors.[10] If all the components of the permittivity tensor are positive, conventional elliptic isofrequency surfaces are observed when nonlocal spatial dispersion effects can be neglected.[11] The transition from elliptic to hyperbolic dispersion takes place through the so-called epsilon-near-zero (ENZ) regime when the real part of one of the permittivity tensor components vanishes. The ENZ regime occurs in the spectral range near the effective plasma frequency of the metamaterial and depends on both dimensional parameters and material composition of the metamaterial.[10,12] Strong and ultrafast nonlinear response of a gold nanorod-based hyperbolic metamaterial under interband femtosecond excitation has been achieved, recording a change in the metamaterial's transmission of up to 80% with a subpicosecond recovery time.[2] Such an enhanced nonlinearity was identified as originating from nonlocal (spatial dispersion) effects associated with the free-electron dynamics related to cylindrical surface plasmons.[13,14]

In this paper, we numerically analyze the hot-electron-induced nonlinear optical dynamics of plasmonic nanorods forming a metamaterial by following its Kerr-type nonlinear ultrafast response under interband and intraband excitations. We demonstrate how the modal properties of these metamaterials, including waveguided and cavities modes, can influence the nonlinear behavior of the medium as well as its temporal response in different dispersion regimes, despite being governed by the same electron scattering processes in gold. In particular, we characterize the interplay between the spatial distribution of the mode excited by the control light field, the associated microscopic electron temperature profile in the nanorods, and the nonlinear optical dynamics of the metamaterial as probed in transmission and reflection measurements. The methodology and results of the present study are also relevant to the design of hybrid photonic devices, for example based on two-dimensional materials, such as, e.g., graphene and MoS_2, combined with plasmonic films or nanostructures to increase light-matter interaction strength.[15] The spatially resolved, ultrafast response of the plasmonic metamaterial described here can be used to engineer ultrafast, strong optical modulation and optimize light harvesting when coupled with such monoatomic layers. The possibility of spatially shaping the electron temperature profile by controlling the metamaterial's geometry at the nanoscale opens up an additional degree of freedom for designing the strength and dynamics of the nonlinear response of integrated photonic components and nanodevices but also has implications for hot-electron extraction and applications in photochemistry and optoelectronics.

2. Numerical Models

2.1. Metamaterial Geometry

We consider a plasmonic metamaterial geometry consisting of an assembly of gold nanorods embedded in a porous alumina (AAO) matrix and supported by a transparent substrate (**Figure 1**a). The nanorods, vertically aligned in the z-direction in the Cartesian frame of Figure 1a, form a uniaxial metamaterial that can be represented within the effective medium theory (EMT) by a diagonal permittivity tensor of the form $\varepsilon = \mathrm{diag}[\varepsilon_x, \varepsilon_y = \varepsilon_x, \varepsilon_z]$, where the spectral dependence is implicit and the z-direction is along the optical axis of the metamaterial. Expressions for the components of the permittivity tensor can be obtained via the Maxwell-Garnet effective medium approximation as $\varepsilon_{x,y} = \varepsilon_h \frac{(1+p)\varepsilon_{Au} + (1-p)\varepsilon_h}{(1-p)\varepsilon_{Au} + (1+p)\varepsilon_h}$ and $\varepsilon_z = p\varepsilon_{Au} + (1-p)\varepsilon_h$, where $p = \pi(r/d)^2$ is the nanorod concentration, with r and d being the nanorod radius and the average separation between nanorods respectively, ε_{Au} and ε_h are the permittivities of Au and the host medium (anodized aluminium oxide, AAO), respectively.[16] This model is valid, in general, away from the Brillouin zone edges of the nanorod array of period d, but fails to accurately reproduce the optical response of the metamaterial when losses are "small," in which case the nonlocal corrections to the effective medium theories need to be considered.[11,13]

The spectral dependence of the effective permittivity components of the studied metamaterial is shown in Figure 1b,c for a metamaterial with a nanorod radius of $r = 15$ nm and an average interrod distance of $d = 90$ nm. Here, the permittivity of Au was modeled as $\varepsilon_{gold} = \varepsilon_{intra} + \varepsilon_{inter}$, where ε_{intra} is a Drude contribution, describing the response from free-electrons in the 5sp conduction band, while ε_{inter} accounts for electronic processes involving interband transitions from the 5d to the 5sp bands as a Lorentz-type contribution.[17] The intraband contribution to the permittivity was corrected to take into account the restricted

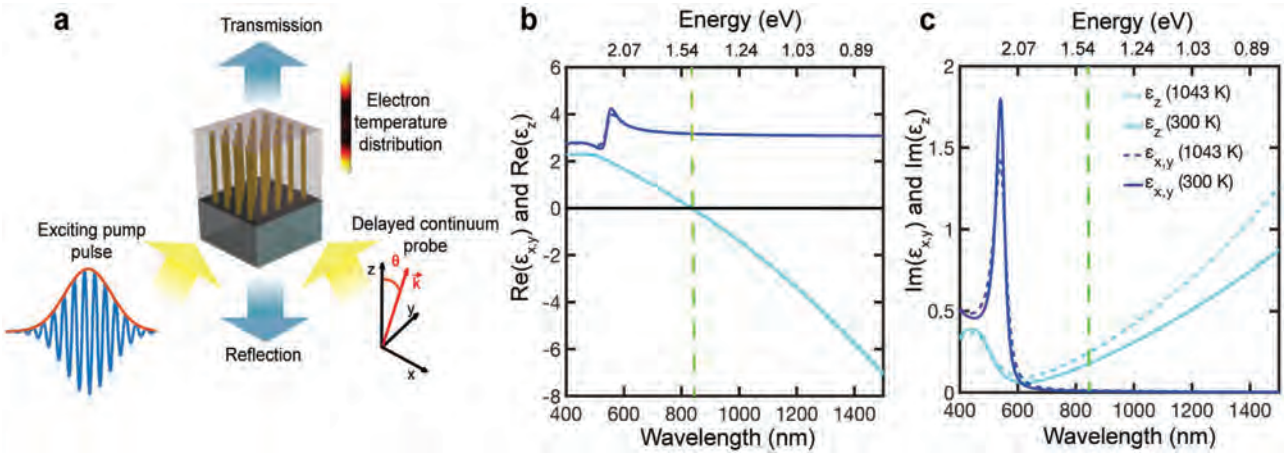

Figure 1. a) Schematic of the pump–probe experiment. An array of gold nanorods embedded in an AAO matrix on a glass substrate is illuminated by the excitation pulse, resulting in the electron temperature modification, and transmission and reflection of a white light is studied. b,c) Spectra of the real and imaginary parts of the diagonal components of the effective permittivity tensor of the metamaterial for different electron tempertures in the Au nanorods (the temperure is assumed to be uniform across the nanorods). The nanorod array parameters are $r = 15$ nm and $d = 90$ nm. The effective permittivities have been obtained using a restricted mean free path of electrons of $R = 30$ nm, considering electrons temperatures of 300 K in the ground state and 1043 K in the excited state. The dashed green lines in panels (b) and (c) indicate the effective plasma frequency.

mean free path R of electrons in the electrochemically grown nanorods with respect to the mean free path in bulk Au (R_{bulk} = 37.5 nm).[13a] Depending on metamaterial postprocessing conditions, such as thermal annealing, the restricted mean free path can take typical values ranging from $R = 3$ nm to $R = 30$ nm.

The real part of the effective permittivity component $\mathrm{Re}(\varepsilon_{x,y})$, for light polarized normal to the nanorod axis, is similar to that of a resonant dielectric while the permittivity tensor component $\mathrm{Re}(\varepsilon_z)$, for light polarized along the nanorod axis, varies monotonically from positive values at short wavelengths to negative values at longer wavelengths, crossing zero at around 830 nm, defining a transition in the metamaterial's dispersion between the regions of elliptic dispersion where $\mathrm{Re}(\varepsilon_{x,y,z}) > 0$ and hyperbolic dispersion where $\mathrm{Re}(\varepsilon_{x,y}) > 0$ and $\mathrm{Re}(\varepsilon_z) < 0$. The cross-over frequency from the elliptic to the hyperbolic regime is defined by the metamaterial's effective plasma frequency $\omega_p^{eff} = \omega(\mathrm{Re}(\varepsilon_z) = 0)$[10] around which the metamaterial behaves as the so-called ENZ medium. Nonlocal spatial dispersion effects become especially important in the description of the optical response of the metamaterial in both linear and nonlinear regimes as $\mathrm{Im}(\varepsilon_z) \to 0$.[2–11] In particular, when modal losses are low enough, the metamaterial supports the so-called additional (nonlocality-enabled) electromagnetic waves, with a significant contribution to the optical response of the system as is discussed below.[3b,11,13] These additional modes provide high-wavevector waves when $\varepsilon_h + \varepsilon_{Au} < 0$, leading to strong local fields supported by the metamaterial. It should be noted that these spatial-dispersion effects are automatically taken into account in the numerical simulations of the composite nanorod metamaterial which do not rely on effective metamaterial parameters.

2.2. Electron Gas Dynamics Modeling

Figure 1a illustrates a schematic of the pump–probe experiment reproduced in the simulations. The metamaterial is illuminated with an ultrashort control pulse and a white-light continuum probe, both transverse-magnetic (TM) polarized. The probe pulse is used to characterize the modifications of the optical properties of the metamaterial induced by the control pulse either through reflection or transmission spectra at increasing time delays following the excitation by the control pulse.

The control pulse has a Gaussian envelope with a time-dependent power $P(t) = P_0\exp(-(t - t_0)^2/t_p^2)$. The pulse is centered at $t_0 = 100$ fs and has half-width $t_p = 50$ fs. Due to absorption in gold, some of the pulse energy is deposited in the electron gas in the nanorods. The excitation process is followed by fast electron gas thermalization, establishing a Fermi-Dirac energy distribution of the electrons, characterized by an elevated temperature T_e.[2,18] This increased electron temperature is then mapped to a corresponding change of the Au permittivity through a random phase approximation (RPA) model, allowing modelling of transient optical properties of the metamaterial.[19] Figure 1b,c exemplifies the modifications of the effective permittivity tensor components for two different electron temperatures. In general, the component ε_z experiences an increase in both its real and imaginary parts in most of the frequency range except in a narrow range near the interband transitions. The effective plasma frequency ω_p^{eff} of the metamaterial decreases as the condition $\mathrm{Re}(\varepsilon_z) = 0$ red-shifts with the increasing electron temperature and, at the same time, the metamaterial experiences increased losses, which may contribute to changes in its nonlocal behavior.

The two-temperature model (TTM) is used to describe dynamics of the thermalized electron gas in gold, governed by electron–phonon and phonon–phonon scattering processes. Subsequently to the thermalization phase mainly achieved within the first few hundred femtoseconds through electron–electron scattering, electron–phonon scattering becomes the main relaxation pathway for times up to several picoseconds while phonon–phonon scattering dominates on typical timescales of tens to hundreds of picoseconds. Therefore, the

simulation of nonlinear optical processes with the THz response rates, relevant to recent experimental observations and practical applications, can neglect the influence of both electron–electron and phonon–phonon scattering on the metamaterial dynamics to a good approximation. While this affects the overall simulated dynamics of the system, it does not impact the interrelation between field distributions and ultrafast dynamics at the nanoscale, which is of interest to us here, but rather greatly simplifies numerical simulations and interpretations. With these assumptions, the temporal evolution of the electron temperature can be described by a TTM,[20] which is based on the supposition that the excited hot electrons reach thermal equilibrium instantaneously, so that the electron gas can always be described by a Fermi-Dirac distribution with a well-defined equilibrium temperature T_e. The time-space evolution of electrons temperature then follows the coupled differential heat equations[20]

$$\begin{cases} C_e(T_e)\dfrac{\partial T_e}{\partial t} = \vec{\nabla}\left(k(T_e)\vec{\nabla}T_e\right) - G\left(T_e - T_p\right) + s(\vec{r},t) \\ C_p\dfrac{\partial T_p}{\partial t} = G\left(T_e - T_p\right) \end{cases} \quad (1)$$

where $C_e(T_e) = 67.69\ \mathrm{J\ m^{-3}\ k^{-2}} \times T_e$ and $C_p = 3.5\ \mathrm{J\ m^{-3}\ k^{-2}}$ are the volumetric heat capacity of electrons and phonons, respectively, T_p is the phonon temperature, $k(T_e) = k_0(T_e/T_p) = 318(T_e/T_p)$ $\mathrm{W\ m^{-1}\ K^{-1}}$ is the electron thermal conductivity, $G = 2 \times 10^{16}\ \mathrm{W\ m^{-1}\ K^{-1}}$ is the electron–phonon coupling constant, and $s(\vec{r},t)$ is the incident light power density absorbed by the metamaterial. During the first few picoseconds following the optical excitation, the electron temperature increase exceeds that of phonons by up to several orders of magnitude due to the much higher heat capacity of phonons, providing good ground to assume T_p being constant during the time of interest to us. The second equation of the TTM is thus neglected in the simulations, keeping the phonon temperature constant at 300 K. Equation (1) is solved numerically for the electron equilibrium temperature in the nanorod geometry, so that a temperature-dependent permittivity distribution in the nanorods is monitored at various time delays following the excitation.

The time-dependent modifications of the effective permittivity tensor obtained using the TTM are plotted in **Figure 2** as the relative changes of the tensor components, assuming uniform electron temperature in the nanorods. The strongest relative changes of the real parts of effective permittivities are observed at different wavelengths for different light polarizations, with $\mathrm{Re}(\varepsilon_z)$ varying strongest near the effective plasma frequency, while $\mathrm{Re}(\varepsilon_{x,y})$ and the imaginary parts of the tensor components experience the biggest change in the range of interband transitions. Both real and imaginary parts of the permittivity components are modified, with the imaginary part being affected strongest in relative terms. While effective parameters provide interesting insight and guidance for intuitive nonlinearity understanding, how the modifications of the effective permittivity are reflected in the changes of the optical properties depends on the modal structure of the metamaterial slab, and, generally, considerations beyond the local effective medium theory are required to adequately describe the processes involving electromagnetic fields inside the metamaterial.[11] In the following, we will make use of the effective medium properties solely to understand the

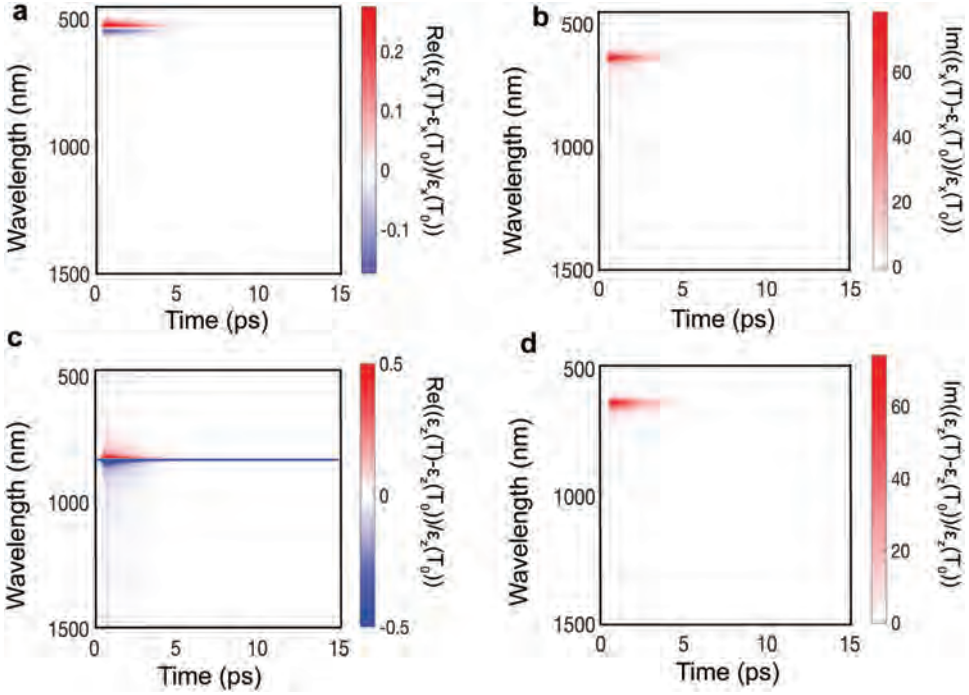

Figure 2. Time dependence of the relative volume-averaged changes in the effective permittivity components $(\varepsilon(T) - \varepsilon(T_0))/\varepsilon(T_0)$ for a) $\mathrm{Re}(\varepsilon_x)$, b) $\mathrm{Im}(\varepsilon_x)$, c) $\mathrm{Re}(\varepsilon_z)$, and d) $\mathrm{Im}(\varepsilon_z)$ for an absorbed power density of 0.1 μW cm^{-2}. Electron temperature is assumed to be uniform along the nanorods. Note that the scale was constrained in panel (c) since the relative change in $\mathrm{Re}(\varepsilon_z)$ diverges at $\mathrm{Re}(\varepsilon_z) \to 0$. The absolute values of the permittivities are shown in Figure 1b,c.

results of numerical simulations of the nonlinear behavior of the metamaterial, which is based on direct solutions of vectorial Maxwell equations for a nanorod array.

2.3. Nonlinear Response Modeling

Transient spectra recorded in a pump–probe experiment can be reproduced in numerical simulations applying two independent steps. In a first step, the pump-induced changes in the Au nanorod permittivity are simulated at different times following optical excitation. This first step provides a set of time-dependent Au permittivities, which are introduced in the linear optical simulations in a second step to compute the transient transmission or reflection of the metamaterial as independent steady-state effective permittivities seen by the probe light. This approximation is valid as long as nonlinear interactions between pump and probe pulses can be neglected. In our study, we considered the AAO matrix to be nondispersive and with linear optical response in the frequency range and pump intensity range of interest. The effect of modal structure on the ultrafast dynamics of the metamaterial was further assessed by comparing it to the dynamics of the same system when the spatial profile of the electron temperature is neglected. In this geometry, the dynamics was simulated setting the electronic temperature to be homogeneous across the nanorods with a value set by the TTM without the diffusion term.

3. Results and Discussion

3.1. Linear Optical Properties of the Metamaterial Slab

In order to understand the modal structure of the metamaterial, both its linear reflection and extinction spectra were calculated with local and nonlocal EMTs (**Figure 3**).[11,13] Here, we restrict the study to the optical properties of the metamaterial under TM-polarized plane-wave excitation with which both elliptic and hyperbolic dispersion regimes can be assessed. The local EMT assumes that the metamaterial supports propagation of a single TM-polarized mode with the dispersion given by the EMT parameters in Figure 1b,c. The nonlocal EMT shows the existence of two TM-polarized modes simultaneously propagating in the metamaterial. Both models adequately describe the optical response of the nanorod metamaterial for relatively small angles of incidence (AOI). However, as the AOI increases, the accuracy of the local EMT diminishes. At the same time, the nonlocal EMT adequately describes the optical properties of the nanorod metamaterial for the whole range of frequencies and incident angles and is in excellent agreement with the full vectorial numerical simulations of the nanorod array composite (**Figure 4**a,c).

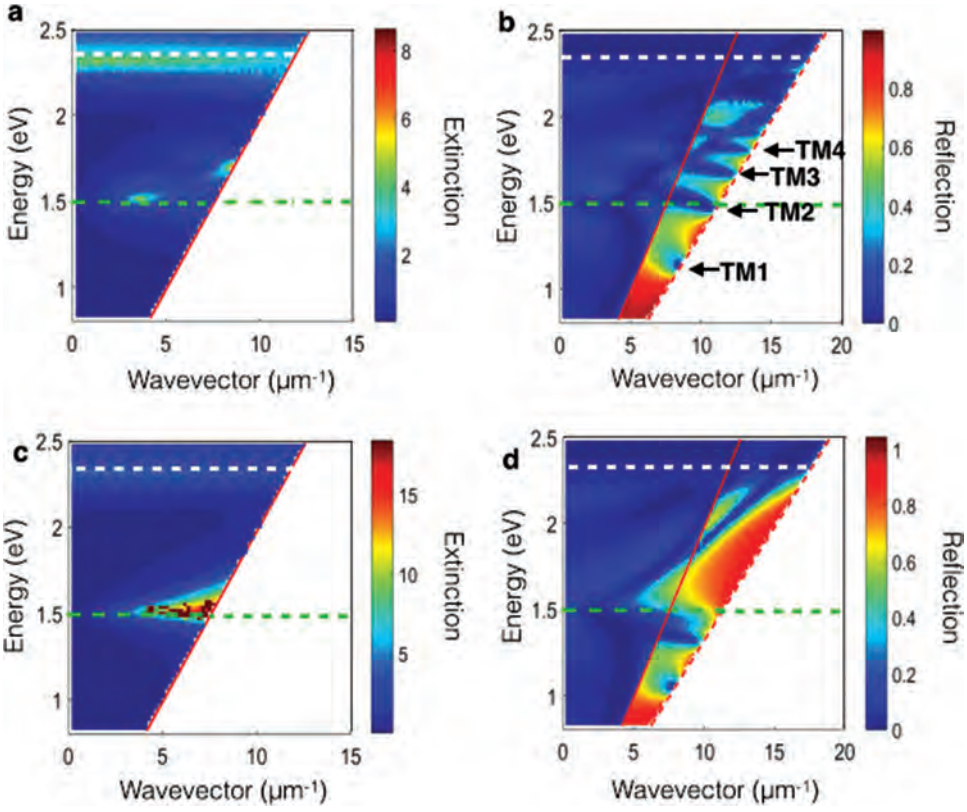

Figure 3. Dispersions of the linear a,c) extinction and b,d) reflection of the metamaterial slab, calculated with a,b) nonlocal and c,d) local effective medium theory. The nanorod array parameters are as in Figure 1 and the metamaterial slab thickness (the nanorod length) is 350 nm. The light lines in air and the substrate are indicated as continuous and dashed red lines, respectively. The effective plasma frequency obtained from the local EMT is shown with a green line. The condition $\varepsilon_h + \varepsilon_{Au} < 0$ is indicated with a white dashed line. The waveguided mode orders are identified in panel (b).

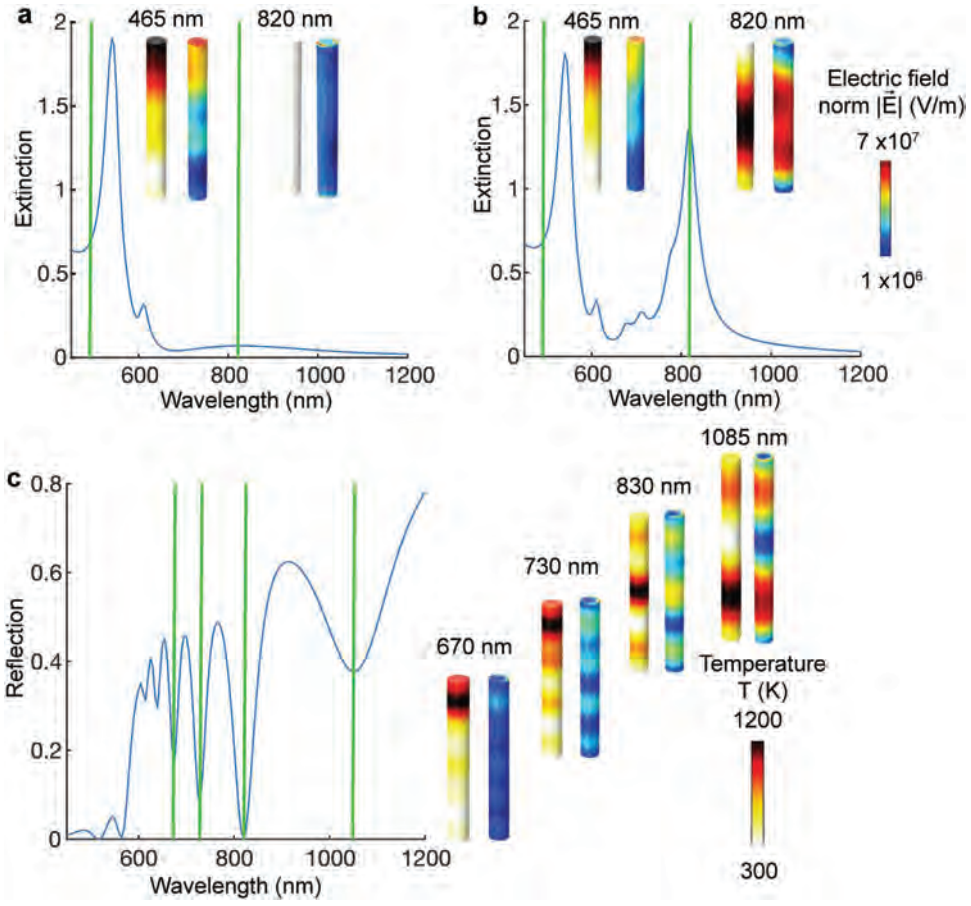

Figure 4. a,b) Linear extinction and c) reflection spectra of the metamaterial. The spatial distribution of the norm of the electric field and the associated electron temperature distribution in the nanorods achieved during the excitation are also shown for selected excitation conditions: (a) 465 nm and 820 nm at normal incidence, (b) 465 and 820 nm at 20° AOI, (c) 670, 730, 830, and 1085 nm at 60° AOI. The nanorods are illuminated from the top. The excitation fluence is 0.1 mJ cm^{-2}. The metamaterial parameters are as in Figure 3.

The extinction dispersion, plotting angular and spectral dependence of OD = $-\log_{10}(T)$, where T represents the transmission of the metamaterial, reveals two distinct resonances at around 525 nm (2.36 eV) and a double-peak resonance at 820 nm (1.51 eV) and 730 nm (1.7 eV) (Figure 3a). The short-wavelength peak is essentially dispersion-less and corresponds to the resonance in the spectrum of ε_x seen in Figure 1b,c which can be excited with an electric field component polarized normal to the nanorod axes. For light polarized along the nanorod axes, the extinction has strong angular dependence. In particular, a mode splitting is observed at around 30° near the effective plasma frequency, which corresponds to the existence of an additional TM wave in the metamaterial as compared to the local response. This is a signature of nonlocality originating from the cylindrical surface plasmons nature of the modes supported by the nanorods.[3b,13] This behavior is determined by the internal structure of the metamaterial, which cannot be recovered in a conventional, local effective medium theory.

The minima in the reflection dispersion correspond to the incident light coupling to cavity modes of the metamaterials slab (Figure 3b). Above the light line in the superstrate (air), these modes are unbound Fabry–Perot-type resonances of the planar metamaterial slab accessible from both the superstrate and the substrate. Between the light line in air and the light line in the substrate, the modes are evanescent at the metamaterial–air interface and leaky in the substrate, therefore, only accessible to plane waves from the substrate side at the angles of incidence above the critical total internal reflection angle.[10] These modes have the unusual property of low negative group velocity, appearing relatively flat in the dispersion plots.[10,21] They can be identified from their characteristic field distributions with several lower order modes ($q = 1, 2, 3, 4$) shown in Figure 3b. The TM-guided modes above the effective plasma frequency originate from the additional wave in the nonlocal material and exist in the range of frequencies where $\varepsilon_h + \varepsilon_{Au} < 0$. The predictions of the nonlocal EMT agree with the full-wave solutions of Maxwell equations that take into account the composite structure of the material.

To underline the importance of nonlocality in the description of the observed guided modes, we have repeated the simulations with a conventional (local) EMT (Figure 3 c,d). Both extinction and reflection spectra fundamentally change as the result of this approximation. The double resonance observed in the nonlocal extinction disappears in the local regime, leaving only a single resonance at a wavelength of around 820 nm. In addition, the negative group velocity modes are only present below the effective plasma frequency where the local effective

medium theory provides adequate description of the optical response of the metamaterial. Only TM1 and TM2 modes are predicted by the local EMT model. Higher order modes are eneabled by nonlocality and cannot be predicted by the local EMT. Interestingly, the increased losses in Au primarily affect the high-index nonlocal waves, thus driving the metamaterial response toward the predictions of the local EMT.

We will now study the potential of various modes of the metamaterial slab for optimization of the magnitude and dynamics of the nonlinear response of the metamaterial.

3.2. Transient Nonlinear Dynamics for Local and Average Electron Temperatures

The dynamics of the optical response of the metamaterial can be expressed as $\frac{\mathrm{d}O}{\mathrm{d}t} = \frac{\partial O}{\partial \varepsilon}\frac{\partial \varepsilon}{\partial T_\mathrm{e}}\frac{\partial T_\mathrm{e}}{\partial t}$, where O symbolizes the monitored optical properties, such as, e.g., reflection or transmission determined by the modal structure of the metamaterial, ε is the effective permittivity of the metamaterial, and T_e is the electron temperature (Equation (1)). The first term on the right-hand side depends on the modal properties of the metamaterial slab and incorporates the spectral dependence of the resonant response of the supported modes. The second term describes how the effective permittivity depends on an electron temperature, which is modelled via the RPA. The third term bears the intrinsic transient dynamics of the electron gas, which can be modeled via the TTM. Both the electron temperature diffusion term $\vec{\nabla}(k(T_\mathrm{e})\vec{\nabla}T_\mathrm{e})$ and the source term $s(\vec{r},t)$ in Equation (1) are of importance when considering nanostructured materials because they incorporate a spatial dependence of the electron temperature dynamics, being driven by the modal properties of the metamaterial. Indeed, the energy deposited by the excitation pulse in the metamaterial, which is expressed as $s(\vec{r},t) \approx \sum_{\mathrm{mode}i} \mathrm{Im}(\alpha_i(\vec{r},t,\omega_\mathrm{pump}))\int_V \vec{E}_\mathrm{pump}(\vec{r},t,\omega_\mathrm{pump})\cdot\vec{E}_i^*(\vec{r},t,\omega_\mathrm{pump})\mathrm{d}V$, depends on both the overlap between the modes supported by the metamaterial $\vec{E}_i(\vec{r},t)$ and the excitation field $\vec{E}_\mathrm{pump}(\vec{r},t)$, as well as the modal absorption $\mathrm{Im}(\alpha_i(\vec{r},t,\omega_\mathrm{pump}))$ with $\alpha_i(\vec{r},t,\omega_\mathrm{pump})$ being the polarizability of mode i. The choice of the illumination conditions will, therefore, determine the energy transferred from the excitation pulse to the metamaterial and, through Equation (1), the subsequent dynamics of hot electrons and the associated nonlinear response. Figure 4 shows the correspondence between the selected metamaterial modes, which can be excited by plane waves, and the induced electron temperature. The volume-averaged temperature increase is of the order of 10^3 K for a 0.1 mJ cm^{-2} fluence of the excitation light at a 465 nm wavelength and is weakly angular dependent, with an absorption mainly determined by a small spectral overlap with the maxima of the imaginary parts of the effective permittivity (Figure 4a). In contrast, detuning the excitation conditions from both material and geometrical resonances, e.g., for a wavelength of 820 nm at normal incidence, leads to a relatively negligible temperature increases on the order of 10 K (Figure 4a). For this wavelength, a more significant $\approx 10^3$ K increase of electron temperature is only observed at oblique incidence for which the excitation is resonant with a mode supported by the metamaterial slab (Figure 4b). In addition to the magnitude

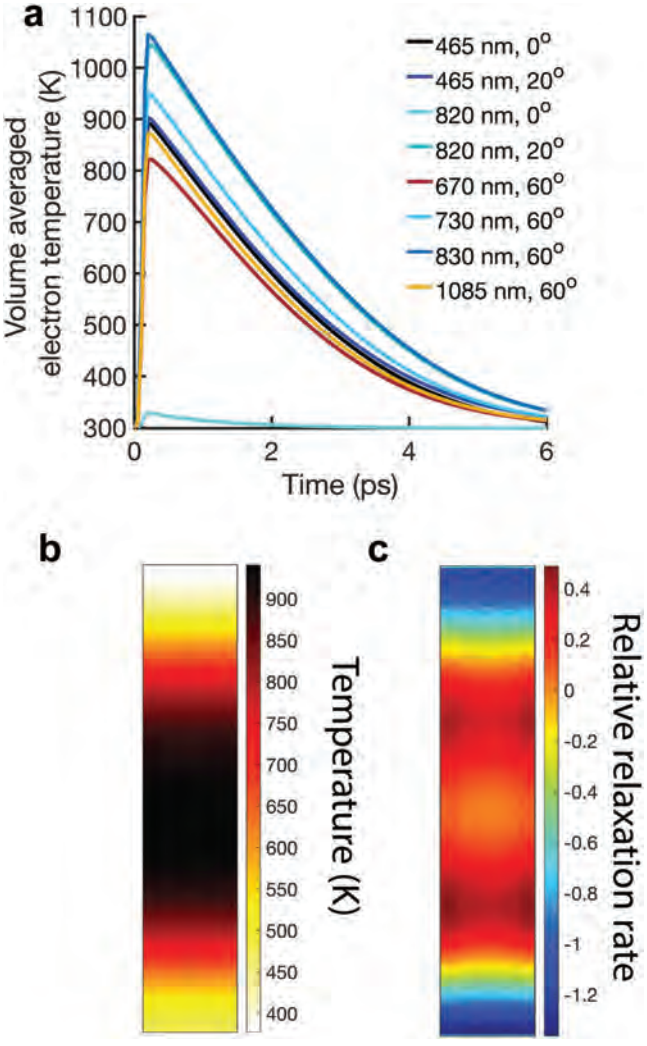

Figure 5. The dynamics of a) volume-averaged electron temperature in the nanorods for various excitation conditions. b) Position-dependent electron temperature at different points inside the nanorods for a TM-polarized excitation pulse (820 nm wavelength, 20° AOI, 0.1 mJ cm^{-2} fluence) at t = 200 fs plotted in the plane containing the symmetry axis of the nanorod. c) Relative instantaneous electron temperature dynamics $(\mathrm{d}T_\mathrm{e}(\vec{r})/\mathrm{d}t - \mathrm{d}<T_\mathrm{e}>_{\vec{r}}/\mathrm{d}t)/(\mathrm{d}<T_\mathrm{e}>_{\vec{r}}/\mathrm{d}t)$ showing non-uniform, position-dependent electron cooling in the nanorod.

of the absorption, tuning the illumination conditions to excite specific metamaterial modes enables the control of the electron temperature spatial distribution (Figure 4). This is particularly remarkable when the excitation of the metamaterial in reflection (Figure 4c) clearly recovers the spatial field distribution of modes q = 2 through q = 5 in the electron temperature maps. Moreover, while the third term in Equation (1) allows to map the incident power to the position-dependent absorbed power, the heat diffusion term in Equation (1) establishes a direct link between the modal field distribution and the local electron relaxation dynamics. Assuming a temperature-independent electronic temperature diffusion rate $k(T_\mathrm{e}) \approx k$, this contribution to the dynamics is governed by the curvature of the temperature profile $\nabla^2 T_\mathrm{e}$ which together with the electron–phonon coupling term establishes an interrelationship between modal properties

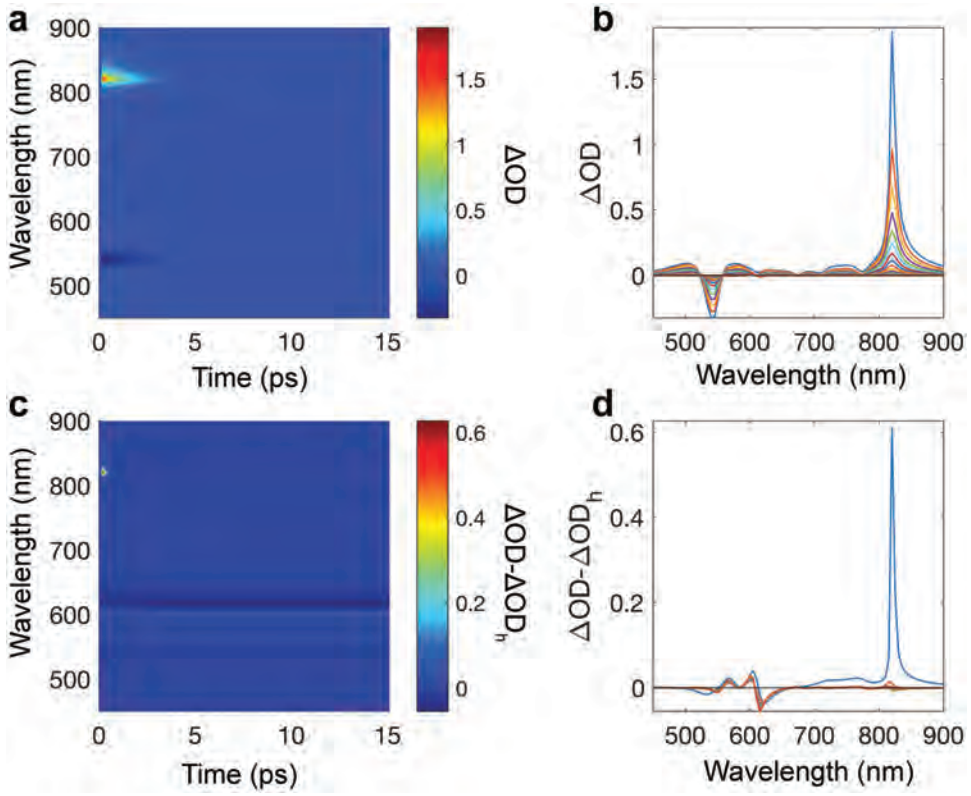

Figure 6. a) Spectral map of the transient extinction ΔOD of the metamaterial for a TM-polarized excitation pulse (820 nm wavelength, 20° AOI) as observed with a white-light TM-polarized probe at 20° AOI. b) Transient extinction spectra at different times after the excitation (cross-sections obtained from panel (a)). c) Transient extinction dynamics of the metamaterial as in panel (a) relative to the transient extinction of the metamaterial considering a volume-averaged (uniform) electron temperature in the nanorods. d) Spectral cross-sections obtained from panel (c) at different times after the excitation showing the spectral sensitivity of the nonlinear responce on the position-dependent electron temperature.

and ultrafast time response. This enables an opportunity to use nanostructured systems and their intricate and tailorable resonant field distributions to design the ultrafast response at the nanoscale by geometrical means.

Let us now compare the dynamics associated with the local electron temperature effects to the volume-averaged dynamics of the electron gas. In the latter case, we assume that a uniform electron temperature distribution along the nanorods is established instantaneously. In this case, the time constant of the recovery of the electron temperature, as expressed by the TTM, is determined by the electron–phonon scattering rate for a given absorbed energy, since the difusion term is absent (Equation (1)). **Figure 5**a shows that the general trend is for this time constant to increase with the amount of energy deposited in the electron gas by the excitation pulse, as expected from the temperature dependence of the elecron scattering rates. However, Equation (1) tells us that the electron temperature relaxation dynamics is potentially more complex when considering resonant structures in the presence of the heat diffusion term.

To show the influence of the diffusion term in the electron cooling dynamics, Figure 5c plots the relative changes in the instantaneous dynamics $(\mathrm{d}T_e(\vec{r})/\mathrm{d}t - \mathrm{d} < T_e >_{\vec{r}}/\mathrm{d}t)/(\mathrm{d} < T_e >_{\vec{r}}/\mathrm{d}t)$ of the electron temperature corresponding to the temperature distribution in Figure 5b, where $T_e(\vec{r})$ is the position-dependent electron temperature and $< T_e >_{\vec{r}}$ is the position-averaged electron temperature obtained in the absence of the diffusion term. The diffusion term can significantly influence the electron temperature dynamics at selected locations within the nanorod (Figure 5c). In particular, while at some locations within the nanorods the electron relaxation is accelerated by the inhomogeneous electron temperature distribution by more than 40%, other locations show a slowed down relaxation process by more than 120%, with an average dynamics described by the TTM in the absence of the diffusion term.

The transient spectral maps ΔOD(λ, t) for the metamaterial with the linear optical properties as in Figure 3a are shown in **Figure 6**a for the excitation conditions as in Figure 5c,d when probed in transmission at an AOI of 20°. As mentioned above, the dynamics of the optical properties of the metamaterial at selected wavelengths is not necessarily that of the electronic temperature since $\frac{\partial O}{\partial T_e} = \frac{\partial O}{\partial \varepsilon}\frac{\partial \varepsilon}{\partial T_e}$ comes into play when characterizing the dynamics of optical properties. In particular, the resonant response of the metamaterial adds to the complexity of the dynamics through this dependence, which is determined by both the absorptive and dispersive behavior of the resonances present in the transient extinction or reflection spectra. This will usually result in a non-monoexponential relaxation behavior of the nonlinear response at any given frequency of the resonant nanostructured material.

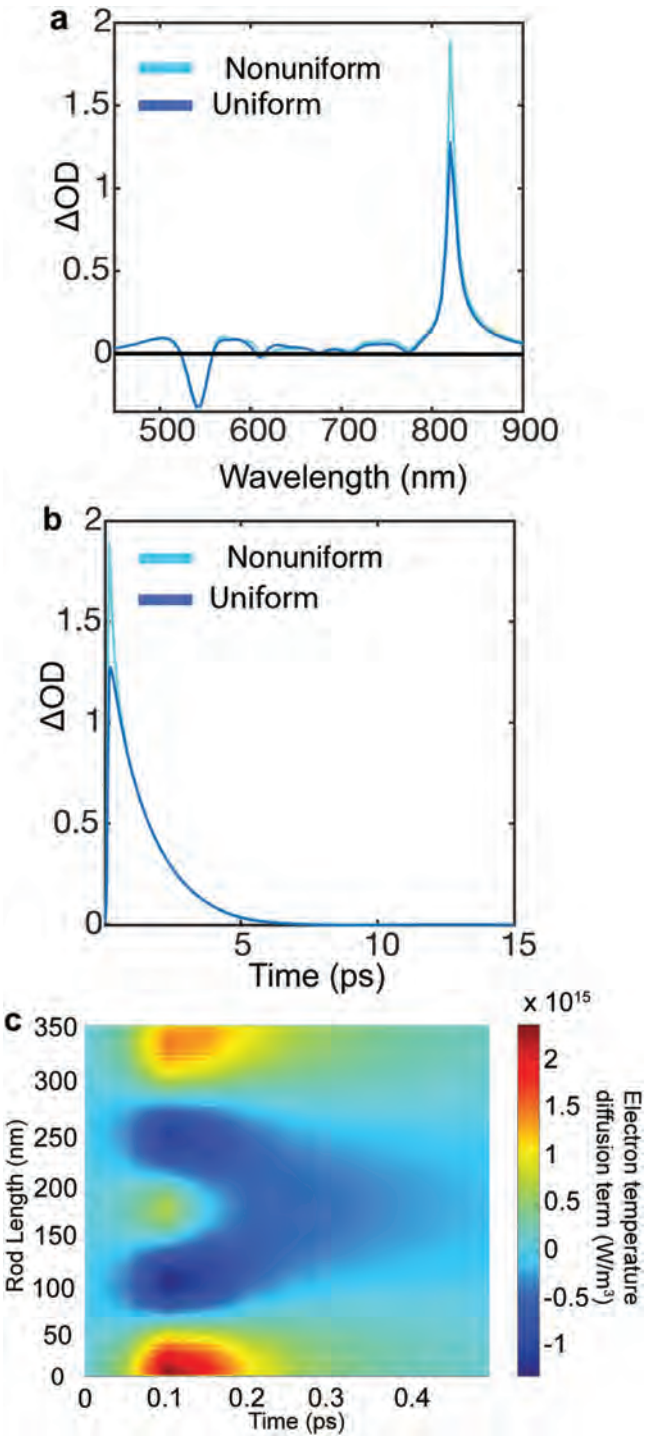

Figure 7. a) Transient extinction for both position-dependent and uniform electronic temperatures at t = 200 fs after the excitation and b) associated dynamics at a probe wavelength of 820 nm, corresponding to the maximum in transient extinction in panel (a). c) Time dependence of the diffusion term plotted along the axis of a nanorod. Note that the time scale in panel (c) is different from panel (b), focusing on the first 500 fs following the excitation.

Selected spectral cross-sections of the nonlinear dynamics (Figure 6a,b) show the absorptive behavior of the high-frequency resonance, which is governed by a transient broadening, and the more complex spectral behavior in the hyperbolic spectral range. The impact of the position-dependent absorption (and, thus, the position-dependent electron temperature) on the transient optical properties of the metamaterial is shown in Figure 6c, which plots the transient dynamics of Figure 6a relative to the dynamics of the metamaterial assuming a uniform electron temperature across the nanorods. The strongest difference in dynamics is observed at very short time scales (within 100 fs of the excitation) in the ENZ regime (Figure 6d). In fact, the relative transient transmission change for the nonuniform electron temperature exceeds by almost one order of magnitude that of the uniform temperature assumption at the wavelength of 820 nm (cf. **Figure 7**). This difference results from the strong spatial overlap between the excitation-induced electron temperture distribution and the field distribution of the probe as clearly revealed in the transient transmission for both the nonuniform and uniform electron temperature distributions (Figure 7a). It shows that for both metamaterial resonances accessible in transmission, at around 525 nm and 820 nm, an enhanced nonlinear response is recorded in the wavelength range corresponding to the maximum spatial overlap between the probe mode and the spatial distribution of the excitation-induced permittivity changes. Here, this maximum overlap is achieved when probing in the ENZ spectral range where the excitation energy is initially deposited. In addition to affecting the magnitude of the transient extinction in the early times following optical pumping, the dynamic response in the ENZ regime experiences a deacreased recovery time. In fact, the dynamics for the nonuniform temperature distribution shows two time constants of 0.1 ps and 1.4 ps, compared to a single time constant of 1.5 ps obtained for the uniform temperature (Figure 7b). The short sub-ps time constant is related to the modal mapping of the electron temperature distribution, governing the dynamics of the transmission at the time scales of heat diffusion within the nanorod. Both uniform and nonuniform temperture dynamics converge within a time frame of ≈400 fs, corresponding to the time in which the electron temperature has mostly homogenized within the nanorod, minimizing the contribution of the heat diffusion term in Equation (1) with respect to the electron–phonon scattering term (Figure 7c).

3.3. Nonlinear Optical Response of the Metamaterial Slab

We now consider the full dispersion dynamics of both the extinction and reflection of the metamaterial after the excitation by a control pulse at a wavelength of 820 nm and an angle of incidence of 20°. This excitation configuration has been chosen as it induces the electron temperature changes which overlap the spatial distribution of various metamaterial modes, thus providing a pathway to assess their nonlinear optical properties. The restriction path was kept at R = 30 nm allowing the investigation of the role of a rich modal structure of the metamaterial slab and the role of nonlocal behavior. The nonlinear response of the metamaterial slab in the local EMT regime has been studied elsewhere.[9] The dispersions of linear extinction OD = $-\log_{10}(T_0)$ and reflection R_0 are shown in **Figure 8**a,c together with the associated disperions of the transient extinction ΔOD = $-\log_{10}(T/T_0)$ and ΔR =

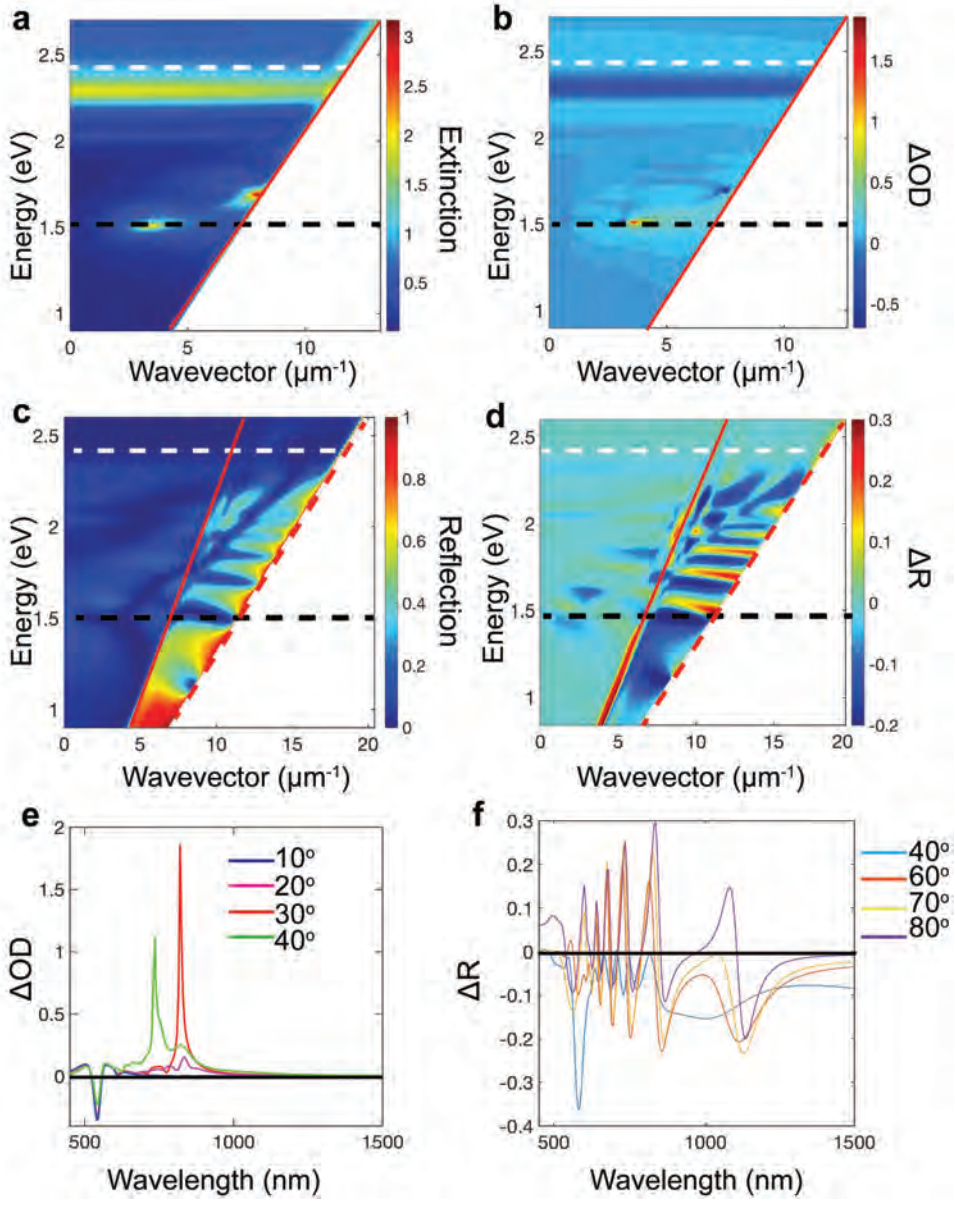

Figure 8. a) Extinction and c) reflection dispersions of the metamaterial with the parameters as in Figure 1. b,d) Nonlinear transient differential dispersions of the metamaterial calculated 200 fs after excitation with a 50 fs excitation pulse centered at a wavelength of 820 nm and at the angle of incidence of 20° for (b) transmission and (d) reflection. Excitation and probe light are TM-polarized. The light line in air and in the substrate are indicated by solid and dashed red lines, respectively. The effective plasma frequency is shown by a horizontal black dashed lines. The condition $\varepsilon_h + \varepsilon_{Au} < 0$ is indicated by white dashed lines. e,f) Cross-sections of nonlinear extinction (e) and reflection (f) from panels (b) and (d), respectively, at the selected angles of incidence.

$(R - R_0)$ shown in Figure 8b,d at the time 200 fs after the excitation (here, T and R are the time-dependent transmission and reflection of the metamaterial, respectively). In the wavelength range of the elliptic dispersion, the strongest changes in the extinction are observed near the resonance of ε_x, essentially determined by an increased damping of the resonance (Figure 8e) as seen in Figure 6a,b. This nonlinear response is not sensitive to the angle of incidence in this spectral range. The induced extinction changes in the hyperbolic dispersion regime are strongly angular dependent but also follow the extinction spectrum features. Similarly, the nonlinear response in reflection are also governed by the modal structure of the metamaterial slab (Figure 8d,f) with the induced changes being much stronger for the leaky modes below the light line than the Fabry–Perot-type modes above the light line.

Varying the excitation wavelength throughout the elliptic and hyperbolic dispersion range and different angles of incidence of the excitation pulse mostly influences the modulation depth and time response, while the shape of the spectral response remains mostly unchanged, completely determined by the linear modal structure of the metamaterial slab. Since the modulation depth is determined by the electron temperature

increase induced by the illumination, it is stronger for the wavelength/angle of incidence combinations for which strong absorption is reached. The absolute modulation in reflection reaches, in absolute values, more than 10% for cavity modes and 30% for guided modes for all pump–probe wavelength and angles of incidence configurations for which these resonances are probed. Interestingly, due to the dominating nonlocal mode structure in the elliptic regime, the nonlinear changes are very strong on both sides of the effective plasma frequency of the metamaterial. When losses in Au are increased, e.g., in the electrodeposited, unannealed Au nanorods, the situation changes and nonlinearity in the elliptic regime is strongly suppressed.

4. Conclusion

We have studied the hot-electron dynamics and diffusion in plasmonic nanorods forming a metamaterial composite. A microscopic model allows us to take into account the nonuniform profile of the electron temperature distribution within the nanorods, which depends on the modal distribution at the excitation wavelength and determines the magnitude and the dynamics of the transient nonlinear response. This opens up the possibility to study nonequlibrium electron dynamics in plasmonic nanostructures via the observation of their nonlinear optical response and, in turn, to engineer the magnitude and dynamics of nonlinear transients in plasmonic metamaterials via reshaping the excitation absorption profile, and, thus, the electron temperature profile, by engineering of the metamaterial's modal structure. For the metamaterial under consideration, the superposition of the control light-induced absorption profile with that of the probe beam in the ENZ spectral region allows to obtain the fastest transient behavior with a time constant of around 100 fs governed only by electron-phonon scattering and electron diffusion. The rich spectrum of the modes of the metamaterial slab provides opportunities to engineer the sign and the temporal response of the nonlinearity in transmission and reflection or for waveguided modes by selectively coupling signal and control light to the modes of the metamaterial slab.

The relaxation time of the optical response monitored through the observation of the transient reflection and extinction, while linked to the relaxation time of the electron temperature distribution within the nanorods, may differ from the latter. The spatial distribution of the electron temperature within the nanorod has an important influence on the metamaterial dynamics at relatively short times following the excitation, when the diffusion term in the TTM is not zero, either accelerating or slowing the relaxation process at different locations within the metamaterial, compared to the uniform electron temperature approximation. The results show the opportunities to control the electron dynamics and, thus, the time response of nanostructured plasmonic systems by tailoring the modal properties of the metamaterial. The engineering of the relaxation dynamics via nanostructuring of plasmonic systems may have many implications in nonlinear optics as well as for hot-electron effects in photophysics and optoelectronics.

Acknowledgements

This work was supported, in part, by the EPSRC (UK) projects EP/H000917/2, EP/J8457/1 and EP/M013812, the ERC iPLASMM project (321268), and the US Army Research Office (Grant Nos. W911NF-12-1-0533 and W911NF-16-1-0261). A.V.Z. acknowledges support from the Royal Society and the Wolfson Foundation. G.A.W. acknowledges support from the EC FP7 project 304179 (Marie Curie Actions). The data access statement: All data supporting this research are provided in full in the results section.

Conflict of Interest

The authors declare no conflict of interest.

Keywords

hot electrons, nonlinear photonics, plasmonic metamaterials, ultrafast optics

Received: March 29, 2017
Revised: May 4, 2017
Published online: July 13, 2017

[1] a) M. L. Brongersma, N. J. Halas, P. Nordlander, *Nat. Nanotechnol.* **2015**, *10*, 25; b) S. Linic, U. Aslam, C. Boerighter, M. Morabito, *Nat. Mater.* **2015**, *14*, 567; c) P. Narang, R. Sundararaman, H. A. Atwater, *Nanophotonics* **2016**, *5*, 96; d) A. Pescaglini, A. Martin, D. Cammi, G. Juska, C. Ronning, E. Pelucchi, D. Iacopino, *Nano Lett.* **2014**, *14* : 6202; e) H. Harutyunyan, A. B. F. Martinson, D. Rosenmann, L. K. Khorashad, L. V. Besteiro, A. O. Govorov, G. P. Wiederrecht, *Nat. Nanotechnol.* **2015**, *10*, 770.

[2] G. A. Wurtz, R. Pollard, W. Hendren, G. P. Wiederrecht, D. J. Gosztola, V. A. Podolskiy, A. V. Zayats, *Nat. Nanotechnol.* **2011**, *6*, 106.

[3] a) C. M. Soukolis, M. Wegener, *Nat. Photonics* **2011**, *5*, 523; b) K.-T. Tsai, et al., *Nano Letters* **2014**, *14*, 4971; c) N. I. Zheludev, Y. S. Kivshar, *Nat. Mater.* **2012**, *11*, 917.

[4] M. Kauranen, A. V. Zayats, *Nat. Photonics* **2012**, *6*, 737.

[5] a) K. F. MacDonald, N. I. Zheludev, *Laser Photonics Rev.* **2010**, *4*, 562; b) A. D. Neira, M. E. Nasir, W. Dickson, G. A. Wurtz, A. V. Zayats, *Nat. Commun.* **2015**, *6*, 7757.

[6] M. X. Ren, B. H. Jia, J. Y. Ou, E. Plum, J. F. Zhang, K. F. MacDonald, A. E. Nikolaenko, J. J. Xu, M. Gu, N. I. Zheludev, *Adv. Mater.* **2011**, *23*, 5540.

[7] a) A. Marini, M. Conforti, G. Della Valle, H. W. Lee, T. X. Tran, W. Chang, M. A. Schmidt, S. Longhi, P. S. J. Russell, F. Biancalana, *New J. Phys.* **2013**, *15*, 033850; b) N. Rotenberg, J. N. Caspers, H. M. van Driel, *Phys. Rev. B* **2009**, *80*, 245420.

[8] O. Lysenko, M. Bache, N. Oliver, A. V. Zayats, A. Lavrinenko, *ACS Photonics* **2016**, *3*, 2324.

[9] N. Vasilantonakis, G. A. Wurtz, V. A. Podolskiy, A. V. Zayats, *Opt. Express* **2015**, *23*, 14329.

[10] N. Vasilantonakis, M. E. Nasir, W. Dickson, G. A. Wurtz, A. V. Zayats, *Laser Photonics Rev.* **2015**, *9*, 345.

[11] P. Ginzburg, D. Roth, M. Nasir, P. Segovia Olvera, A. Krasavin, J. Levitt, L. Hirvonen, B. Wells, K. Suhling, D. Richards, V. Podolskiy, A. Zayats, *Light: Sci. Appl.* **2017**, *6*, e16273.

[12] A. D. Neira, G. A. Wurtz, P. Ginzburg, A. V. Zayats, *Opt. Express* **2014**, *22*, 10987.

[13] a) R. J. Pollard, A. Murphy, W. R. Hendren, P. R. Evans, R. Atkinson, G. A. Wurtz, A. V. Zayats, V. A. Podolskiy, *Phys. Rev. Lett.* **2009**, *102*, 127405; b) B. M. Wells, A. V. Zayats, V. A. Podolskiy, *Phys. Rev. B* **2014**, *89*, 035111.
[14] a) R. L. Chang, H. P. Chiang, P. T. Leung, D. P. Tsai, W. S. Tse, *Solid State Commun.* **2005**, *133*, 315; b) R. L. Chern, *Opt. Exp* **2013**, *21*, 16514.
[15] T. J. Echtermeyer et al., L. Britnell, P. K. Jasnos, A. Lombardo, R. V. Gorbachev, A. N. Grigorenko, A. K. Geim, A. C. Ferrari, K. S. Novoselov, *Nat. Commun.* **2011**, *2*, 458; b) N. K. Emani, T. F. Chung, X. J. Ni, A. V. Kildishev, Y. P. Chen, A. Boltasseva, *Nano Lett.* **2012**, *12*, 5202; c) A. M. Gilbertson, Y. Francescato, T. Roschuk, V. Shautsova, Y. G. Chen, T. P. H. Sidiropoulos, M. H. Hong, V. Giannini, S. A. Maier, L. F. Cohen, R. F. Oulton, *Nano Lett.* **2015**, *15*, 3458.
[16] J. Elser, R. Wangberg, V. A. Podolskiy, E. E. Narimanov, *Appl. Phys. Lett.* **2006**, *89*, 261102.
[17] R. W. Boyd, Z. M. Shi, I. De Leon, *Opt. Commun.* **2014**, *326*, 74.
[18] G. A. Wurtz, J. Hranisavljevic, G. P. Wiederrecht, N. Grp, *Org. Optoelectron. Photonics* **2004**, *5464*, 176.
[19] a) R. W. Boyd, *Nonlinear Optics*, Academic Press, Burlington, MA **2008**; b) T. Holstein, *Phys. Rev.* **1954**, *96*, 535; c) S. J. Youn, T. H. Rho, B. I. Min, K. S. Kim, *Phys. Status Solidi B* **2007**, *244*, 1354.
[20] J. K. Chen, D. Y. Tzou, J. E. Beraun, *Int. J. Heat Mass Transfer* **2006**, *49*, 307.
[21] A. D. Neira, G. A. Wurtz, A. V. Zayats, *Sci. Rep.* **2015**, *5*, 17678.